

Creep Behaviour of Flax Fibre Composites

An assessment of the stepped isostress method for predicting long-term creep behaviour of flax fibre-reinforced polymer composites

Emma van Amsterdam

Creep Behaviour of Flax Fibre Composites

An assessment of the stepped isostress method
for predicting long-term creep behaviour of flax
fibre-reinforced polymer composites

by

Emma van Amsterdam

to obtain the degree of Master of Science, Civil Engineering
Building Engineering track, with Structural Design specialization
at the Delft University of Technology

Student: E. L. N. van Amsterdam
Student number: 4590872

Thesis committee: Dr. Y. (Yasmine) Mosleh, TU Delft (chair)
Dr. ir. R. C. (René) Alderliesten, TU Delft
Dr. ir. F. P. (Frans) van der Meer, TU Delft
Ir. V. P. (Valentin) Perruchoud, TU Delft (daily supervisor)
Ir. W. (Wouter) Claassen, Witteveen+Bos (company supervisor)

Project duration: September 2023 – February 2025
Faculty: Civil Engineering and Geosciences, Delft University of Technology
Company: Witteveen+Bos, Deventer

Cover credits: <https://noorderland.nl/artikel/608575>

A digital version of this thesis is available at <http://repository.tudelft.nl/>.

Preface

This thesis marks the end of my graduation project for the MSc Building Engineering at the Faculty of Civil Engineering and Geosciences, at Delft University of Technology. Throughout this project, I have really enjoyed the hands-on lab work and the opportunity to collaborate with the many people who contributed to this project in different ways.

First, I am deeply grateful to my graduation committee, Yasmine Mosleh, René Alderliesten, Frans van der Meer, Valentin Perruchoud, and Wouter Claassen, for their guidance, enthusiasm, and positivity during the project. A special thank you to Yasmine for her enthusiasm, as well as her valuable advice, both professionally and personally. I also extend my heartfelt thanks to Valentin for his willingness to always help me during the project, for his patience, positivity, and for taking the time to introduce me to the lab, assist with my tests, sample preparations, and additional accelerated creep tests. A special thanks to Wouter from Witteveen+Bos for the opportunity to start on this research topic and for his enthusiasm, guidance, and support throughout the process. I am also grateful to my colleagues at Witteveen+Bos for their warm welcome and for inviting me to their nice activities.

I would like to thank Lightweight Structures Engineering and Delft Infra Composites B.V., especially Willem Souren for his guidance in designing the composite laminates and for sharing his insights into creep testing methods, and Paul Honing and his colleagues for manufacturing the composite material used in my experiments.

A big thank you to the staff of the Stevin 2 Laboratory, particularly Peter de Vries, Fred Schilperoort, and Derek van Bochove, for their expertise and help with designing, building, and executing the long-term creep tests and the quasi-static tensile tests. I also extend my gratitude to the staff of the Delft Aerospace Structures and Materials Laboratory (DASML), in particular Dave Ruijtenbeek and Chantal de Zeeuw, for their help and guidance with the accelerated creep tests, almost on a daily basis in the period of testing.

I am also thankful to Kay Weidenmann for showing his interest in my project and his valuable help and advice on solving clamping issues during the accelerated creep tests. Additionally, I want to express my appreciation to Cor Kasbergen for sharing his knowledge of the stepped isostress method and for taking the time to brainstorm with me on various methodological questions.

Finally, my deepest gratitude goes to my family, friends, and boyfriend for their continuous support, patience, and love. Thank you for always being there, for the much-needed distractions, and for putting a smile on my face. I am very grateful to have you all by my side.

*Emma van Amsterdam
Delft, February 2025*

Summary

The world is facing the challenge of climate change, a problem acknowledged by many governments in the Paris Agreement. All sectors, including the construction industry, must take responsibility for reducing their environmental impact. Using renewable bio-based materials, such as flax fibre composites, offers a promising solution towards reducing the construction sector's environmental footprint. Flax fibre-reinforced polymer composites, which consist of flax fibres embedded in a polymer resin, have gained attention for their potential application in structural elements. However, the lack of standardized long-term performance data, for example, its creep behaviour, limits its broader use in structural applications.

Creep is the gradual deformation of materials under a constant load, which can also affect their strength over extended periods of time. Conventional creep tests are often considered impractical as they are time-consuming and costly. Accelerated creep tests, such as the stepped isostress method (SSM), can offer a faster alternative for predicting long-term creep behaviour. The SSM predicts the long-term creep behaviour of a material by incrementally increasing the applied stress while maintaining constant environmental conditions. This method requires only a single test sample and approximately one day of testing to generate a prediction of the long-term creep master curve for a specific reference stress. However, the SSM is an empirical method that has not yet been standardized in any design codes. This research assesses the reliability of the SSM for flax fibre-reinforced polymer composites through an experimental study. Aiming to support the development of sustainable construction practices and encourage using renewable materials in the building industry.

To validate the SSM predictions, long-term creep tests are conducted using a custom-designed tensile creep test setup, supported by quasi-static tensile tests. Additionally, three different composite laminate configurations are compared, demonstrating the fibres' function as the main load-bearing component in the composite. One of the main findings of this research is the material's sensitivity to temperature. Although the SSM predictions produce creep master curves, these predictions are conservative compared to the long-term creep test results. Moreover, the data handling procedure of the SSM, particularly the horizontal shift, is extremely sensitive and partially subjective. Based on the findings, the current form of the SSM is deemed insufficiently reliable to replace conventional creep tests for structural material characterization. However, its potential as a highly time-efficient testing method should not be overlooked. With further refinement in both the experimental procedure and data processing procedure, SSM could become a more reliable approach, making further research on standardizing its methodology essential.

This research urges the need for further research to improve the reliability of the SSM and to standardize its data processing steps. An essential step in this development is understanding the relationship between the activation volume and the applied stress, which may be material-specific. Clarifying this relationship could help reduce the sensitivity and subjectivity of the horizontal shifting process in the SSM data analysis. Additionally, this research aims to inspire continued investigation into bio-based construction materials, contributing to a more sustainable building industry.

Contents

Preface	i
Summary	ii
Nomenclature	vi
1 Introduction	1
1.1 Research Motivation	1
1.2 Aim of this Research	3
1.2.1 Research Questions	3
1.3 Scope	4
1.4 Research Methodology	4
1.5 Structure of Report	4
I Literature Review	5
2 Fibre-Reinforced Polymer Composites	6
2.1 General Fibre-Reinforced Composites	6
2.1.1 Types of Fibres	7
2.1.2 Types of Resins	9
2.2 Properties of Flax Fibres	10
2.2.1 Flax Fibre Structure and Chemical Composition	10
2.2.2 Mechanical Properties of Flax Fibres	11
3 Creep in Flax Fibre-Reinforced Polymer Composites	13
3.1 Creep	13
3.1.1 Creep Rupture	14
3.1.2 Creep in Polymers	14
3.1.3 Creep in Flax Fibres and Their Role in Composites	15
3.1.4 Creep in Flax Fibre-Reinforced Polymer Composites	15
3.1.5 Parameters Influencing Creep Behaviour	16
3.2 Methods to Test Creep	17
3.2.1 Design Codes that Describe Creep	17
3.2.2 Conventional Creep Test	17
3.2.3 Accelerated Creep Test Methods	18
3.3 Conclusion	21
4 Stepped Isostress Method	22
4.1 Introduction to the Stepped Isostress Method	22
4.2 Stepped Isostress Data Analysis Procedure	22
4.2.1 Vertical Shifting	22
4.2.2 Rescaling	23
4.2.3 Horizontal Shifting	23
4.2.4 Validation of the Stepped Isostress Method	24
4.3 Comparison of Previous Research Using the Stepped Isostress Method	25
4.3.1 SSM Test Methods of Different Researchers	25
4.3.2 SSM Data Handling by Different Researchers	26
4.4 Conclusion	27

II Methodology	28
5 Materials and Methods	29
5.1 Samples	29
5.1.1 Laminate Layup Configurations	30
5.1.2 Sample Preparations	34
5.2 Quasi-Static Tensile Test Procedure	37
5.3 Long-Term Tensile Creep Test Procedure	39
5.3.1 Development of the Long-Term Creep Test Setup	42
5.4 Accelerated Creep Test Procedure Using SSM	45
III Experimental Results and Discussion	49
6 Quasi-Static Tensile Test	50
6.1 Results	50
6.1.1 Failure Mechanisms	53
6.2 Discussion	53
6.3 Conclusion	55
7 Long-Term Tensile Creep Test	56
7.1 Disruptions During the Long-Term Creep Test	56
7.1.1 Cleaning and Compensating the Long-Term Creep Curves	58
7.2 Results	58
7.3 Discussion	62
7.4 Conclusion	64
8 Accelerated Creep Test Using the Stepped Isostress Method	65
8.1 Initial Results	65
8.1.1 Failure Mechanisms	67
8.2 Stepped Isostress Method Data Analysis	69
8.2.1 Vertical Shifting	69
8.2.2 Rescaling	70
8.2.3 Horizontal Shifting	71
8.3 End Results and Validation	72
8.4 Discussion	73
8.5 Conclusion	82
IV Conclusion and Recommendations	83
9 Conclusion	84
10 Recommendations	88
References	90
Appendices	95
A Calculation of the Laminate Configurations	95
B Sample Locations on Original Plates	97
B.1 Samples Plate A	98
B.2 Samples Plate B	102
B.3 Samples Plate C	106
B.4 Plate Part 6	110
C Measured Sample Thickness	111
D Design of Clamps for Long-Term Test Setup	115

E	Preliminary Quasi-Static Tensile Test	121
E.1	Detailed Method	121
E.1.1	Sample Preparation	122
E.2	Results	123
E.2.1	Failure Modes	124
E.3	Discussion	125
F	Numerical Overview of Quasi-Static Tensile Test Results	127
F.1	Numerical Results Layup A (UD)	128
F.2	Numerical Results Layup B (QI)	129
F.3	Numerical Results Layup C (UD+QI)	130
G	Long-Term Tensile Creep Test Results	131
G.1	Uncorrected Longitudinal Long-Term Creep Curves	131
G.1.1	Longitudinal Strain Measured in Dummy Samples	132
G.2	Transversal Long-Term Creep Curves	133
G.2.1	Transversal Strain Measured in Dummy Samples	134
G.3	Re-Alignment of Cleaned Creep Curves to Compare the Slopes	135
H	Accelerated Creep Test Results	136
H.1	Specifications of Each SSM Test	136
H.2	Raw Data of the SSM Tests with Large Stress Increments	144
H.3	SSM Processed Creep Master Curves on Full Timescale	145

Nomenclature

Abbreviations

Abbreviation	Definition
CCT	Conventional Creep Test
DIC	Digital Image Correlation
DMA	Dynamic Mechanical Analysis
FFRP	Flax Fibre Reinforced Polymers
FRC	Fibre Reinforced Composite
FRP	Fibre Reinforced Polymer
FVF	Fibre Volume Fraction
GUTS	Guaranteed Ultimate Tensile Strength
QI	Quasi-Isotropic
RH	Relative Humidity
SIM	Stepped Isothermal Method
SSM	Stepped Isostress Method
TSSP	Time-Stress Superposition Principle
TTSP	Time-Temperature Superposition Principle
TTSSP	Time-Temperature-Stress Superposition Principle
UD	Unidirectional
UTS	Ultimate Tensile Strength

Introduction

The research background and motivation are explained in this introductory chapter, from which the objectives and aims of this research will follow. The main research question is introduced and refined into multiple sub-questions. The scope of this research is defined, and the methodology used to answer the research questions is explained. The chapter ends with an outline of this report, detailing the structure of the chapters.

1.1. Research Motivation

Construction materials are responsible for approximately 10% of the global greenhouse gas emissions (United Nations Environment Programme, 2023). Reducing these emissions is an important step towards addressing the world's environmental challenges, but also represents a huge challenge for the construction industry. There is an urgent need for sustainable solutions, especially when considering the growing resource scarcity coupled with the rising global demand (Merrild et al., 2016). Governments worldwide have set ambitious targets to promote sustainability, such as the Paris Agreement (2015), where 195 parties have agreed to mitigate climate change. In line with these goals, the Dutch government aims to establish a fully circular construction industry by the year 2050 (Ministerie van Infrastructuur en Waterstaat, 2024). To reach these goals, the United Nations Environment Programme (2023) suggested three strategies in their report, as shown in figure 1.1. Of particular relevance to this thesis, is the decision to shift towards regenerative bio-based materials. To achieve these environmental targets and enhance the sustainability of the building industry, research efforts towards innovative solutions are essential.

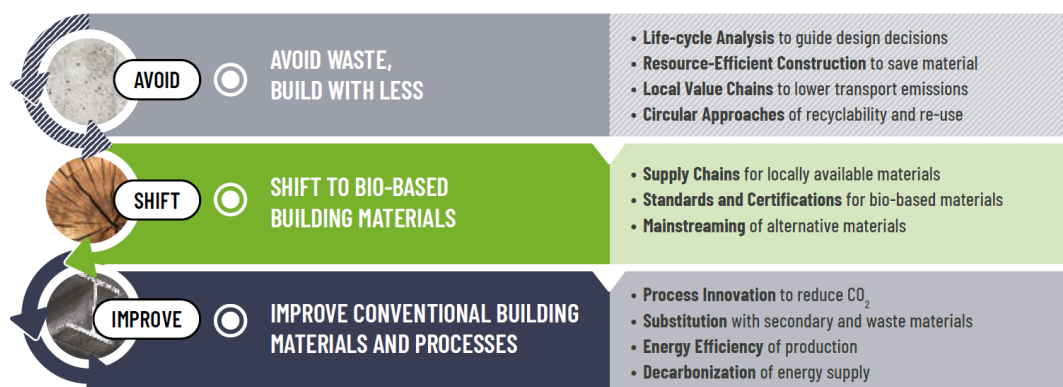


Figure 1.1: Three strategies stated by the United Nations Environment Programme to reduce the carbon emissions of the construction industry (United Nations Environment Programme, 2023)

Recently, four bio-based composite bridges have been constructed using natural (flax) fibres and a partially bio-based resin, aligning with the strategy to incorporate bio-based materials as stated by the United Nations Environment Programme (2023). The first bio-composite bridge was built in 2016 at

Eindhoven University of Technology (figure 1.2a). This 14-metre spanning footbridge is made from a combination of flax and hemp fibres with a bio-epoxy resin (Blok et al., 2019). This project was followed by a second bio-composite bridge, built in 2020 in Ritsumasyl. This bridge has a total length of 66 metres, with a movable swing bridge part with a free main span of 22 metres. The bridge is fully made out of flax fibres with a bio-epoxy resin (Claassen & Zarifis, 2020). In 2022 a third bio-composite bridge was completed in Almere (figure 1.2c), using flax fibres with a bio-polyester resin (Claassen & Veltkamp, 2022). At the start of this research, the fourth bio-composite bridge was being built in Ulm, which opens in February 2025 (figure 1.2d) composed of a similar material as the bridge in Almere. To evaluate the long-term behaviour of these materials, all four bridges are equipped with sensors monitoring the structural performance under daily use and across seasonal changes. According to the research of Manconi and Moonen (2024), the material's degradation has been evaluated through short-term tests, but conclusive long-term evaluations remain insufficient. This has led to conservative design approaches, resulting in uneconomical structures (Claassen & Veltkamp, 2022). A better understanding of the material's (long-term) properties is essential for optimizing its design and expanding its application in engineering practices.



(a) Bio-based bridge built in 2016 at TU Eindhoven (Blok et al., 2019)



(b) Bio-based openable bridge built in 2020 in Ritsumasyl (Claassen & Zarifis, 2020)



(c) Bio-based bridge built in 2022 in Almere (Claassen & Veltkamp, 2022)



(d) Bio-based bridge built in 2024 in Ulm (photo by Wouter Claassen)

Figure 1.2: Recently built bridges made out of a flax fibre composite with a partly bio-based resin

Structures, such as bridges, usually have a design lifespan of 50 to 100 years, so the long-term properties of the structural materials are crucial for a safe design. Testing materials or structural elements for such extended periods is impractical and costly, hence there is a need for accelerated methods for characterizing the material's long-term properties to ensure structural safety (Luo et al., 2012). The long-term behaviour of natural fibres and flax fibre composites remains insufficiently explored, requiring further research to enhance our understanding (Hristozov et al., 2016; Manconi & Moonen, 2024). Additionally, the natural variability of the structure of natural fibres results in a spread of their mechanical properties, which must be accounted for when using natural materials in structural applications (Baley et al., 2020; Charlet et al., 2009). Further research is necessary to explore their durability, safety, and long-term performance (Kamarudin et al., 2022).

Creep behaviour, the gradual deformation of a material under a constant load, is one of those critical long-term properties that must be considered in structural design. Creep, over long periods of time,

leads to a reduction of strength and stiffness. However, the lack of standardized creep factors for natural fibres in design codes, makes testing of these materials essential to characterize their properties. Real-time long-term creep tests are not only time-consuming but also very costly. Therefore, construction parties are likely to favour less sustainable but standardized materials.

This research aims to address this knowledge gap by conducting an experimental study, to assess the reliability of an accelerated creep test method. Specifically, it explores the potential of the stepped isostress method (SSM) (further explained in chapter 4) as an accelerated method to predict the long-term creep behaviour of the flax fibre composite material. B. Xu et al. (2023) published a study on the long-term creep behaviour, using the stepped isothermal method (SIM) as an accelerated creep test method. They found the SIM feasible for predicting the creep behaviour of flax fibre composites. In the SIM tests, the temperature is increased in steps over time, however, flax fibres are very sensitive to environmental changes and their properties can change with higher temperatures. It would therefore be important to keep the temperature and the relative humidity constant for the duration of the creep test. The stepped isostress method (SSM) is therefore a promising alternative to predict the creep behaviour of the flax fibre composite. With the SSM, the environmental conditions remain constant, while the stress is increased in steps. The SSM method has not been used to predict the creep deformation of flax fibre composite before.

This research aims to improve the accuracy of creep predictions to eventually contribute to standardized creep factors for flax fibre composites, with the ultimate goal of enhancing its adoption in structural applications. A broader use of bio-based materials in the construction industry can help reduce its carbon footprint, allowing progress towards meeting global sustainability goals.

1.2. Aim of this Research

The main goal of this research is to support the standardization of natural fibre-based structural materials, by studying their long-term behaviour. Specifically, this study aims to assess and refine an accelerated test method to predict the long-term creep behaviour of a flax fibre-reinforced polymer composite within a reduced timeframe. Specifically, the stepped isostress method (SSM) is used. A key goal is to establish a systematic and repeatable SSM data processing procedure that can contribute to the development of a standardized creep factor for flax fibre composites. By improving the predictability and reliability of these materials, this research aims to enhance their attractiveness for structural applications, promoting their use in the construction industry.

1.2.1. Research Questions

This research aims to assess the use of the stepped isostress method as an accelerated creep test method, to predict the long-term creep behaviour of a flax fibre-reinforced polymer composite. The main research question is formulated to address the research objective:

To what extent does the stepped isostress method provide a reliable prediction of the long-term creep behaviour of flax fibre-reinforced polymer composites across different laminate layup configurations?

To help answer the main research question, the following sub-questions are formulated:

1. How does the structural composition of flax fibres affect the creep behaviour of flax fibre-reinforced polymer composites?
2. Which parameters play a significant role in influencing the creep behaviour of flax fibre-reinforced polymer composites?
3.
 - a. What are the prevailing industry standards and testing protocols for estimating creep behaviour in composite materials?
 - b. How well do these standards apply to flax fibre composites, and are there unique characteristics requiring tailored testing standards and protocols for an accurate creep assessment?
4. What factors contribute to variations in the accuracy of the stepped isostress method when predicting creep behaviour for different flax fibre composites?
5. What are the advantages and limitations of the stepped isostress method as an accelerated creep test method, compared to other creep testing methods, for a flax fibre-reinforced polymer composite, and what is the impact of its layup configuration?

1.3. Scope

This research investigates the application of the stepped isostress method as an accelerated creep test method to predict the long-term creep behaviour of a flax fibre composite. The study specifically aims to investigate their potential application as structural elements in light-traffic bridges. Given the lightweight nature of flax fibre composites, the research focuses on creep deformation under a relatively low constant stress of 10 MPa, prioritizing serviceability (think of deformations) over creep strength. The scope includes testing material coupons of three different laminate configurations. The study focuses on tensile creep behaviour in the longitudinal direction, under constant environmental conditions. Transversal strains and the Poisson ratio are excluded. To ensure consistency, all tested specimens use the same types of fibres and a thermosetting unsaturated polyester resin. This study examines creep deformation under a permanent load, excluding the effects of cyclic loads, creep recovery, and creep damage mechanisms.

1.4. Research Methodology

This study investigates the use of the stepped isostress method (SSM) as an accelerated creep test method for predicting the long-term tensile creep behaviour of a flax fibre composite. The study starts with a literature review, then experimental testing is performed, and lastly, the results are analysed. The literature review is conducted to understand the properties of flax fibre-reinforced polymer composite materials and the fundamental principles of creep behaviour. Specific focus is given to accelerated creep test methods, explaining the selection of the stepped isostress method. Relevant studies using the SSM are analysed to compare their methodologies and establish a framework for its implementation in this study.

The experimental phase involves applying the SSM to evaluate its effectiveness in predicting long-term creep behaviour, where three distinct layup configurations are designed and compared. To determine the tensile strength of the materials, quasi-static tensile tests are performed initially. For each experiment, the specimens are carefully prepared, and repetitions are conducted to ensure the reliability of the results. Alongside the SSM tests, a real-time long-term creep test is conducted for at least 90 days. This real-time test provides reference data for validating the SSM creep predictions. The data collected from both the real-time creep tests and SSM tests are analysed to refine the SSM data processing procedure. Ultimately, the experimental results are evaluated to assess the advantages and limitations of the stepped isostress method for flax fibre composites.

1.5. Structure of Report

This thesis report is organized into four main parts, containing a total of nine chapters. Part one focuses on the literature review, with chapter 2 examining the material properties of flax fibre-reinforced composites. Chapter 3 explains the concept of creep and reviews various accelerated creep testing methods, including the reasoning behind choosing the SSM. Chapter 4 delves deeper into the SSM, comparing methodologies and findings from existing research.

Part two, with chapter 5, describes the experimental setups and procedures. First, the materials and the design of the different layup configurations are explained, along with the sample preparation techniques for each experiment. Then the experimental setups and procedures for all tests are explained, including the custom design of the long-term creep test setup.

Part three presents the results and analysis of all experiments. Chapter 6 focuses on the quasi-static tensile test results, chapter 7 discusses the findings from the long-term creep tests, and chapter 8 analyses the results of the accelerated creep test. This chapter also compares the SSM outcomes with the real-time creep test results and discusses the SSM's methodology and applicability for creep testing.

Part four concludes the report with chapter 9, which summarizes the findings and answers the research questions. Chapter 10 offers recommendations for future research and practical applications related to the SSM methodology, and working with flax fibre-reinforced polymer composites.

Part I

Literature Review

2

Fibre-Reinforced Polymer Composites

A composite material is composed of two or more distinct components that have different properties and that complement each other (Abbood et al., 2021; Waghmare et al., 2022). This chapter introduces fibre-reinforced composites, focusing on the types of fibres and polymer matrices that are commonly used, with a particular emphasis on flax fibre composites. The chapter concludes with a more detailed examination of the properties of flax fibres.

2.1. General Fibre-Reinforced Composites

A fibre-reinforced composite (FRC) consists of two key components: fibres that provide reinforcement, and a resin-based matrix (often a polymer) that acts as an interface between the fibres, as illustrated in figure 2.1. The fibres have a primary load bearing function, while the matrix performs multiple functions. The matrix holds the fibres in place in the desired arrangement, it transfers and distributes forces among the fibres, it prevents buckling of the fibres, and it protects the fibres from environmental and mechanical damage (Abbood et al., 2021; Kolstein, 2008). The combination of the fibres and the polymer matrix results in mechanical properties that exceed those of the individual components, creating a synergistic effect.

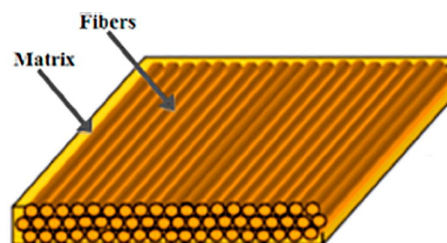


Figure 2.1: The components of a typical fibre-reinforced composite: fibres in a matrix (Abbood et al., 2021)

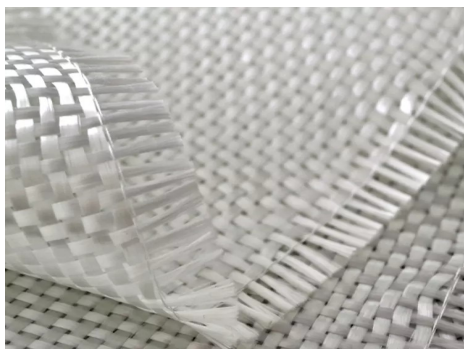
FRC's are constructed by layering fibre sheets on top of each other, each sheet with a primary orientation. This orientation is typically aligned with the direction of the highest stress, known as the 0° direction (Staab, 2015). Fibres may also be oriented at various angles relative to this primary direction. A laminate configuration can be customized for a single application to meet its specific requirements, ensuring sufficient strength in all desired directions of the composite. A unidirectional (UD) layup, where all fibres are aligned in the same direction, offers high strength along that direction but may be vulnerable to imperfections and stress concentrations perpendicular to the fibre direction. To improve the stress distribution, fibres can be oriented in multiple directions, creating a quasi-isotropic (QI) layup. Although QI laminates have lower tensile strength in the primary direction compared to UD laminates, they provide more uniform strength in all directions of the composite. When using fibres in various directions in a laminate, it is important to ensure a proper distribution of the different angles throughout the laminate to reduce anisotropy and ensure an even load distribution. Additionally, it can be desirable to design the layup with mirror symmetry about the laminate's centre. Asymmetrical laminates can ex-

perience differential expansion or contraction on either side of the mid-plane due to thermal or moisture changes. This causes bending moments in the laminate, leading to warping or distortions. Asymmetry can also result in coupling effects, where an in-plane load can cause out-of-plane deformations, and vice versa. These effects are uncoupled in symmetrical laminates (Staab, 2015).

FRC's offer several advantages to conventional building materials, such as concrete or steel, including being a lightweight material, having high tensile strengths, and being corrosion resistant (Abbood et al., 2021). However, they also have drawbacks, such as the absence of a pronounced yielding stage and the technical difficulties associated with recycling FRC materials with a thermosetting polymer matrix (Abbood et al., 2021; Waghmare et al., 2022).

2.1.1. Types of Fibres

The most commonly used fibres in composites are glass fibres, followed by carbon and aramid fibres (Abbood et al., 2021; Waghmare et al., 2022). Recently, natural fibres have also gained popularity due to the increasing concerns on the environment (Elfaleh et al., 2023). Table 2.1 provides an overview of the mechanical properties of different fibres, and figure 2.2 illustrates the appearances of the different fibres.



(a) Glass fibres in a bidirectional weave (Afzir, 2023)



(b) Carbon fibres in a bidirectional weave (SageZander, 2022)



(c) Aramid (kevlar) fibres in a bidirectional weave (CA Composites Limited, 2019)



(d) Natural (flax) fibres, on the left a unidirectional sheet and on the right a bidirectional weave (Bcomp, n.d.)

Figure 2.2: Four different types of fibres that are often used in fibre-reinforced composites

Glass fibres

Glass fibres are the most widely used reinforcement material in fibre-reinforced polymers, accounting for over 90% of such applications (Waghmare et al., 2022). They are often used in the construction industry for their relatively low cost, high strength, isotropy, and resistance to water and chemicals (Abbood et al., 2021). However, glass fibres have a lower elastic modulus and reduced long-term strength due to stress rupture (Abbood et al., 2021; Waghmare et al., 2022). The production of glass fibres involves melting glass at very high temperatures and stretching it into thin strands which, while cheaper than carbon fibre production, is still energy intensive (Nijssen, 2015). Glass fibres come in various types with specific properties. E-glass (electrical grade) is the most commonly used, A- and

C-glass have a better chemical resistance, and R- or S-glass have an extra high strength (Nijssen, 2015; Waghmare et al., 2022).

Carbon fibres

Carbon fibres are known for their exceptional tensile strength and low density, making them ideal for applications requiring these high strength to weight ratios. They also exhibit low conductivity, have a high elastic modulus, and are hydrophobic, so they cannot absorb water (Abbood et al., 2021; Waghmare et al., 2022). However, carbon fibres are anisotropic and have a relatively low compressive strength. Their production is complex and energy-intensive, leading to high material costs (Abbood et al., 2021; Nijssen, 2015). Due to these factors, carbon fibres are primarily used in industries like automotive and aerospace, where performance is prioritized over costs (Kolstein, 2008). In civil engineering, however, their high costs often outweigh their benefits, leading to the preference for more economical materials.

Aramid fibres

Aramid fibres, such as Kevlar, are characterized by their high tensile strength and elastic modulus, making them suitable for tension-based applications such as cables. Despite their strength in tension, aramid fibres have a low compressive and radial strength and are anisotropic (Abbood et al., 2021). These factors limit their use to specific applications such as impact resistance (Waghmare et al., 2022). Aramid fibres are more expensive than glass fibres and are challenging to process, which further restricts their widespread use (Abbood et al., 2021).

Natural fibres

Natural fibres can be derived from three primary sources: animals, plants, and minerals. They are generally considered to be a more cost-effective alternative to synthetic fibres (Waghmare et al., 2022). Compared to glass fibres, natural fibres offer several advantages: they are more environmentally friendly, renewable, and require low energy consumption. They are also potentially less expensive, with lower investment costs, while still providing good mechanical properties and a low density (Dittenber & Gangarao, 2012; Karimah et al., 2021; Waghmare et al., 2022). As shown in table 2.1, some natural fibres exhibit mechanical properties comparable to those of glass fibres, but with significantly lower density (Hristozov et al., 2016; Waghmare et al., 2022). This high strength-to-weight ratio makes natural fibres particularly attractive for lightweight composite structures. Dittenber and Gangarao (2012) compared various natural fibres with E-glass fibres to assess their potential as more environmentally friendly replacements. Their analysis showed that flax, and hemp fibres are the most promising candidates for replacing glass fibres due to their lightweight, high strength, and stiffness.

However, natural fibres have limitations, such as easily absorbing water due to the presence of hemicellulose, which results in hydrophilic properties (Karimah et al., 2021). This hydrophilicity makes them less compatible with hydrophobic polymers, potentially compromising the bond between the matrix and the fibres (Kamarudin et al., 2022; Karimah et al., 2021). Additionally, natural fibres show a greater variability in their properties compared to synthetic fibres, as natural materials naturally contain flaws and irregularities (Charlet et al., 2009; Kamarudin et al., 2022). The properties of natural fibres can highly depend on the environmental conditions (Perruchoud et al., 2024).

Despite their potential, the application of natural fibres in structural elements is limited by the lack of standardized guidelines. In outdoor applications, natural fibres must be protected from weather and biological degradation. Further research is necessary to explore their safety, long-term behaviour, durability, and recallability (Kamarudin et al., 2022). A comparison of the properties of synthetic and natural fibres is presented in table 2.1. The table shows that flax fibres have one of the highest tensile strengths among natural fibres. This suggests that flax fibres can be a feasible replacement for glass fibres, potentially reducing the environmental impact of composite production.

Table 2.1: Overview of basic properties of a few synthetic and natural fibres (most values in the table are from the CUR 96 (2019), combined with values found by Abbood et al. (2021), Kamarudin et al. (2022), Lau et al. (2018), and Yan et al. (2014))

Fibre	Density [g/cm³]	Tensile Strength [MPa]	Young's Modulus [GPa]	Elongation at Failure [%]
Carbon	1.8	3600-5670	240-436	1.0-1.8
Glass	2.5	2750-3450	73-86	3.8-4.0
Aramid	1.4	2800-3450	62-175	1.4-4.4
Flax	1.4	700	60	1.2-4.0
Hemp	1.4	550	45	1.5-4.0
Jute	1.4	350	40	2.0-3.0
Bamboo	1.2-1.5	500-575	27.0-40.0	4.0-7.0

2.1.2. Types of Resins

The resin forms the matrix in composite materials, with polymeric resins being the most commonly used and the least expensive (Staab, 2015). There are two types of polymer resins: thermoplastic polymers and thermosetting polymers. Thermoplastic polymers have non-cross-linked chains, allowing them to be reshaped upon heating (Staab, 2015). In contrast, thermosetting polymers consist of extensively cross-linked chains, which prevent them from softening or reshaping after curing, even under high temperatures (Abbood et al., 2021; Staab, 2015). Due to their rigidity and stability, thermosetting polymers are very often used in the manufacturing of fibre-reinforced polymers (FRP's), therefore this chapter will focus on these types of resins. A drawback of thermosetting polymers is that they tend to be more brittle (Abbood et al., 2021). In the following sections, three common thermosetting polymer resins are discussed, with an overview of their properties provided in table 2.2. It is important to note that the exact properties of these resins can vary based on their exact chemical composition and curing processes, which can be customized and tailored for a single project (Staab, 2015).

Epoxy resin

Epoxy resins are often used due to their superior mechanical properties compared to other thermosetting resins (see table 2.2). One reason for their strength is that most of the shrinkage occurs while the resin is still in its liquid phase, resulting in fewer residual stresses once it hardens. Additionally, epoxy resins are resistant to corrosion and have a wide range of applications besides serving as a matrix material. For example, epoxy resins are also used as coatings, adhesives, and casting materials (Abbood et al., 2021; Nijssen, 2015; Staab, 2015). A drawback of epoxy resins is that they are usually more expensive compared to other resins. An example of the application of an epoxy resin is in the construction of the flax fibre composite bridge in Ritsumasyl, which uses flax fibres with an epoxy resin (Claassen & Zarifis, 2020; Souren & Velds, 2019).

Unsaturated polyester resin

Polyester resins, which always contain unsaturated polyester monomers, are often used for their low cost and quick curing. However, their mechanical properties are inferior to those of epoxy resins, and they are more sensitive to water (Abbood et al., 2021; Staab, 2015). During the curing process, unsaturated polyester resins can develop residual stresses due to uneven shrinkage, as the resin shrinks while the fibres do not (Staab, 2015). In the flax fibre composite bridge in Almere, the composite bridge deck consists of flax fibres with an unsaturated polyester resin (Claassen & Veltkamp, 2022; Polynt-Group, 2022).

Vinyl ester resin

A Vinyl ester resin offers a balance between the strength and cost of epoxy and polyester resins, but with a much lower viscosity. Vinyl ester resins are often used in applications requiring a higher chemical resistance than polyester resins can provide. They are often used in marine industries for their waterproof characteristics and corrosion resistance. Additionally, they can be applied as a waterproof coating over polyester structures. However, vinyl ester resins may discolour over time, turning yellow, which can be undesirable for aesthetic purposes (Abbood et al., 2021; Staab, 2015).

Table 2.2: Overview of properties of three thermoset resins that are often used as matrices for fibre-reinforced composites (CUR 96, 2019)

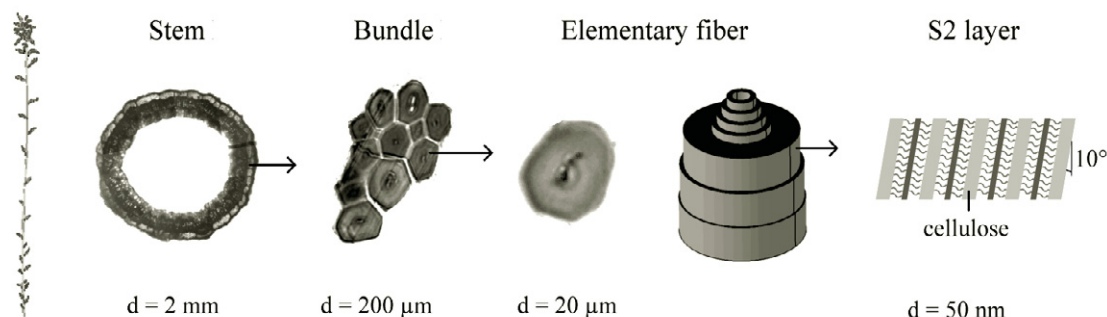
Property	Polyesters	Epoxy	Vinyl-ester
Density (gm/cm ³)	1.2	1.25	1.1
Tensile Strength (MPa)	55	75	75
Young's Modulus (GPa)	3.55	3.10	3.35
Poisson's ratio	0.38	0.39	0.26
Elongation at failure [%]	1.8	2.5	2.2
Coefficient of Thermal Expansion (10 ⁻⁶ /K)	55–120	45–65	50–75

2.2. Properties of Flax Fibres

Flax (*Linum usitatissimum*) is one of the most widely used bio-fibre, valued for its mechanical properties, which are comparable to glass fibres (Yan et al., 2014). Historically, flax has been utilized over centuries for textiles and basket weaving. Currently, Canada is the leading producer and exporter of flax, while in Europe France, Belgium, and the Netherlands are significant producers of flax (Yan et al., 2014), making it a locally available material in the region of the Netherlands. Flax has a relatively short growing cycle, taking approximately 100 days from sowing to harvesting (Charlet et al., 2009; Yan et al., 2014), much quicker than for example wood.

2.2.1. Flax Fibre Structure and Chemical Composition

The structure of flax is shown in figure 2.3. A flax stem can grow up to 90 cm in height, with the strong fibres located along the stem's circumference. The strong fibres are grouped in bundles of 10 to 40 and are mainly held together by pectin. The fibres are extracted from the plant with special machines (Baley et al., 2020). The diameter of a flax fibre can range from 12 to 600 μm , often much larger than the diameter of glass fibres, which is less than 17 μm (Yan et al., 2014).

**Figure 2.3:** The structure of flax from the stem to the cellulosic fibrils (Charlet et al., 2009)

A single flax fibre, known as an elementary fibre, consists of concentric cell walls of varying thickness (see figure 2.4) (Charlet et al., 2009; Yan et al., 2014). Each layer consists of cellulose microfibrils that run parallel to one another under a slight angle with the fibre direction. The thickest layer (S2) is the most responsible for its high tensile strength, due to its composition of crystalline cellulose microfibrils and amorphous hemicellulose, oriented at a 10° angle to the fibre axis. In the centre of an elementary fibre is a small hollow channel known as the lumen, which contributes to the water absorption of the fibre. The primary cell wall (P) of an elementary fibre is relatively thin (0.2 μm) and coats the secondary cell walls (Yan et al., 2014). On a nanoscale, a microfibril is made up of cellulose chains embedded in a matrix of pectins and hemicelluloses. When the microfibrils are orientated in a spiral to the fibre axis, it gives the fibre some ductility (Yan et al., 2014).

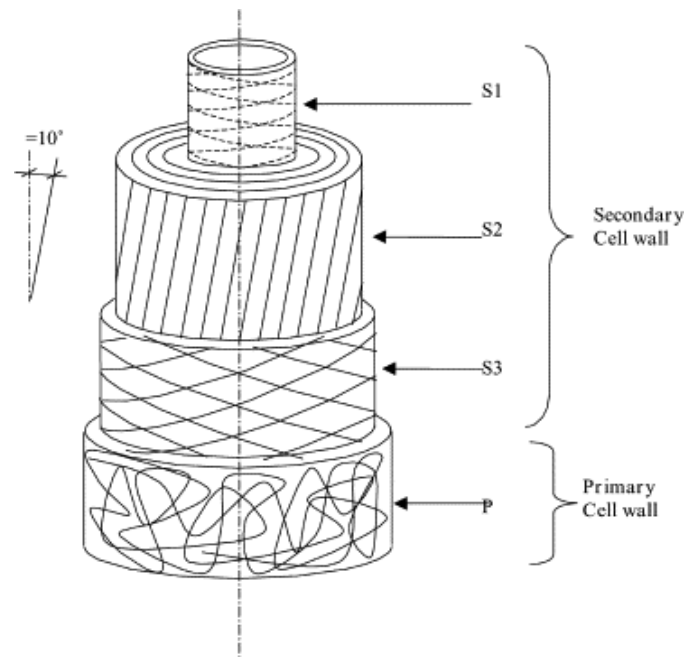


Figure 2.4: The structure of a flax fibre cell (Yan et al., 2014)

The properties of the flax fibre are mostly defined by the chemical composition, and the location of constituents within the flax stem. The primary components of a flax fibre are cellulose (64.1 – 75%), hemicellulose (11 – 20.6%), lignin (2.0 – 2.9%), pectin (1.8 – 2.3%), wax (± 1.5 – 1.7%), and water (More, 2021; Yan et al., 2014). These first three constituents are the basic components that determine the physical properties of the fibres. Cellulose is the stiffest and strongest organic constituent in the fibre, but also gives the fibre its hydrophilic nature. Hemicellulose is bound to the cellulose fibrils and is hygroscopic, with an open structure that can absorb water. Lignin and pectin serve as a bonding between the microfibrils. Wax on the fibre surface can affect the adhesion and hydrophilicity of the fibre surface. The exact composition of constituents can differ between species and due to natural variability such as the quality of the soil and the weather conditions. These factors can therefore also have an impact on the mechanical properties of a flax fibre (Yan et al., 2014).

2.2.2. Mechanical Properties of Flax Fibres

The mechanical properties of flax fibres can vary, and are dependent on factors such as growing conditions, location of growth, harvesting methods, and environmental conditions during processing (Baley et al., 2020). For a single flax fibre, it can be challenging to determine its properties since the fibre cross-section is not perfectly circular and long fibres can have different diameters over their length (Baley et al., 2020). For example, Charlet et al. (2009) tested the tensile properties of single flax fibres on an MTS tensile test machine, revealing a typical stress-strain curve (see 2.5a). Charlet et al. (2009) divided this curve into three distinct phases: an initial linear region (0-0.3%), a non-linear region (0.3-1.5%) due to the reorganization of the cellulose microfibrils in the direction of the fibre axis, and a final linear region (1.5%-failure) representing the elastic response of the aligned microfibrils to the applied tensile load (Charlet et al., 2009; Yan et al., 2014). Yan et al. (2014) identified a similar curve, but distinguished only two phases: the non-linear region (from 0-0.5%), followed by a linear region (0.5%-failure). They explained that the orientation of the fibrils relative to the fibre axis influences the tensile properties of the fibre. A tensional force activates a change in the orientation of the microfibrils (Yan et al., 2014).

The stress-strain behaviour of flax fibre composites differs from the behaviour of an elementary flax fibre. Baley et al. (2020) investigated the stress-strain behaviour of a UD flax fibre composite for different fibre volume fractions. Their results show that the flax fibre composite shows a bilinear stress-strain diagram, with the kink in the graph being more pronounced at higher fibre volume fractions (see figure 2.5b). The stiffness of a flax fibre composite is therefore often determined on two parts of the stress-strain curve, one for lower stresses and one for higher stresses (Baley et al., 2020).

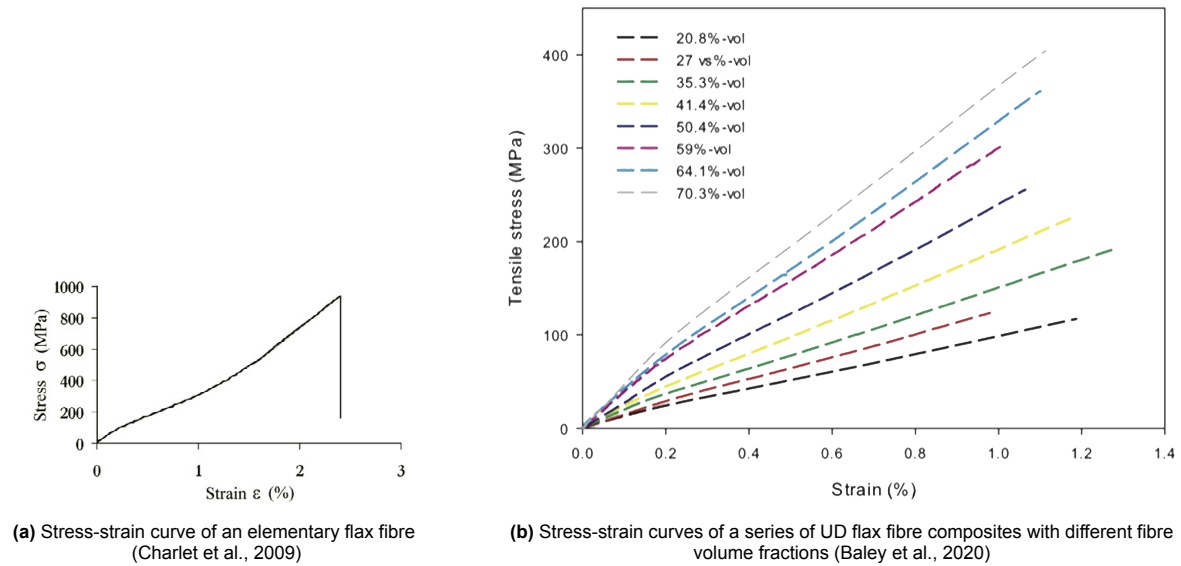


Figure 2.5: Comparison of stress-strain behaviour of elementary flax fibres and UD flax fibre composites

In glass fibre composites, there are three main failure mechanisms: failure of the fibre, cracking of the matrix, and interfacial failure between the fibre and the matrix (Baley et al., 2020). These types of damage mechanisms are shown in figure 2.6a. Unlike glass fibres, flax fibres consist of stacked layers (see figure 2.4) that can exhibit interlayer damage such as separation between the cell walls (Baley et al., 2020; Yan et al., 2014). According to Yan et al. (2014), the secondary cell wall splits relatively easily over the length of the fibre, indicating that the lateral strength of the fibre is lower than its tensile strength. Furthermore, the tensile strength and stiffness of flax fibre composites are very sensitive to environmental conditions, particularly temperature and relative humidity, as shown in recent work of Perruchoud et al. (2024). Moisture can induce additional damage in natural fibre composites. Natural fibres swell when absorbing water, which causes extra stresses and cracks in the matrix material, introducing additional damage mechanisms in the composite, as shown in figure 2.6b (Azwa et al., 2013). It is therefore very important to check the conditions when testing the mechanical properties of flax fibres. Chemical treatments can improve the performance of flax fibres (Yan et al., 2014). However, it is important to consider that such treatments may reduce the environmental benefits of using natural fibres.

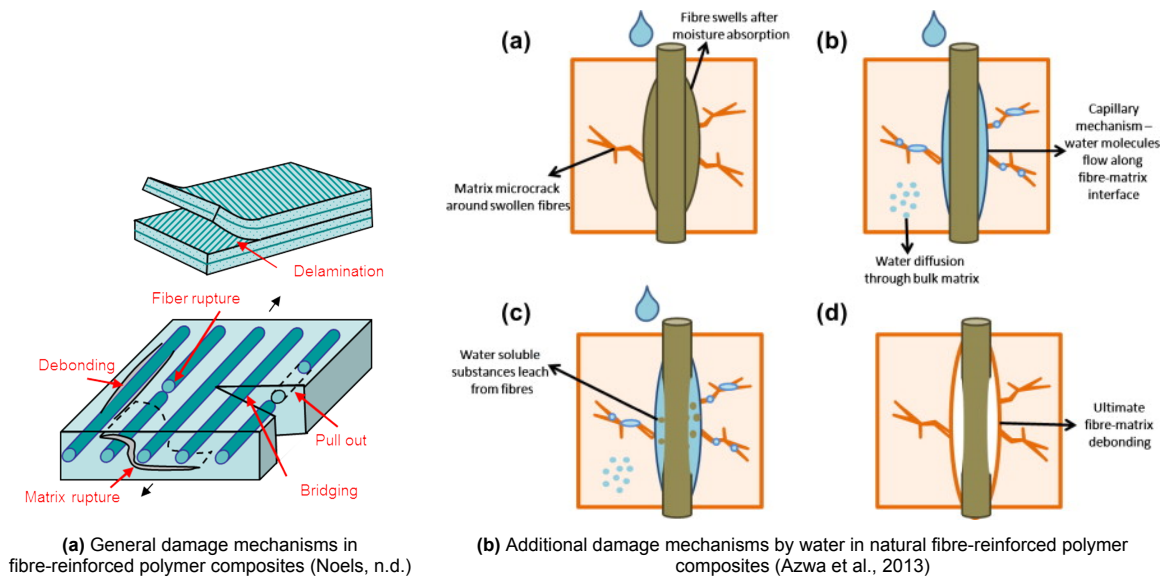


Figure 2.6: Summary of damage mechanisms in natural fibre-reinforced polymer composites

3

Creep in Flax Fibre-Reinforced Polymer Composites

In this chapter, the phenomenon of creep is explored, particularly creep in flax fibre polymer composites. The factors influencing the creep behaviour are examined, and different methods for creep testing are discussed. A distinction is made between conventional creep tests and accelerated creep tests, highlighting the importance of accelerated creep test methods. The choice for the stepped isostress method is explained and the method is further elaborated in chapter 4.

3.1. Creep

Creep is the time-dependent, permanent deformation of a material that is subjected to a constant load over an extended period of time (based on the definition of Lee (2007)). For instance, a polymer will keep stretching under this constant load until it finally breaks. This failure is known as creep rupture (Staab, 2015). Creep deformation is measured as strain, which is a dimensionless quantity expressed as a ratio (mm/mm), percentage ($\varepsilon[\%] = \varepsilon \cdot 100\%$), or microstrains ($\varepsilon\mu = \varepsilon \cdot 10^6$). Strain is calculated as stated in equation 3.1.

$$\varepsilon = \frac{\Delta L}{L_0} \quad (3.1)$$

With:

ε = strain [-]

ΔL = change in length [mm]

L_0 = original length of material [mm]

Creep can typically be characterized in three stages, illustrated in figure 3.1. The first stage, known as primary creep, involves an instantaneous deformation followed by a rapidly decreasing strain rate. The second creep stage, referred to as secondary creep, is characterized by having a steady, nearly constant strain rate. The creep strain rate can be determined by the slope of the curve creep strain curve, equation 3.2. The secondary creep stage normally spans most of a material's or structure's lifespan. In the final creep stage, called tertiary creep, the strain rate accelerates until the material fails (Findley et al., 1989; Huda, 2022; Lee, 2007). Understanding the creep behaviour of a material is crucial for designing structures with creep-sensitive materials, as creep deformation can determine the service life of a component and affect its serviceability limit state. Creep rupture, on the other hand, is critical for assessing how creep weakens the material's strength, influencing the ultimate limit state (CUR 96, 2019).

$$\dot{\varepsilon} = \frac{\Delta \varepsilon}{\Delta t} \quad (3.2)$$

With:

$\dot{\varepsilon}$ = creep rate

$\Delta\varepsilon$ = strain increment over time period Δt

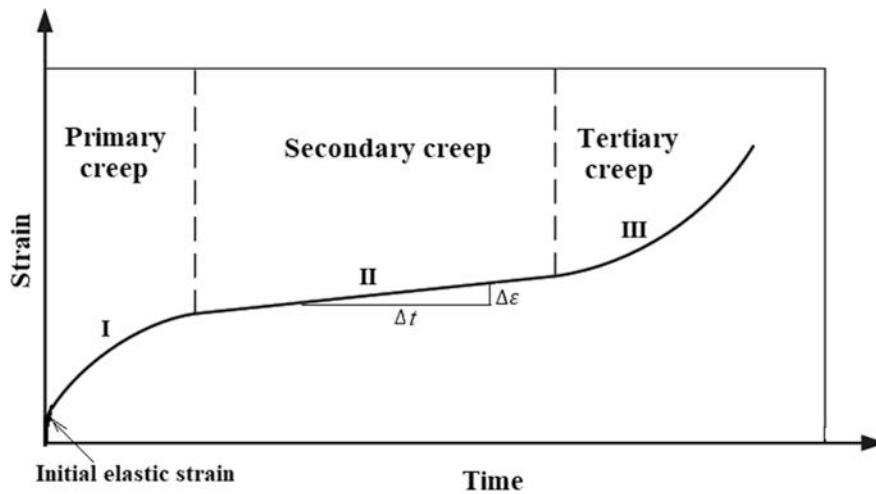


Figure 3.1: Three typical stages of the creep strain response of a material under a constant applied load (Huda, 2022)

In some studies, for instance, that of B. Xu et al. (2023), the creep behaviour is examined through creep compliance, which is the ratio of strain to the applied constant stress (equation 3.3) (Papanicolaou & Zaoutsos, 2011).

$$J(t) = \frac{\varepsilon(t)}{\sigma_0} \quad (3.3)$$

With:

$J(t)$ = creep compliance [MPa^{-1}]

$\varepsilon(t)$ = total strain [-]

σ_0 = applied constant stress [MPa]

3.1.1. Creep Rupture

Creep rupture occurs when the permanent applied load results in high stresses in a component, leading to structural failure (CUR 96, 2019). The damage development at high creep stresses influences both the creep behaviour and creep rupture time of a material (Jia & Fiedler, 2020). Creep can lead to fracture as the material weakens over time and the effective stress increases under the constant load, due to the gradual reduction of the cross-sectional area caused by creep deformation.

3.1.2. Creep in Polymers

Polymers, being viscoelastic, show a unique time-dependent behaviour. Polymers can recover their deformation when a constant load is removed or experience stress relaxation under constant strain (Papanicolaou & Zaoutsos, 2011). In fibre-reinforced polymers (FRPs), creep is often more pronounced in the off-axis direction, where the matrix primarily bears the load. In FRPs, the matrix is generally more susceptible to creep than the fibres (Lee, 2007). A polyester resin, for instance, is composed of long molecular chains that are initially flexible, but become rigid after curing due to crosslinking between the polymer chains (Silva et al., 2020). When a stress is applied, the polymer chains initially stretch and align in the direction of the stress (primary creep), but as the stress is sustained over a longer period of time, these chains can begin to rotate and slide past one another at a molecular level (secondary creep) (Boyer, 1968; Silva et al., 2020; W. H. Wang et al., 2015). This molecular mobility is more pronounced at higher temperatures or stresses, though it also occurs at room temperature and under relatively low stresses (Lee, 2007; Silva et al., 2020).

3.1.3. Creep in Flax Fibres and Their Role in Composites

Glass fibres, and especially carbon fibres, show a low creep sensitivity, whereas natural fibres are more susceptible to creep (Staab, 2015). Ascione et al. (2012) found that in glass fibre composites, creep primarily occurs in the polymer resin rather than in the fibres. In contrast, flax fibres demonstrate significant creep behaviour within the fibre itself, making it important to study both their standalone creep properties and their behaviour in combination with a polymer.

Jia and Fiedler (2020) found that flax fibres in unidirectional composites exhibit notable creep deformation in the fibre direction, even at low creep stresses, although creep damage development remained negligible. In contrast, carbon and glass fibre composites exhibit such behaviour only when the load is applied off-fibre axis, where the polymer matrix is responsible for the creep behaviour. While, in fibre direction, these synthetic fibres show minimal creep deformation. Jia and Fiedler (2020) provided two explanations for this creep behaviour of flax fibres in the fibre direction.

Firstly, the structure of flax fibres plays a role in their creep behaviour. As explained in paragraph 2.2.1, flax fibres are composed of cellulose microfibrils embedded in a hemicellulose and pectin matrix, where the microfibrils are helically aligned at a slight angle of approximately 10° off the fibre axis. When loading a flax fibre in the fibre direction, the viscoelastic response of the matrix can induce time-dependent shear deformation, causing the fibrils to move and realign within the fibre axis, even at low stresses.

Secondly, the manufacturing process of flax fibres often involves twisting individual fibres into bundles. Since flax fibres are naturally short, twisting them creates longer, continuous yarns that are more practical for use. This twist introduces slight misalignments (up to $\theta=10^\circ$) of the elementary fibres to the fibre bundle axis. This off-axis alignment, even if it is very small, can lead to shear stresses at the interface between the composite matrix material and the fibres when a load is applied. Over a longer period of time, this shear stress can lead to creep in the fibre direction (Jia & Fiedler, 2020). In the research of (Nedjar, 2011), a similar phenomenon is observed in carbon fibre composites with minor off-axis fibre orientations ($\theta=5^\circ$).

Given the structural composition and misalignment effects, flax fibres are particularly susceptible to creep, even at low stress levels. At higher stresses, creep behaviour is further influenced by damage progression (Jia & Fiedler, 2020).

3.1.4. Creep in Flax Fibre-Reinforced Polymer Composites

In composites, both the matrix and fibres share the applied loads. When the load is applied off-fibre axis, the matrix primarily carries it, while in the fibre direction, the load is initially shared by both the fibres and the matrix. Over time, the stress in the fibre direction, migrates from the matrix to the fibres due to their different viscosity, depending on the matrix-fibre interfacial bonding (Ascione et al., 2012).

Several studies have examined the creep behaviour of flax fibre composites (Giuliani et al., 2023; Hao et al., 2024; Jia & Fiedler, 2020; B. Xu et al., 2023). Jia and Fiedler (2020) investigated the response of unidirectional (UD) flax fibre composites with an epoxy resin, under different tensile stress levels at room temperature, measuring creep strain and acoustic emissions to determine the creep damage mechanisms. They found damages such as matrix cracking, fibre-matrix debonding, and fibre pull-outs, to cause the early rupture and a shorter creep life. They also found that the strain at failure is larger for a quasi-static tensile test than for a high-stress creep test. For low creep stresses (22% of the UTS, in this case, 66 MPa), Jia and Fiedler (2020) did not detect any acoustic emissions, indicating that negligible creep damage occurs at low-stress levels. However, they tested the creep behaviour at these lower load levels for only two hours. It would be interesting to investigate if creep damage propagates over a longer period of time at these low creep stresses.

B. Xu et al. (2023) studied the creep behaviour of flax fibre composites using the stepped isothermal method (SIM). The composite consisted of flax fibres with a polyester resin and was compared in three different laminate orientations (0° , 90° , and $\pm 45^\circ$) under low bending stresses (2 MPa and 5 MPa). Their results showed good consistency between the SIM results and conventional long-term creep tests and achieved more accurate SIM data by shifting based on the viscoelastic property analysis rather than by a visual method.

Giuliani et al. (2023) focused their research on the creep and relaxation behaviour of UD flax fibre composites with an epoxy resin, noting the complex and nonlinear nature of both phenomena. They reported that modelling this behaviour is challenging due to the difficulty of identifying the material

parameters experimentally.

Hao et al. (2024) explored the damage mechanisms due to high creep loads in UD flax fibre composites with different matrix materials. They observed that the creep damage was initiated by matrix cracking during the primary creep stage, followed by fibre-matrix debonding and fibre pull-out in the secondary creep stage (figure 3.2). These damage mechanisms significantly reduced the creep strength of the composites compared to quasi-static tests. However, Hao et al. (2024) did not look further into the creep deformation of flax fibre composites.

Overall, while some research has been conducted on the creep behaviour of flax fibre composites, long-term creep deformation remains largely unexplored, despite its importance for designing constructions that meet the serviceability limit requirements.

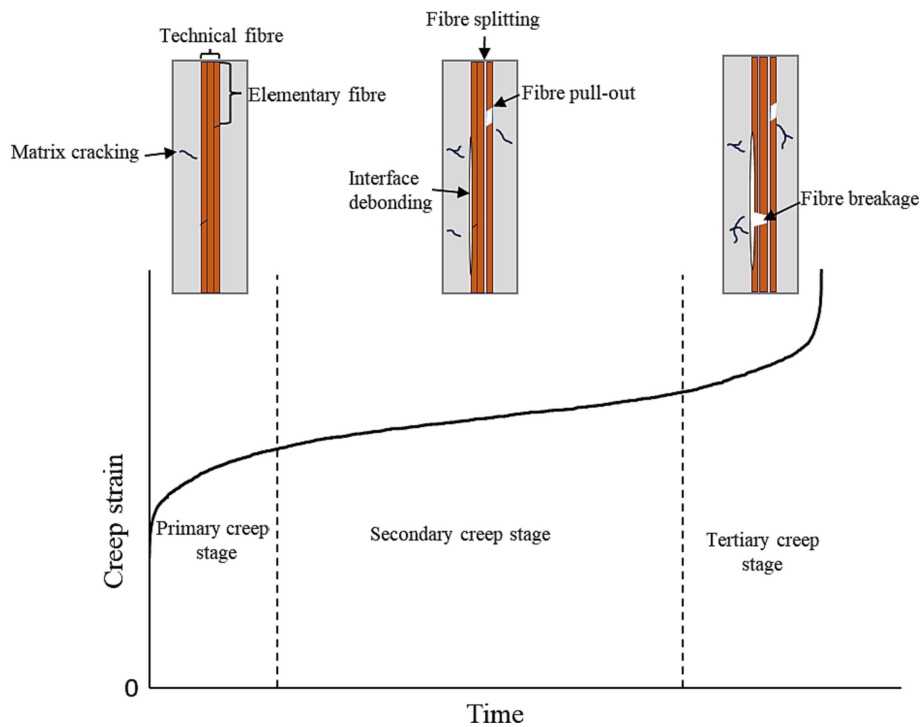


Figure 3.2: Damage evolution under creep load, found by Hao et al. (2024)

3.1.5. Parameters Influencing Creep Behaviour

The creep behaviour of most materials is strongly influenced by stress and temperature, with both higher stress and temperature accelerating the creep rate (Huda, 2022). The Eurocomp (1996) guidelines categorize the factors affecting the creep behaviour of composites into two groups: material properties and environmental conditions. Additional factors are suggested in CEN/TS 19101 (2022).

Material properties

- Type of resin and the extent of curing
- Interfacial bonding between fibres and matrix
- Fibre volume fraction
- Form of reinforcement (woven, non-woven, mats)
- Fibre orientation and arrangement relative to the applied load
- Method of processing
- Fibre moisture content

Environmental conditions

- Temperature
- Relative humidity
- Type of loading
- Exposure to chemicals
- Applied stress level
- UV degradation

Creep is primarily dominated by the matrix (Eurocomp, 1996), particularly in carbon fibre composites, where the fibres exhibit almost no creep. However, in natural fibre composites, both the fibres and matrix contribute to creep. Environmental factors, particularly temperature and relative humidity (RH),

can greatly influence the creep behaviour (Staab, 2015). For natural fibres, even the temperature and RH history of the samples influences their creep behaviour, as it affects the water absorption and desorption of the fibres during testing. If a specimen is not in moisture equilibrium with the RH of the test environment, it may expand or contract due to moisture changes, leading to inaccurate or distorted strain measurements (ISO 899-1:2017, 2017). The ISO 899-1:2017 (2017) (the ISO standard for tensile creep testing of plastics) recommends conducting the creep tests in the same atmosphere as used for the conditioning of the specimens. Additionally, unloaded dummy samples can be placed alongside the creep test to monitor their deformation and weight to identify any unexpected strains or moisture absorption or desorption during the test.

3.2. Methods to Test Creep

Creep tests are essential for predicting a material's long-term behaviour under sustained loads, including its dimensional changes and structural integrity (ASTM D2990-09, 2009). Since most structural components are designed for a lifespan of a decade or more, it is crucial to incorporate long-term material properties into the design process to ensure a safe structure. However, testing materials over such extended periods is often impractical and very expensive. Consequently, emphasizing the need for accelerated methods to characterize long-term material properties and significantly reduce both testing times and research costs (Luo et al., 2012).

3.2.1. Design Codes that Describe Creep

There are several design codes and recommendations that explain how to take creep into account for different materials. The most widely used standard in the construction industry is the Eurocode (EN 1990 to EN 1999). However, these standards are often focused on traditional construction materials such as steel, concrete, and timber. A new Eurocode for fibre-reinforced polymers (FRPs), CEN/TS 19101 (2022), addresses synthetic fibres such as glass, carbon, basalt, and aramid, but does not cover natural fibre composites. For materials outside these addressed categories, creep coefficients must be determined experimentally, following standards like ASTM D2990-09 (2009).

Creep testing for innovative materials can be time-consuming and expensive, leading many in the construction industry to favour standardized materials. The ASTM D6992-16 (2023) provides recommendations for accelerated creep testing of geosynthetic materials using the time-temperature superposition (TTSP) and the stepped isothermal method (SIM). Nevertheless, these are not yet standardized for (natural) fibre-reinforced polymer composites.

Another document that offers guidelines for FRP composites is the CUR 96 (2019), again focussing primarily on glass, carbon, and aramid fibre composites. Since natural fibres exhibit more creep deformation than synthetic fibres, it is crucial to assess the creep performance of natural fibre composites to ensure they meet the serviceability requirements. Ideally, standardized creep coefficients for natural fibres should be established to provide accurate, non-conservative values, making these materials more attractive and viable for structural applications. In an annex of the CUR 96 (2019), recommendations and additional comments are written on the use and testing of bio-based fibre-reinforced composites, including a testing method for creep.

3.2.2. Conventional Creep Test

A conventional creep test (CCT), involves applying a dead weight to a specimen and measuring its deformation over time, which can span months or even years. This real-time test provides insight into creep deformation and, at higher loads, creep rupture behaviour. However, the duration of a CCT is inevitably its main limitation (Giannopoulos & Burgoyne, 2011). Additionally, challenges, such as maintaining consistent environmental conditions and preventing any disruptions that could compromise the test results, increase with the duration of a CCT.

The ASTM D2990-09 (2009) outlines testing methods for tensile, compressive and flexural creep and creep rupture of plastics. During these CCT tests, the deformation is measured over time, under a constant load in constant environmental conditions. Different tests can be conducted on the same material at different temperatures and different load levels to investigate multiple scenarios and get a broader view of the material's long-term behaviour. The resulting data helps to predict a material's creep modulus and its long-term strength. The ASTM D2990-09 (2009) recommends a minimum test duration of 1000 hours (about 42 days), but CCTs often run much longer (sometimes years) to study

the material's real-time behaviour. Therefore, CCTs can be very time-consuming and very costly.

Given the time and expenses involved in CCTs, shorter experiments can be conducted to gather preliminary data. The results of the creep tests can be extrapolated and extended using mathematical models that can vary for different materials. Typically, a power law function is used to fit and extrapolate an experimentally obtained creep curve to predict the long-term creep behaviour (Eurocomp, 1996).

3.2.3. Accelerated Creep Test Methods

Given the excessive time and costs of conducting full-lifetime creep experiments, accelerated methods are essential for predicting the long-term creep behaviour of materials, especially for ensuring structural safety and serviceability (Peng et al., 2022). Accelerated creep tests could reduce the need for overly conservative safety factors, which often result in less efficient material use. Without sufficient long-term data, engineers may resort to alternative (maybe less suitable) materials, simply because there is more confidence about their long-term performance (Giannopoulos & Burgoyne, 2011). Accelerated testing offers a practical solution, to assess the long-term behaviour of new materials, while saving time and resources. Evaluating the reliability of these accelerated test methods and their data.

The creep test method for bio-based fibre-reinforced composites that was used in the construction of the bio-based bridges mentioned in the introduction, is described in the annex of the CUR 96 (2019). The creep factor for the serviceability limit state is based on a series of creep-rupture tests, and must be tested for each type of composite laminate. The method describes performing a minimum of seven tests each with a different stress level which leads to creep failure after approximately 1 hour, 10 hours, 30 hours, 100 hours, 300 hours, 1000 hours (42 days), and 3000 hours (4 months) (CUR 96, 2019). The test results are plotted on a double logarithmic scale showing the applied stress versus the time to creep failure (see figure 3.3). A linear regression line is drawn from the data points from which the creep factor is derived. This method takes at least one to three months. Other accelerated creep test methods are available but are not standardized for bio-based materials.

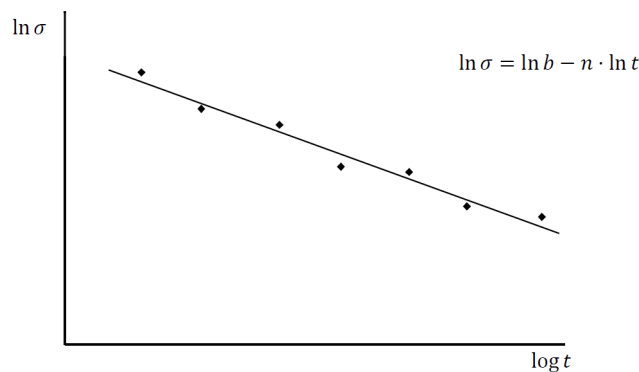


Figure 3.3: A schematic example of the creep (rupture) test results used in the CUR annex to determine the creep factor for creep deformation of a bio-based composite (CUR 96, 2019)

Time-Temperature-Stress Superposition Principle

The time-temperature superposition principle (TTSP) is based on the observation that the short-term behaviour of a viscoelastic material at higher temperatures resembles its long-term behaviour at a lower reference temperature (Lee, 2007). The method was originally applied to solid polymers but is now used for FRPs too (Goertzen & Kessler, 2006). TTSP assumes that the effect of a higher temperature is equivalent to an extension of the real-time creep behaviour by a certain shift factor, mathematically represented by equation 3.4 (Goertzen & Kessler, 2006; Hadid et al., 2014).

$$\varepsilon(T_r, t) = \varepsilon(T, t \cdot \alpha_T) \quad (3.4)$$

With:

T_r = reference temperature

T = test temperature

α_T = temperature shift factor

TTSP involves conducting a series of short-term creep tests at the same stress but at a range of different temperatures. The resulting curves can each be based on a shift factor, to form a continuous long-term creep curve. One curve serves as the reference temperature, the others are adjusted on a logarithmic timescale with respect to that reference temperature. For each TTSP test at a specific temperature, a new sample of the same material is used (Hadid et al., 2014). Figure 3.4 illustrates this TTSP shifting of the curves, where the tests performed at a lower temperature than the chosen reference temperature are shifted to the left, and tests at higher temperatures are shifted to the right. The shift factor, $\log(\alpha_T)$, can be calculated graphically, by manually lining up the curves till they overlap or form a smooth line. Alternatively, the shift factor can be estimated by the activation energy of the glass transition relaxation from the frequency dependence of the glass transition temperatures measured with dynamic mechanical analysis (DMA) (Goertzen & Kessler, 2006). The activation energy for creep is the minimum energy that is required to cause creep and is a material constant measured in Joules per mol (J/mol) (Huda, 2022). TTSP is typically used for linear viscoelastic materials (Luo et al., 2012).

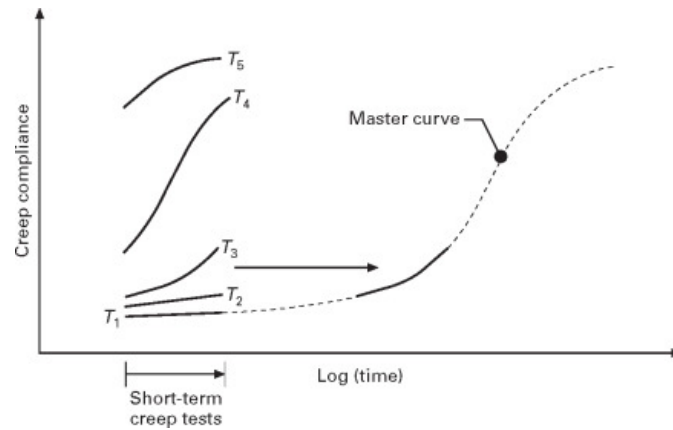


Figure 3.4: A schematic example on how to obtain a creep master curve by shifting the short-term creep curves according to the TTSP (Lee, 2007)

A similar method to TTSP is the time-stress superposition principle (TSSP) (Hadid et al., 2014). The TSSP method tests all the short-term creep tests at the same constant temperature but at varying stress levels. Again, using a new specimen for each test at a different stress level. As with TTSP, the curves are shifted relative to the reference stress to create a smooth continuous master curve, and the mathematical model adjusts accordingly (equation 3.5) (Hadid et al., 2014; Lee, 2007).

$$\varepsilon(\sigma_r, t) = \varepsilon(\sigma, t \cdot \alpha_\sigma) \quad (3.5)$$

With:

σ_r = reference stress

σ = test stress

α_σ = stress shift factor

Combining TTSP and TSSP results in the time-temperature-stress superposition principle (TTSSP), which accounts for the interdependence of stress and temperature on creep behaviour (Hadid et al., 2014; Luo et al., 2012). The TTSSP theory states that there is a fundamental relationship between time, temperature, and stress in terms of creep behaviour, which can be used to reduce the testing duration of a creep test (Hossain et al., 2020). The assumption is made that the increase in stress provides energy to the tested material that is similar to that provided by heat (Hadid et al., 2014). This principle has been validated for nonlinear viscoelastic materials, such as poly-methyl methacrylate (Luo et al., 2012), and for natural fibres such as bamboo (Peng et al., 2022). TTSSP offers valuable tools for predicting the long-term creep behaviour of a material while significantly reducing the experimental testing time.

Stepped Isothermal Method

The stepped isothermal method (SIM) is derived from the time-temperature superposition principle (TTSP) (Hadid et al., 2014). It was first introduced by Thornton and Sandri (1999) to predict the long-term creep behaviour of geogrids in soil reinforcement. Unlike TTSP, which requires testing multiple specimens at different temperatures, the SIM uses only a single specimen. The specimen is subjected to a constant stress, starting at a reference temperature, which is then gradually increased in a series of controlled steps. At each step, the temperature is maintained at a constant level for a certain dwell time, allowing a small creep curve to develop before moving to the next temperature step. The last step can go up to creep rupture, but this is not a necessity for the method to be used. The obtained curves are individually processed, shifted and scaled to create a long-term creep master curve for the specified reference temperature (Achereiner et al., 2013; Hadid et al., 2014; Yeo & Hsuan, 2009).

The SIM data analysis involves several steps to construct the master creep curve, which are visualized in figure 3.5. First, the thermal expansion effects unrelated to creep are removed by vertically shifting the data of each temperature step downward (figure 3.5.a). In the second step, called rescaling, the steps are treated as individual creep curves, each having its own extrapolated virtual starting time t'_i . The curves are then rescaled to match their virtual starting times, similarly as in a TTSP test (figure 3.5.b&c). The curves can then be shifted horizontally in the same way as in TTSP (figure 3.5.d). The horizontal shift factor can be empirically determined by the Williams-Landel-Ferry (WLF) equation (equation 3.6), or the Arrhenius equation (equation 3.7). The WLF equation is often used for amorphous polymers above the glass transition temperature. However, it is not valid for semi-crystalline polymers well below their melting points. In that case, the Arrhenius equation can be used to describe the shift factor (Achereiner et al., 2013). In the SIM, the horizontal shifting factors are typically larger than in TTSP due to the vertical shifting in the first step of the SIM data processing (Yeo & Hsuan, 2009). Unlike TTSP, where the curves often overlap, gaps between curves in SIM make the graphical alignment more challenging, though it remains the preferred method for constructing creep master curves. ASTM standards for SIM include the ASTM D6992 for tensile creep and ASTM D7361 for compressive creep. Recent research by B. Xu et al. (2023) successfully applied the SIM to predict the long-term creep behaviour of a flax fibre composite.

$$\log(\alpha_T) = \frac{-C_1(T - T_r)}{C_2 + T - T_r} \quad (3.6)$$

With:

- α_T = temperature shift factor
- C_1 = empirical material constant
- C_2 = empirical material constant
- T = temperature during test
- T_r = reference temperature

$$\log(\alpha_T) = \frac{Q}{2.303R} \left(\frac{1}{T} - \frac{1}{T_r} \right) \quad (3.7)$$

With:

- Q = activation energy
- R = universal gas constant
- 2.303 = approximation of $\ln(10)$, factor used to convert the base number in the logarithm from the natural logarithm with the base number e to the common logarithm with the base number 10

Stepped Isostress Method

The stepped isostress method (SSM) is derived from the time-stress superposition principle (TSPP), similarly as the stepped isothermal method (SIM) is derived from the time-temperature superposition (TTSP). In the SSM the acceleration of creep is obtained by the stepwise increase of the stress, rather than the temperature as in SIM. Throughout the SSM test, the environmental conditions such as temperature and relative humidity (RH) are kept constant. Like the SIM, the SSM uses a single specimen

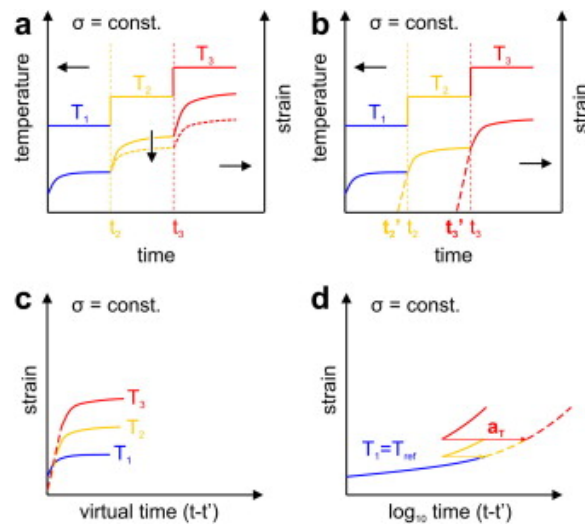


Figure 3.5: The principle steps to construct the master creep curve through SIM (Achereiner et al., 2013). With (a) vertical shift to correct for thermal expansion, (b) determining the virtual starting time t'_i , (c) rescaling, and (d) curve shifting with time on a log scale according to TTSP

for a test, which makes it much faster than the TSSP test. Both SIM and SSM tests can be completed with one sample within 24 hours, a significant time-saving advantage compared to conventional creep tests (CCT), which can last for months or even years. In SSM, the master creep curve is constructed through the similar three steps as in SIM, using the time-temperature-stress superposition (TTSSP). The difference between the TTSSP and the SIM and SSM is that the latter two first have to account for the specimen's strain history, since all stress- or temperature steps are performed on the same sample before the TTSSP shift can be applied (Hadid et al., 2014; Yeo & Hsuan, 2009).

Unlike SIM, the SSM lacks a standardized data treatment method for constructing the creep master curve (Guedes, 2018; Hadid et al., 2014). More research is needed to find a systematic and automated standard approach for handling the SSM data for specific materials. The main advantage of the SSM over the SIM is that as the environmental conditions are kept constant during the SSM, the temperature does not affect the material properties, avoiding issues such as non-uniform heating (Hadid et al., 2014). This is particularly useful when testing thick polymeric materials with a low thermal conductivity, where heating can result in uneven temperature distributions within the specimen, affecting the creep strain measurements (Hadid et al., 2014; Huang et al., 2018).

3.3. Conclusion

Creep is a critical aspect in designing structures with flax fibre composites due to the time-dependent deformation of both the flax fibres and the polymer matrix. Understanding this behaviour is important for ensuring structural integrity, especially when the material is exposed to sustained loads over time. Little research has been done on the long-term creep deformation of flax fibre composites at a low creep stress. The stepped isostress method (SSM) and stepped isothermal method (SIM) are both promising alternatives for conventional creep tests, by significantly reducing the testing time and costs. Given the sensitivity of flax fibre composites to temperature and humidity, along with their low thermal conductivity and the thickness of the samples used in this study, the SIM seems unsuitable. Instead, the SSM is a more appropriate choice for accelerated creep testing in this case. However, the SSM has not been used on flax fibre composites before, so further research is needed to validate its effectiveness. Comparing SSM results with CCT tests can contribute to verifying the SSM's accuracy. It would be very interesting to use the SSM to predict the long-term creep deformation in the flax fibre composite and compare the results with the findings of B. Xu et al. (2023) who used the SIM to predict the long-term creep deformation of a flax fibre composite.

4

Stepped Isostress Method

In this chapter, the stepped isostress method (SSM) is elaborated in more detail. The chapter starts by explaining the methodology of the SSM. Subsequently, each step of the data handling procedure is explained in detail, referring to the approaches adopted by various researchers who have applied the SSM. It also discusses the validation of the SSM method based on prior studies, and concludes with a comparison of the SSM test designs and data handling techniques used by different researchers.

4.1. Introduction to the Stepped Isostress Method

The stepped isostress method (SSM) was first introduced by Giannopoulos and Burgoyne in 2009, to predict the creep behaviour of aramid fibres. Unlike the traditional time-stress superposition principle (TSSP) methods, which involve testing multiple samples at varying stress levels, the SSM test is performed on a single sample that is subjected to incrementally increasing stress levels. Each stress step is held constant for a specific duration, also called dwell time, before increasing the stress to the next stress step. In contrast to the stepped isothermal method (SIM), the temperature and relative humidity are kept constant throughout the SSM test. In the initial stress step, the sample is loaded with the reference stress, which forms the basis for the creep master curve that will later be constructed from the SSM data via TSSP. Additionally, the SSM can provide information on creep rupture when the sample is tested up to creep failure. However, going to failure is not a requirement for utilizing the SSM (Tanks et al., 2017). At each stress step, a small creep curve is obtained, which is shifted and scaled individually to construct a prediction of the creep master curve for the set reference stress (Giannopoulos & Burgoyne, 2011; Hadid et al., 2014; Tanks et al., 2017). Unlike the SIM, the SSM does not have a standardized approach for data treatment, making the construction of the creep master curve less methodical (Guedes, 2018; Hadid et al., 2014). Further research is needed to establish a systematic and automated data processing method for the SSM, which would make the data processing quicker and less subjective and would make comparisons across different studies much easier.

4.2. Stepped Isostress Data Analysis Procedure

The data handling procedure for the SSM involves three primary steps. The first step is a vertical shift, the second step is rescaling and the last step is a horizontal shift. Before initiating these steps, the test data must first be divided into individual smaller creep curves, corresponding to each stress step, allowing for their independent shifting and scaling. In the following sections, each of the three steps in the data analysis procedure is explained in more detail.

4.2.1. Vertical Shifting

The vertical shifting involves adjusting for elastic strains at each load step and connecting the end of each small creep curve to the start of the next curve (Hadid et al., 2014; Tanks et al., 2017). When, during an SSM test, the stress jumps to the next stress step, the material is subjected to a sudden increase in stress, and an immediate strain response occurs due to its elasticity (Giannopoulos & Burgoyne, 2011). The total strain is defined as the combination of instantaneous strain and creep strain,

where the former can include both elastic and plastic strains, caused by the stress jumps between the load steps (Tanks et al., 2017). In SSM, it is assumed that with a constant temperature, the thermal strains are negligible. The vertical shifting is performed to create a continuous creep master curve that represents only creep strains. Eliminating the instantaneous response of each small creep curve of the SSM data assumes that during the stress jumps, only elastic strains occur and no creep strains are measured as the stress change is nearly instantaneous (Giannopoulos & Burgoyne, 2011; Hadid et al., 2014). The vertical shift can be calculated using the material's elastic modulus, assuming it remains unaffected by creep (Giannopoulos & Burgoyne, 2011). Alternatively, the vertical shift can be determined graphically, although this method introduces some subjectivity, it addresses the elastic strain of each curve individually, rather than relying on an average elastic strain obtained from tensile tests (Giannopoulos & Burgoyne, 2011; Tedjini et al., 2022). A more objective method of the vertical shift involves setting a boundary value for the creep rate to locate the strain jumps (Tanks et al., 2017). This method still accounts for each individual creep curve and can also be used to distinguish between primary creep and secondary creep, which is necessary for the rescaling step. The outcome of the vertical shift is a curve that reflects only creep strains.

Some researchers, such as Hadid et al. (2014) and Tedjini et al. (2022), apply an initial vertical shift before the vertical shifting as explained above, to account for the deformation in the test setup (for example, sliding of the jaws). This initial vertical shift adjusts all the curves downward by the same value, creating a new baseline for constructing the master creep curve.

4.2.2. Rescaling

The rescaling step accounts for the stress history of the specimen, including the effects of creep and damage from previous steps (Tanks et al., 2017). Each curve from a different stress step is treated as an independent creep curve, with a virtual or projected starting time, t'_i . For example, when the stress increases to σ_2 at the start of step 2, some creep deformation would have already occurred if the test on this stress was carried out on a new sample. Therefore, the strain measured in step 2 would have started at a different (earlier) starting time if the test had been performed on a sample with no stress history $t'_2 < t_2$ (Achereiner et al., 2013; Giannopoulos & Burgoyne, 2011; Tanks et al., 2017). The rescaling step takes the form of a horizontal shift to simulate the curve that is obtained in a typical TSSP test, where each stress level is applied to a separate sample (Giannopoulos & Burgoyne, 2011). The virtual starting time is determined empirically, often through extrapolation using graphical methods or numerical curve fitting, such as power-law, polynomial functions, or Prony series. Only the secondary creep region of each curve is used to determine the projected starting time, by extrapolating the secondary creep region to zero creep strain. Tanks et al. (2017) define the secondary creep region as the point where the creep strain rate varies by less than 0.025% from the start of that load step. The rescaling step makes the separate creep curves independent of their previous load steps (Hadid et al., 2014; Tanks et al., 2017). Rescaling is performed for all stress levels except the reference stress, typically the first stress level. After rescaling, a set of independent creep curves under different stress levels is obtained, allowing them to be processed similarly to the curves obtained in TSSP (Hadid et al., 2014).

4.2.3. Horizontal Shifting

The horizontal shifting step can be conducted similarly to the TSSP, requiring a horizontal shift along the logarithmic time axis to construct the creep master curve (Giannopoulos & Burgoyne, 2011; Hadid et al., 2014; Tanks et al., 2017). The magnitude of this shift is a function of the stress level and is expressed as the time-stress shift factor that must be determined for each stress step (Hadid et al., 2014; Tanks et al., 2017). Similarly to the rescaling step, the horizontal shifting involves only the secondary creep regions of each load step, as the master creep curve should represent a single applied stress level synthesized from multiple stress levels. Only the primary creep region of the reference stress is retained for the start of the master creep curve of that reference stress (Tanks et al., 2017). The master creep curve can be constructed either graphically, which can be subjective, or empirically, using the stress-modified Williams-Landel-Ferry (WLF) equation (equation 4.1) or the Eyring model (equation 4.2) (Giannopoulos & Burgoyne, 2011; Hadid et al., 2014; Tanks et al., 2017).

$$\log(\alpha_\sigma) = \frac{C_1(\sigma + \sigma_r)}{(C_2 + \sigma - \sigma_r)} \quad (4.1)$$

With:

- α_σ = stress shift factor
- C_1 = empirical material constant
- C_2 = empirical material constant
- σ = stress during test
- σ_r = reference stress

$$\log(\alpha_\sigma) = \log\left(\frac{\dot{\epsilon}}{\dot{\epsilon}_r}\right) = \frac{V^*}{2.303kT}(\sigma - \sigma_r) \quad (4.2)$$

With:

- V^* = activation volume
- k = Boltzmann's constant
- T = absolute temperature [K]
- 2.303 = approximation of $\ln(10)$, factor used to convert the base number in the logarithm from the natural logarithm with the base number e to the common logarithm with the base number 10

The choice between the stress-modified WLF equation and the Eyring model depends mostly on the temperature of the test environment. The WLF equation is typically used when the temperature is close to the glass transition temperature, whereas the Eyring equation is preferred at lower or moderate temperatures, far below the glass transition temperature (Brostow, 2000; Giannopoulos & Burgoyne, 2011; Hadid et al., 2014).

Hadid et al. (2014) highlight the rescaling step as the most critical step in forming the creep master curve with the SSM. This is because the rescaling step adjusts the individual curves on the laboratory timescale to align them at a common point on the material timescale. Subsequently, the horizontal shift, moves the curves over the material timescale, reflecting the relation between time and stress in the material's behaviour on the material timescale. Errors in the rescaling operation can lead to misalignment of the curves, complicating the horizontal shifting process and potentially causing a loss of the material timescale (Hadid et al., 2014). Giannopoulos and Burgoyne (2011) also emphasize the subjectivity in the fitting parameters for constructing a smooth master curve. It is therefore important to create a standardized approach for the SSM data handling, to replace the empirical and graphical methods. Ultimately, the goal of the SSM data processing steps is to achieve a smooth creep master curve at a certain reference stress, σ_r (Giannopoulos & Burgoyne, 2011).

4.2.4. Validation of the Stepped Isostress Method

The first step in validating the SSM-derived creep master curve is to ensure the curve is smooth. Additionally, the SSM creep master curve can be compared with a conventional creep test (CCT) conducted under the same environmental conditions and the same stress as the reference stress in the SSM (Giannopoulos & Burgoyne, 2011). The extent to which the SSM curve can be validated with a CCT depends on the duration of the CCT. Huang et al. (2018), B. Xu et al. (2023), and Yang et al. (2021) all use a CCT with a duration of 90 days to validate their SSM and SIM predictions. While extrapolation of the CCT creep curve can extend the validation timeframe, this introduces additional uncertainty due to the comparison of two estimates. Tanks et al. (2017) validated the SSM results by fitting a power-law function to the first (reference) stress step, assessing the smoothness of the derived creep master curve.

Furthermore, the horizontal shift factors can be validated using the Eyring equation (equation 4.2) and their relationship with the stress or the activation volume. Various interpretations of these relationships exist in the literature, explained in more detail in the paragraph below, and summarized in table 4.1. Giannopoulos and Burgoyne (2011) observed a linear increasing relation between the stress-shift factor $\log(\alpha_\sigma)$ and the stress as well as between the activation volume and the stress. However, a linear relationship between the activation volume and the stress would imply, according to the Eyring model, that the relationship between the stress-shift factor and the stress is more likely parabolic or polynomial. Hadid et al. (2014) found a power function relationship between the stress-shift factor and the stress, and a linear relationship between the activation volume and the creep stress. Additionally, Hadid et al.

(2014) suggested that the alignment of stress-shift factors under different test conditions would indicate the robustness of the SSM. Tanks et al. (2017) identified a linear relationship between the stress-shift factor $\log(\alpha_\sigma)$ and the stress in terms of $(\sigma_i - \sigma_r)$, suggesting that this linear trend indicates a consistent dominant creep mechanism and validates the SSM's superposition method. Tanks et al. (2017) also proposed that the activation volume is inversely proportional to the reference stress but did not address the actual stress during a single SSM test. Tedjini et al. (2022) stated that the activation volume can be presented as the slope between the shift factor $\log(\alpha_\sigma)$ and the accelerated stress $(\sigma_i - \sigma_r)$ and found a parabolic relation between the stress-shift factor and the stress. However, Tedjini et al. (2022) also stated that this parabolic function was very close to a linear function. Yang et al. (2021) also found a linear relation between the stress-shift factor $\log(\alpha_\sigma)$ and the stress in terms of $(\sigma_i - \sigma_r)$, just like Tanks et al. (2017) did. Research by Kubát and Seldén (1978) on the stress dependence of activation volumes for different materials, including cellulose, showed a linear decreasing relationship between the activation volume and the effective stress for secondary creep.

Table 4.1: Relation between the stress-shift factor and the stress ($\log(\alpha_\sigma)$ and $(\sigma_i - \sigma_r)$), and the activation volume and the stress V^* and σ

Author	$\log(\alpha_\sigma)$ and $(\sigma_i - \sigma_r)$	V^* and σ
Giannopoulos and Burgoyne (2011)	Linear increasing	Linear increasing (with reference stress, expressed in %ABL = average breaking load)
Hadid et al. (2014)	Power function	Linear
Tanks et al. (2017)	Linear increasing	Non-linear decreasing (for different reference stresses)
Yang et al. (2021)	Linear increasing	-
Tedjini et al. (2022)	Parabolic (but very close to linear increasing)	-
J.-W. ; Xu et al. (2023)	Linear increasing	Constant

The stepwise increase in stress during SSM affects the activation volume, leading to a new configuration of the material's molecular chains (Hadid et al., 2014). In SSM, the chain configuration at each step is influenced by all prior creep loadings of previous steps. The activation volume of a previously strained material is larger than that of an unstrained material (Hadid et al., 2014; Tedjini et al., 2022). This suggests that the activation volume of the material at (for example) the third stress step in SSM, σ_3 , would be higher than that of a new, unstrained sample subjected to the same load, as would occur in classical TSSP.

4.3. Comparison of Previous Research Using the Stepped Isostress Method

Although the stepped isostress method (SSM) is gaining popularity, the stepped isothermal method (SIM), with a more standardized method, is more commonly used. Additional research is needed to standardize the SSM and reduce its empirical nature. Different researchers have found the SSM valid for all kinds of materials. Giannopoulos and Burgoyne (2011) were among the first to apply SSM, using it to predict the creep behaviour of single Kevlar yarns. Tanks et al. (2017) demonstrated that the SSM can predict long-term creep in polymeric composites, particularly in carbon fibre-reinforced polymer laminates. Hadid et al. (2014) and Tedjini et al. (2022) validated SSM for creep in polyamide 6, while Yang et al. (2021) applied the method to heat-treated moso bamboo. J.-W. ; Xu et al. (2023) confirmed the validity of SSM for predicting creep in Japanese cedar wood.

4.3.1. SSM Test Methods of Different Researchers

There is no standard for the dwell time for the SSM steps. The ASTM D6992-16 (2023) (the standard for the SIM) suggests that the step increments and dwell times should be chosen to ensure that the steady-state creep rate at the start of a new step closely matches that of the previous step, but does not provide specific values. Researchers must therefore determine these parameters for their own studies. Hadid et al. (2014) Argued that the dwell time and reference stress level can be arbitrarily chosen within the material's elastic region. Dwell times in previous research vary widely, from 10 hours (Guedes, 2018)

to 1 hour (Tanks et al., 2017), with 5 hours (Giannopoulos & Burgoyne, 2011; Hadid et al., 2014; Huang et al., 2018; Tanks et al., 2017) and 2 hours (Guedes, 2018; Hadid et al., 2014; Huang et al., 2018; Tedjini et al., 2022; Yang et al., 2021) being the most commonly used. Some researchers (Hadid et al., 2014; Yang et al., 2021; Yeo & Hsuan, 2009) have compared the SSM results from different dwell times and stress increments, concluding that these factors, within certain ranges, give similar results and do not significantly influence the obtained creep master curve. However, this does not imply that the dwell time and stress increments have no effect on the final results, but within certain ranges, this effect seems minimal. Giannopoulos and Burgoyne (2011) compared SSM results with results from SIM tests and CCT, finding agreement among all three methods, which supports the validity of SSM for determining creep deformation. They also noted that SSM can predict creep rupture behaviour when testing up to creep failure in the final SSM stress step.

The number of steps performed during the SSM test varies by researcher, typically ranging from five to ten steps. The stress increments can be expressed either in megapascals (Guedes, 2018; Hadid et al., 2014) or as a percentage of the ultimate tensile strength or average breaking load (Huang et al., 2018; Tanks et al., 2017; Yang et al., 2021).

4.3.2. SSM Data Handling by Different Researchers

In the literature, there are small differences in the details of the SSM data processing, among different researchers. The vertical shift in the first step of the data processing is generally quite straightforward, but the rescaling step and horizontal shift are often handled empirically using graphical methods (Guedes, 2018).

The rescaling methods vary by the researcher. Firstly, the determination of the virtual starting point differs across studies, ranging from graphical methods to various curve fits (figure 4.1 shows that different curve fits are used to extrapolate the individual creep curves). Giannopoulos and Burgoyne (2011) used a purely graphical approach to extrapolate and move the individual creep curves on a linear time axis, which is subjective and recommended only as an initial estimate. A more precise determination can be achieved numerically. Hadid et al. (2014) used a power-law fit to the secondary creep portion of each stress step to extrapolate the virtual starting time. Tanks et al. (2017) applied both a Prony series and a power-law fit to rescale individual creep curves, finding that the power-law fitted the secondary creep region of each load step well but, produced more conservative results and overestimated the total creep strain. The Prony series (with four terms) provided a better fit for each step's creep rate and was considered more reliable, although Tanks et al. (2017) acknowledged that the choice of fit is ultimately up to the engineer. According to Tanks et al. (2017) other methods can be used as long as a good fit for rescaling can be achieved. Tedjini et al. (2022) reported that a power-law fit and an exponential fit gave better results than a third-order polynomial fit, highlighting the significant influence of curve-fitting methods on the resulting creep master curve. In figure 4.1 the influence of different curve fits is shown.

Secondly, the method of moving the curves in the rescaling step varies among researchers (the difference is shown in figure 4.1). Tanks et al. (2017) calculated the shift factor as the difference between the real and virtual starting times for each step and moved along a log timescale (see figure 4.1a). The total shift, according to Tanks et al. (2017), follows equation 4.3, which involves only the secondary creep regions of the individual creep curves.

$$\log(t_{master})_i = \log(t_{actual})_i - \log(\alpha_{res})_i + \log(\alpha_{\sigma})_i \quad (4.3)$$

With:

t_{master} = reduced time of the creep for load step i in the master curve

t_{actual} = actual time of load step i during the test

α_{res} = rescaling shift factor for load step i

α_{σ} = horizontal shift factor for load step i

Where

$$(\alpha_{res})_i = (t_{rescale})_i = (t_{actual})_i - (t_{extrapolated})_i \quad (4.4)$$

Tedjini et al. (2022) moved the curves by aligning the virtual starting times of each step to the reference creep curve's starting time, moved on a normal timescale (see figure 4.1b). The method described by Tedjini et al. (2022) is more often used and seems to recreate the TSSP principle in a better way than the method of Tanks et al. (2017).

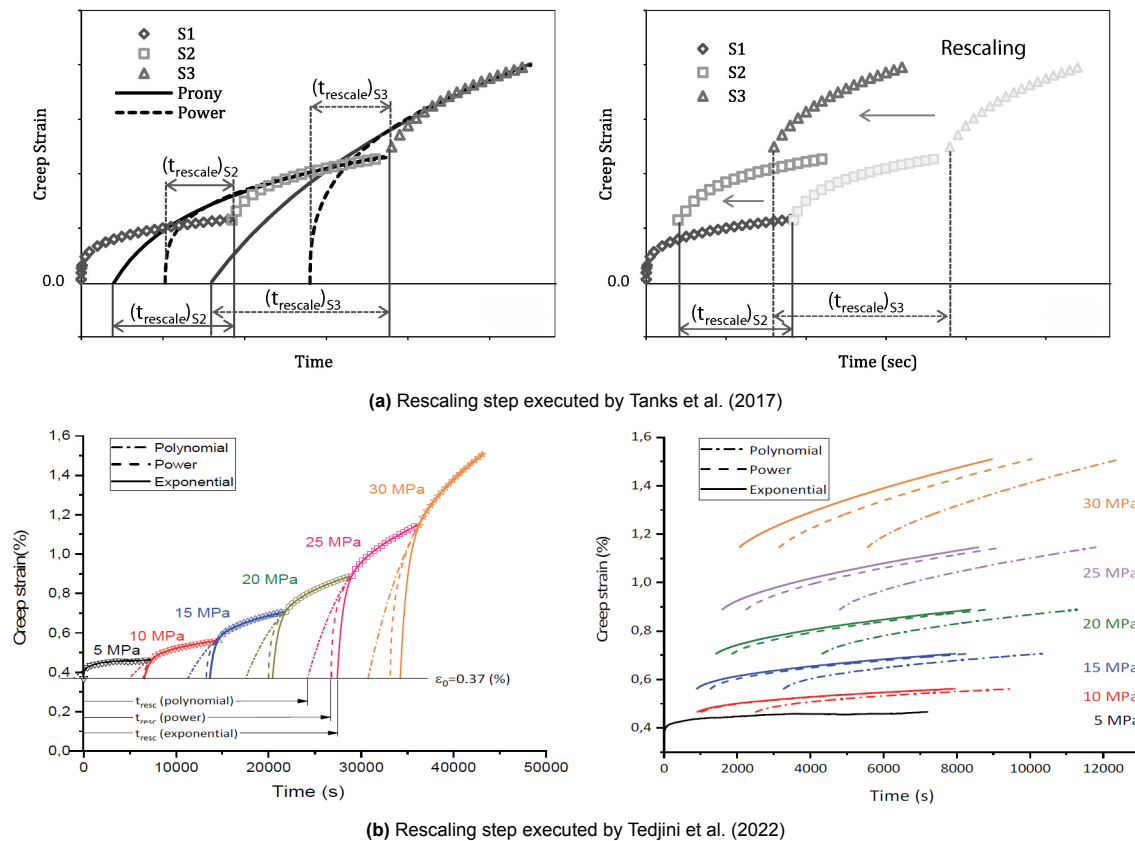


Figure 4.1: Comparison of the execution of the rescaling step in the papers of Tanks et al. (2017) and Tedjini et al. (2022)

The horizontal shift is again often done by a graphical method, constructing a smooth master creep curve. For instance, Giannopoulos and Burgoyne (2011) employed a graphical method to horizontally shift the curves, ensuring the smoothness of the curve by validating it with a polynomial fit. In contrast, Tanks et al. (2017) used a power-law fit based on the first creep step to guide the horizontal shifting of subsequent curves, and then verified the overall smoothness of the creep master curve against this fit. In most studies, such as those by Hadid et al. (2014), Tedjini et al. (2022), J.-W. ; Xu et al. (2023), and Yang et al. (2021), the Eyring model is typically applied to determine or verify the horizontal shift factors. However, as discussed in section 4.2.4, the interpretation and validation of the activation volume within the Eyring model and its relation to the stress-shift factor can vary across different studies.

4.4. Conclusion

The stepped isostress method (SSM) offers a promising approach for predicting the long-term creep behaviour of a material within a relatively short testing timeframe. The SSM not only provides information about a material's creep deformation but also gives insights into the creep rupture behaviour when the test is extended to the point of creep failure. While the primary focus of this research is on the material's creep deformation under a low stress, it is important to keep in mind that a higher applied stress approaches more of the material's capacity limits.

Currently, the SSM lacks standardization, and various data processing techniques are employed in previous research. The most effective approach seems to experiment with multiple methods or curve fits, to identify those that correlate best with the actual creep behaviour. Therefore, it can be very valuable to compare the SSM-predicted creep curves with those obtained from conventional creep tests to enhance the reliability of the SSM results. By applying different data processing techniques or curve-fitting methods, researchers can establish a bandwidth of predicted creep deformation. This range can then be evaluated to determine whether it meets the criteria for acceptable accuracy and if the SSM can be considered a reliable tool for predicting the material's creep behaviour.

Part II

Methodology

5

Materials and Methods

In this chapter, the design and production of the composite material is explained. The design of the laminate layup configurations is elaborated along with the general sample preparation for all tests. The test setup and methodology of the quasi-static tensile test, the long-term creep test, and the accelerated creep test using the SSM are explained, with a detailed description of the used equipment. This chapter includes the design and development of the long-term creep test setup.

5.1. Samples

The flax fibre composites that are used in this study were manufactured by Delft Infra Composites. In this research, three different laminate layup configurations are tested and compared, each with a thickness between 6 and 7 mm. For each layup configuration, a 1.27 m x 1.0 m plate was produced (the three layup configurations will be further explained in section 5.1.1). The flax fibres used in the composite of this research are made by Bcomp (Fribourg, Switzerland). The exact type of fibres used in the composite plates are Bcomp Amplitex 5025 fibres for the unidirectional layers, and Bcomp Amplitex 5008-2 fibres, which has a biaxial weave of $\pm 45^\circ$. Both types of flax fibre mats are stitched with a polyester thread. The resin used in the composite, Polynt 9759 IB, is an unsaturated polyester resin that was left over from the smart circular bridge project involving the construction of a flax fibre composite bridge. The resin is developed with a bio content of 46% and a recycled content of 14%. A microscopic image of one of the samples, shown in figure 5.1, clearly displays the flax fibres and the polyester stitching thread inside the hardened polyester resin.

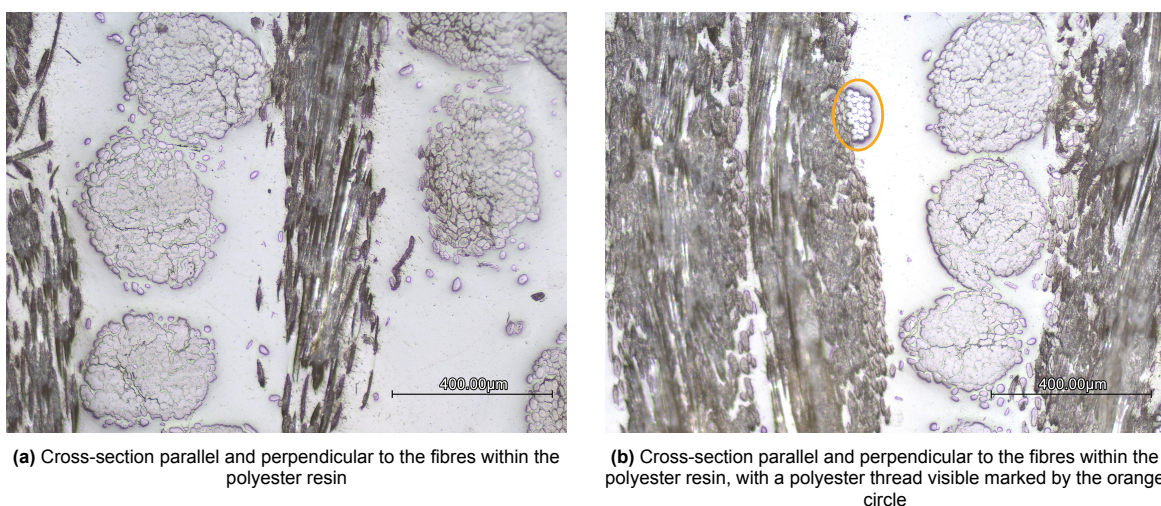


Figure 5.1: Microscopic pictures of a part of the cross-section of the composite, cut both parallel and perpendicular to the fibres, showing the fibre yarns and even the single elementary fibres within the yarns (both pictures are from a sample of plate C)

Initially, it was considered to apply a coating to the composite material as a way to protect it from moisture absorption and desorption. However, previous tests by Wouter Claassen indicated a risk of delamination of the coating during tensile tests. Since strain measurements are often taken from the surface of the sample, think of using cameras, extensometers, or strain gauges, the decision was made to not use a coating on the samples for this research. As a result, greater attention to environmental conditions is necessary during testing.

Delft Infra Composites manufactured the three composite plates by vacuum infusion under foil. Before the resin injection, the fibres were aligned in the desired directions and placed under a vacuum of 0-2 mbar. The resin was then injected at 50 mbar for approximately 40 minutes, after which the resin supply was closed and the pressure was increased to 85 mbar. The production conditions included an average relative humidity of $54\% \pm 5\%$ and a temperature of $19^\circ\text{C} \pm 1.5^\circ\text{C}$. Photos of the production of the plates are shown in figure 5.2.

After curing, the plates underwent a post-cure for 24 hours at 70°C to ensure the composite reached its full strength. Typically, composites for bridge constructions are not subjected to hot post-curing, as they gradually cure over the first few months of use. For this research, a hot post-curing was necessary to prevent post-curing during the creep experiments, which could interfere with results. The plates were stored in a climate-controlled room at a temperature of 20°C and 53% relative humidity, until further processing.

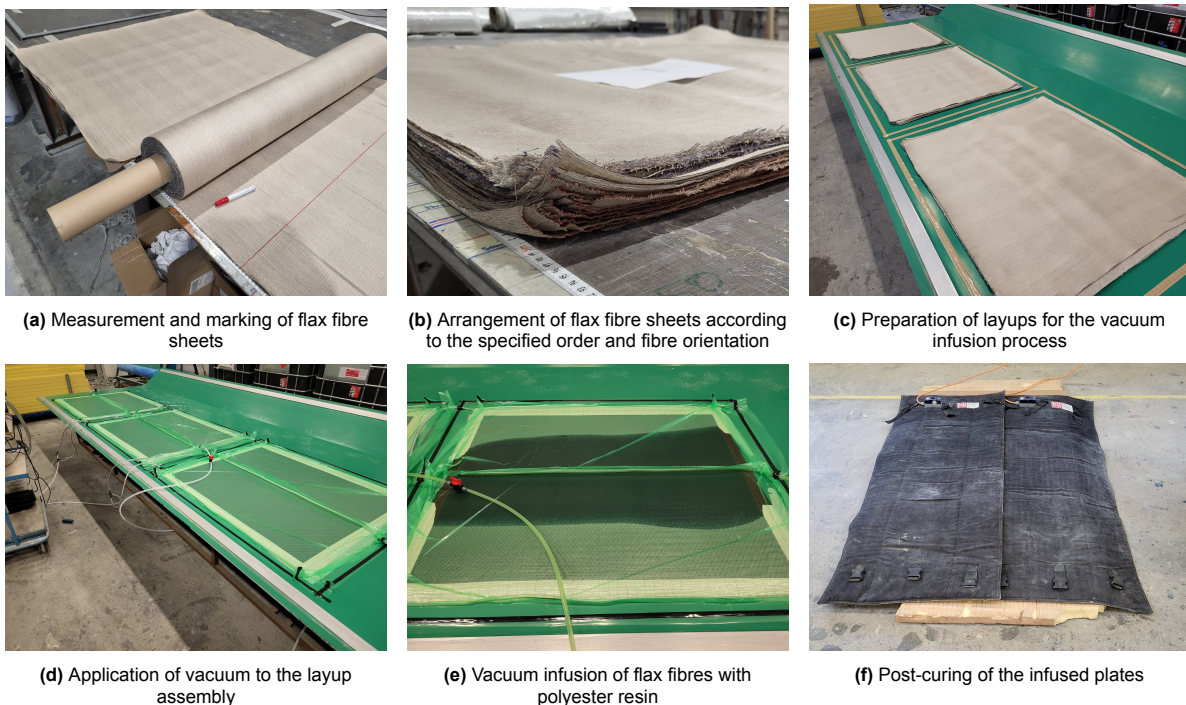


Figure 5.2: Stages in the production of the test plates, photographs by Paul Honing

5.1.1. Laminate Layup Configurations

This research compares three laminate layup configurations: (A) 100% unidirectional (UD) in the 0° direction, (B) 100% quasi-isotropic (QI), and (C) a combination of UD ($\pm 40\%$) and QI ($\pm 60\%$), which is often used in practice. In structural applications such as bridges, it is often desirable to align most fibres along the primary load direction, as this increases the strength in that axis. However, to maintain structural integrity, sufficient strength in all directions is essential to ensure the material can accommodate and redistribute forces from various directions. According to the guidelines of the CUR 96 (2019), the fibres must be distributed so that in all directions at least 12.5% of fibres are placed. Following this guideline (taking into account the four directions: 0° , $+45^\circ$, 90° , and -45°), this allows for 60% of the fibres to be strategically oriented along a preferred primary direction (0°).

Most prior research on creep in flax fibre composites has used thin specimens (1-3 mm thick), such as X. Wang and Petru (2022) with 1.35 mm thick samples in their research, Jia and Fiedler (2020) and B. Xu et al. (2023) with 2 mm thick samples and Giuliani et al. (2023) with 3 mm. In contrast, the flax fibre composite bridge in Ritsumasyt has elements with a thickness of 15 mm (Souren & Velds, 2019). To explore the behaviour of thicker specimens, this study uses samples of 6-7 mm thick. Thicker specimens allow for more optimal layup configurations, especially when combining the UD and QI layup in plate C. For example, a 2 mm thick sample would typically use around five sheets of flax fibres (assuming the use of Bcomp Amplitex fibres and a fibre volume fraction of 50%). Achieving the target of 60% fibre alignment in the primary direction and 12.5% in other directions becomes more manageable with a greater number of fibre sheets. On the other hand, thicker specimens pose a drawback, as they require a higher force to achieve the same stress levels as thinner specimens, which then requires heavier testing equipment. Given the time constraints of this research, the sample thickness was selected to balance practical testing considerations and the need for significant creep deformation at a low stress, within 2-3 months.

The total composite thickness was calculated based on the fibre density, the areal weight of the fibre sheets, and an estimated feasible fibre volume fraction (FVF) (see appendix A). The fibre volume fraction represents the fibre content as a percentage of the total composite volume. Delft Infra Composites estimated a feasible FVF of 45% for the composite plates. The number of flax fibre mats in a certain direction can be calculated with equation 5.1, based on a predetermined aimed thickness and layup.

$$n_{needed,0^\circ} = \frac{t_{tot,wanted} \cdot fvf \cdot D_{0^\circ,wanted} \cdot \rho_f \cdot 10^{-3}}{\rho A_{0^\circ}} \quad (5.1)$$

With:

$n_{needed,0^\circ}$ = the number of layers of fibre sheets in the 0° direction that is needed to achieve the aimed total thickness with a set ratio or percentage of fibres in each direction

$t_{tot,wanted}$ = total thickness that is aimed for the composite [mm]

fvf = fibre volume fraction [%]

$D_{0^\circ,wanted}$ = the total percentage of fibres that is aimed in the 0° direction in the composite [%]

ρ_f = the density of the fibres = 1400000g/m³

ρA_{0° = the areal weight of the fibres in the 0° direction [g/m³]

The fibre layers in the 0° and the 90° direction are made with the same type of fibres (Bcomp Amplitex 5025), and thus have the same areal weight. Therefore, $\rho A_{0^\circ} = \rho A_{90^\circ} = 275 \text{ g/m}^2$. The $\pm 45^\circ$ layers are made with a different type of fibres (Bcomp Amplitex 5008-2 Biax), which have an areal weight of $\rho A_{\pm 45^\circ} = 363 \text{ g/m}^2$. The needed number of layers can then be calculated for each direction in a layup, in this case: $n_{needed,0^\circ}$, $n_{needed,90^\circ}$, and $n_{needed,\pm 45^\circ}$. The required number of sheets must be rounded to integers since a fibre mat cannot be cut in half. When the desired number of layers is known for each direction, the total thickness of the fibres can be calculated with equation 5.2. The thickness of the matrix, based on the total fibre thickness and the expected FVF, can be calculated according to equation 5.3. The total thickness of the composite is then the summation of the fibre thickness and the matrix thickness (see equation 5.4).

$$t_{f,tot} = \frac{\rho A_{0^\circ} \cdot (n_{needed,0^\circ} + n_{needed,90^\circ})}{\rho_f \cdot 10^{-3}} + \frac{\rho A_{\pm 45^\circ} \cdot n_{needed,\pm 45^\circ}}{\rho_f \cdot 10^{-3}} \quad (5.2)$$

With:

$t_{f,tot}$ = total thickness of the fibres in the composite layup [mm]

$$t_{m,tot} = \frac{t_{f,tot}}{fvf} \cdot (100\% - fvf) \quad (5.3)$$

With:

$t_{m,tot}$ = the total thickness of the matrix in the composite [mm]

$$t_{tot} = t_{f,tot} + t_{m,tot} \quad (5.4)$$

With:

t_{tot} = the total thickness of the composite [mm]

In the sections below, the calculations of each of the three layups (A, B, and C) are shown using formulas 5.1 through 5.4, and the exact layup configurations are presented. Specific attention was paid to evenly distributing the different fibre direction layers across the laminate to reduce anisotropy and ensure an even load distribution. The layups were designed symmetrically to avoid coupled effects, as described in section 2.1. The maximum tensile stress for each layup was estimated based on the research of Jia and Fiedler (2020) and B. Xu et al. (2023), and with the Kolibri V4 software, which uses the classical laminate theory to determine the strength properties of a laminate.

After the production of the plates by Delft Infra Composites, the real thickness of each plate was measured and the real FVF was calculated. For every sample used in the tests, the width, and thickness are measured in three places within the gauge length. Based on these measurements, the FVF is determined with equation 5.5. All the measurements of the samples are presented in appendix C.

$$fvf = \frac{t_{f,tot}}{t_{tot,mean}} \cdot 100\% \quad (5.5)$$

With:

fvf = fibre volume fraction [%]

$t_{tot,mean}$ = mean of the measured total thickness of the composite plate [mm]

Layup A: 100% UD 0°

For layup A, the calculation for the number of layers needed to achieve a thickness of 6 mm indicated that 14 flax sheets were needed, as shown in table 5.1. Since this layup configuration is fully unidirectional, all fibres are aligned in the 0° direction (see table 5.4 for the exact layup configuration of each plate). The estimated maximum tensile strength for this layup is between 300 and 360 MPa.

After the arrival of the plate and cutting of the samples, the actual average thickness of layup A was measured at 5.62 mm, with a standard deviation of ± 0.11 mm. The average fibre volume fraction for layup A was calculated at $48.99\% \pm 0.95\%$, which is higher than initially estimated.

Table 5.1: Calculation of the amount of layers in layup A

Wanted total thickness				6.00 mm
Fibre volume fraction				45%
	UD 0	UD 90	±45	
Wanted Layup	100%	0%	0%	
Amount of layers needed	13.75	0.00	0.00	Total
Amount of layers used	14	0	0	14
Thickness fibres [mm]	2.750	0	0	2.750
Thickness of resin [mm]	3.361	0	0	3.361
Total expected thickness of layup A				6.11 mm
Actual measured mean thickness				5.62 mm
Actual measured fibre volume fraction				49%

Layup B: 100% QI

For layup B, the target thickness was set to 7 mm, one millimetre thicker than the other layups. This adjustment was made to compensate for its lower tensile strength, as this layup has the fewest fibres in the 0° direction. With a thicker sample, the tensile capacity of the B layup lies closer to the capacity of the other layups, which is helpful during testing and choosing an appropriate testing setup. The calculation of needed fibre layups in each direction for layup B with an aimed thickness of 7 mm is given in table 5.2. The fibres are equally distributed over all directions, keeping in mind that the \pm

45° layers are biaxial, the 25% +45° and the 25% –45° are added up to 50% ± 45°, for a fully quasi-isotropic layup. The actual symmetrical layup configuration of layup B is shown in table 5.4. The maximum tensile strength of the QI layup was estimated to be between 80 and 100 MPa.

After the arrival of the plate and cutting the samples, the mean thickness of plate B was measured at 7.29 mm with a standard deviation of ± 0.05 mm. The average FVF for layup B was calculated at 42.93% ± 0.31%.

Table 5.2: Calculation of the amount of layers in layup B

Wanted total thickness				7.00 mm
Fibre volume fraction				45%
	UD 0	UD 90	±45	
Wanted Layup	25%	25%	50%	
Amount of layers needed	4.01	4.01	6.07	Total
Amount of layers used	4	4	6	14
Thickness fibres [mm]	0.786	0.786	1.556	3.127
Thickness of resin [mm]	0.960	0.960	1.901	3.822
Total expected thickness of layup B				6.95 mm
Actual measured mean thickness				7.29 mm
Actual measured fibre volume fraction				43%

Layup C: 40% UD 0° + 60% QI

Layup C had a target thickness of 6 mm, with 55% of its fibres aligned in the 0° direction, 15% at 90°, and 30% at ± 45°. This layup configuration was based on table 3-16 (CUR 96, 2019, p.54) meets the guidelines in the CUR 96 (2019), stating a minimum of 12.5% of fibres must be placed in each direction of the laminate, to accommodate for incidental loads that cannot be foreseen and to prevent creep or fatigue being solely carried by the resin. The final fibre distribution, as calculated in table 5.3, slightly deviates from the aimed ratio, with 58% of fibres aligned in the 0° direction, 14% at 90°, and 28% at ±45°. Despite this, the layup still meets the recommendations of the CUR 96 (2019). Further on in this report, this layup C will be referred to as the UD+QI layup, which means the layup described in this section. The actual symmetrical layup configuration of layup C is shown in table 5.4. The estimated maximum tensile stress of layup C ranged from 120 to 140 MPa.

After the arrival of the plate and cutting the samples, the mean thickness of plate C was measured at 6.09 mm with a standard deviation of ± 0.07 mm. The average FVF for layup C was calculated at 45.04% ± 0.56%. The FVF is closely matching the estimated values beforehand.

Table 5.3: Calculation of the amount of layers in layup C

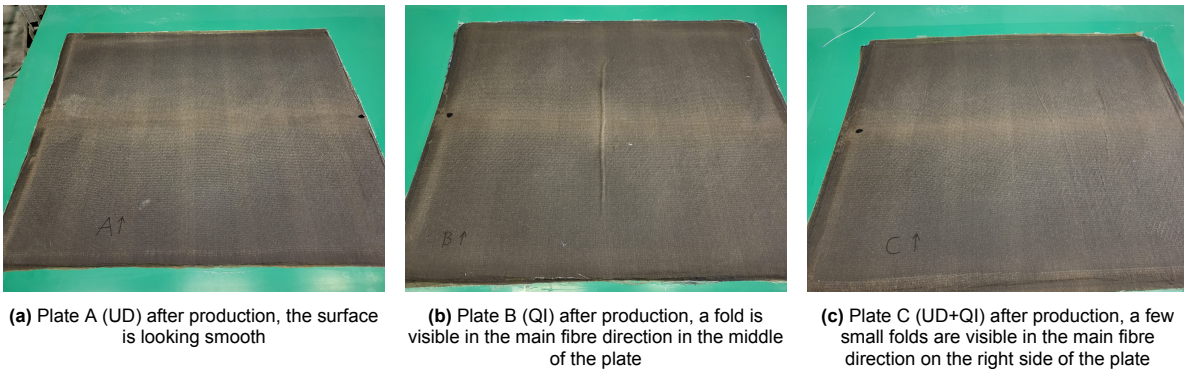
Wanted total thickness				6.00 mm
Fibre volume fraction				45%
	UD 0	UD 90	±45	
Wanted Layup	55%	15%	30%	
Amount of layers needed	7.56	2.06	3.12	Total
Amount of layers used	8	2	3	13
Thickness fibres [mm]	1.571	0.393	0.778	2.742
Thickness of resin [mm]	1.921	0.480	0.951	3.352
Total expected thickness of layup C				6.09 mm
Actual measured mean thickness				6.09 mm
Actual measured fibre volume fraction				45%

Table 5.4: Layup configurations of the three types, A: 100% UD, B: 100% QI, C: 58% 0°, 14% 90°, and 28% ±45°

Layer	1	2	3	4	5	6	7	8	9	10	11	12	13	14
Layup A	0°	0°	0°	0°	0°	0°	0°	0°	0°	0°	0°	0°	0°	0°
Layup B	0°	±45°	90°	±45°	90°	±45°	0°	0°	±45°	90°	±45°	90°	±45°	0°
Layup C	0°	±45°	0°	0°	90°	0°	±45°	0°	90°	0°	0°	±45°	0°	-

5.1.2. Sample Preparations

Figure 5.3 shows the three finished plates. Plate A (figure 5.3a) seems to have a smooth surface, while plate B and C seem to have a few surface defects. Plate B (figure 5.3b) exhibits quite a big fold in the centre of the plate aligned in the main fibre direction (0°), and plate C (5.3c) has a few smaller folds on the right side of the plate. These imperfections must be considered when selecting samples from the plates for testing, as defective samples may not accurately represent the material properties.

**Figure 5.3:** Final result of the 1.27 m x 1 m plates after production, photographs by Paul Honing

Each plate, originally around 1.27 m x 1.0 m, was cut into four main sections and two smaller strips (see figure 5.4, and appendix B), using a circular wood saw. The sections were numbered 1 to 6 with a corresponding letter (A, B, or C) indicating the layup configuration. The test samples were cut using a water jet cutter. The plate part was placed on an open rack during cutting to prevent it from becoming drenched in the water. All samples were cut based on standardized dimensions according to Table 2 in ASTM D3039 (2002). Two shapes of samples have been cut, rectangular samples were cut from plate part 1 (15x250 mm for UD and 25x250 mm for QI and UD+QI) and dog bone-shaped samples were cut from plate part 2 of each layup. The dog bone-shaped samples had slightly wider ends, visualized in figure 5.5. The gauge width of all UD samples was 15 mm, while the gauge width of the QI and UD+QI samples was 25 mm, conform the recommendations of table 2 in ASTM D3039 (2002). The sample measurements are shown in figure 5.5, note that both types of samples have the same width in the gauge area of the samples as the rectangular samples. After cutting, the samples were numbered using a three-digit system. The first number represents the plate section, and the remaining two digits indicate the sample's location within that section. A letter prefix corresponds to the layup configuration of the sample. All detailed sample locations and cutting lines are provided in appendix B. For each test, samples were taken from various areas of the plate to avoid concentrating on potential defects in one area, ensuring more representative test results. All plates and samples were stored in a climate-controlled room at a temperature of 20°C and a relative humidity of 50-55%.

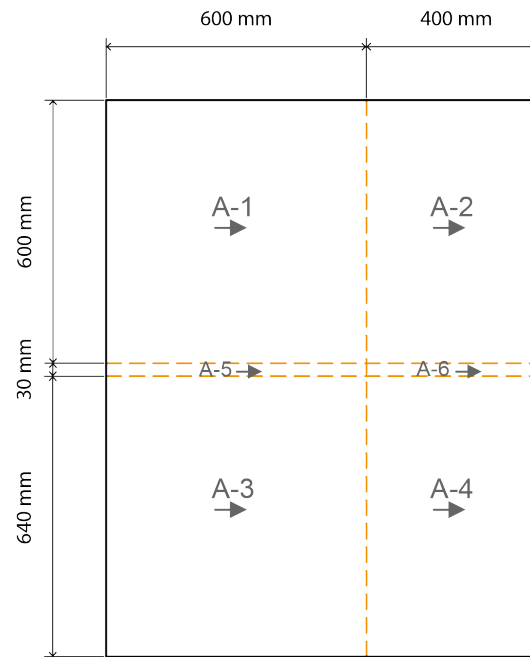
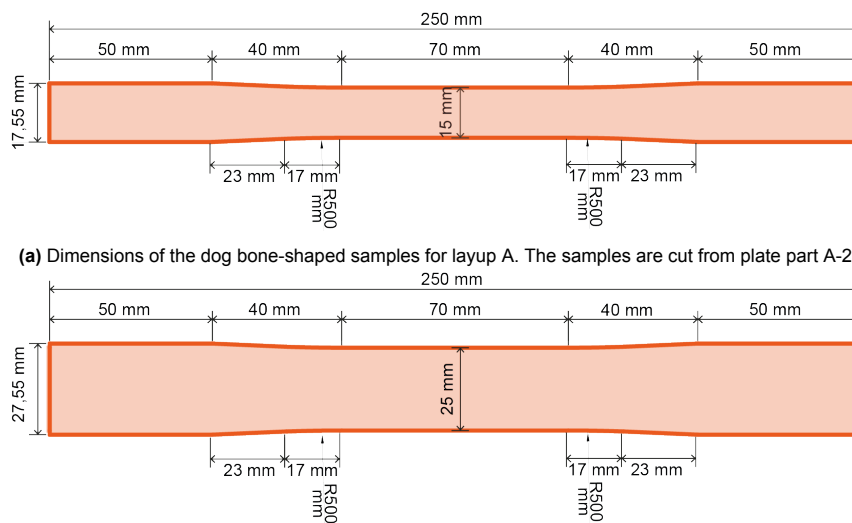


Figure 5.4: The cutting lines (in orange) of the original plates into four main sections and two smaller strips, with corresponding numbers. This example is for plate A, but the cutting lines are the same for all three original plates. More details on the cutting lines and sample locations are shown in appendix B



(b) Dimensions of the dog bone-shaped samples for layout B and C. The samples are cut from plate part B-2 and C-2

Figure 5.5: Dimensions of dog bone-shaped samples

Sample Preparation For Quasi-Static Tensile Tests

For the quasi-static tensile tests, dog bone-shaped samples were used, to reduce the chances of clamp-related failure. To improve clamping grip and prevent slippage from the clamps, both ends of the samples were lightly sanded and paper end tabs were glued on them using Sencys universal contact adhesive (see figure 5.6). The samples were stored and conditioned in a climate-controlled room, at 20°C and 52% RH. A clip-on extensometer was positioned on the rough side of the samples to minimize the chances of slippage of the extensometer teeth on the sample (visible in figure 5.9).

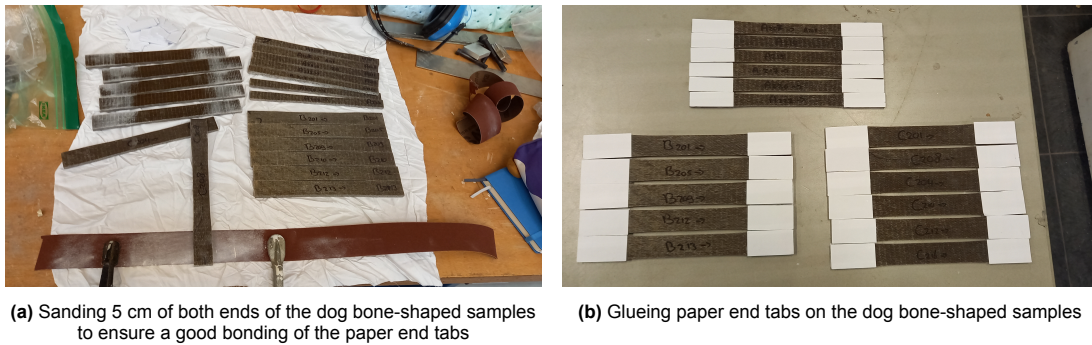


Figure 5.6: Sample preparation for the quasi-static tensile tests with dog bone-shaped samples

Sample Preparation For Long-Term Tensile Creep Tests

The samples for the long-term tensile creep test were rectangular samples, taken from plate part 1 of each layup, sized 15x250 mm for layup A (UD) and 25x250 mm for layups B (QI) and C (UD+QI). All samples were stored and conditioned at 20°C and 52% RH. To prevent slippage from the clamps, both ends of each sample were sanded, and end tabs made from P150 sandpaper were glued on them with quick-set epoxy adhesive (RS PRO 132-605). Strain gauges were applied to the smooth side of each sample. Preparation involved lightly sanding the surface at $\pm 45^\circ$, cleaning it with acetone, marking the strain gauge placement, and adhering the strain gauges with the Kyowa CC-33AX5 adhesive. The strain gauges were pressed down for 30 seconds till the adhesive was fully set. The start of the wires attached to the strain gauges was taped to the sample to prevent accidental forces on the wires, while the other ends were connected to the Wheatstone bridge circuits. Two examples of the finished prepared samples are shown in figure 5.7.

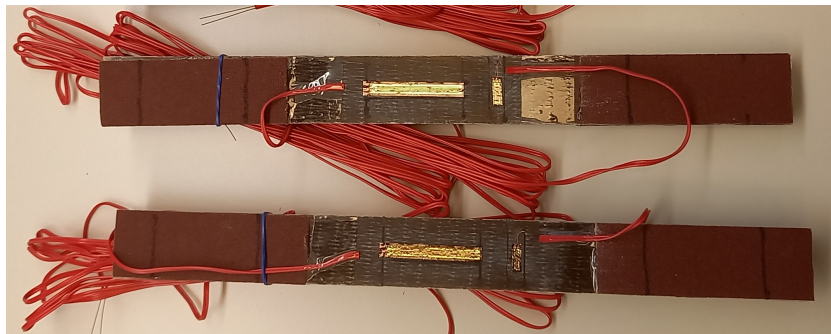


Figure 5.7: Prepared samples for the long-term creep test with sandpaper end tabs and two strain gauges on the smooth side of the sample

Sample Preparation For Accelerated Tensile Creep Tests

For the accelerated creep test, mostly dog bone-shaped samples were used. A few preliminary tests with layup A were done with rectangular samples. However, due to the dimensions of the temperature chamber around the testing machine, the samples had to be cut shorter. The height of the temperature chamber was 30 cm and the samples had an original length of 25cm, so there was little room left for the clamps and additional displacement due to the creep strain. Therefore, the samples were cut 2 cm shorter (to 230 mm), 1 cm of each end, and smaller clamps were used with a clamping length of 4 cm instead of 5 cm. The end tabs were improved during the testing, the type of end tabs and failure mechanism for each sample are written in the test overview in appendix H. The samples of layup B and C were prepared with paper end tabs, which were glued with the two-component epoxy adhesive, Loctite EA 3425. Since the Sencys universal contact adhesive, used for glueing the paper tabs on the quasi-static tensile test samples, showed slippage in the accelerated creep test, a different adhesive was used. The samples of layup A (UD) proved to be more difficult, so for the final two tested samples of layup A, a composite end tab was used from a flax fibre-epoxy composite with a $\pm 45^\circ$ layup. The end tabs were tapered in the direction of the sample to introduce the forces even more gradually into the

sample (see figure 5.8). The samples are conditioned in the same climate room as all other samples, at 20°C and an RH of about 52%. For a second round of SSM tests, similar samples were used with paper end tabs but glued using the Sencys universal contact adhesive as a different machine with different clamps was used.



(a) Glueing the composite end tabs on a layup A sample with a two component epoxy adhesive



(b) Side view of a prepared sample of layup A with tapered composite end tabs

Figure 5.8: Sample preparation for the stepped isostress method as accelerated creep test

5.2. Quasi-Static Tensile Test Procedure

A quasi-static tensile test was conducted to determine the material's ultimate tensile strength, stiffness, and tensile strain. The ultimate tensile strength is of particular interest because it is needed for designing the final steps of the accelerated creep test in the stepped isostress method (SSM). The quasi-static tensile test is based on the recommendations in the ASTM D3039 (2002) and ISO 527-5:2021 (2022) standards. In essence, it involves mounting a flat rectangular specimen (a coupon) in a mechanical testing machine (here an Instron-100 kN) and applying a monotonically increasing tensile load while recording the axial deformation and the force (ASTM D3039, 2002). The strain was measured using an Instron static axial clip-on extensometer, measuring the longitudinal strain over a gauge length of 50 mm. All data, including time, force, displacement (both machine head and extensometer), temperature and RH, were recorded at a rate of 10 Hz (different from the 2 Hz that is recommended in the ASTM D3039 (2002)). The test was displacement controlled at a machine head speed of 2mm/min, following the ASTM D3039 (2002) and ISO 527-5:2021 (2022) guidelines. Given that flax fibre composites are highly sensitive to temperature and relative humidity, the tests were performed with the Instron-100 kN machine inside a climate chamber, ensuring stable environmental conditions. The temperature was consistently maintained at 20°C and the RH was kept between 50% and 60%. The samples were held by hydraulic wedge clamps with a serrated surface and a 50 mm clamping length (see figure 5.9 for the setup). It is important to align the coupon sample properly within the clamps to prevent bending or torsional forces, ensuring that purely the tensile strength is measured. The strain was zeroed after clamping the sample in the bottom grip, then the top of the sample was clamped and the test was started. At least five repetitions of each layup were tested.

The ultimate tensile strength (UTS) is calculated from the maximum measured force before failure and can be expressed as a maximum tensile stress (equation 5.6). The tensile stress at any required data point during the test is determined by equation 5.7 (ASTM D3039, 2002). The determination of strain was already covered in paragraph 3.1 and equation 3.1, where it is explained that strain can be expressed as a ratio (mm/mm), a percentage ($\varepsilon[\%] = \varepsilon \cdot 100\%$), or in microstrains ($\varepsilon\mu = \varepsilon \cdot 10^6$). The results are used to plot a stress-strain curve, from which the stiffness (tensile modulus of elasticity) is determined by the slope, as per equation 5.8. The modulus of elasticity is often calculated over a part



Figure 5.9: Quasi-static tensile test setup in a climate chamber, with a dog bone-shaped sample in the hydraulic wedge clamps, and an extensometer on the sample

of the slope of the stress-strain curve. For a linear curve, ASTM D3039 (2002) recommends calculating the modulus of elasticity over the portion of the stress-strain curve between 0.1% and 0.3% strain. ISO 527-5:2021 (2022) suggests using the range between 0.05% and 0.25% strain. However, for some materials, such as flax fibre composites, the stress-strain curve is not linear, and different parts of the curve can be chosen by the researcher to determine the tensile modulus of elasticity, relevant to the study. In this study, a creep stress of 10 MPa is investigated. Therefore, the stiffness was measured on a selected part of the stress-strain curves determined after the data was collected. For each layup, the bending point of the stress-strain curve was different (see the results in chapter 6), so the selected part of the stress-strain curve was slightly different for each layup. For layup A, the stiffness was measured between 0.05-0.15% strain, for layup B between 0.05-0.25% strain, and for layup C between 0.05-0.20% strain. The results of the quasi-static tensile tests are presented in chapter 6. The preliminary tensile tests are described in appendix E. Additional quasi-static tensile tests on the same material were conducted by Wouter Claassen at the University of Eindhoven. These results are provided in appendix F.

$$F^{tu} = \frac{P^{\max}}{A} \quad (5.6)$$

$$\sigma_i = \frac{P_i}{A} \quad (5.7)$$

With:

- F^{tu} = Ultimate tensile strength [MPa]
- P^{\max} = Maximum force before failure [N]
- σ_i = Tensile stress at i^{th} data point [MPa]
- P_i = Force at i^{th} data point [N]
- A = Average cross-sectional area of the sample [mm²]

$$E = \frac{\Delta\sigma}{\Delta\varepsilon} \quad (5.8)$$

With:

- E = Tensile modulus of Elasticity [GPa]
- $\Delta\sigma$ = Difference in applied tensile stress between the two chosen strain points [MPa]
- $\Delta\varepsilon$ = Difference between the two chosen strain points

5.3. Long-Term Tensile Creep Test Procedure

To validate the accelerated creep test results, a long-term tensile creep test is performed at the same stress as the reference stress in the SSM tests, set at 10 MPa. Given the time constraints of this research, the long-term test duration is limited to 90 days, as used in previous studies (Huang et al., 2018; B. Xu et al., 2023; Yang et al., 2021). This duration also meets the minimum of 1000 hours (approximately 42 days) that is recommended for conventional creep testing in the ASTM D2990-09 (2009).

There was no existing long-term creep test setup available, therefore a new test setup was designed and built. The setup consisted of three steel frames, with deadweight to apply the creep stress on the samples. The dead weights required to reach a stress of 10 MPa in the samples were very high, up to 175 kg. Therefore, a lever-arm system was designed to reduce this required amount of mass, while still applying the correct force on the samples (see figure 5.10). The design of this custom-built long-term tensile creep setup is elaborated in paragraph 5.3.1. The system can accommodate up to nine samples, allowing for three repetitions per layup. The system can accommodate up to nine samples, allowing for three repetitions per layup. To ensure controlled environmental conditions, the setup was built inside a climate-controlled room, with a temperature of 20°C and a relative humidity of 50-55%.



(a) A front view of the long-term creep test setup with samples



(b) The back view of the long-term creep test setup with samples, with a good view of the lever arm system with the applied weights

Figure 5.10: Pictures of the running long-term creep test setup, in a climate-controlled room

The required dead weights to achieve a stress of 10 MPa were calculated using equation 5.9, with each layup requiring slightly different weights due to the varying sample thickness and width. The weights in the setup were calibrated based on preliminary thickness measurements (as the samples were not cut

yet) for determining the target force and using a load cell. The load on the load cell was measured till the target force was reached and the lever arm was checked to be exactly horizontal. After calibration, the load cell was replaced for a sample. A steel safety plate temporarily held the loaded lever arms in place, allowing the specimen to be mounted without being loaded (see figure 5.11). The samples were clamped in custom clamps (explained in section 5.3 and figure 5.14), with each sample's end held by two screws tightened up to 20 Nm using a torque wrench. Once clamped, the strain was set to zero and the measurements were started. The steel plate, holding the lever arm, was slowly removed, and the lever arm was precisely levelled by adjusting the top nut on the steel threaded rod, attached to the specimen's upper clamp (see figure 5.11).

$$W = d \cdot t \cdot 10MPa \cdot \frac{101.9}{1000} \quad (5.9)$$

With:

W = weight [kg]

d = width of sample [mm]

t = thickness of sample [mm]

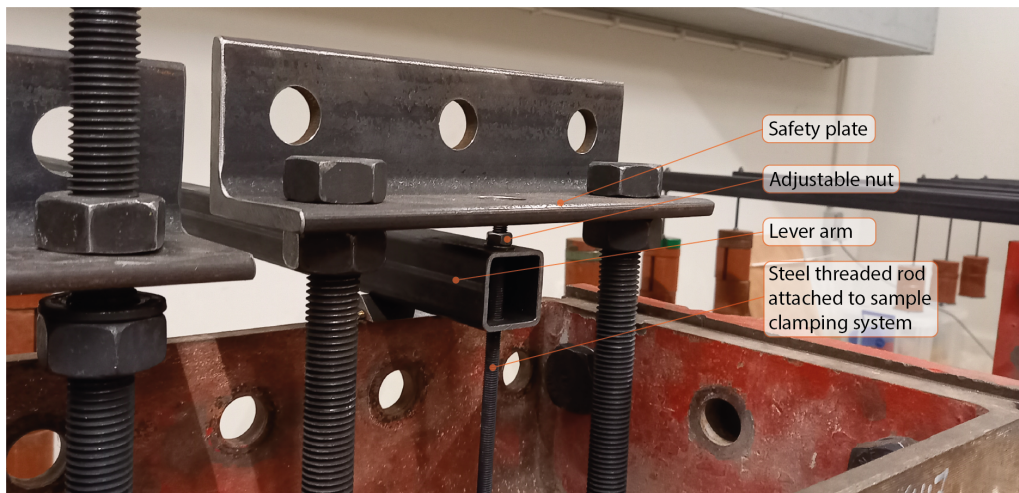


Figure 5.11: Picture of the top part of the long-term creep test setup with the steel safety plate and the adjustable nut to level the lever arm

Table 5.5 summarizes the difference between the calibrated loads and the actual needed loads for each spot in the test setup. The table shows that the calibrated weights based on the preliminary thickness measurements vary slightly from the needed forces with the actual measured mean thickness. The applied stress in the samples is therefore not exactly 10 MPa. However, each specimen was placed in the most suitable position in the test setup, based on their individual measured cross-sections reported in appendix C, to approximate the target stress of 10 MPa. The exact stress applied to each sample is summarized in table 5.6.

The strain on each sample was measured by two strain gauges (Kyowa, Japan), placed on the smooth side of the samples to avoid slippage. A 30 mm strain gauge (type: KFGS-30-120-C1-11 L3M2R) was used to measure the longitudinal strain and a 6 mm strain gauge (type: KFGS-6-120-C1-11 L3M2R) was used for transversal strain. Each strain gauge, with a resistance of 120 Ω , came with three-metre pre-attached wires for a straightforward setup and minimizing handling errors, and was installed in a Wheatstone quarter bridge circuit, powered at 6 volts (which was later during the test turned down to 1 Volt, further explained in section 7.1). Each strain gauge came with 3m pre-attached wires for a straightforward setup and minimizing handling errors. Data acquisition of each test started at a frequency of one measurement per second but was reduced to one measurement per 10 minutes after the first few hours of starting the test. Alongside strain, time, temperature, and RH were also recorded during the tests.

Table 5.5: Weight calibrations for long-term creep test, compared to the samples' actual measured mean thickness

		Lever arm length	885	mm		
		Arm to sample	88.5	mm		
		Stress level	10	MPa		
Layup	Sample width [mm]	Average thickness [mm]	kN needed for 10 MPa [kN]	Calibrated force per spot in test setup [kN]		
				Spot 1	Spot 2	Spot 3
A (UD)	15	5.62	0.8436	0.872	0.875	0.872
B (QI)	25	7.23	1.8072	1.817	1.807	1.814
C (UD+QI)	25	6.14	1.5344	1.559	1.561	1.562

The setup accommodated a total of nine samples, so three repetitions for each layup variant could be tested simultaneously. Initial tests, with one sample per layup, began on February 27, 2024, to verify the setup. On April 8, the six remaining samples were mounted, along with an unloaded dummy sample for each layup, to conduct baseline corrections if necessary. The dummy samples were prepared similarly to the tested samples, with the same strain gauges but without sandpaper end tabs. The unloaded samples were positioned on three flanges of the test setup's steel frame. These dummy samples were used to monitor potential strain fluctuations that were not caused by the applied creep load, such as those resulting from environmental changes. For example, if the temperature rises during testing, additional strain from thermal expansion may occur, which would be visible in the dummy samples. This thermal strain can introduce noise in the strain measurements of the samples in the creep test setup. By measuring the thermal strains in the dummy samples, this noise in the creep strain measurements could be compensated by subtracting the dummy strain from the test strain measurements so that only the creep strains remain.

On April 17, additional dummy samples were placed, only for tracking their weight, as the relative humidity (RH) in the climate room had shown some irregularities. By tracking their weight (about once a week) along with the RH in the room, these dummy samples helped to investigate whether moisture absorption was happening with the increased RH in the climate room. Moisture absorption or desorption could form noise in the strain measurements, as flax fibres expand when absorbing moisture.

Due to disruptions during the creep test, three new samples (one of each layup) were added on July 4, to replace one of the disrupted samples that were placed on April 8, aiming to obtain an uninterrupted creep curve. These new samples, along with three new dummy samples, began testing with a voltage of 1 volt over the strain gauge bridge circuits. Further discussion of the events disrupting the long-term tensile creep test is provided in section 7.1.

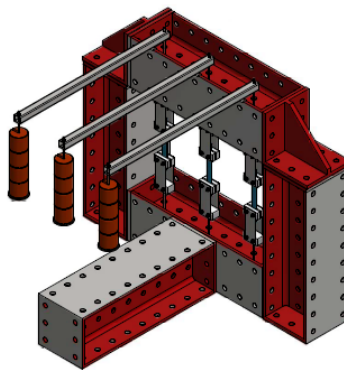
The date of placement and exact applied stress on each sample in the long-term tensile creep test setup is summarized in table 5.6. The results of the long-term tensile creep test are presented and discussed in chapter 7. The real-time creep curves for each layup were retrieved on August 16. The curves had to be cleaned and compensated for disruptions, which is further explained in section 7.1. A creep bandwidth was obtained from the long-term tensile creep test data, which was used to validate and assess the SSM creep predictions.

Table 5.6: The date of placement and applied stress of each sample in the long-term tensile creep test setup

Sample	Mean cross-sectional area [mm ²]	Applied force on sample [kN]	Stress in sample [MPa]
Samples placed on February 27			
A-105	84.82	0.872	10.281
B-102	183.55	1.817	9.899
C-103	154.15	1.559	10.114
Samples placed on April 8			
A-124	85.85	0.875	10.193
A-133	85.07	0.872	10.251
B-120	180.63	1.807	10.004
B-125	181.17	1.814	10.013
C-118	153.29	1.561	10.183
C-121	153.41	1.562	10.182
Samples placed on July 4 (replacing samples A-133, B-125, and C-118)			
A-157	84.78	0.872	10.286
B-117	138.11	1.814	9.91
C-116	153.261	1.561	10.185

5.3.1. Development of the Long-Term Creep Test Setup

Since no existing setup was available for long-term creep tests, a new test setup was designed and built. The simplest approach for a creep test setup involved hanging dead weights to a sample. However, due to the large masses required for a stress of 10 MPa (up to 175 kg), a lever-arm construction was developed in collaboration with the lab technicians of the Stevin lab at the faculty of Civil Engineering. The lever arm design allowed for a safer and better manageable setup by reducing the amount of needed weight. The complete setup consisted of three frames, with each a capacity of 3 creep tests. In figure 5.12 a sketch of the design of one of the three identical frames is presented, each frame having three spots for tensile creep testing. To make the design of the setup as simple as possible, the elements in the structure were chosen to be relatively small and in mostly repetitive sizes. The structure as shown in figure 5.12 consists of three main components: the frame, lever arm, and clamping system of the samples.

**Figure 5.12:** Sketch of the lever arm creep test setup design (made by Derek van Bochove)

The Frame

The frame itself is the superstructure that holds the lever arms and the samples in place. It should be able to carry all the loads that are applied to the samples. The frame is built from heavy H-beams with holes in the flanges and web every 10 cm. These beams are quite heavy, so the choice was made to make three separate identical frames so that the beams in each frame itself are relatively small (0.9 m long) and therefore easier to handle. The setup is divided into three smaller frames, each holding

three samples, ensuring the load-bearing capacity of each frame is sufficient.

The Lever Arm Structure

The lever arm structure consists of a steel SHS profile with a hole at each end. One side carries the weights, while the other attaches to the sample clamps, both with a steel threaded rod. Detailed drawings of the setup are shown in figure 5.13. The SHS profile has a small slit that is placed on a triangular profile, which is welded to the flange of the H-beam, ensuring the SHS profile remains in position and creating a defined rotation point of the lever arm (see figure 5.13 (c), with the triangular profile indicated by number 3). The lever arm has a ratio of 1:10 (see figure 5.13 (e), where number 3 indicates the triangular profile and number 4 indicates the steel SHS profile). The length between the flange and the first hole in the H-beam web is 88.5 mm. The length of the lever arm from the flange to the weights is then 885 mm to satisfy the 1:10 ratio. A total length of 1 m for the SHS profile would be sufficient to accommodate the drilled holes for the threaded rods and the 1:10 ratio lever arm. For uniformity and workability, all bolts and threaded rods are the same size as M8. As a result, all holes that must be bored in the components can be the same size, avoiding confusion or mistakes during assembly.

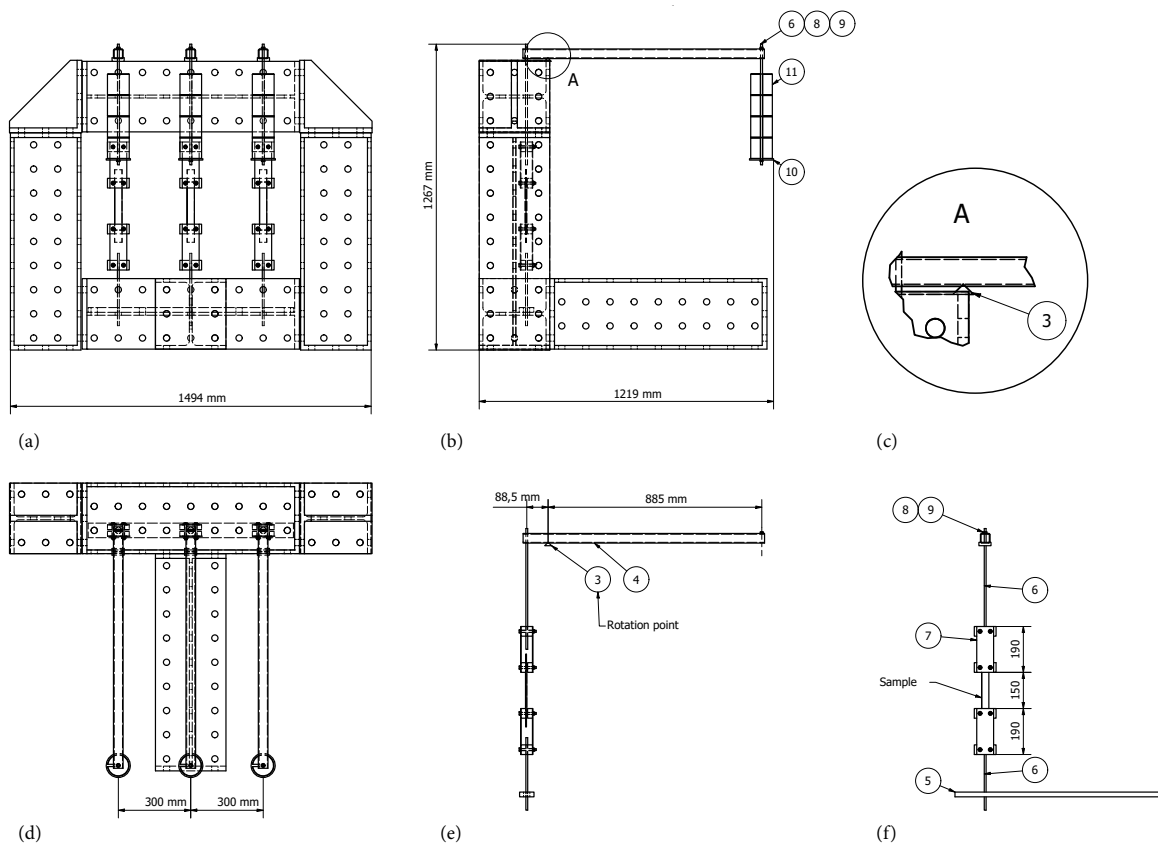


Figure 5.13: Detailed drawings of the long-term creep test setup design, with 3: triangular steel profile, 4: steel SHS profile, 5: steel strip with holes to attach the steel threaded rods to, 6: steel threaded rod M8, 7: clamping system, 8: M8 washer, 9: M8 hexagon nut, 10: round plate to hold the weights, 11: calibration weights. (a) front view of one of the three frames with three samples, (b) side view of one frame with samples, (c) zoomed-in view at the rotation point of the hinge, (d) top view of one frame with samples, (e) side view of lever arm elements with the sample clamping system, (f) front view of lever arm elements with the sample clamping system, (made by Derek van Bochove)

The SHS profile and the steel threaded rod must be verified for their structural integrity. The maximum tensile force in the steel threaded rod is the same as the force that is applied to the sample, which was calculated to be 1.8 kN. A steel threaded rod of M8-4.6 is checked on its tensile capacity (equation 5.11). The smallest surface area of the threaded rod gives the least favourable tensile strength according to formula 5.11. The minor diameter of the M8 threaded rod is 6.647 mm (Accu, n.d.), and the minor

surface area of the steel threaded M8 rod is then calculated according to equation 5.10.

$$A = \pi r^2 = \pi \left(\frac{d}{2}\right)^2 = \pi \left(\frac{6.547}{2}\right)^2 = 34.70 \text{ mm}^2 \quad (5.10)$$

With:

r = circle radius

d = circle diameter

Filling in the minor surface area of the steel threaded rod in equation 5.11, gives:

$$N_{Rd} = \frac{A \cdot f_{y,b}}{\gamma_{M2}} = \frac{34.7 \cdot 240}{1.25} = 6663 \text{ N} = 6.67 \text{ kN} > 1.8 \text{ kN} \quad (5.11)$$

With:

N_{Rd} = design tensile strength

A = surface area

$f_{y,b}$ = yield strength, for a M8-4.6: 240 N/mm²

γ_{M2} = safety factor = 1.25

The unity check for the M8-4.6 steel threaded rod is calculated as: $UC = \frac{1.8}{6.67} = 0.27$ which indicates more than enough spare capacity for its tensile strength.

The steel SHS profile must be checked on its moment capacity. The maximum moment that is created in the profile is the force multiplied by the lever arm length to the rotational point of the lever arm. The maximum acting bending moment in the profile is then: $M_{Ed} = 1.8 \text{ kN} \cdot 0.0885 \text{ m} = 0.16 \text{ kNm}$. The SHS profile that is checked, is an SHS 40x40x3 mm profile with steel grade S235. Its cross-sectional properties are retrieved from Dlubal Software (n.d.). The bending moment capacity of the profile can be calculated with equation 5.12. According to Dlubal Software (n.d.), the elastic section modulus about the y-axis of this profile is $W_{el,y} = 4600 \text{ mm}^3$. Filling in equation 5.12 a bending moment capacity of 1.08 kNm is determined.

$$M_{el,Rd} = \frac{W_{el,y} \cdot f_y}{\gamma_{M0}} = \frac{4600 \cdot 235}{1.0} = 1081000 \text{ Nmm} = 1.08 \text{ kNm} > 0.16 \text{ kNm} \quad (5.12)$$

With:

$M_{el,Rd}$ = bending moment capacity

$W_{el,y}$ = elastic section modulus about the y-axis

f_y = yield strength, for steel grade S235: 235 N/mm²

γ_{M0} = safety factor = 1.0

The unity check for the steel SHS 40x40x3 profile is: $UC = \frac{0.16}{1.08} = 0.15$, demonstrating again sufficient spare capacity for its bending moment.

The Sample Clamping System

The sample clamping system is based on the clamping system used by B. Xu et al., 2023. Each sample end is clamped by the system visualized in figure 5.14. A clamp is constructed from two steel plates of 2 mm thick (figure 5.14(b), number 1) with three aluminium blocks in between them, held together by four M8 bolts. The sample end is clamped between two aluminium blocks, called Block A in the design drawings (figure 5.14(b), number 2). The dimensions of Block A are 20x40x90 mm, with two holes for M8 bolts through them. Block B is on the other side of the clamps than where the sample is held in place (figure 5.14 (b), number 6). The dimensions of Block B are 47x40x90, with again two holes through it for the M8 bolts, but another threaded hole (see figure 5.14(c)) for the M8 threaded rod that connects the clamps to the frame at the bottom, and the lever arm at the top. Some space between the sample and the steel threaded rod is left to be able to adjust the sample by screwing the rod further inside the clamps. Detailed drawings of the clamps can be found in appendix D.

This custom setup design ensures precise and reliable long-term tensile creep testing while minimizing risks associated with handling large weights. Placing the setup in a climate-controlled room ensures a constant temperature and relative humidity during the duration of the creep test.

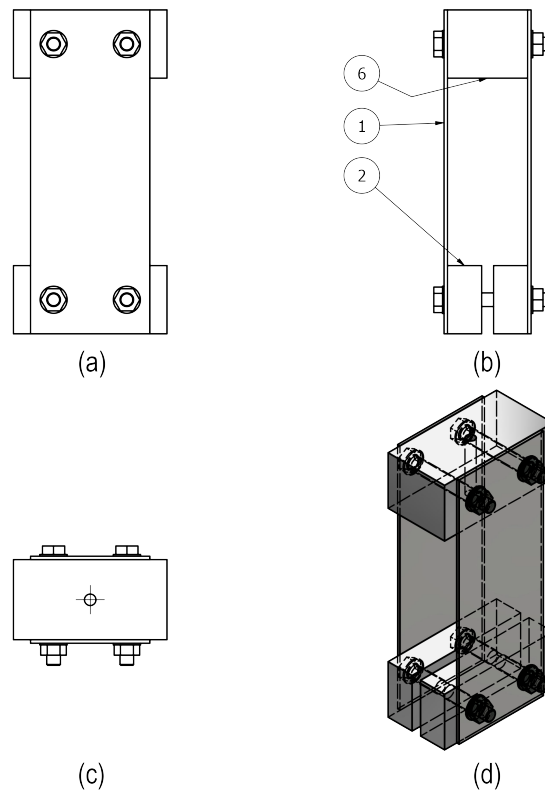


Figure 5.14: Detailed drawings of clamping system, specifically the clamp holding the top of a specimen. (a) front view, (b) side view, (c) top view, (d) 3D view (drawings made by Derek van Bochove)

5.4. Accelerated Creep Test Procedure Using SSM

The stepped isostress method (SSM) is used as an accelerated tensile creep test method to predict the long-term creep behaviour of the flax fibre composite. During an SSM test, a single sample is subjected to a series of stress steps, each applied for a certain set duration (dwell time). This process is repeated for multiple stress steps, continuously recording the sample's deformation. The first stress step in SSM represents the reference stress. For all three layup variants in this study, the same reference stress was applied to compare their final creep master curves for the same reference stress. The reference stress is based on realistic creep stresses. Typical creep stresses in a flax fibre composite bridge are 5 MPa, 10 MPa, and 15 MPa. For the scope of this study, only one creep stress can be investigated, therefore the choice was made to study the creep stress of 10 MPa.

The SSM tests were conducted using an MTS 15 kN fatigue machine located in an open laboratory environment without controlled temperature or humidity. The lab temperature mostly ranged between 23°C and 25°C, dependent on the outdoor conditions (tests were performed in summer months, mostly June and July). To regulate the temperature in the SSM tests, a small climate chamber was placed over the MTS machine clamps (see figure 5.15). A nitrogen tank was connected to this chamber, which cooled it to 20°C. The climate chamber could only control the temperature and not the relative humidity, and is therefore referred to as a temperature chamber. The system was capable of either cooling or heating but could not alternate between the two while running. As the lab temperature was consistently above 20°C, the system was set to cooling. However, cooling with liquid nitrogen caused the temperature to drop too rapidly, far below the target temperature. Once the temperature fell below 20°C, the cooling system stopped until the temperature rose above the target temperature, triggering the cooling system again. It took about 90 minutes before the system reached a stable 20°C temperature.

Cooling with liquid nitrogen affected the relative humidity (RH) in the temperature chamber. There was, however, no method available for constantly recording the RH. A device that was available mea-

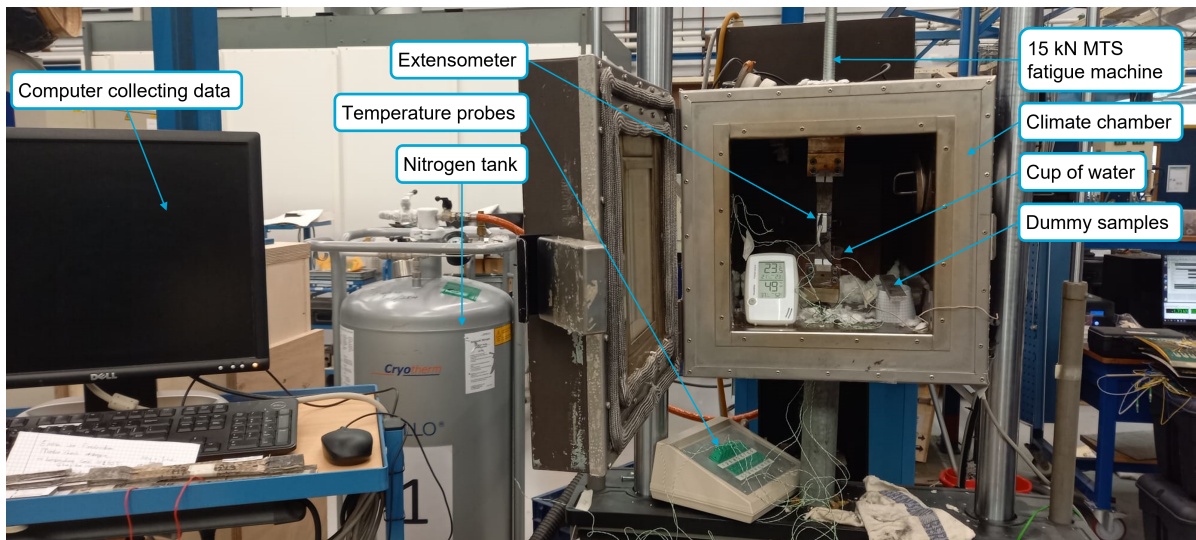


Figure 5.15: The accelerated creep test setup for the stepped isostress method

sured the current RH and could track the maximum and minimum observed value over a certain period of time. During the start of the cooling, the RH ranged between 20% and 60%. After the temperature was stabilized, the RH ranged between 25.5% and 47.6%. To mitigate moisture desorption of the samples and reduce the drop in RH, a cup of water was added inside the temperature chamber. This solution reduced the average moisture drop, by bringing the RH during a test between a range of 35% and 45%. To track the amount of moisture loss in the sample during an SSM test, two dummy samples were placed inside the temperature chamber, next to the tested sample. Their weight was measured before and after a test to check the difference in moisture content. The weight loss without a cup of water (for a UD sample) was about 0.095% while the weight loss with a cup of water in the temperature chamber was about 0.042%. It was therefore chosen to add this cup of water for all following SSM tests. However, this setup still does not control the RH, though it seems to decrease the moisture desorption of a sample during an SSM test.

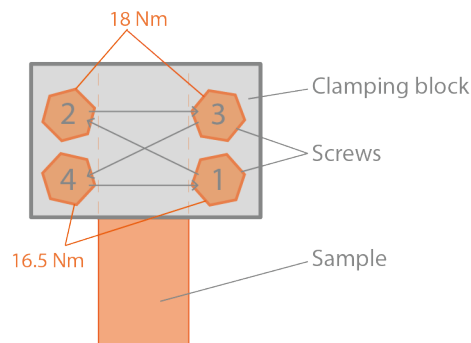


Figure 5.16: Clamping pattern during the accelerated creep tests, clamping the outer bolts tighter than the inner bolts. This diagram shows the upper clamp, the pattern of the lower clamp is mirrored horizontally

The SSM used mechanical clamps consisting of two serrated surfaces of 4 cm high, held together by four screws. The screws were tightened with a torque wrench in a d in a crosswise circular pattern (illustrated in figure 5.16), to gradually apply clamping force. The screws were slightly fastened tighter and tighter one by one in this pattern until the torque wrench indicated the desired torque was reached. Initially, the clamping strengths varied per test as clamping failure and slippage were observed. Eventually, the optimal setup was to tighten the outer screws slightly tighter (18 Nm) than the inner screws (16.5 Nm). This simulated the gradual stress application of hydraulic wedge clamps. The screws were tightened in the same crosswise circular pattern (shown in figure 5.16) up to 16.5 Nm, followed by the outer screws to 18 Nm, and then the inner screws were rechecked on still being 16.5 Nm.

During the accelerated tests, the strain was measured using an MTS extensometer with a gauge length of 25 mm. The extensometer teeth were placed on the rough side of the sample, tied to the sample with elastic bands. The strain was recorded with a rate of 1 Hz throughout the test. In addition to the strain the force, time, machine head displacement, and temperatures, measured by five temperature probes, were measured. The first temperature probe was placed on the lower clamp of the MTS machine. The lower clamp was warmed by the hot oil in the machine system. However, with the cooling system, the clamp was cooled and resulted being about 22°C during a test. The second probe was placed on the front of the sample, the third measured the air temperature inside the temperature chamber, the fourth measured the temperature outside the temperature chamber, and the fifth probe measured the temperature on the back of the sample. The temperature probes were calibrated by putting them in the same cup of water, reading their measurements they only deviated about 0.15°C.

In preliminary tests, the extensometer was combined with the same type of strain gauges used in the long-term creep tests. However, due to the lack of a noise filter for strain gauge signals in the accelerated creep tests, the strain gauge results were unusable. Therefore, only the extensometer was used for strain measurements in the accelerated creep test, meaning that transversal strain was not measured.

SSM Test Design

The design of the stepped isostress method depends on parameters including the number of steps, step sizes, and dwell times, which can be influenced by the researcher's decisions and equipment constraints (as discussed in paragraph 4.3.1). In this study, machine availability was the primary constraint in the design of the SSM tests. Therefore, the number of steps and the dwell time of each step were determined at an early stage in the project, based on previous research using the SSM tests (discussed in paragraph 4.3.1). For this study, six steps were selected, each with a dwell time of two hours, resulting in a total test duration of approximately 12 hours for a single SSM test.

The initial load steps were designed to push the material to failure, utilizing the material's full capacity, and predicting its creep behaviour as far in the future as possible. When proceeding to failure in the final step, it is important to carefully select the appropriate stress level. According to Tanks et al. (2017), it is important to avoid a prolonged failure in the last step and lose the advantage of accelerated testing. However, the stress must also not cause immediate failure upon application to ensure the sample doesn't break during the instantaneous strain phase and allows for measurable creep deformation in the last step. Therefore, Tanks et al. (2017) recommend setting the final stress step at 90% of the guaranteed ultimate tensile strength (GUTS). The GUTS is derived by subtracting the standard deviation from the mean ultimate tensile strength obtained in the quasi-static tensile tests. The GUTS values of the samples were based on the results of the preliminary quasi-static tensile tests, presented in appendix F. During the SSM tests, this 90% GUTS boundary must be evaluated and if necessary adjusted.

However, the available testing machine had a capacity of 15 kN which became the new constraint of maximum force, as the stress required to reach a stress of 90% GUTS exceeded the machine's load capacity. Therefore, the maximum stress in the last step was adjusted to the stress reached at 15 kN (the maximum machine capacity). For layup B (QI), the force required to reach 90% GUTS was slightly below the machine's capacity, based on the results of the preliminary quasi-static test and additional tests conducted by Wouter Claassen (see appendix F).

The revised SSM test design started at a reference stress of 10 MPa, with six evenly divided stress increments up to either 90% of the GUTS or the stress corresponding to 15 kN, depending on the laminate. Each step had a dwell time of two hours. The specific stress increments varied across the three laminate variants due to differences in their thicknesses and GUTS. Table 5.7 provides an overview of the stress increments for each layup and the corresponding forces. For reference, the maximum stress in the SSM test is expressed as the percentage of GUTS that is calculated from the quasi-static tensile tests, presented in chapter 6. These GUTS values differ from those resulting from the preliminary quasi-static tensile test, therefore even the GUTS of layup B is lower than 90% in table 5.7. In appendix H, an overview of all accelerated creep tests is presented, with each test its clamping strength, the lab temperature and relative humidity, the tracked weight of the dummy samples, and the type of failure, schematically ordered for each sample.

Table 5.7: SSM steps for each layup, expressed as stress and the corresponding needed force (based on the average thickness of each layup)

Layup	Steps [MPa]						% of GUTS
	Step 1	Step 2	Step 3	Step 4	Step 5	Step 6	
A	10 MPa	43.56 MPa	77.13 MPa	110.69 MPa	144.25 MPa	177.82 MPa	62%
	0.844 kN	3.675 kN	6.506 kN	9.337 kN	12.169 kN	15.00 kN	
B	10 MPa	23.99 MPa	37.97 MPa	51.96 MPa	65.94 MPa	79.93 MPa	74%
	1.807 kN	4.335 kN	6.862 kN	9.39 kN	11.92 kN	14.44 kN	
C	10 MPa	27.55 MPa	45.1 MPa	62.66 MPa	80.21 MPa	97.76 MPa	51%
	1.534 kN	4.228 kN	6.921 kN	9.614 kN	12.307 kN	15.00 kN	

Explanation of the machine control program

The stepped isostress method (SSM) test controls for the MTS 15 kN fatigue machine, were programmed in MTS TestSuite MP Elite. The global workflow is a parallel path, with the machine controls on one side and the reading and sampling of the time, force, displacement of the machine head, and displacement of the extensometer on the other side. These parameters were measured continuously throughout the test at a sampling rate of 1 Hz. On the machine control path, the steps of the SSM are implemented sequentially. At the start of each step, a parallel path is initiated. The first path commands the machine to ramp to 10 mm at a speed of 2 mm/min under displacement control. The second path stops this ramp once a predefined force, corresponding to the step's target stress, is reached. Once the force limit is detected, the machine switches to force control, maintaining the specified force for two hours. After the two-hour force-controlled period, the program proceeds to the next step, repeating the same pattern: a displacement-controlled ramp followed by force control at the new target stress. This cycle continues until the final step. The force-controlled command for the last step is extended to 24 hours to accommodate potential sample failure after a two-hour dwell time. For layup B (QI), failure is expected at the 15 kN limit, whereas layups A (UD) and C (UD+QI) are expected to have higher bearing capacities and may not fail at all during testing. Extending the duration of the last step provides additional creep deformation data. The total test duration, excluding ramp times of a few seconds, then ranges from 12 to 32 hours.

The MTS 15 KN fatigue machine was driven by hydraulics and all hydraulics of all machines in the lab were connected to a shared circuit, leading to fluctuations in oil pressure when other machines were in use. This variability caused extra noise in the force control, visible as minor cyclic variations in force and thus strain signals. These fluctuations differ between tests and even within a single test.

The result of the SSM test is a stepped strain-over-time curve that must be segmented by step. The first step of the SSM data processing is a vertical shift, to adjust for elastic strains at the start of each load step. In the second step, the curve segments are rescaled by extrapolating them back to zero creep strain and shifting the curves by a virtual starting time. Lastly, the rescaled curves are shifted over a logarithmic timescale to construct the final creep master curve prediction. As explained in chapter 4, various data handling techniques can be employed, and empirical testing is often necessary to determine the most suitable SSM data analysis method for a specific material. In this study, different methods, described in chapter 4, are explored and compared. The findings provide a range of SSM-predicted long-term creep behaviour of the flax fibre-reinforced polymer composite. The results from the SSM tests and comparison of data handling techniques are described in chapter 8.

Part III

Experimental Results and Discussion

6

Quasi-Static Tensile Test

Quasi-static tests were conducted to determine the ultimate tensile strength of the material. This parameter is necessary for determining the load steps in the subsequent accelerated creep tests using the stepped isostress method. The stiffness of the material can also be calculated through the data obtained in the quasi-static tensile tests. This chapter presents the results of the quasi-static tensile tests and concludes with a discussion. A preliminary test series was done, but the results were deemed inconsistent. These results are presented in appendix E. Additionally, appendix E section E.2.1 treats the discovery of a defect in plate C-1, resulting in avoiding samples located at the right part of that plate. For the second series of quasi-static tests, the test method was improved, and the results are presented and discussed in this chapter. An overview of all quasi-static test results for all three layups is given in appendix F.

6.1. Results

The numerical results of the quasi-static tensile tests are summarized in table 6.1, and the cleaned stress-strain curves are shown in figures 6.1, 6.2, and 6.3. The mean values and standard deviations were calculated using the ASTM D3039 (2002). The individual sample results for all layups are presented in appendix F. The cleaned stress-strain curves were adjusted to remove slippage in the clamps and were realigned by shifting over the strain axis so that 0% strain corresponds to 0 stress.

Table 6.1: Numerical summary of results of quasi-static tensile tests on dog bone-shaped samples for each layup

	Layup A (UD)	Layup B (QI)	Layup C (UD+QI)
Average max stress [MPa]	299.495	107.444	190.508
Standard deviation	14.464	1.866	4.550
Coefficient of variation [%]	4.829	1.737	2.388
Average stiffness [GPa] (<0.3%)	21.933	8.207	14.311
Standard deviation	0.733	0.116	0.409
Coefficient of variation [%]	3.342	1.416	2.855
Average thickness [mm]	5.62	7.31	6.08
Fibre volume fraction [%]	48.96	42.78	45.07
Expected max stress [MPa]	300-360	80-100	120-140
Expected thickness [mm]	6.1	6.9	6.1
Expected FVF [%]	0.45	0.45	0.45

The stress-strain curves of layups A and C show a distinct bilinear elastic behaviour, with a bending point between 0.2% and 0.3% strain. In contrast, layup B shows an almost non-linear stress-strain response. The bilinear or non-linear curves could be explained by the reorganization of the microfibrils within the fibres, as discussed in section 2.2. All specimens failed brittle, with minimal warning before

fracture.

When calculating the material stiffness (using equation 5.8), it is important to select the appropriate portion of the stress-strain curve relevant to the intended application. Since this research focuses on creep behaviour under relatively low stress, the stiffness was derived from the lower portion of the stress-strain curve. For layup A, the stiffness was measured between 0.05-0.15% strain, for layup B between 0.05-0.25% strain, and for layup C between 0.05-0.20% strain.

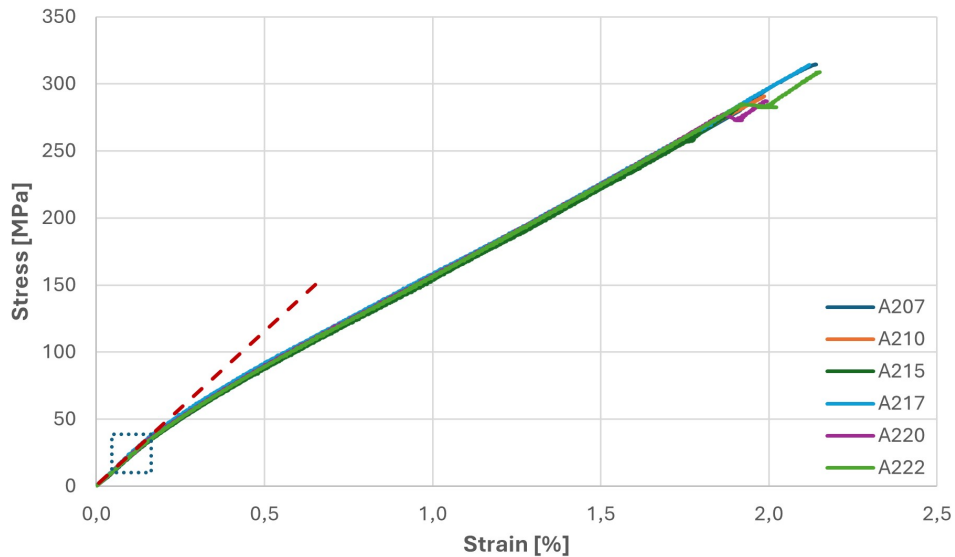


Figure 6.1: Cleaned stress-strain diagram layup A, the stiffness calculated between 0.05-0.15% strain, indicated by the blue dotted square and the red dashed gradient

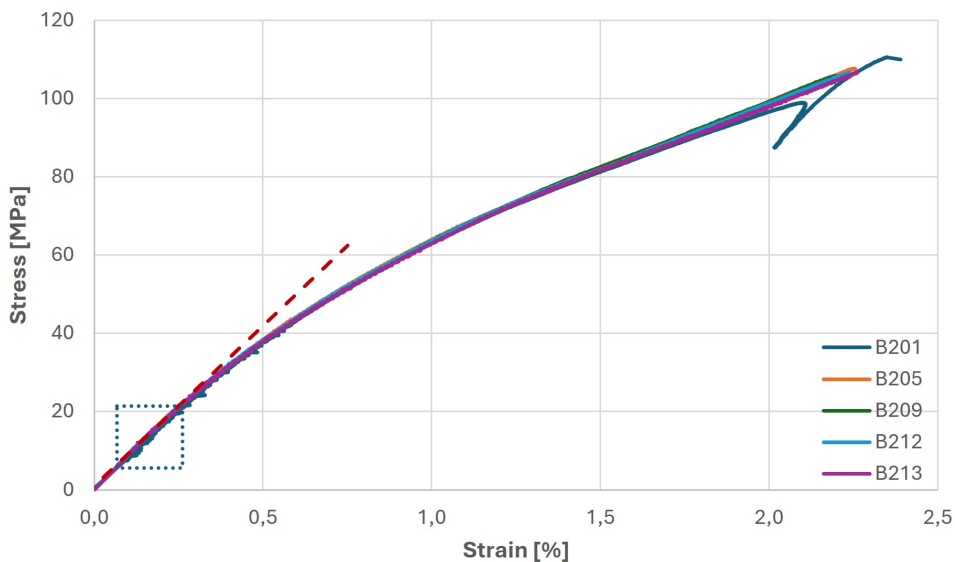


Figure 6.2: Cleaned stress-strain diagram layup B, the stiffness calculated between 0.05-0.25% strain, indicated by the blue dotted square and the red dashed gradient

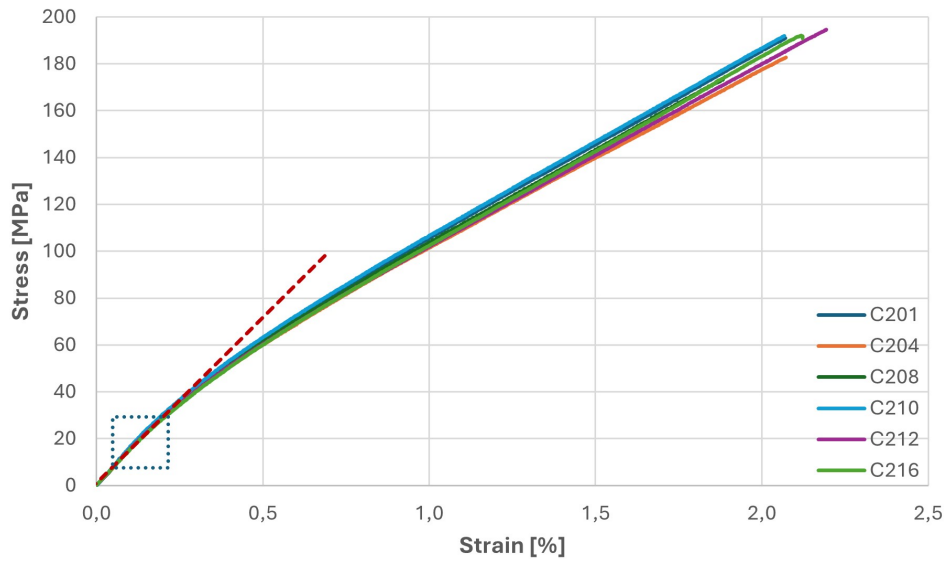


Figure 6.3: Cleaned stress-strain diagram layup C, the stiffness calculated between 0.05-0.20% strain, indicated by the blue dotted square and the red dashed gradient

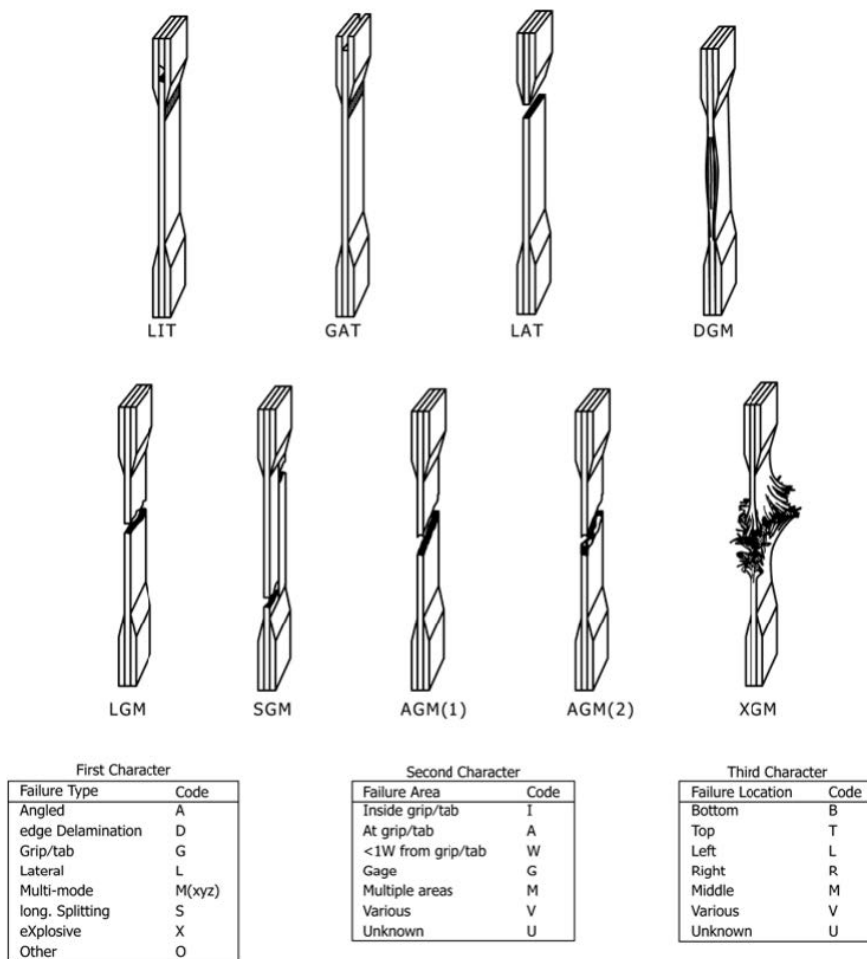


Figure 6.4: Failure mechanism classification for longitudinal tensile testing according to ASTM D3039 (2002)

6.1.1. Failure Mechanisms

The failure mechanisms in quasi-static tensile tests can be categorized according to ASTM D3039 (2002), using a three-letter code, visualized in figure 6.4. Figure 6.5 shows the failed samples from the quasi-static tensile tests. The wider end tabs of the dog bone-shaped samples were used to introduce the forces more gradually in the sample and prevent failure near the clamps. However, as seen in figure 6.5a, layup A still exhibited failures either in the clamps or by shear. The dog bone shape may not be ideal for UD layups, as the wider ends transfer the forces to the narrower middle section through the matrix, which is weak in lateral force transfer (as the fibres in the wider tabs are cut off and not continuous over the length of the specimen, forces introduced in the wider tabs have to be transferred to the continuous fibres in the narrower cross-section, through the matrix). The failure modes for layup A are, therefore, categorized as G/SAT or G/SAB.

In layup B, in figure 6.5b, the failures occurred primarily in the transition zone between the wider tabs and the narrow middle section. The failure modes can be categorized as A/LGT or A/LGB. This failure pattern indicates that the results of these tests can be more representative than the results from the preliminary quasi-static tensile tests, which failed mostly near the clamps.

Figure 6.5c shows similar failure modes for layup C as for layup B, where most failures occurred in the transition zone between the wider end tabs and the slimmer middle section, except for sample C208, which failed near the clamps. As shown in figure 6.5c, sample C208 has a longitudinal fold on the surface, which is marked with a black line. This fold extends into the clamped section, potentially causing uneven clamping pressure, which can lead to stress concentrations and premature failure.



(a) Layup A



(b) Layup B



(c) Layup C

Figure 6.5: Dog bone-shaped samples failed after the second round of quasi-static tests

6.2. Discussion

The second round of quasi-static tensile tests provided more consistent results compared to the preliminary tensile tests, thanks to a more appropriate load cell capacity, controlled environmental conditions, and dog bone-shaped samples, resulting in fewer clamp-related failures. The average ultimate tensile strength (UTS) for each layup was higher than found in the preliminary tests (see appendix F).

Looking at figure 6.3, sample C208 has a significantly lower UTS than the other samples. This confirms the expected premature failure due to the visible surface defect, causing a local stress concentration in the clamps. Therefore, this sample was excluded from the calculation of the average UTS for layup C, although its stiffness was not affected and was included in the average stiffness determination.

Sample B201 experienced slippage near the end of the test. The clamps were tightened during the test, and the test was finished. This slippage was not removed from the graph, as it provides insight into the curve's irregular ending. Additionally, early irregularities in the B201 curve (up to 0.6% strain) were due to machine settings and were resolved during the testing process.

The results in table 6.1 show that the ultimate tensile strength (UTS) aligns with the expectations from paragraph 5.1.1, although layup C (UD+QI) slightly exceeded its tensile strength expectations. Since a UD+QI layup is not often used in scientific research, limited data was available on its tensile properties, making predictions less certain. When comparing the three different layup configurations, layup A (the UD layup) was the strongest laminate, as expected, demonstrating that the fibres are the primary load-bearing component in the composite. Layup B was the weakest, as it has the smallest amount of fibres in the main load-carrying direction. However, layup B showed the lowest standard deviation in its strength, which can be explained by the distribution of forces. A UD layup has all fibres aligned in a single direction, making any imperfections in that direction significantly impact the material's strength. Such imperfections can be localized, resulting in a larger variation of the ultimate tensile strength. In contrast, QI layups, like layup B, have fibres distributed over multiple directions, leading to a more even distribution of the loads across the fibres. So, the effect of imperfections in a single ply is reduced, resulting in a more consistent performance. The strength values of layup C fell between the results of layup A and B, which was expected from the mixed layup.

To validate the test results, the strengths and stiffnesses were compared with the characteristics found in previous research. In table 6.2, a comparison is made between the tested materials and their found strengths and stiffnesses in quasi-static tensile tests. Since other studies tested only UD samples, the comparison focuses on those results. The UTS values found in this research closely match those reported by Jia and Fiedler (2020) and are slightly higher than those reported by Giuliani et al. (2023) and B. Xu et al. (2023) but remain within a similar range. The stiffness values across the studies were similarly consistent. It's important to note that the selection of the stress-strain segment used for stiffness calculation greatly impacts the result. In this study, all stiffness values were determined below 0.3% strain.

Table 6.2: Comparison of tensile properties found in previous research and this research

	Jia and Fiedler (2020)	B. Xu et al. (2023)	Giuliani et al. (2023)	This research (2024)
Materials	Flax fibres bio-epoxy	Flax fibres unsaturated polyester	Flax fibres bio-epoxy	Flax fibres unsaturated polyester
Layup	UD	UD	UD	UD, QI, 40% UD + 60% QI
Thickness	2 mm	2 mm 4 mm	3 mm	UD: 5.6 mm QI: 7.3 mm UD+QI: 6.1 mm
Environmental conditions	Room temperature	20°C 60% RH	Room temperature	20°C 50-60% RH
UTS [MPa]	300.29±7.09	2 mm: 264.44±5.65 4 mm: 265.16±4.26	221 MPa±18	UD: 299.50±14.46 QI: 107.44±1.87 UD+QI: 190.51±4.55
Tensile modulus [GPa]	0.05-0.25% strain: 24.36±0.57	2 mm: 21.03±0.59 4 mm: 20.92±0.64	0-0.15% strain: 21.3±1.15	UD: 21.93±0.73 QI: 8.21±0.12 UD+QI: 14.31±0.41

A minor issue during testing was that the strain measurements started before the samples were fully clamped, causing a small, noisy section at the start of the stress-strain curves due to pre-tensioning. This part of the curve was removed, and the remaining curves were extrapolated to 0 stress. Then, the curves were shifted over the strain axis so that 0% strain corresponded with zero stress. Future tests could benefit from zeroing the strain after a small pretension and then starting the measurements and test.

6.3. Conclusion

The preliminary quasi-static tensile test results (reported in appendixE) were deemed not representable for the material's true performance. The results presented in this chapter, with improved testing conditions, were deemed more accurate and should be used for determining the material's properties. While the dog bone-shaped samples reduced clamp-related failures for layups B and C, further improvements are needed for layup A to prevent clamping-induced failure.

The orientation of the fibres along the main load-carrying direction ensures a higher tensile strength, but redistributing the fibres across multiple directions allows for better stress distribution over the fibres and a more consistent ultimate tensile strength compared to a fully UD layup. Due to the bilinear or non-linear stress-strain response of flax fibre-reinforced polymer composites, researchers must carefully select the relevant part of the stress-strain curve to determine its stiffness, ensuring it aligns with the specific application or test conditions.

7

Long-Term Tensile Creep Test

This chapter presents the results of the long-term tensile creep test, including a chronological overview of disruptions that occurred during the test and the measures taken to address them. A distinction between cleaned and compensated curves is explained before the test results are introduced. The long-term creep curves, which capture the real-time creep behaviour of the flax fibre-reinforced polymer composite, are analysed and discussed. The curves provide a baseline for evaluating the predicted creep behaviour from the accelerated tests conducted using the stepped isostress method. The sample preparation and test methodology for the long-term creep tests are described in chapter 5, sections 5.1.2 and 5.3.

7.1. Disruptions During the Long-Term Creep Test

The long-term creep test encountered multiple disruptions that may have affected the accuracy of the resulting creep curves in reflecting the true material behaviour under a constant load and a given environmental condition. This section describes each of these events in chronological order, along with the corrective measures taken to mitigate these disruptions. From figure 7.3, the timeline of the disruptions along with the placement of the samples becomes clear, as well as the actual temperature and relative humidity during the complete test. The cleaned and corrected curves are presented in this chapter, with the original data provided in appendix G.

As explained in section 5.3 and table 5.6, three samples of each layup (so a total of nine samples) were tested in the long-term creep test setup. A fourth sample of each layup was tested later, but only nine samples could be tested simultaneously. The first three samples were installed in the long-term creep test set up on February 27. On April 8, the remaining six were installed, and on July 4, three of them were replaced by three new samples.

The first disruption occurred on March 12 when a climate control failure raised the room temperature of the climate-controlled room up to 25° until March 21. Only the three initial samples, installed on February 27, were exposed to this temperature increase. Due to the difficulty of distinguishing between thermal expansion effects and potentially accelerated creep strain caused by higher temperatures, this portion of the data was left uncorrected.

On April 8, a second disruption was introduced by human error when the second batch of samples was installed. The signals of all strain gauges were zeroed, rather than only the strain gauges on the newly mounted samples. This resulted in a visible jump in most graphs, except for samples B120 and B125. The error was corrected by vertically shifting each affected curve to realign the data following the jump with the curve segment prior to the jump.

A third issue came up on April 17 when the dummy samples placed on April 8 showed deformation patterns similar to the tested samples (see the transversal strain graphs in appendix G.2). Investigation revealed that the strain gauges had become quite warm, leading to localized heating of the specimens. This warming resulted from the 6 V voltage applied to the bridge circuits connected to the strain gauges. The low thermal conductivity of the material trapped this heat near the strain gauges (see figure 7.1a), influencing the strain measurements. The gauge circuit voltage was therefore lowered from 6V to 1V

on April 17, which stabilized the sample temperature at 20°C, matching the room conditions (see figure 7.1b). This change in the bridge voltage required a correction factor of 6 to be applied to the recorded strain gauge signal, resulting again in a shift in the creep strain graphs. For layup B, an error in applying this shift factor was corrected on July 4, with the data adjusted manually between April 17 and July 4. The jump in the graphs was cleaned, similar to the shift caused on April 8. The noise generated from this strain gauge cooling can be compensated by subtracting the measured strain in the dummy samples from the primary creep data.

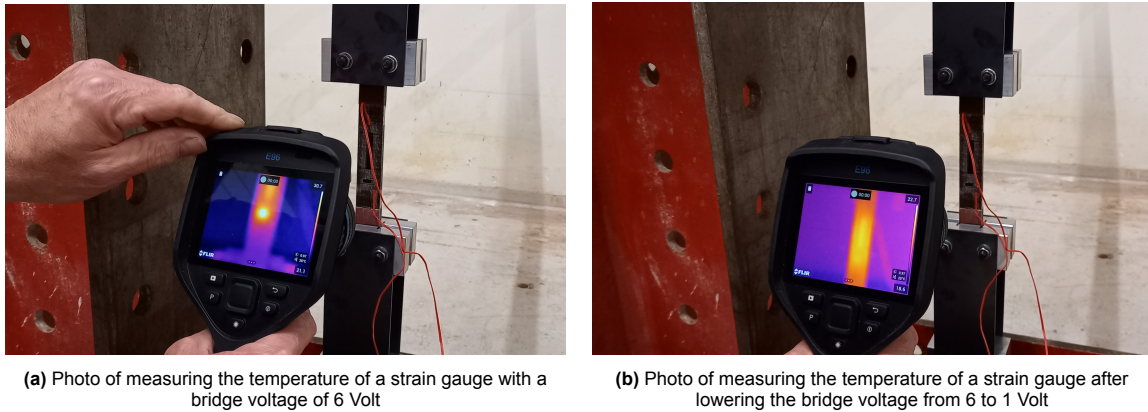


Figure 7.1: Photos of checking the temperature of the strain gauges on the samples with a heat camera

From April 17 onwards, the weights of nine additional dummy samples (without strain gauges) were monitored to identify any moisture absorption, which could impact the strain measurements in the primary tested samples. These dummy samples, stored in the same climate-controlled room as where the tests were conducted, were weighed with microgram precision to detect moisture variations in the samples. In figure 7.2, the weight of the samples is expressed as the percentage of weight changed since the first weight measurement. For more context, the temperature and relative humidity (RH) are plotted on the same timescale. The figure shows a gradual increase and instability in the RH during the second half of the test. The observed increase in sample weight appears to align with the rise in RH, suggesting that the samples absorbed moisture. However, weight measurements began only a few days before the RH became unstable, with just the first three weight measurements showing stability. This limited data creates some uncertainty in assuming the weight had been stable before the RH rise. As the flax fibres absorb moisture, they tend to swell and expand (Lu et al., 2022), which can create noise in the creep strain measurements.

To obtain clean creep strain data, three new test samples were placed in the creep test setup on July 4. The new samples replaced one sample of each layup in the setup that was affected by the heated strain gauge. The new samples started their tests with the lower bridge voltage of 1V. Additionally, all lever arms were verified to maintain their levelled position and were re-levelled where necessary, introducing minor jumps in the creep strain curves. These jumps were cleaned by vertically shifting each affected curve to realign the data following the jump with the curve segment before the jump.

A final climate system failure on August 13 lowered the room temperature to 14°C, and room conditions could not be restored for the next two months. The data reported in this chapter is therefore cut on August 16. The onset of the climate system failure is visible in the creep curves but can be disregarded when extrapolating the data. To compensate for thermal strains, the strain measurements from the dummy samples were subtracted from the primary creep data, though there remained some noise in the curves.

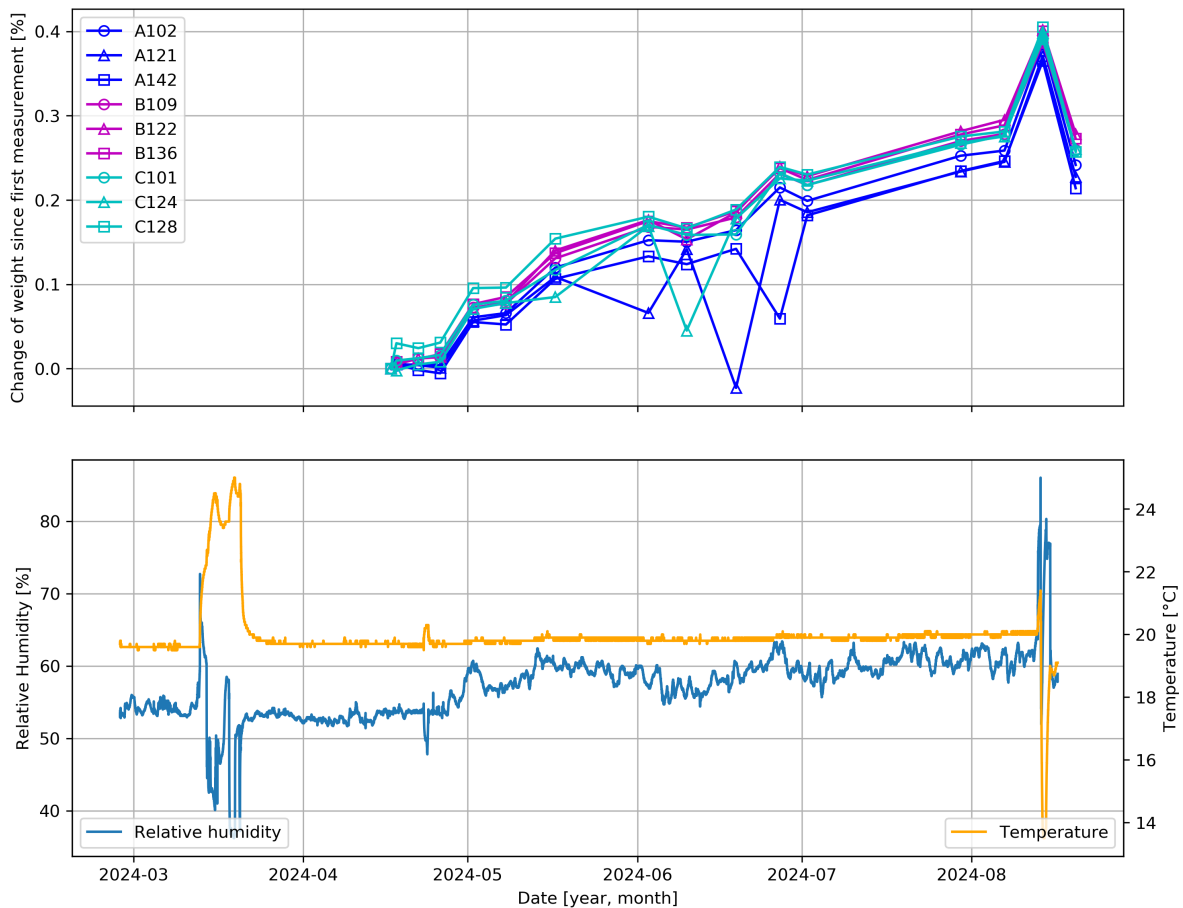


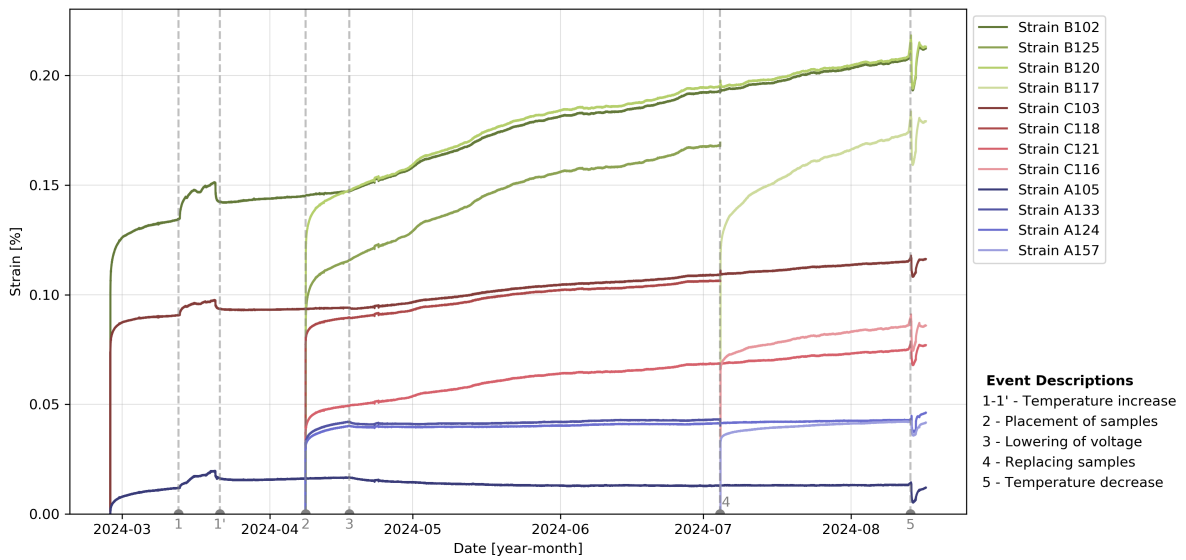
Figure 7.2: The tracked weight of the dummy samples over time, with the weight expressed as the percentage of change from the initial weight measurement. The temperature and RH are plotted on the same timescale

7.1.1. Cleaning and Compensating the Long-Term Creep Curves

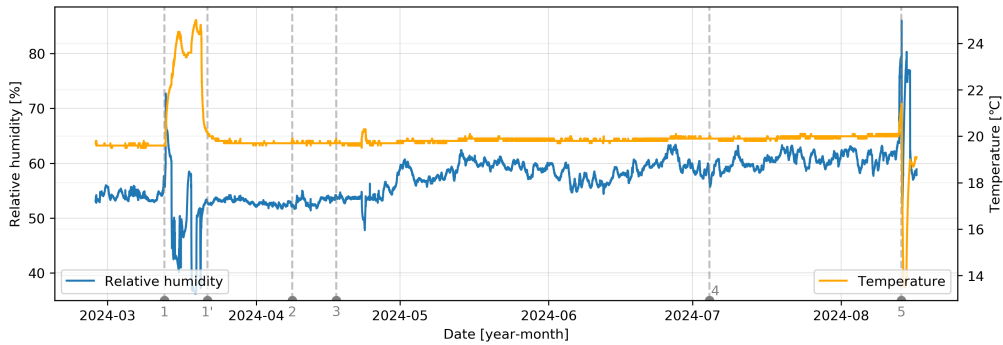
Section 7.2 presents the results of the long-term tensile creep tests, where a distinction is made between cleaned and compensated curves. The cleaned curves are presented in figure 7.3, showing corrections made by eliminating strain jumps caused by slippage, sample (re)placement, and gauge factor adjustments. The curves were shifted vertically to align with the strain measured prior to the disruptions and to start at 0% strain. Figure 7.4 shows the cleaned strain for the dummy samples, correcting only for gauge factor changes. In figure 7.5, the compensated curves are shown. To compensate for the curves, the cleaned dummy strain is subtracted from the cleaned creep strain data by matching the data sets by the exact time and date. Dummy samples were placed on April 8 and July 4 to correspond with the tested samples placed on the same dates. However, no dummy samples were placed with the samples on February 27, so the April 8 dummy strains were also subtracted from the February 27 samples. This limitation means that the curves starting from February 27 are uncompensated till April 8. Consequently, the strain measured in the dummy samples may not fully represent the effects of the heated strain gauge or the response after the voltage reduction. Due to the material's non-linear viscoelastic behaviour, its stress-strain history may impact its response to new stresses. This consideration is essential in analysing the results in the following section.

7.2. Results

The cleaned long-term creep curves are presented in figure 7.3 on an absolute timescale, with extension set as positive. Only the longitudinal strain of each specimen is shown, and the events explained in section 7.1 are marked on the timeline with dashed grey lines. Additionally, temperature and RH are plotted on the same timescale as the creep curves (7.3b) to illustrate how environmental fluctuations have influenced the material's creep behaviour. The curves are coloured by layup, having slightly



(a) Cleaned longitudinal creep strain of all layups with the absolute time on the horizontal axis.



(b) Temperature and relative humidity during the long-term creep test.

Figure 7.3: Cleaned longitudinal creep strains measured in the long-term tensile creep tests, with the absolute time on the horizontal axis. To give extra context, the temperature and RH are plotted on the same timescale. The interruptions during the tests are marked by the vertical grey dashed lines

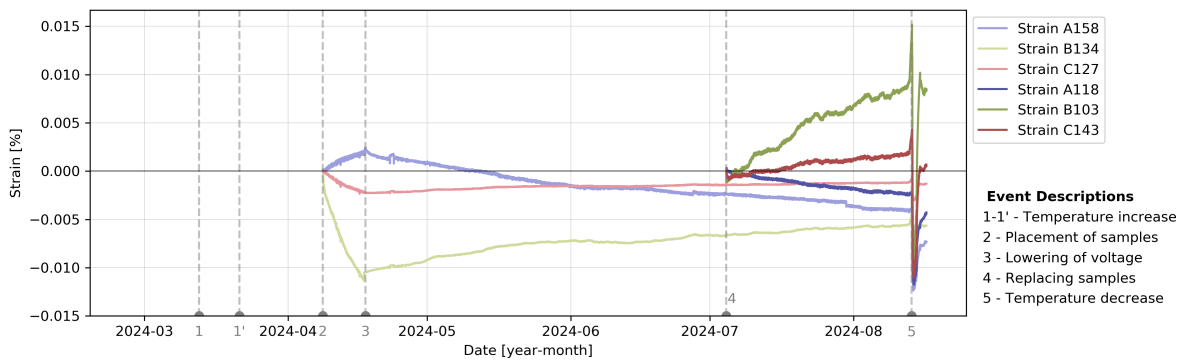


Figure 7.4: Cleaned longitudinal strain measured on the dummy samples

different shades for the different samples of the same layup. In summary, the cleaning process removed jumps in the strain curves caused by slippage (only for sample C-103), (re)placement of samples, and changing the gauge signal factor. The temperature disruptions in March and August remain unfiltered, and all curves are vertically adjusted to start at 0% strain. Figure 7.4 shows the longitudinal strains on the dummy samples, similarly cleaned and adjusted to start at 0% strain. When comparing the

different layups in figure 7.3, it is visible that each layup exhibits a distinct slope. Layup A (UD) has the shallowest slope, which is consistent with its higher stiffness compared to layup B (QI) and C (UD+QI) (see chapter 6, for the stiffnesses found through quasi-static tensile testing). Layup C (UD+QI) has a creep curve with a slope that falls between those of layups A and B, again consistent with its stiffness compared to the other layups.

Notably, the slope of the curves changed after April 17, when the strain gauge voltage was lowered (indicated by event number 4 in figure 7.3). Layups B and C appear to become steeper and more irregular following this event, while layup A briefly shows a negative slope after the voltage reduction before gradually resuming an upward trend.

Initially, it was expected that the unloaded dummy samples would not exhibit strain. However, figure 7.4 clearly shows that strain is indeed present in the dummy samples. This indicates that non-creep factors may be influencing the strain readings across all samples, including the tested samples. Furthermore, the strain trend in the dummy samples reverses after the strain gauge voltage adjustment. Layup A (UD) first exhibits a positive strain trend, while layups B (QI) and C (UD+QI) show a negative trend, or shrinkage, along the longitudinal axis. After the voltage reduction, these behaviours reverse in all layups of the dummy samples. The dummy samples placed in July, with a stable voltage setting, continued to exhibit strain in line with the trends observed in the other dummy samples after the voltage adjustment. These strains may be induced by the RH fluctuations in the climate room and the possible moisture absorption, as discussed in section 7.1. However, this does not fully explain the negative strain trend observed in the dummy samples of layup A. Additionally, it is notable that the temperature drop in August had a more pronounced effect on the dummy samples placed in July than on those installed in April, with larger thermal strains appearing in the newer dummy samples.

Comparing the initial strains across all three layups in figure 7.3, it shows that layup A (UD) has the lowest initial strains, layup B (QI) the highest, and layup C (UD+QI) sits in between, reflecting the expectations based on the stiffnesses found in the quasi-static tensile tests. Within the same layup, however, the initial strain variability was unexpectedly high. To compare the curves within each layup on consistency, the curves were adjusted to a relative timescale, setting each starting time to $t = 0$, and shifting them to a common approximate initial strain value (see figure 7.5). This common initial strain value was estimated based on the applied stress (10 MPa) and stiffness values from the quasi-static tensile tests (see equation 7.1 and table 7.1). While this vertical alignment introduces uncertainty in the absolute strain values, it allows for a better comparison of the curves' slopes.

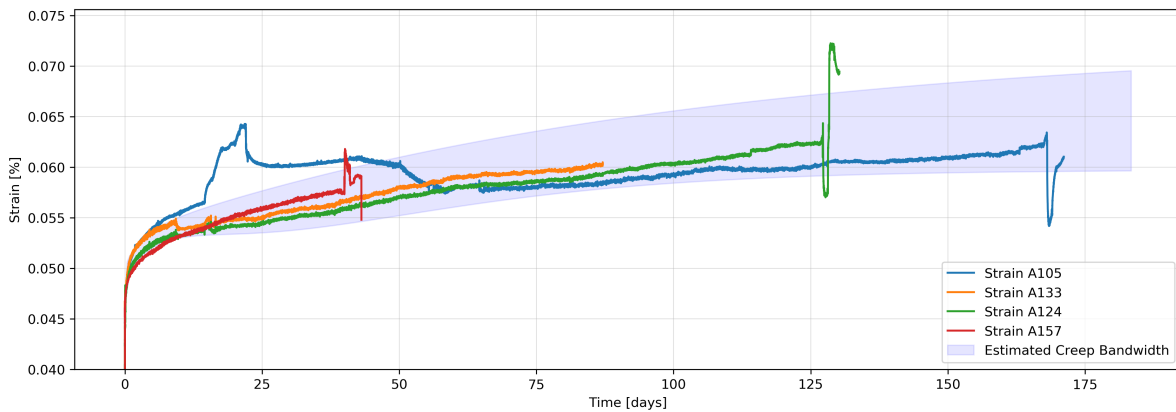
In figure 7.5, the creep curves are grouped by layup and shifted to align to a common starting time and initial strain. The curves have been cleaned and compensated, meaning that the cleaned longitudinal dummy strains were subtracted from the corresponding cleaned longitudinal creep curves by data points matched by exact date and time. The curves are coloured based on the duration of each sample's test, with each different layup having a slightly different shade. The blue curves are placed on February 27, the orange and green curves on April 8, and the red curves represent the samples that replaced the orange samples on July 4. The curves in figure 7.5 are plotted on a timescale in days, with the strain scale zoomed in on the upper portions of the curves to show more details in them. The long-term creep test was conducted to establish a control curve for comparison with the accelerated creep tests. A bandwidth representing the expected range of creep behaviour for each layup was estimated using a four-term Prony series fitted to all curves. This bandwidth serves as a reference for evaluating the results of the accelerated creep tests.

$$\varepsilon_{initial} = \frac{\sigma}{E} \quad (7.1)$$

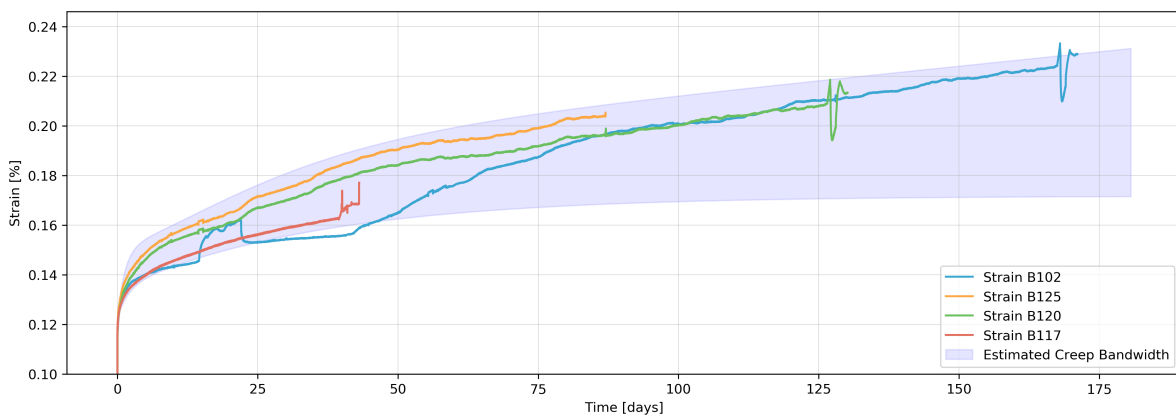
Table 7.1: Summary of calculation of estimation of initial strain for long-term tensile creep test

	Layup A	Layup B	Layup C
Average applied stress [MPa]	10.25	9.96	10.17
Average stiffness [GPa]	21.93	8.21	14.31
Estimated initial strain [%]	0.047	0.121	0.071

(a) Cleaned, compensated, and shifted longitudinal creep strain of layup A (UD) with the relative time on the horizontal axis and an estimated bandwidth of the creep strain behaviour



(b) Cleaned, compensated, and shifted longitudinal creep strain of layup B (QI) with the relative time on the horizontal axis and an estimated bandwidth of the creep strain behaviour



(c) Cleaned, compensated, and shifted longitudinal creep strain of layup C (UD+QI) with the relative time on the horizontal axis and an estimated bandwidth of the creep strain behaviour

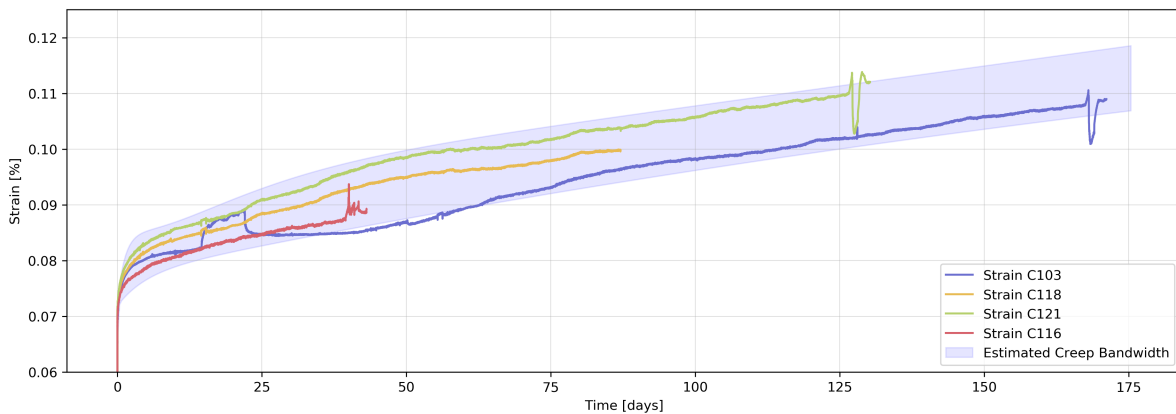


Figure 7.5: Shifted, cleaned, and compensated long-term creep curves, with the relative time in days on the horizontal axis. Each curve is adjusted to align its initial strain with an estimated baseline based on stiffness values found in the quasi-static tensile tests, allowing for better comparison of slopes and curve progression. Note that not all curves experienced the same conditions or disruptions, as they began at different absolute times

Only the blue curves in figure 7.5 (corresponding to the tests started on February 27) endured the climate system failure in March (day 14 to 23), indicated by the early noisy sections of the blue curves in figure 7.5. This period of elevated temperature visibly increased the strain in those curves, suggesting an acceleration of creep due to this event. Note that the blue curves do not have a corresponding

dummy sample, so they are only compensated starting from day 40 with the dummy samples placed on April 8. The red curves, unaffected by the heated strain gauge, highlight the impact of the heating in the other curves. The blue curves show a flatter creep development during the period with the heated strain gauges compared to the other curves. For the orange and green curves, the voltage was lowered before they reached a stable strain rate, adding variability when comparing the curves. All curves appear to become less smooth after the reduction of the voltage.

The initial curvature of the creep curves differs by sample set. The green and orange curves are relatively consistent, while the red and blue curves show more variation. The blue, orange, and green curves had similar initial test conditions, but the curvatures of the green and orange curves were compensated by the dummy strain, while the blue curve was not. To align the slopes after the initial curvature, figure G.8 in appendix G realigns all curves just before their major disruptions (the temperature rise in the blue curves and the voltage change in the green and orange curves). Assuming the red curves reflect the undisturbed creep behaviour, layup A (UD) likely underestimates the creep deformation due to the disruptions, while layups B (QI) and C (UD+QI) may overestimate the creep strain in comparison to their red reference curves.

An interesting finding from figure 7.5a, is that after the adjustment of the voltage and compensation of the dummy strain, layup A (UD) shows a temporary negative strain, suggesting shrinkage. This effect is most prominent in the blue curve, indicating that the strain gauge heat and voltage change had a significant influence on the strain measurements.

7.3. Discussion

The first climate control failure in March, where the temperature rose temporarily to 25°C, led to increased strain and creep strain, likely due to thermal expansion and accelerated creep under higher temperatures. While thermal expansion is reversible when temperatures return to baseline, the extent to which this temperature rise affected creep acceleration is uncertain. The curves appear to remain slightly elevated after the temperatures stabilized, suggesting some degree of creep acceleration. Comparison across the curves is complicated by the effects of the heated strain gauges and voltage reduction, which introduce noise in the other curves, complicating direct correlations between the curves of the same layup. This thermal strain and residual strain were, therefore, not removed from the final long-term creep curves.

The observed sensitivity of the material to small temperature fluctuations, only 4-5°C above the target temperature for roughly a week, raises questions about the duration and level of temperature needed to significantly influence its creep behaviour. Given this sensitivity, future studies could examine the impact of cyclic temperature changes on creep, such as day-night or sun-shadow variations. Such an investigation could provide insights into real-world applications, like bridges, where materials experience similar cyclic conditions.

Figure 7.3 shows that all creep curves behave differently after voltage reduction. The lines become more irregular and the slopes seem to increase, especially those of layups B (QI) and C (UD+QI). Around this same period, the RH in the climate room also became unstable, and figure 7.2 indicates an increase in sample weight during this same period, suggesting the samples absorbed moisture. However, a reduced bridge voltage also causes more noise in the output signal of the strain gauges. This makes it difficult to isolate the effects of the strain gauge settings from those of the fluctuating RH.

Notably, directly after the voltage reduction, the slopes of layups B and C increase abruptly, while layup A's slope appears to decrease. In particular, the blue curve of sample A105 shows a clear initial decrease before gradually increasing again, a phenomenon that is difficult to explain, as longitudinal shrinkage would not typically occur under constant tensile stress.

A hypothesis was that local heating from the strain gauges locally dried the fibres in the composite, leading to moisture reabsorption when the strain gauge temperature was lowered. Flax fibres typically swell when absorbing moisture, especially in radial direction (Lu et al., 2022). This could account for transverse shrinkage under the heated strain gauge and later elongation after lowering the voltage (see transversal strains in appendix G.2). However, swelling in the longitudinal direction, expected during moisture uptake, did not align with the observed shrinkage of the dummy samples in layup A (UD) after lowering the voltage, leaving this phenomenon partially unresolved.

Another possibility is that the longitudinal shrinkage in layup A resulted from the strain gauges

themselves contracting due to the sudden temperature change as the voltage was lowered. However, if this were the case, similar effects would likely be observed in the other layups, which they were not, suggesting a possible link with layup configuration. The potential for strain gauge delamination causing the shrinkage in layup A was dismissed since shrinkage occurred consistently across all samples in layup A, including the control samples, starting all at the same moment.

ASTM D3039 (2002) notes that strain gauges with a high resistance (above 350Ω) require a lower bridge excitation voltage (1-2V) to minimize heating of the strain gauge. According to ASTM D3039 (2002) heating of the strain gauges may affect the performance of the material directly or can affect the indicated strain as a result of the difference between the gauge temperature compensation factor and the coefficient of thermal expansion of the tested material. Although the strain gauges in this study had a normal resistance of 120Ω , the 6V excitation voltage still generated noticeable heat, influencing the strain measurements. The heat accumulated around the strain gauges, especially at the smaller strain gauge (see figure 7.1a) used for measuring the transversal strain. Selecting the appropriate bridge excitation voltage requires careful consideration of material conductivity, strain gauge resistance, and gauge dimensions. While a higher voltage can reduce output signal noise and improve measurement quality, these benefits must be balanced against the potential for heat effects, depending on the material's properties. Careful voltage selection optimizes strain measurement accuracy and reliability. Misalignment or improper adhesion of strain gauges can also impact measurement accuracy, highlighting the importance of carefully choosing a reliable strain measurement technique. The strain gauge voltage reduction significantly impacted the creep strain measurements in the results, though the exact role of the strain gauge itself versus the material response is uncertain. In future research, cross-verifying these measurements with alternative measurement devices could enhance the reliability of the results. However, for long-term tests, it is recommended to use a device that is stuck on the sample, such as a strain gauge or an extensometer. Measurements based on a camera or laser, such as DIC, are not recommended as they have to measure very precisely while they are very sensitive to changes, for example, light or position, and are, therefore, too sensitive for a test that takes months.

The inconsistent initial strains, in figure 7.3, likely result from the test setup. The samples were clamped first, and the load was applied manually by removing the steel plate holding the lever arm, then adjusting the arm by tightening a bolt on the steel threaded rod, going through the end of the lever arm to the top clamp (see figure 5.11). The strain measurements started after clamping the specimen, just before the load was applied. The steel plate's position while a sample was being clamped could have introduced pre-stress by positioning the plate slightly too high (introducing pre-tension) or too low (introducing compression). Because the force could not be measured during the clamping of the sample, this pre-stress remains unknown, possibly explaining the variation in initial strain within the same layups. Starting strain measurements before clamping could reduce this variability but might introduce noise from the manual clamping process. In the quasi-static tensile tests in chapter 6, a similar clamping noise was observed when measurements began before the complete clamping of the specimens. Those tests used hydraulic clamps, while the long-term creep test used manual clamps, which may introduce even more noise during clamping.

To improve the accuracy and reliability of the long-term creep tests, it would have been beneficial to place dummy samples with every round of tests and begin monitoring the weight of dummy samples from the start. This could offer valuable insights into moisture absorption or desorption under variable environmental conditions, which may occur unexpectedly. From the recorded weight data (visualized in figure 7.2), it remains unclear whether the observed weight increase coincides with the unstable, rising relative humidity (RH) or if it had already begun beforehand. Although the first few weight measurements appeared to be stable, an increase began after the third measurement, creating some uncertainty about the prior weight stability. Starting the weight measurements from the beginning of the tests would have allowed a more confident attribution of weight changes to fluctuating RH conditions.

In figure 7.2, several data points, particularly in layup A (UD), deviate from the overall weight trend. Those are considered outliers, likely due to the variability of the initial weighing scale. The last four measurements, performed with a more stable scale, showed consistent readings across layups, suggesting that all samples followed a similar weight trend.

Layups B (QI) and C (UD+QI) showed a slightly higher percentage of weight increase than layup A (UD), possibly due to moisture absorption differences. QI layups generally have more exposed fibre

ends, which tend to absorb moisture, than UD layups, where the fibres are aligned in a single direction. As the hydrophilic nature of flax fibres encourages moisture uptake (see chapter 2), exposed fibre ends in QI laminates likely drive this increase in moisture absorption.

The corrected curves in figure 7.5 account for the strain of only one dummy sample per layup, which introduces some uncertainty. In larger studies, using multiple dummy samples per layup could reduce this uncertainty and allow cross-checking of strain behaviour. This is particularly important when measuring with strain gauges, where incorrect placement can affect the measurements.

Subtraction of dummy strain from creep curves is challenging because the temperature may vary slightly across the room, yet only one central measurement location is used to track the temperature. The dummy samples may have a delayed response to temperature changes, as they experience less air-flow than the samples in the creep test setup. When synchronizing measurements between dummy samples and test samples based on date and time, these delays can introduce additional noise in the compensated creep curves.

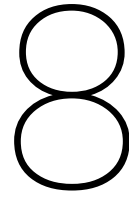
Conducting long-term tests on materials sensitive to temperature and humidity poses challenges, especially if stable conditions are critical. Even a brief climate system malfunction can significantly affect the test outcomes, as seen in this study. To address these risks, a robust plan for managing climate control failures is essential. Selecting reliable environmental control equipment or adjusting the stability requirements for RH and temperature can further improve test reliability. In future cases, replacing affected samples immediately upon system failure could help ensure the validity of creep data despite requiring additional efforts.

7.4. Conclusion

The creep strain measurements in the long-term creep test in this study were impacted by various uncertainties, primarily due to climate control failure, heated strain gauges, and fluctuations in relative humidity (RH) that potentially lead to moisture absorption by the samples. The blue curves in figure 7.5 appear to be most affected by these factors and are deemed unreliable for accurately representing the material's true creep behaviour under stable conditions. In contrast, the green and orange curves show greater consistency, while the red curves, which were only exposed to a temperature disruption near the end of testing and unaffected by the heated strain gauges, provide a more stable baseline for interpreting the material's true creep behaviour. The creep curves provide an estimate of the range within which the true creep response for a creep stress of 10 MPa is expected to fall in each layup. More tests, under more stable conditions, are necessary to obtain a reliable long-term creep curve for each layup.

This study highlights that a stable climate-controlled environment is essential for obtaining accurate long-term creep measurements in temperature- and moisture-sensitive materials. The unknown pre-stress introduced by the manual clamping and setup process also contributes to uncertainty in the absolute strain values. The initial strain was here calculated based on the material stiffness rather than direct measurements.

In general, these long-term creep tests showed that the flax fibre-reinforced polymer composite is highly sensitive to minor environmental fluctuations. A temperature variation as small as 5°C had a measurable and lasting effect on the long-term creep curves, which becomes particularly pronounced in low-stress tests where the expected deformations are relatively small. Consequently, the effects of environmental instability are amplified, underscoring the need for a stable climate and reliable climate control to obtain reliable creep data for this material. Given the material's non-linear viscoelastic behaviour and susceptibility to material memory, any interruption in loading can affect its subsequent responses.



Accelerated Creep Test Using the Stepped Isostress Method

This chapter presents the results of the accelerated tensile creep test conducted using the stepped isostress method (SSM). First, an overview of the raw data and failure mechanisms are analysed, followed by a detailed explanation of the data processing steps to construct the creep master curves from the SSM test data. Emphasis is placed on the SSM method and the interpretation of the data handling procedure rather than solely on the final creep master curves. The SSM-derived creep master curves are compared with the creep bandwidth found in the long-term tensile creep tests. In the discussion of this chapter, various interpretations of the data and test procedures are addressed, as well as the uncertainties and sensitivity associated with the SSM method.

8.1. Initial Results

Figures 8.1, 8.2, and 8.3 present the raw data from the accelerated tensile creep tests using the stepped isostress method (SSM), showing the time on the horizontal axis and the measured strain on the vertical axis. For both layups A (UD) and B (QI), additional tests were conducted with smaller stress increments and extended dwell times, as detailed in section 5.4. These tests are on a much larger timescale, therefore distorting comparisons with the tests involving larger stress increments and shorter dwell times (see figures 8.1 and 8.2). Therefore, graphs focusing solely on the tests with the larger stress increments are included in appendix H.2 for clearer comparisons across all three layups. In each layup, one sample from the large stress increment series was not cooled during testing.

Figure 8.1, (more clearly displayed in appendix H.2), shows that some specimens of layup A (see for example samples A151, A168) failed before reaching the sixth step, even though the maximum stress in the final step was well below their ultimate tensile strength. The rectangular specimens (cut from plate part 1, identified by the first digit being "1" in their IDs) exhibited slightly more strain than the dog bone-shaped specimens (cut from plate part 2). This difference is more subtle at lower stress levels but becomes more pronounced at higher stress steps. The tests with smaller stress increments reached strain levels of only 0.4-0.5%, about half the strain observed in the tests with larger stress increments. These smaller stress increments resulted in a reduced elastic strain between the steps and produced flatter individual creep curves for each step.

For layup B (figure 8.2), tests with large stress increments showed consistent strain behaviour throughout the accelerated creep tests. All curves failed at around 1.6% strain, aligning with the stress levels predicted to induce creep failure (see section 5.4). Interestingly, the smaller stress increment tests for layup B also failed at similar stress and strain levels as the samples tested with the large stress increments. As in layup A, the tests with smaller stress increments in layup B gave flatter curves with lower initial strains.

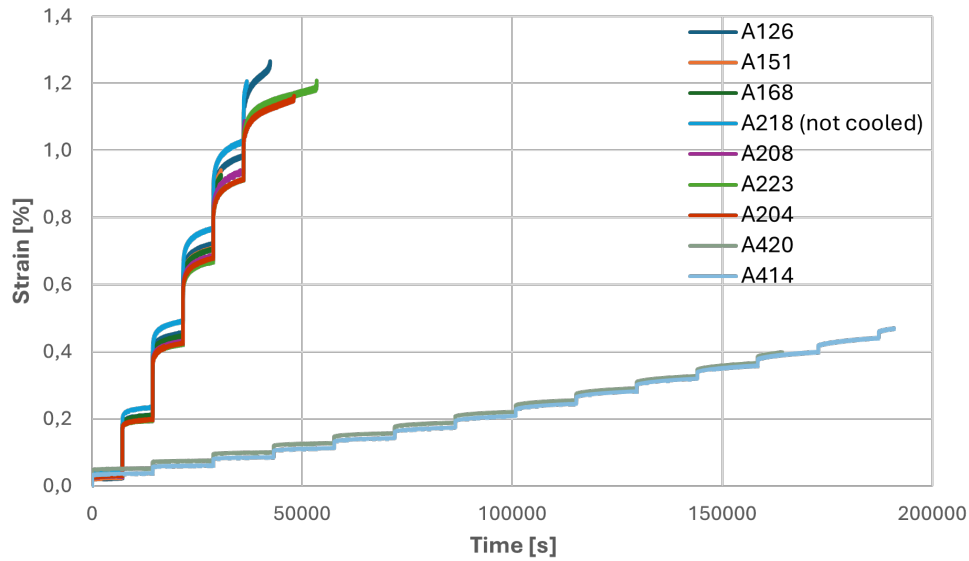


Figure 8.1: Raw data of the accelerated tensile creep test using the SSM for layup A, note that for samples A420 and A414, the test was stopped manually before failure

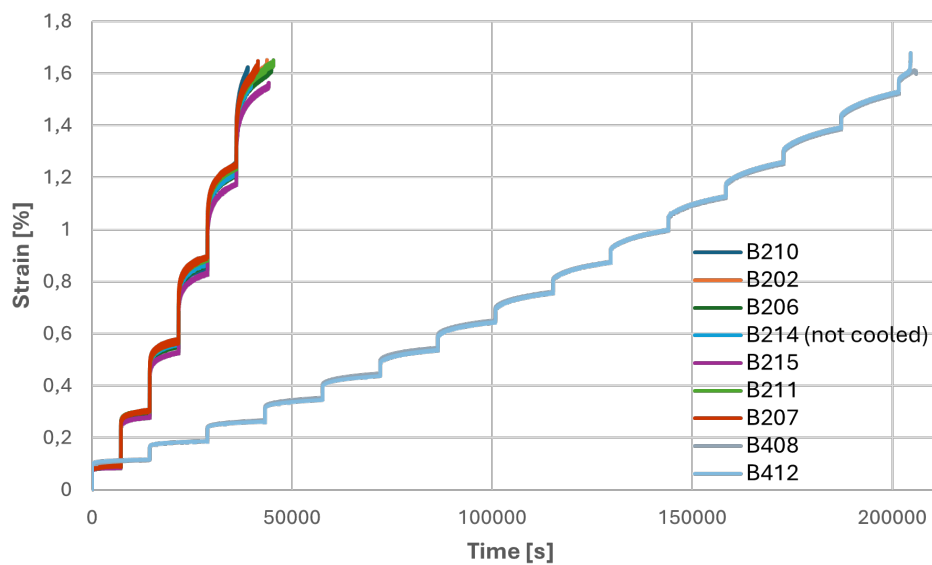


Figure 8.2: Raw data of the accelerated tensile creep test using the SSM for layup B

For layup C, only tests with large stress increments were conducted. The timescale for layup C in figure 8.3 differs from that of layups A and B in figures 8.1 and 8.2. The raw strain curves of layup C show a general consistency. Notably, the final steps in layup C did not show the strain rate increase typically associated with creep failure. Instead, the curves for samples C217, C213, and C207 extended well beyond the two-hour duration of the last step, showing no failure during this period. The tests were stopped manually before the samples had failed. This outcome aligns with the expectations, as the maximum force applied by the testing machine was only 50% of the guaranteed ultimate tensile strength (GUTS).

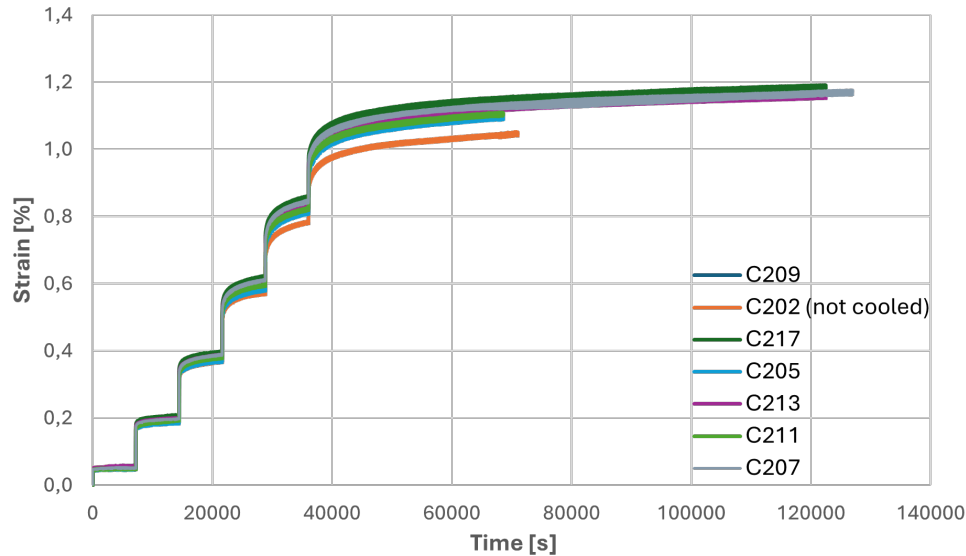


Figure 8.3: Raw data of the accelerated tensile creep test using the SSM for layup C, note that most tests were stopped manually before failure of the samples

8.1.1. Failure Mechanisms

During the accelerated tensile creep tests, five distinct types of failure mechanisms were observed, as shown in figure 8.4. These failure mechanisms were partly influenced by the evolution of the clamping method and end tab design throughout the experiments. The observed failure modes included:

1. Clamping failure at the edge of the clamps
2. Slippage of the paper end tabs from the sample
3. Failure in the middle of the specimen
4. No failure as the test was stopped manually before the failure of the specimen
5. Longitudinal splitting combined with failure in the end tabs near the clamps (observed only in two samples of layup A, A223 and A204)

The detailed outcomes of each test are schematized in appendix H.1, and a summary of the failure mechanism per sample is provided in table 8.1. Notable is that clamping failures were observed when no end tabs were used and when the four bolts in the clamps were tightened evenly rather than applying slightly greater torque to the outer screws compared to the inner screws. Slippage was associated with paper end tabs glued with the Sencys universal contact adhesive, which was probably not strong enough. Table 8.1 shows that particularly layup A (UD) was prone to failures near the clamps, suggesting again that this layup has a high sensitivity to stress concentrations. Layup B showed a mix of clamping failures and failure in the middle of the specimen, while layup C frequently did not fail at all, as tests were stopped before reaching the ultimate tensile strength.

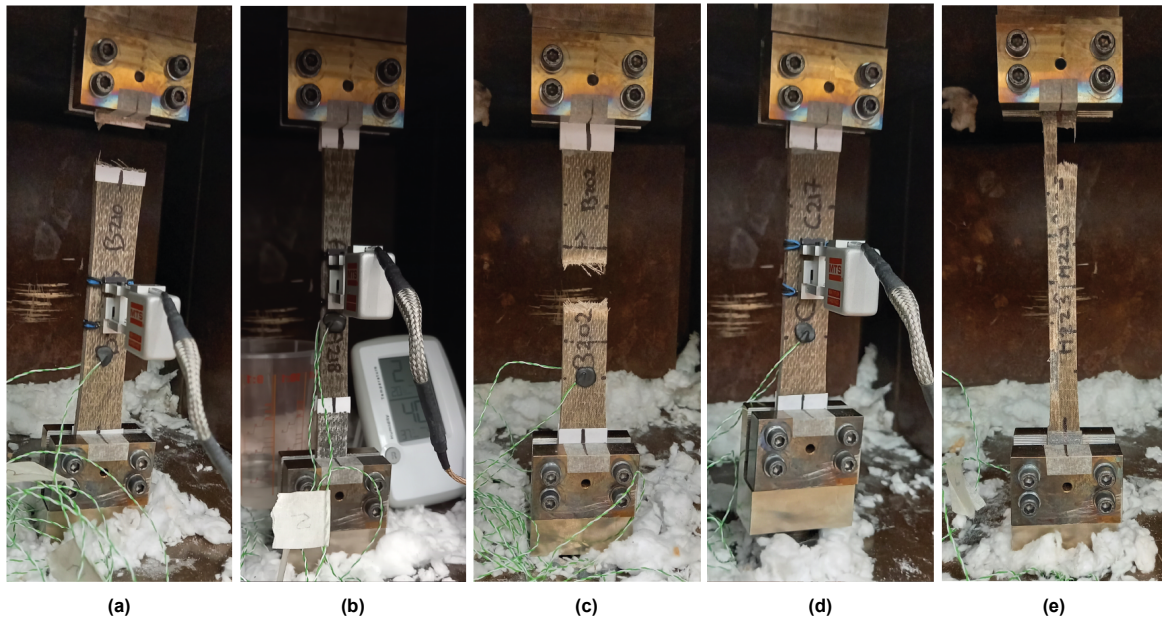


Figure 8.4: Pictures of the various failure mechanisms found during the accelerated creep test: (a) clamp failure, (b) slippage from clamps, (c) sample failure, (d) stopped the test before failure, and (e) longitudinal splitting

Table 8.1: Summary of failure mechanisms during the accelerated tensile creep tests using the stepped isostress method (ordered on testing date per layup, corresponding to the overview in appendix H.1)

Sample	Failure type	Classification
A126	clamp failure (lower clamp)	GAB
A151	clamp failure (upper clamp)	GAT
A168	clamp failure (lower clamp)	GAB
A208	slippage from clamp (lower clamp)	OAB
A218	slippage from clamp (lower clamp)	OAB
A223	failed in tab and over length	G/SIT/V
A204	failed in tab and over length	G/SIT/V
A414	test stopped before failure	-
A420	test stopped before failure	-
B210	clamp failure (upper clamp)	GAT
B214	clamp failure (upper clamp)	GAT
B202	sample failure (middle, straight)	LGM
B206	sample failure in upper transition zone	LGT
B215	sample failure in upper transition zone	LGT
B211	sample failure in upper transition zone	LGT
B207	sample failure in lower transition zone	LGB
B408	sample failure (middle)	LGM
B412	sample failure (middle)	LGM
C209	slippage from clamp (lower clamp)	OAB
C202	test stopped before failure	-
C217	test stopped before failure	-
C205	test stopped before failure	-
C213	test stopped before failure	-
C211	test stopped before failure	-
C207	sample failure in upper transition zone	LGT

8.2. Stepped Isostress Method Data Analysis

The data handling procedure for the stepped isostress method (SSM) involves vertical shifting, rescaling, and horizontal shifting. For this research, this procedure was scripted step by step in Python code using Jupyter Notebook. Before the analysis can begin, the raw data must first be segmented into individual segments to handle each small creep curve separately. This segmentation was done by identifying distinct load steps based on a strain rate or force change threshold. The threshold selection varied per sample, as for each test the signal noise was different. After manually merging and cleaning the segments at the initial and final data points where necessary, the resulting segmentation is shown in figure 8.5. The analysis aimed to develop a systematic and repeatable procedure, avoiding the visual or graphical methods commonly used in literature. The segmented data was then processed through the three SSM data handling steps, detailed in the next sections.

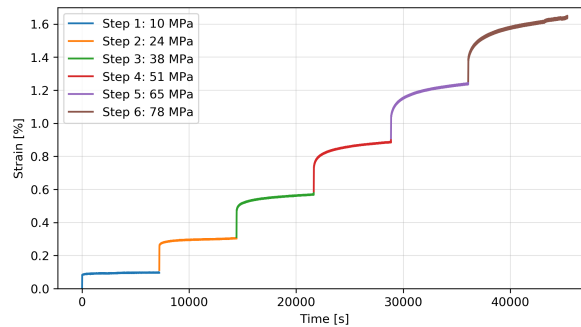


Figure 8.5: Example for segmentation of raw data for sample B211

8.2.1. Vertical Shifting

The first step in the SSM data processing involves a vertical shift to adjust for elastic strains at the start of each load step, isolating the creep strains (see section 4.2). This adjustment assumes that no creep strain occurs during the initial elastic strain jump at the start of each step. So that the remaining curves involve only creep strains. The elastic strain was eliminated by defining a strain rate boundary (often between 0.001-0.004 %/s, based on the noise bandwidth of the test) and removing the data points above this threshold. Noise in the force and strain signals required additional manual cleaning and visual inspection of each segment, as the optimal boundary value varied across tests. After removing the elastic strain (see figure 8.6a), the curves were vertically shifted to align the first value of each step with the last value of the previous step (see figure 8.6b). This vertical shift starts with the second curve, leaving the first curve (at the reference stress of 10 MPa) unshifted. The elastic strain in the first step was not removed, as this elastic strain is part of the creep master curve for a certain reference stress.

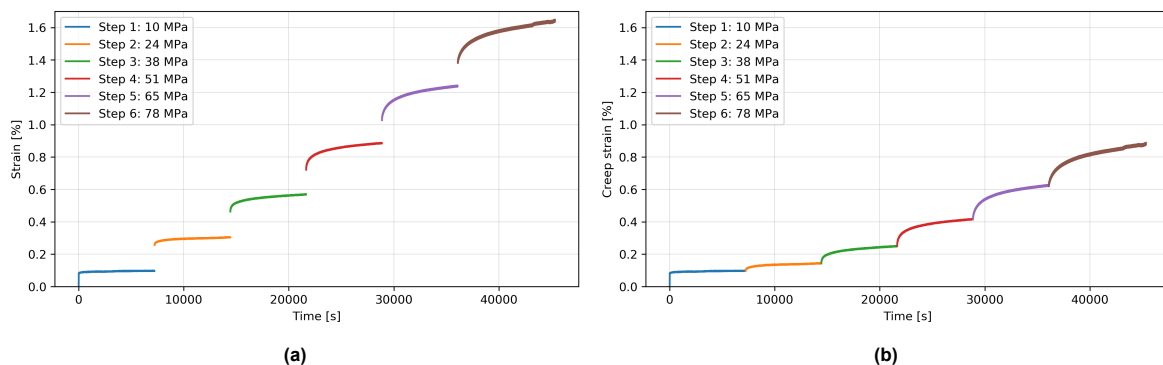


Figure 8.6: Visualization of the vertical shift for sample B211, (a) Eliminating the initial strains of each step, except the first step (at the reference stress), (b) Performing the vertical shift for each segment

8.2.2. Rescaling

The rescaling step adjusts for the stress history of the specimen by determining a virtual starting time for each step's creep curve. This involves two intermediate steps: (1) identifying the secondary creep portion of each small creep curve and (2) extrapolating it back to a baseline defined as the zero creep strain of the reference step. Each curve is then shifted back in time by its virtual starting time.

To identify the secondary creep region, the strain rate was plotted alongside the stepped strain curves. Due to noise in the force signal and, therefore, noise in the strain and strain rate signal, an overlapping average of the strain rate over 100 data points was used. Figure 8.7 shows the strain curves with their respective strain rates on the secondary y-axis. Particularly in the final load step, the noise in the strain rate signal is visible. For a systematic definition, a threshold, based on the stabilization of the strain rate, was set at the last 80% of the data points to distinguish the transition from primary to secondary creep. This boundary, marked by the red dashed vertical lines in figure 8.7, defines the secondary creep region for each step. The primary creep was not removed, but was ignored for the rescaling step.

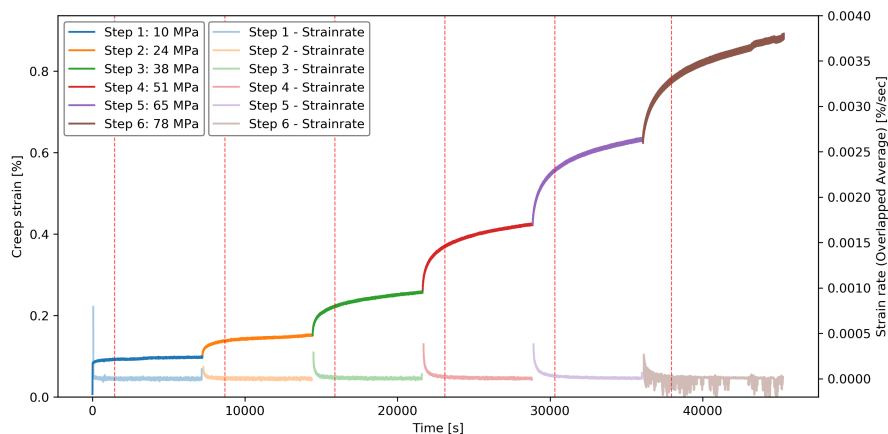


Figure 8.7: Determining secondary creep in the SSM curves for sample B211 with the creep strain rate, by marking the last 80% of the data set of each step

Three types of curve fits (based on curve fits used in previous research) were tested for extrapolating the secondary creep region of each step: a third-order polynomial, an exponential, and a power-law curve fit. While polynomial fits worked well for the secondary creep portions, the exponential and power-law fits required application to the entire curve (the primary creep and secondary creep portions) in order to get a reasonable fit. Figure 8.8a illustrates these fits, showing their intersections with the start of creep of the reference step (for sample B211 at 0.08% strain) to determine the virtual starting times. Each curve was then rescaled by shifting each curve as $t_{\text{rescaled}} = t_{\text{original}} - t_{\text{virtual}}$, visualized in figure 8.8b. The figure shows that the power-law-based rescaling gave large virtual starting times, bringing the curves close to $t = 0$, while the polynomial-based rescaling resulted in smaller virtual starting times, leaving the curves further apart in time.

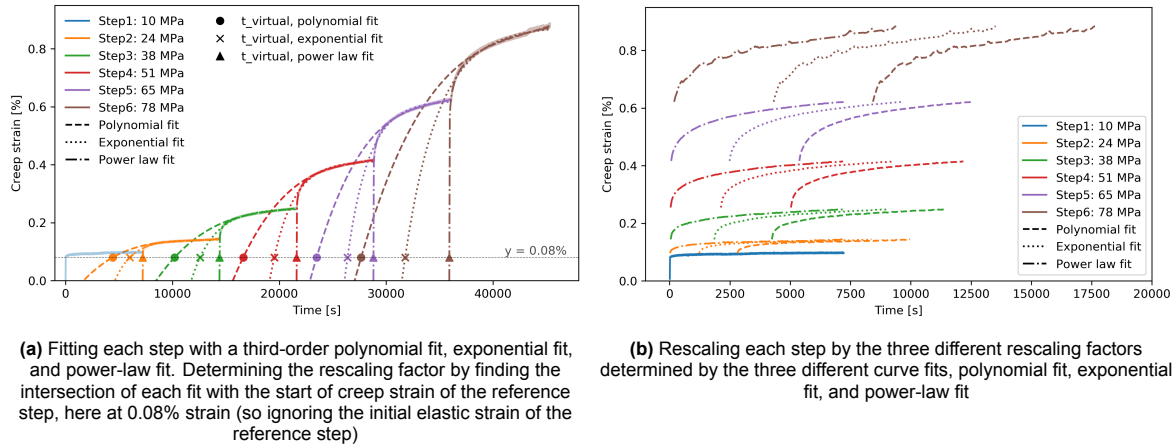


Figure 8.8: Visualization of the rescaling step with three different curve fits for sample B211

8.2.3. Horizontal Shifting

The final step of the SSM, the horizontal shift, aligns the rescaled creep curves using the time-stress superposition principle (TSSP). This involves shifting the curves horizontally along a logarithmic time axis, based on the shifting factor α_{σ} . This horizontal shifting factor was derived from the slope of the secondary creep region of each individual creep curve. The calculation of α_{σ} is based on equation 8.2 (derived from equation 4.2, on page 24). Equation 8.1 then shows how the horizontal shifting factor is applied to shift the individual creep curves over the logarithmic time axis.

$$\log_{10}(t_{i,\text{master}}) = \log_{10}(t_{i,\text{rescaled}}) + \alpha_{\sigma_i} \quad (8.1)$$

With:

- $t_{i,\text{master}}$ = time of the creep for load step i in the constructed SSM master curve
- $t_{i,\text{rescaled}}$ = rescaled time of the creep curve for load step i
- α_{σ_i} = horizontal shift factor for load step i

Where

$$\alpha_{\sigma_i} = \frac{\dot{\epsilon}_i}{\dot{\epsilon}_r} \quad (8.2)$$

With:

- $\dot{\epsilon}_i$ = strain rate or slope of the secondary creep region of the creep curve of load step i
- $\dot{\epsilon}_r$ = strain rate or slope of the secondary creep region of the reference creep curve (the first load step)

To determine the slope of the secondary creep region of each curve, a linear function was fitted to the last 80% of data points for each load step. This slope, representing the strain rate, was used to calculate the shifting factor for each step. The shifting factor is applied to the corresponding load step according to equation 8.1, to align the curves and construct the creep master curve for the reference creep stress. The result is presented in figure 8.9, where the same horizontal shifting factor is applied to the different rescaled curves. The figure shows that the power-law-based rescaled curves appear more stretched compared to those rescaled with the polynomial or exponential fits. While the power-law curves exhibit a smoother profile initially, all rescaled curves converge towards the same time range at their endpoints. Despite the differences, the overall shifting factor forms a similar trend across all rescaled curve types, with the curve being the best visible in the power-law-based rescaled curves. The constructed creep master curve spans a logarithmic timescale exceeding 10^{16} seconds, which is equivalent to approximately 300 million years.

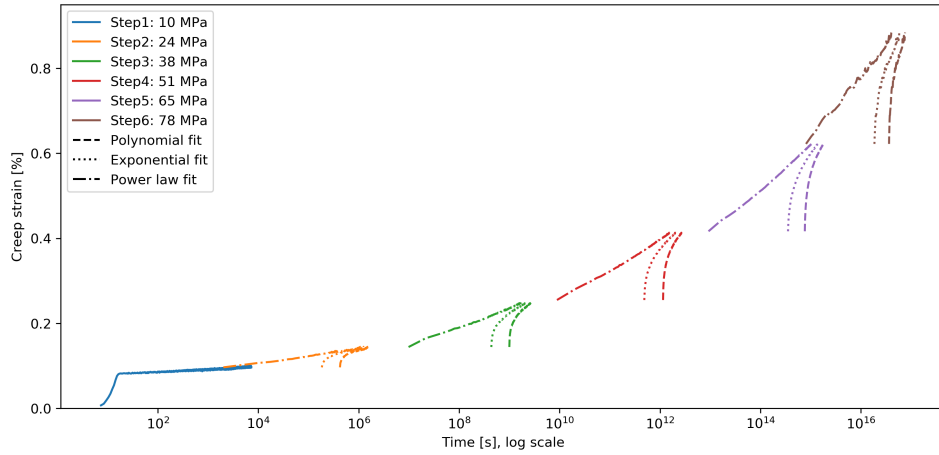
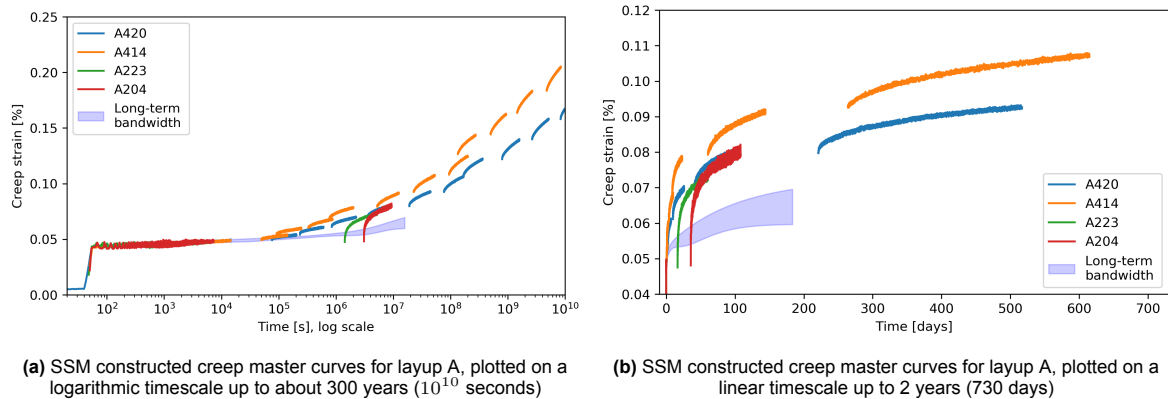


Figure 8.9: Horizontal shift for three types of rescaled curves, based on horizontal shifting factor: α_{σ} , for sample B211. Forming the SSM constructed creep master curve

8.3. End Results and Validation

The final constructed creep master curves are presented in figures 8.10 and 8.11. Due to time constraints and a primary focus on methodology development and experimentation, not all tests underwent complete data processing. The creep master curves were constructed using a third-order polynomial fit to determine the virtual starting time in the rescaling step, as this approach used only the secondary creep portion during the rescaling step. The plots are cut off at a time of 10^{10} seconds, corresponding to approximately 300 years. This time frame aligns more with a possible design lifespan of typical structures (which is often about 100 years). Beyond this point of time is 10^{10} seconds, further predictions are not relevant. Additionally, the creep bandwidth observed in the long-term tensile creep tests is included and serves as a reference for real-time creep measurements, enabling validation of the SSM predictions.

Figures 8.10 and 8.11 show that for both layups A (UD) and B (QI) the constructed creep curves from the SSM tend to overestimate the creep deformation measured in the long-term creep test. Notably, the tests with large stress increments fall mostly outside the 300-year (10^{10} seconds) time frame, while tests with smaller stress increments produce more curves within this range. Interestingly, although the raw data plots (see figure 8.1, and 8.2) showed a strong resemblance between the tests, the resulting creep master curves displayed a significant divergence. This difference is particularly evident for layup B, as shown in figure 8.11a.



(a) SSM constructed creep master curves for layup A, plotted on a logarithmic timescale up to about 300 years (10^{10} seconds)

(b) SSM constructed creep master curves for layup A, plotted on a linear timescale up to 2 years (730 days)

Figure 8.10: The SSM constructed creep master curves for layup A (UD), two tests with small stress increments and two tests with large stress increments, with the expected creep bandwidth resulting from the long-term creep test serving as a reference to validate the final SSM creep curves

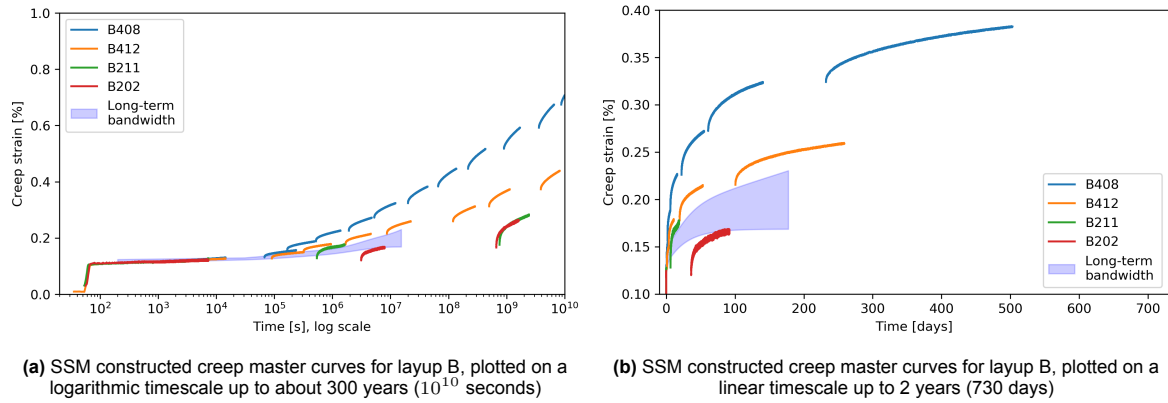


Figure 8.11: The SSM constructed creep master curves for layup B (QI), two tests with small stress increments and one test with large stress increments, with the expected creep bandwidth resulting from the long-term creep test serving as a reference to validate the final SSM creep curves

In the literature, horizontal shifting factors are typically validated by examining their relationship with the applied stress at each step. Figure 8.12 illustrates this relationship for both layups, with the horizontal shifting factors (calculated from the slopes) plotted against the stress relative to the reference stress of 10 MPa. For the reference step, no horizontal shift is applied, so the corresponding horizontal shifting factor is expected to be zero. Ideally, the curves in figure 8.12 should originate from the origin. For layup A, the shifting factors, especially those from the tests with small stress increments (samples A414 and A420), seem to exhibit a linear relationship with the applied stress. Besides, the data points form a trend that appears to converge towards the origin. However, for layup B, only the curves for samples B202 and B211 show a clear tendency to start at zero, while the other curves seem to flatten near the origin. Additionally, especially in figure 8.12a, the shifting factors of the highest load steps deviate significantly from the trends formed by the earlier load steps. Overall, for layup A, the shifting factors closely follow a single linear trend across the different tests, while for layup B, the curves show a greater divergence, especially at higher load steps.

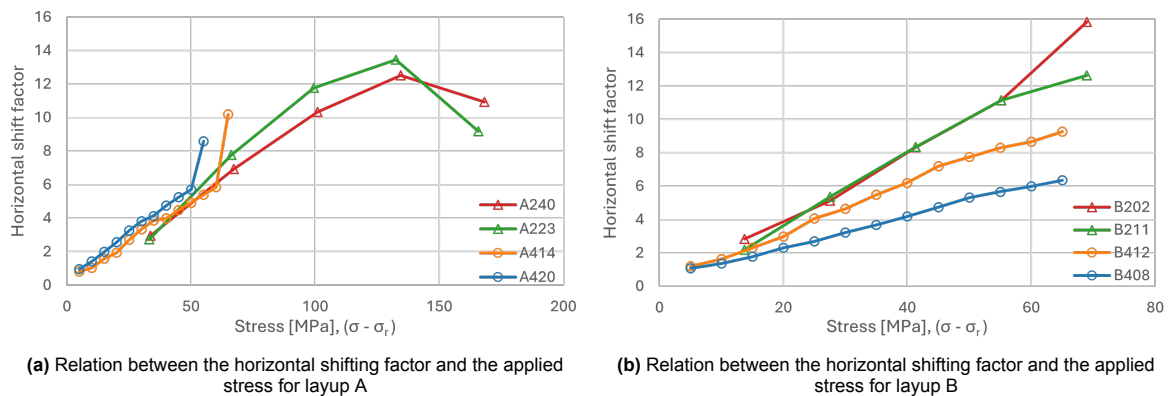


Figure 8.12: Validation of the horizontal shift, by plotting the horizontal shifting factor against the applied stress for each step. Note that the stress is plotted as the difference between the applied stress and the reference stress (10 MPa)

8.4. Discussion

The discussion in this chapter addresses several key topics: The methodology of the stepped isostress method (SSM), the execution of SSM tests, the observed failure mechanisms, the SSM data processing steps vertical shifting, rescaling, and horizontal shifting, and the sensitivity of the rescaling factor ($t_{rescale}$) and the horizontal shifting factor (α_σ).

SSM Methodology

For this research, the SSM stress steps in the tests with large increments were designed based on the GUTS (guaranteed ultimate tensile strength) found in the preliminary quasi-static tensile tests (results

can be found in appendix F). The objective was to utilize the material's full capacity and extend the prediction of its creep behaviour as far in time as possible. Therefore, the final stress levels were planned to go up to 90% of the GUTS.

However, limitations arose due to the MTS machine's 15 kN load cell capacity. For layups A (UD) and C (UD+QI), the maximum designed stress was adjusted to this limit, with six evenly spaced stress steps ranging from 10 MPa to the maximum achievable stress by a load of 15 kN. In layup B (QI), the 90% GUTS was just below the machine's maximum capacity, allowing for unaltered stress steps. Interestingly, the GUTS values from the second round of quasi-static tensile tests exceeded those of the preliminary tests. This meant that even layup B's maximum stress did not reach 90% of its updated GUTS. Despite this, all samples of layup B failed at similar strain levels, suggesting that even lower stress levels, such as 75% of the updated GUTS, may be sufficient to induce creep failure. Future tests could benefit from adjusting the final load step for layups A and C to 75-80% of their GUTS when aiming for creep failure in an SSM test.

Predicting creep failure for very low reference stresses (e.g., 10 MPa) is likely impractical, as projections can exceed 10^{14} seconds (300 million years). Predictions beyond 100 years (10^{10} is about 300 years) are generally less relevant, as other factors become more significant in determining the lifespan of a structure. Instead, creep deformation is a more practical focus for a creep test at a relatively low reference stress. Therefore, smaller stress increments might have yielded more valuable data in the SSM tests, avoiding excessively high stress levels.

Research by Jia and Fiedler (2020) suggests that flax fibre composites do not develop creep damage at low stress levels, although creep deformation in the fibre direction is still evident. However, their study was limited to two-hour creep test durations, while the objective of this research is to predict the long-term creep behaviour of a flax fibre composite. Testing this hypothesis of no creep damage at low stress over much longer periods (e.g., years) could reveal whether creep damage eventually develops under low stresses.

This raises another critical question and potential limitation of accelerated creep testing: as stress levels increase, the creep mechanism may shift, potentially introducing damage that would not occur under the low reference stress. Such changes could reduce the accuracy of the SSM predictions for a low reference stress. Nonetheless, the resulting creep master curve is likely more conservative, as it accounts for damage effects from higher stresses. Balancing the efficiency of accelerated creep testing with the risk of over-conservatism requires careful consideration. While accelerated methods save time, they may underestimate a material's true performance. Further research is needed to validate these findings and refine the methodology to balance accuracy with efficiency.

SSM Test Execution

The execution of the SSM tests faced several challenges related to equipment, environmental conditions, and load stability. Different tensile testing machines and measurement devices were used for the SSM test compared to the quasi-static and long-term creep tests, introducing potential variability in clamping and measurements. Ideally, the same machine and measurement devices would have been used to avoid such differences. However, the lack of a signal filter for strain gauges made them unsuitable for the accelerated creep tests. As a result, only a MTS extensometer was used, limiting the strain measurements to the longitudinal direction.

In the SSM, the assumption is made that thermal strains are negligible. To neglect these strains, the temperature during the tests must be held constant. While a temperature chamber was installed, its reliance on a nitrogen tank led to fluctuations of about $\pm 0.5^\circ\text{C}$. This influence could not be verified using a dummy sample due to noisy strain gauge readings and the inability to use a second extensometer. Another challenge was the lack of control of the relative humidity (RH). Although a cup of water was added inside the chamber to stabilize the RH, the liquid nitrogen had a big influence on the RH in the temperature chamber. The RH could only be monitored at minimum and maximum values over a period of time, with no information on stability or duration. By manually monitoring a test, an idea of the fluctuations could be formed. During each test, the RH initially dropped sharply to 20%, before stabilizing within a range of 35-50% after about one hour. This range was 10-20% lower than the RH in the long-term tests. The influence of the cup of water was tested by measuring the weight of two

dummy samples placed inside the temperature chamber. The weight measurements showed that the cup of water reduced the weight loss of a sample during one test from $\tilde{0}.094\text{-}0.095\%$ to $\tilde{0}.038\text{-}0.048\%$. It was, therefore, concluded that the water cup reduced the moisture desorption of the samples, so it was included in all subsequent tests.

The MTS machine, used for the SSM tests, was connected to a shared hydraulic oil pressure system, together with other mechanical testing machines in the lab. This shared system caused fluctuations in the oil pressure as other machines were running other tests. The fluctuations in oil pressure caused instability in the force control system, leading to deviations of $\pm 40\text{-}150$ N from the target force, with larger deviations occurring at higher load steps. These fluctuations, along with minor temperature changes and hydraulic pump cycles, introduced noise into the strain measurements, which were difficult to distinguish from one another. While this noise affected the curve smoothness, it likely had a minimal impact on the long-term creep behaviour. However, it made the SSM data handling procedure a bit more difficult. For example, linear trend fitting was preferred over point-to-point slope calculation to reduce the impact of the data variability when calculating the horizontal shifting factor.

Despite these challenges, the SSM test results remained suitable for analysing the overall creep behaviour of the composite. However, future tests should address these limitations to improve the reliability and accuracy of the measurements.

Failure Mechanisms during SSM testing

The clamping failures in the samples of layup A (UD) during the accelerated creep tests indicate premature failure. The quasi-static tensile tests had already revealed the sensitivity of UD layups to stress concentrations. The manual tightening of the mechanical clamps in the SSM tests worsened the stress concentrations, as uneven bolt tightening created a non-uniform force application. As a result, many UD specimens failed near the clamps rather than through typical creep mechanisms, as the applied load was only $\tilde{6}0\%$ of their ultimate tensile strength (UTS). Therefore, these failures could be considered premature and not representative of true creep failure.

However, creep-related mechanisms, such as matrix cracking, may cause a sample to fail earlier. Over time, creep can introduce defects that act as stress concentrators, which can accelerate creep failure. For instance, samples A223 and A204, which had composite end tabs, showed failure both near the clamps and along the specimen length. It remains unclear whether the failure started at the clamps or along the sample length. Further testing is required to determine whether UD layups consistently fail at such low loads or under a creep strain of approximately 1.2%.

Dividing the Raw Data Into Separate Load Steps

Before starting the SSM data handling procedure, the data is divided into individual load steps. This division was complicated by the noise in the force signal, particularly in the tests with large stress increments, making identification of each step difficult. The stress increments were displacement-controlled, with no fixed duration for the increment. Additionally, the force signal was so noisy and unstable that it was difficult to identify whether the program had reached its limit and switched over to force control or if the fluctuations were simply noise within the force-controlled system. As the noise in the signal was different per test, step, and even moment, the exact start and end points of each step were hard to identify. Consequently, the division of the individual load steps had to be cleaned and checked manually after filtering the data by strain rate or force.

The tests with small stress increments, performed on a different machine with less noise (± 10 N), were less problematic. These tests used a set time period for each stress increment and monitored the target force alongside the measured force. This allowed for much easier identification of the different load steps and the transition point from instantaneous strain to creep strain.

SSM Data Processing: Vertical Shift

In the first step of the SSM data processing, the curves are vertically shifted, eliminating the elastic strains during the load increments. Therefore, the assumption is made that no creep strain occurs during these jumps, attributing all strains in this phase to elastic deformation. However, Blum et al. (2002) argue that there is always some portion of creep strain during the loading of a specimen. However, in SSM testing, this creep strain portion is likely negligible compared to the elastic strain over the few seconds required for the load application. Thus, neglecting this small creep strain introduces a reasonable simplification.

As with identifying the separate load steps, distinguishing the loading period within each step was challenging due to the noise in the force control system, particularly in the tests with the large stress increments. Variations in force, strain, and strain rate made it difficult to identify the elastic strain jumps, necessitating manual adjustments. In contrast, the tests with small stress increments benefited from tracking the target force, enabling clearer identification of the loading and force-controlled periods. These data processing challenges demonstrate the importance of noise reduction and precise force control in ensuring the accuracy of the SSM test results.

SSM Data Processing: Rescaling

In the existing literature, limited justification is provided for selecting specific curve-fitting methods beyond achieving a smoother creep master curve. Notably, curve fits that result in a larger virtual starting time are often considered superior to methods resulting in a lower virtual starting time. This study reached a similar conclusion, finding that the power-law curve fit produced a smoother creep curve due to their logarithmic stretching. While the literature typically recommends using only the secondary creep region for curve fitting and determining the virtual starting times, this research found that incorporating the primary creep region improved the performance of both the exponential and power-law curve fits. Further research is needed to clarify the advantages of specific curve-fitting methods and provide justification for their use. Consistency across methods is essential, but this was not achieved in the current study. The polynomial fits were applied exclusively to the secondary creep region of the individual creep curves, while other fits used both primary and secondary creep regions, introducing inconsistencies in the methodology.

Identifying the secondary creep phase systematically for the data sets of this research was challenging, especially when the strain rate signal was noisy. In this study, a moving overlapping average over 100 data points was applied to reduce the noise in the strain rate signal. The secondary creep phase could then be identified as the portion where the strain rate stabilized. For most tests, the secondary creep phase was identified as approximately the last 80% of data points for each step (visualized in figure 8.7). This approach was chosen to establish a systematic and repeatable method for handling the data, ensuring consistency across all analyses. However, for the tests with larger stress increments, the primary creep phase sometimes exceeds the first 20% of the data, so a smaller percentage than the last 80% of data would be more appropriate to label as the secondary creep portion. Conversely, for the tests with small stress increments, the 80% threshold might be on the conservative side and could potentially be increased. A more accurate estimate for the higher steps in the large stress increments could be the last 70% of data points. The identification of the secondary creep portions must be more refined by finding a systematic and automated method that takes into account the individual creep curves and their strain rates.

For the higher steps in the tests with large stress increments, the two-hour dwell time seemed to be insufficient to reach a fully stabilized secondary creep phase. Figure 8.13 shows the differences in strain rate behaviour for a test with large stress increments and two tests with small stress increments for a similar stress level. The strain rate in sample B211 (large stress increments) requires more time to stabilize compared to the strain rates of samples B408 and B412 (small stress increments), which stabilize much faster. In B211, the strain rate appears to stabilize only near the end of its dwell time, suggesting a longer dwell time might provide more certainty about the stabilized strain rate for that step. As used in the small stress increment tests, a four-hour dwell time would likely capture a larger portion of secondary creep and might therefore be more suitable. However, further testing is required, using the same large stress increments but with extended dwell times (e.g., four hours) to draw definitive conclusions. Currently, the small stress increment tests combine longer dwell times with smaller stress increments, both of which can reduce the primary creep portion. This makes it impossible to isolate the separate effects of stress increment and dwell time on the primary creep from these results, though it is evident that the behaviour is different.

Improvements to the data analysis, in this case the Python script, could allow for a more precise definition of primary and secondary creep phases for the individual load steps rather than relying on generalized thresholds (e.g., the last 80% of data points). The percentage of data points corresponding to the secondary creep phase likely varies per test design, being higher for smaller stress increments and lower for larger ones, as well as differing between the load levels within the same SSM test.

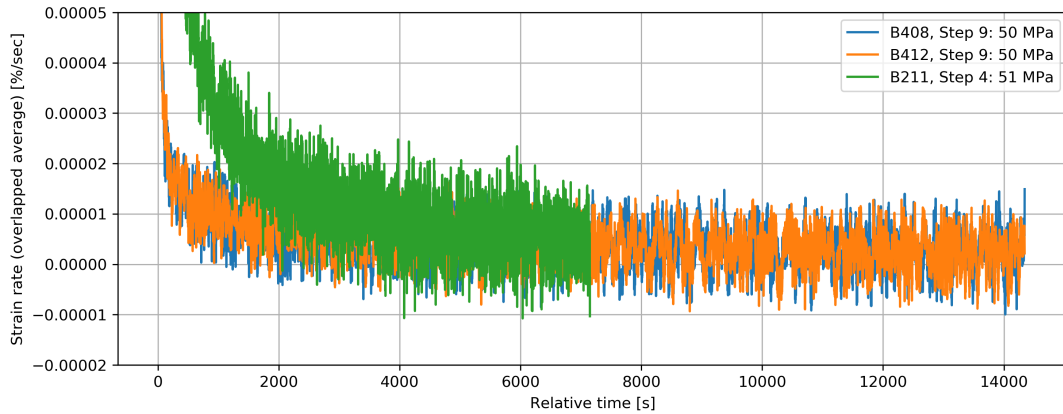


Figure 8.13: Comparing the strain rates for a similar stress level of about 50 MPa for the large stress increment test (sample B211) and the small stress increment test (samples B408 and B412)

The literature also lacks clarity on whether virtual starting times should be extrapolated to zero total strain or to zero creep strain of the reference stress step. Some figures suggested that researchers favour extrapolation to zero creep strain, effectively ignoring the initial strain of the reference step. In this study, both methods were tested, and extrapolation to zero creep strain consistently produced better results for a smoother creep master curve. Extrapolating a polynomial fit back to zero total strain often gave the second load step a negative virtual starting time, creating inconsistencies. However, as explained in section 4.2, some researchers perform an initial vertical shift to eliminate initial strains, accounting for deformations in the testing setup and creating a new baseline. In this research, the strain was measured directly on the sample, making these initial adjustments unnecessary. Nevertheless, applying an initial vertical shift to align the baseline with zero creep strain (with respect to the reference stress step), rather than zero total strain, may improve the extrapolation of virtual starting times.

It could be argued that the initial elastic strain of the reference stress step should not be removed from the final creep master curve, as it represents an inherent part of the typical creep curve (as visualized in figure 3.1). Instead, the baseline for extrapolating virtual starting times should align with the strain value marking the start of the primary creep phase in the reference step. This approach preserves the initial elastic strain in the final creep master curve while ensuring it is distinguished from creep strain during extrapolation.

SSM Data Processing: Horizontal Shift

In the horizontal shift step, the timescale is set to a logarithmic scale, and the individual creep curves are shifted accordingly using the horizontal shifting factor α_σ . This factor is calculated based on the strain rate, i.e. the slope of the secondary creep portion of each step's creep curve. In this study, a linear fit was applied to the last 80% of the strain data for each step (the secondary creep region) to determine its slope. This approach, however, is highly sensitive to errors caused by force instability or inaccuracies in curve fitting, which can significantly affect the results. Because the slopes are such small values, even a minor error or difference in the found slope can have a large effect on the horizontal shifting factor.

A more reliable and robust method for determining the horizontal shifting factor could involve the Eyring equation (equation 4.2 on page 24). However, the activation volume required for this calculation is unknown and appears to depend on the applied stress rather than being a constant material property. By calculating the horizontal shifting factor using the strain rate ratio, the activation volume could be reverse-engineered to explore potential relationships between applied stress, activation volume, and horizontal shifting factors (see equation 8.3, rewritten Eyring model equation to reverse-calculate the activation volume based on equation 4.2 on page 24). Further research is needed to clarify these relationships and learn more about the activation volume. If the activation volume is a constant for a given stress, the Eyring equation provides a straightforward calculation of the horizontal shifting factor. However, if the activation volume also depends on the stress history of the material, the situation becomes more complex. In contrast, for the stepped isothermal methods (SIM), the Arrhenius equation (equation 3.7, on page 20) uses the activation energy, which is typically considered as a material constant, making the SIM's horizontal shifting step less empirical and more systematic to calculate.

$$V^* = \frac{2.303kT}{\sigma - \sigma_r} \log(\alpha_\sigma) \quad (8.3)$$

Another observation regarding the horizontal shift is that the shifting factor for the final steps often deviates from earlier steps. This difference likely arises from variations in the duration of this last step (which was set to continue for a longer period if the sample had not failed within the normal dwell time) and the calculation of its slope. For instance, if the sample fails shortly after the stress has increased, the slope is often steeper and the secondary creep region may not have been reached. The step might then be neglected when constructing the creep master curve. Conversely, if the sample sustains the force over a longer period than the set dwell time of all other steps, the secondary creep region is much longer, resulting in a shallower slope. Since the horizontal shifting factor depends on the ratio of the slope to the slope of the reference stress step, these variations result in an inconsistent ratio compared to the other steps. Figure H.4 in appendix H.3 illustrates this phenomenon for layout A's constructed master creep curves on a full timescale. In the curves of samples A414 and A420, the final steps have a shorter dwell time than the standard four hours, leading to a steeper slope and, therefore, a larger horizontal shift factor. Conversely, in the tests of A204 and A223, the final steps had longer dwell times than the standard two hours, calculating the slope over the last 80% of data of these extended steps produced shallower slopes, thereby reducing the horizontal shifting factor. This inconsistency is visible in figure H.4, where the last steps are misaligned with the earlier ones. Layout B, in figure H.5, shows fewer issues with this misalignment because the final steps maintain a similar dwell time as the earlier steps.

These findings show that determining the horizontal shifting factor from slopes alone is insufficient unless all slopes are calculated over consistent timeframes. The selected portion of the curve, used to determine the slope, significantly affects the resulting creep master curve. Alternative methods, such as the visual approach or employing the activation volume (if known), would mitigate the impact of different dwell times on the final steps.

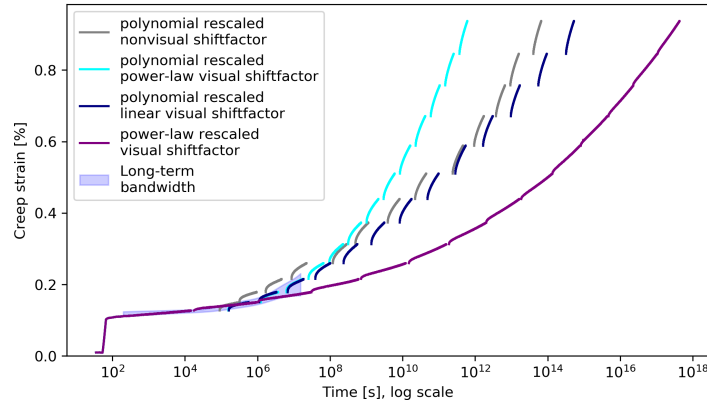
The literature does not provide clear guidance on how the horizontal shifting factor should be applied to the individual creep curves. The horizontal shifting factor is often referred to as a $\log(\alpha_\sigma)$ due to its derivation from the Eyring model. This gives the impression that the shift factor is applied additively within the logarithmic framework. However, experimental results showed that the horizontal shifting factor is applied outside the logarithm, as described by equation 8.1. On a linear timescale, this corresponds to a scalar of 10^{α_σ} , as shown in equation 8.4. On a logarithmic timescale, the final step in the SSM data processing appears as a horizontal shift, while on a linear timescale, it functions as a scalar transformation.

In previous studies, the horizontal shift was often performed visually, adjusting the rescaled curves to create a smooth master curve. However, after experimentation with the visual method, this approach seemed subjective and could yield different outcomes depending on the person and the method used. For instance, with a polynomial rescaling fit, larger gaps appear between the individual creep curves, making visual alignment more difficult, whereas a power-law rescaling fit produces more stretched curves that are easier to align visually. Moreover, curves with larger stress increments also exhibit a larger spacing between the steps than those with smaller stress increments, making the visual shift more straightforward for the latter ones. These variations demonstrate the arbitrary nature of the visual method.

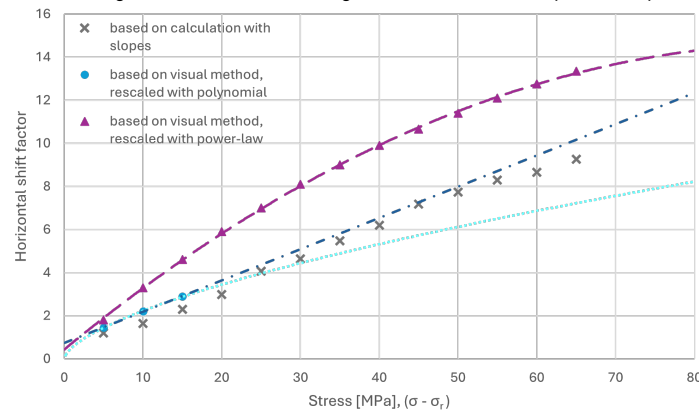
To mitigate its subjectivity, the visual shift is often cross-validated using the Eyring model, which attempts to establish a relationship between the horizontal shifting factor and the applied stress (as discussed in section 4.2.4 and table 4.1, in chapter 4). However, the nature of this relationship remains uncertain, with some studies suggesting a linear trend and others indicating a parabolic or power-law behaviour. If the activation volume depends on stress, a non-linear relationship between the horizontal shift factor and the applied stress is more likely than a linear one. Figure 8.14a shows experimental results of visually shifting the SSM creep curves of sample B412, rescaled with a polynomial fit. The visual shift is based on the creep bandwidth found in the long-term creep tests (visualized as the blue mesh in the figure). The first three steps were adjusted to align with the creep behaviour observed in the long-term test. The shifting factors were plotted against the applied stress, similar to figure 8.14b, and were extrapolated using a linear and power-law function to find the horizontal shift factors for the higher

stress steps. Figure 8.14 shows that a different relation between the shifting factor and the stress gives a different constructed creep master curve. Additionally, a visually shifted power-law rescaled curve of sample B412 is plotted in figure 8.14a. The stretched curves are visually aligned sequentially, forming a smooth line. A polynomial relationship is found between these horizontal shifting factors and the stress, creating a distinct creep master curve for the same sample, which still fits within the long-term creep bandwidth.

While the horizontal shifting factors derived from slope calculations may suggest a linear relationship with the applied stress, this does not confirm the superiority of the linear approach. Instead, it shows the sensitivity of SSM data processing choices and the subjective nature of visual shifting. A real-time creep test is essential for validating the reliability of the SSM-constructed creep master curves, especially when using the visual method for the horizontal shift.



(a) Different visual shifts of the rescaled curves of sample B412, with small stress steps. The polynomial-based rescaled curves are visually shifted along a power-law and linear relation between the shifting factor and the stress, and a power-law-based rescaled curve is shifted based on the start and ends of the stretched curves. As a reference, the curve resulting from the calculated shifting factors based on the slopes is also plotted



(b) Relation between the horizontal shifting factor and the applied stress. Note that the stress is expressed as the applied stress minus the reference stress (10 MPa)

Figure 8.14: Comparison of different visual horizontal shifts of the curves of sample B412

Sensitivity Of Rescaling Method And Horizontal Shifting Factor

The sensitivity of the rescaling method and horizontal shifting factor significantly impact the construction of the SSM creep master curve. From figure 8.9, it is evident that the choice of rescaling curve fit and determination of the virtual starting time strongly influence the shape of the individual curves, but have less of an effect on the final curve positions. Conversely, the horizontal shifting factor primarily dictates the horizontal alignment of the curves.

Equation 8.1 expresses the horizontal shift as a logarithmic function, which can be rewritten in linear terms to show how the virtual starting time (t_{virtual}) and the horizontal shifting factor (α_{σ}) affect the construction of the creep master curve. On a linear timescale, equation 8.1 can be rewritten as:

$t_{i,\text{master}} = t_{i,\text{rescaled}} \cdot 10^{\alpha_{\sigma_i}}$. Filling in that $t_{i,\text{rescaled}} = t_{i,\text{original}} - t_{i,\text{virtual}}$, the influence of the virtual starting time and the horizontal shifting factor, on the final constructed creep master curve, become more clear in equation 8.4.

$$t_{i,\text{master}} = (t_{i,\text{original}} - t_{i,\text{virtual}}) \cdot 10^{\alpha_{\sigma_i}} \quad (8.4)$$

With:

- $t_{i,\text{master}}$ = time of the creep curve for load step i in the constructed SSM creep master curve
- $t_{i,\text{original}}$ = original time of a load step i in the SSM test
- $t_{i,\text{virtual}}$ = virtual starting time for load step i
- α_{σ_i} = horizontal shift factor for load step i

Equation 8.4 shows that the virtual starting time, determined by the rescaling curve fit, serves as an additive adjustment along the timescale. A higher t_{virtual} reduces t_{master} , compressing the creep master curve on a linear timescale. However, on a logarithmic timescale, a higher t_{virtual} results in a horizontally more stretched curve, as smaller values are expanded over a larger range in logarithmic space. It results in the appearance of a slower time evolution as the curves are stretched. Conversely, a lower t_{virtual} expands t_{master} on a linear timescale but compresses the curves on the logarithmic scale, where larger values appear more condensed. As a result, the individual creep curves will seem more compressed and progress faster on a logarithmic timescale. These effects, illustrated in figure 8.1, demonstrate the visual impact that small changes in t_{virtual} can have on a logarithmic timescale.

The horizontal shifting factor, α_{σ} , is an exponential scaling term, amplifying t_{master} multiplicatively (see equation 8.4). Small variations of α_{σ} result in significant changes of t_{master} due to the shifting factor's exponential nature. A higher horizontal shifting factor will exponentially increase t_{master} and stretch the curve further in time. For instance, an error of $+0.1$ in α_{σ} increases the multiplication factor $10^{\alpha_{\sigma}}$ by almost 26%, while a change of $+0.3$ nearly doubles it. On a logarithmic scale, α_{σ} ensures a uniform shift over the horizontal time axis. A larger horizontal shifting factor shifts the curves further on the time axis and, therefore, extends the creep time. The exponential influence amplifies the sensitivity of α_{σ} in positioning the curves along the time axis.

Interactions between t_{virtual} and α_{σ} further amplify their combined effect. The term $t_{\text{original}} - t_{\text{virtual}}$ is linearly influenced by t_{virtual} , but its impact is magnified exponentially by $10^{\alpha_{\sigma}}$. Consequently, even small errors or differences in t_{virtual} or α_{σ} can substantially alter t_{master} .

The sensitivity of α_{σ} is particularly evident when different methods for its calculation are compared. In this study, this factor was determined by dividing the slope of the creep curve at a given load step by the slope of the reference step. Because the slopes are very small numbers, the method used to calculate them significantly impacts the outcome. Currently, the slopes were computed by a linear curve fit over the final 80% of the data for each step. However, using a shorter portion of the data, such as the last 60% or 40%, results in significant differences, especially at higher load steps, but it also impacts the slopes of lower load steps. Table 8.2 illustrates this variation of shifting factors for sample B211, showing that especially the shifting factors, derived from slopes based on the last 80% and 40% of the data, differ significantly. Even the relatively smaller differences between the calculation based on the last 80% and 60% of the data result in a large exponential change in the multiplication factor $10^{\alpha_{\sigma}}$, ranging from 200% to 400%.

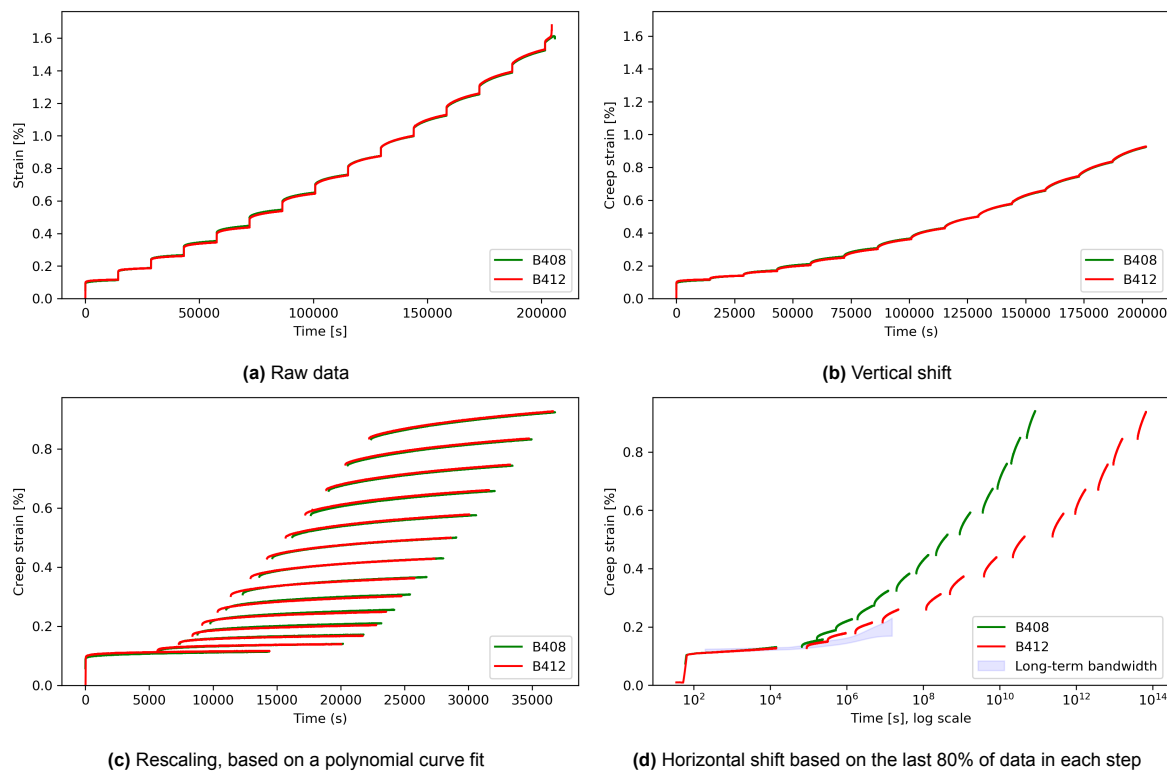
Since these slopes are very small, even minor discrepancies or errors in their determination can have a significant effect on the horizontal shifts. For instance, figure 8.15 compares the consistency of the SSM test curves with small stress increments for layout B (Q1). While the curves are very consistent before applying the horizontal shift, they diverge noticeably afterwards. Table 8.3 illustrates this issue, comparing the slopes (all based on the last 80% of data for each step) and the corresponding shifting factors for the first seven steps in the curves of samples B408 and B412.

The slope of the first step, which serves as the reference strain rate in the denominator for calculating α_{σ} (see equation 8.2), already differs between the two curves, introducing discrepancies in all subsequent shifting factors. As explained above, a small change in α_{σ} has a pronounced effect on multiplication factor $10^{\alpha_{\sigma}}$ (an increase of $+0.1$ of α_{σ} increases multiplication factor $10^{\alpha_{\sigma}}$ by almost 26%). Looking at the second step in table 8.3, the shifting factor α_{σ} differs by 0.14 between samples B408 and B412, corresponding to a 38% difference in the multiplication factor $10^{\alpha_{\sigma}}$. By the seventh step,

Table 8.2: Comparing the slopes and horizontal shifting factors (α_σ) for the same sample (B211), when using different parts of the curves (the last 80%, 60%, and 40% of the curves) to fit the linear function

Part of curve	80%		60%		40%	
	slope	α_σ	slope	α_σ	slope	α_σ
Step 1	1.013×10^{-6}	-	7.686×10^{-7}	-	5.011×10^{-7}	-
Step 2	2.113×10^{-6}	2.085	2.005×10^{-6}	2.608	2.312×10^{-6}	4.613
Step 3	5.671×10^{-6}	5.597	4.765×10^{-6}	6.200	4.304×10^{-6}	8.589
Step 4	8.832×10^{-6}	8.715	7.170×10^{-6}	9.329	6.175×10^{-6}	12.323
Step 5	1.221×10^{-5}	12.052	9.850×10^{-6}	12.815	8.575×10^{-6}	17.113
Step 6	1.345×10^{-5}	13.269	1.194×10^{-5}	15.528	1.172×10^{-5}	23.390

this difference in α_σ grows to 1.43, resulting in a 2600% difference in the multiplication factor. This exponential growth underscores the importance of minimizing errors and ensuring consistency in the calculation of the horizontal shifting factor α_σ .

**Figure 8.15:** Comparison of the SSM data processing steps for two tests with small stress increments (samples B408 and B412), showing that the curves remain consistent until the horizontal shift, after which they diverge significantly.

Noise in the force signal during testing can further affect the slope calculations of the individual creep curves, introducing additional uncertainties. Averaging the strain rate helps mitigate the noise, but this remains an approximation prone to errors. To reduce the sensitivity in the horizontal shifting factor, understanding the exact relationship between the activation volume and the applied stress is essential. Further research is needed to better understand the activation volume and its implications.

In summary, on a logarithmic timescale, the horizontal shifting factor mainly determines the curve alignment and its position in time, while the virtual starting time influences curve stretching. A higher virtual starting time stretches the curves more, reducing the gaps between the steps and producing a visually smoother creep master curve. However, this does not guarantee closer alignment with the actual creep master curve, emphasizing the importance of method consistency and the need for further validation.

Table 8.3: Comparison of slopes and α_σ values for the first seven steps of B408 and B412

Sample	B408		B412	
	slope	α_σ	slope	α_σ
Step 1	7.697×10^{-7}	-	5.301×10^{-7}	-
Step 2	8.226×10^{-7}	1.069	6.386×10^{-7}	1.205
Step 3	1.042×10^{-6}	1.353	8.683×10^{-7}	1.638
Step 4	1.365×10^{-6}	1.773	1.221×10^{-6}	2.304
Step 5	1.765×10^{-6}	2.293	1.578×10^{-6}	2.977
Step 6	2.062×10^{-6}	2.679	2.154×10^{-6}	4.063
Step 7	2.472×10^{-6}	3.211	2.461×10^{-6}	4.643

8.5. Conclusion

The stepped isostress method (SSM) has been utilized both as an accelerated creep test to predict the long-term creep behaviour of a flax fibre polymer reinforced composite and as a framework for evaluating its methodology and data processing steps. This study demonstrates that certain challenges and limitations need to be addressed for greater reliability and accuracy in the SSM.

Failure mechanisms observed during the SSM tests showed the sensitivity of unidirectional layups to stress concentrations, indicating the need for improved clamping methods to avoid premature failure. Furthermore, environmental factors, such as temperature and relative humidity fluctuations, introduced variability that could affect the consistency and reliability of the results.

The final SSM creep master curves showed that the method can provide an idea of the creep master curve, although it tends to overestimate the creep deformation compared to the results of real-time creep tests. For a low reference stress, progressing to the material's creep failure is less relevant, as this often exceeds the realistic lifespan of a structure. Instead, the focus should shift to the creep deformation behaviour, which is better achieved using smaller stress increments. A longer dwell time provides a larger portion of secondary creep, which is especially important for larger stress steps to ensure that the secondary creep phase is sufficiently captured for determining the slope of this region. Ensuring a balance between conservativeness and time efficiency in the SSM procedure is crucial for optimizing the test's practical applicability.

A critical observation from this study is that the SSM data handling procedure is largely empirical and involves subjective decisions that influence the results. For example, the selection of curve-fitting methods during the rescaling step and the approach used to determine the horizontal shift significantly influence the final SSM constructed creep master curve. The rescaling curve fit and virtual starting time primarily affect the shape of the curves, and the horizontal factor determines the alignment of the curves and their position in time. While this study aims to establish systematic procedures for the SSM data processing steps, their reliance on assumptions and visual adjustments makes the process inherently arbitrary. A more robust and objective methodology is required, particularly for determining the horizontal shifting factors and ensuring an accurate alignment of the data across different stress increments and dwell times. Therefore, a better understanding of the activation volume seems to be a critical step in achieving methodological consistency and improving the reliability of SSM-based predictions.

Overall, this study emphasizes the importance of optimizing SSM test parameters and addressing equipment and environmental limitations to improve the method's accuracy. Further research is recommended to refine the methodology, particularly by addressing the empirical aspects of the data handling steps and understanding the role of the activation volume in creep behaviour. By addressing these challenges, the SSM has the potential to be an efficient method for accelerated creep testing of flax fibre composites.

Part IV

Conclusion and Recommendations

9

Conclusion

This research evaluates the stepped isostress method (SSM) as an accelerated creep test approach for predicting the long-term creep behaviour of a flax fibre-reinforced polymer composite. It aims to contribute to the transition toward more renewable construction materials in the building industry. A literature review, experimental tests, and data analysis were conducted to address the research questions for this study. The conclusions of this research are presented by systematically answering the sub-questions and ultimately, the main research question. The first three sub-questions are answered by the literature review in part I, and the other questions are answered by experimental research and data analysis in part III.

1. How does the structural composition of flax fibres affect the creep behaviour of flax fibre-reinforced polymer composites?

Unlike synthetic fibre composites, where creep is primarily governed by the polymer matrix, flax fibres themselves exhibit significant creep deformation in the fibre direction due to their microstructural composition, even under relatively low loads. Flax fibres are composed of cellulose, hemicellulose, lignin, pectin, wax, and water. The cellulose microfibrils, which are the main load-bearing component, are embedded within a viscoelastic matrix of hemicellulose and pectin. These microfibrils are helically aligned at an angle of approximately 10° to the fibre axis, allowing for shear-induced realignment when put under a constant load. This gradual reorientation contributes to the time-dependent creep deformation. At the fibre bundle level, technical flax fibres also exhibit a helical alignment. Similar to the microfibrils within the fibre structure, these fibre bundles can progressively realign within the polymer matrix of the composite when subjected to a constant stress. As a result, creep in the fibre direction is more pronounced in flax fibre-reinforced polymer composites than in synthetic alternatives, where creep typically occurs in the off-axis direction, governed by the polymer matrix rather than the fibres themselves.

2. Which parameters play a significant role in influencing the creep behaviour of flax fibre-reinforced polymer composites?

The creep behaviour of flax fibre composites is influenced by both internal and external factors. Internally, the creep behaviour is influenced by the fibre structure and the viscoelasticity of the matrix material. Both flax fibres and unsaturated polyester resins have viscoelastic properties. In polyester resin, molecular chains can stretch, realign, and slide over time, contributing to creep deformation. In flax fibres, the helical alignment of cellulose microfibrils within the pectin matrix allows for time-dependent shear deformation under constant loading, causing the cellulose fibrils to realign even at low stresses. The manufacturing process of the technical fibres, such as twisting fibres into bundles, can introduce small misalignments of the elementary fibres to the technical fibre axis, leading to shear stresses at the fibre-matrix interface, further contributing to creep deformations. These properties make flax fibre composites more susceptible to creep in the fibre direction than composites reinforced with synthetic fibres such as glass or carbon fibres.

External factors, such as temperature, moisture, UV light, and the applied stress, also influence the creep behaviour of flax fibre composites. Especially the material's sensitivity to temperature was

observed in this research. Even a minor temperature increase of 4-5°C caused irreversible acceleration in creep strain. Restabilizing the temperature to its original value did not mitigate this effect, indicating a high sensitivity of the material to thermal variations.

3a. What are the prevailing industry standards and testing protocols for estimating creep behaviour in composite materials?

For fibre-reinforced polymers, a new Eurocode (CEN/TS 19101, 2022) has been published, addressing synthetic fibres but excludes natural fibres. For composites reinforced with natural fibres, creep coefficients must be determined experimentally. Commonly, the (ASTM D2990-09, 2009) standard for plastics is applied, although it is not specific to natural fibres. Recommendations for the stepped isothermal method (SIM) are given in the ASTM D6992-16 (2023), but again these are not standardized for natural fibre composites. In the Netherlands, the CUR 96 (2019) provides extra guidelines for building with fibre-reinforced composites, including an appendix with specific guidelines for natural fibres, with numerical examples for flax fibre epoxy composites.

3b. How well do these standards apply to flax fibre composites, and are there unique characteristics requiring tailored testing standards and protocols for an accurate creep assessment?

The existing standards primarily focus on synthetic fibre composites, such as carbon and glass fibres. In synthetic fibre composites, creep is dominated by the matrix material and creep deformation in the fibre direction is minimal. In contrast, flax fibres exhibit significant creep deformation in the fibre direction due to their molecular structure. Therefore, it is important to assess not only creep damage and failure for ultimate limit states but also creep deformation for serviceability limit states. Besides, natural fibres are more prone to environmental degradation by moisture, temperature, and UV light than synthetic fibres. Natural fibres, including flax, have an inherently natural variability due to growth conditions and manufacturing processes, unlike the consistent properties of synthetic fibres. Therefore, design codes for natural fibres must account for this variability. Tailored testing standards are required to accurately capture the creep deformation and damage mechanisms specific to flax fibre composites.

4. What factors contribute to variations in the accuracy of the stepped isostress method when predicting creep behaviour for different flax fibre composite layup configurations?

The accuracy of the stepped isostress method (SSM) depends on several factors related to both the testing methodology and the data handling procedure. Variations in the test setup, particularly temperature fluctuations, significantly impact its accuracy. Temperature effects are not accounted for in the data processing and are instead misinterpreted as creep strain in the master creep curve. This research observed extreme sensitivity of the flax fibre composite material to temperature, with variations as small as $\pm 1^\circ\text{C}$ visibly affecting the curves. Additionally, the hydrophilic nature of flax fibres makes the composite susceptible to moisture uptake, leading to fibre swelling and potential matrix damage. These effects may differ across laminate configurations, further complicating the analysis. Consequently, maintaining a stable testing environment, including precise and reliable climate and force control, is critical for reducing noise and obtaining accurate results.

Another factor, influencing the SSM's accuracy, is the duration of the dwell time for achieving a developed secondary creep phase in each stress step. The optimal dwell time may vary depending on the laminate configuration, which can influence the accuracy of the rescaling curve fits and horizontal shifting factors. Additionally, poor specimen clamping can lead to premature failure, which is especially important to pay attention to when investigating creep failure and unidirectional (UD) layups.

In terms of data handling procedure, the visual shifting method, commonly used in previous studies using SSM analyses, introduces subjectivity. In literature, the validation of visual shifts typically relies on two criteria: the formation of a smooth creep master curve and a recognizable relationship between the horizontal shift factor and the applied stress. However, different ideas exist regarding the nature of this relationship. As demonstrated in figure 8.14 on page 79, applying different visual shifting methods can produce divergent master creep curves.

Another factor that influences the accuracy of the SSM, is the assumption of the secondary creep portion. A more precise definition improves the calculation of secondary creep rates and, consequently, the horizontal shifting factors. However, an even more robust approach would involve basing the horizontal shifting factor on the activation volume's relationship with the applied stress, rather than relying

on strain rates. More research is needed to develop an objective approach to identify the secondary creep region of each individual creep curve resulting from an SSM test or on the activation volume and its relation with the applied stress, to improve the accuracy of the horizontal shift in the SSM.

5. What are the advantages and limitations of the stepped isostress method as an accelerated creep test method, compared to other creep testing methods, for a flax fibre-reinforced polymer composite, and what is the impact of its layup configuration?

The main advantage of the stepped isostress method (SSM) is its time efficiency compared to conventional creep tests, which often require months or years to complete. One SSM can be conducted within one or two days, and with the aid of an automated data processing script, the data can be processed quickly into a creep master curve spanning a much longer timescale. Additionally, the SSM test requires only a single material sample to construct a creep master curve, significantly reducing both the time and resources needed for testing. Compared to the stepped isothermal method (SIM), the SSM has the advantage of using a constant temperature during the test, which may be required for materials that are very sensitive to or dependent on temperature, such as flax fibre composites.

However, the SSM has notable limitations. It is an empirical method relying on assumptions, and there is no standardized data handling procedure, leaving certain steps in the analysis subjective. For instance, the data processing model used in this research, while functional, was based on rough assumptions. A more refined script could potentially improve the accuracy of the constructed creep master curves. Nevertheless, even with a more sophisticated data handling procedure, decisions such as the rescaling curve fit and the visual shift will continue to rely on subjective choices. Furthermore, the method extrapolates the long-term creep behaviour based on short-term data, making it vulnerable to errors in testing or assumptions that could result in inaccurate creep master curves. Stress history dependency effects could further complicate the analysis, as varying stress increments could then lead to differing creep master curves and eventually to a different relation between the horizontal shifting factor and the applied stress. This relation involves the activation volume, which is an unknown parameter in this context. Comparing the SSM horizontal shift with the horizontal shift in the stepped isothermal method, the activation energy is a measurable material property which is a material constant in the horizontal shift. These uncertainties make validation of SSM results through conventional creep tests necessary. Moreover, additional research is required to establish a robust and standardized framework for SSM data handling, tailored for different material types.

Now the main research question can be answered:

To what extent does the stepped isostress method provide a reliable prediction of the long-term creep behaviour of flax fibre-reinforced polymer composites across different laminate layup configurations?

Based on the findings of this research, the stepped isostress method (SSM) cannot be considered a fully reliable tool for predicting the long-term creep behaviour of flax fibre composites. The method is highly dependent on subjective choices, assumptions, testing methodology, and noise in the data, which undermines its reliability.

That said, the SSM provides a general indication of creep progression and often results in conservative predictions. For example, based on the findings in this study, the results suggest that a flax fibre composite subjected to a creep stress of 10 MPa would not experience creep failure within 100 years, excluding other forms of material degradation. However, the exact progression of the creep master curve remains uncertain, requiring additional validation through long-term creep tests. Such validation would enhance the reliability of SSM predictions and provide a better understanding of the method's applicability.

This research found no clear evidence that the reliability of SSM predictions varies across different laminate layup configurations. Nevertheless, it is recommended to further verify this observation, as some layups depend more heavily on the matrix behaviour for creep, while others rely primarily on fibre properties. It is possible that the method performs better for certain layups, but this cannot yet be stated conclusively.

Based on this study, the SSM, in its current state, is not sufficiently reliable to replace conventional long-term creep tests for structural material characterization. However, it holds significant potential as

a time-efficient tool for preliminary investigations into the creep behaviour of innovative materials. To realize this potential, further research is necessary to refine and standardize the method and adapt it specifically for flax fibre composites. Therefore, the main point of research is to improve the reliability of the horizontal shift by finding the relation between the activation volume and the applied stress. Additionally, testing different dwell times and different stress increments in SSM tests can improve the standardization of the test methodology and our understanding of the method.

In conclusion, this research did not resolve the challenge of finding a reliable accelerated method for accurately predicting the long-term creep behaviour of flax fibre composites. However, it contributes to a better understanding of the stepped isostress method as an accelerated creep test method to study creep deformation, and it identified some of the method's uncertainties and limitations. The study advances efforts towards standardizing the SSM data handling procedure and testing methodology. Furthermore, this research aims to inspire continued efforts in the field of bio-based construction materials, to stimulate a more sustainable building industry. A better understanding of the creep behaviour of flax fibre composites is essential for enabling more economical structural designs and increasing the material's appeal as a sustainable option for construction materials.

10

Recommendations

The recommendations following from this research are summarized in bullet points and structured in four categories.

Recommendations: General bio-composites

- Further research into fully bio-based composites, next step is a fully bio-based resin or a way of separating fibres and resin after use, to improve recycling of the composite
- Improvements of construction methods of bio-composite structural components, as it is now fairly labour-intensive

Recommendations: General (tensile) testing of flax fibre-reinforced polymer composites

- Ensure a reliable climate-controlled environment, flax fibre composite is especially sensitive to temperature fluctuations (even an offset of 1°C can influence the test results), the recommendation of a maximum of 2°C in ASTM D2990-09 (2009) is in some cases too lenient
- Pay attention to clamping methods, especially for UD layups to avoid clamping failure (e.g. using end tabs)
- Minimize noise in machine signals (such as force control) due to external factors and choose an appropriate load cell for the tested material
- Consider using the same measurement devices, equipment, and settings when performing different types of tests, to avoid discrepancies caused by the machine or equipment characteristics
- When using strain gauges to measure the deformations, pay attention to the voltage, and the possibility of heating of the strain gauge, eventually perform preliminary tests and measure the heat effect of the strain gauge in an unloaded sample at different voltages
- Further research on the transversal strain in axial testing, for Poisson ratio in tensile tests and creep tests, comparing different layup configurations

Recommendations: Long-term creep testing in flax fibre composites

- Further research into creep damage mechanisms under low creep stresses over an extended period of time (think of years)
- Pay special attention to a reliable climate control system in long-term tests, as a failure in the system can irreversibly affect the results, which is extremely unfortunate as the test might need to be redone
- Based on the experiences in this research, it is recommended to immediately replace disrupted samples in long-term tests with new ones, as the disruptions may not be compensable, be prepared for disruptions (e.g. by preparing extra samples)
- Building on the material's sensitivity to temperature, future research could investigate its creep behaviour under temperature cycles, such as day/night or sun/shadow variations, which reflect the conditions experienced by real structures

Recommendations: Stepped isostress method and flax fibre composites

- Further research on the activation volume and its relation with the applied stress, potentially to ensure a more reliable horizontal shift in SSM data processing
- Further standardize the SSM tests and data processing procedure
- Use small stress increments for the SSM steps (increments in this study were too large)
- If starting at a low reference stress, consider whether it is interesting to test up to creep failure, as this might be unrealistically far in the future
- Ensure a long enough dwell time to have a well-developed secondary creep portion in each stress step (two hours in this research was slightly too short)
- For testing to creep failure in flax fibre-reinforced polymer composites, aim for 75% to 80% of the GUTS in the final stress step, instead of 90% of GUTS
- During SSM tests, monitor the target force simultaneously with the measured applied force, to identify the machine noise and the ramp to the next step
- Try different reference stresses and study how the horizontal shift relates to the applied stress

References

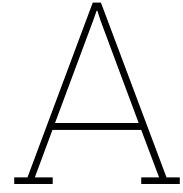
- Abbood, I. S., Odaa, S. A., Hasan, K. F., & Jasim, M. A. (2021). Properties evaluation of fiber reinforced polymers and their constituent materials used in structures - a review. *Materials Today: Proceedings*, 43, 1003–1008. <https://doi.org/10.1016/J.MATPR.2020.07.636>
- Accu. (n.d.). *Metric thread dimensions for iso standard screws and bolts - bolt sizes chart for m1.6 to m69 screws*. Retrieved February 12, 2024, from <https://www.accu.co.uk/p/117-iso-metric-thread-dimensions>
- Achereiner, F., Engelsing, K., Bastian, M., & Heidemeyer, P. (2013). Accelerated creep testing of polymers using the stepped isothermal method. *Polymer Testing*, 32, 447–454. <https://doi.org/10.1016/J.POLYMERTESTING.2013.01.014>
- Afzir. (2023, May). Bidirectional Glass Wrap. <https://afzir.com/en/products/glass-fabric/>
- Ascione, L., Berardi, V. P., & D'Aponte, A. (2012). Creep phenomena in frp materials. *Mechanics Research Communications*, 43, 15–21. <https://doi.org/10.1016/J.MECHRESCOM.2012.03.010>
- ASTM D2990-09. (2009). *Standard Test Method for Tensile, Compressive, and Flexural Creep and creep-rupture of Plastics* (Standard). American Society for Testing and Materials.
- ASTM D3039. (2002, December). *Standard Test Method for Tensile Properties of Polymer Matrix Composite Materials* (Standard). American Society for Testing and Materials.
- ASTM D6992-16. (2023). *Standard Test Method for Accelerated Tensile Creep and Creep-Rupture of Geosynthetic Materials Based on Time-Temperature Superposition Using the Stepped Isothermal Method* (Standard). American Society for Testing and Materials.
- Azwa, Z., Yousif, B., Manalo, A., & Karunasena, W. (2013). A review on the degradability of polymeric composites based on natural fibres. *Materials & Design*, 47, 424–442. <https://doi.org/https://doi.org/10.1016/j.matdes.2012.11.025>
- Baley, C., Gomina, M., Breard, J., Bourmaud, A., & Davies, P. (2020, March). Variability of mechanical properties of flax fibres for composite reinforcement. a review. <https://doi.org/10.1016/j.indcrop.2019.111984>
- Bcomp. (n.d.). ampliTex, Bcomp. <https://www.bcomp.com/products/amplitex/>
- Blok, R., Smits, J., Gkaidatzis, R., & Teuffel, P. (2019). Bio-Based Composite Footbridge: design, production and in situ monitoring. *Structural Engineering International*, 29(3), 453–465. <https://doi.org/10.1080/10168664.2019.1608137>
- Blum, W., Eisenlohr, P., & Breutinger, F. (2002). Understanding creep - a review. *Metallurgical and Materials Transactions A: Physical Metallurgy and Materials Science*, 33, 291–303. <https://doi.org/10.1007/S11661-002-0090-9/METRICS>
- Boyer, R. F. (1968). Dependence of mechanical properties on molecular motion in polymers. *Polymer Engineering & Science*, 8, 161–185. <https://doi.org/10.1002/PEN.760080302>
- Brostow, W. (2000). Time-stress correspondence in viscoelastic materials: An equation for the stress and temperature shift factor. *Materials Research Innovations*, 3, 347–351. <https://doi.org/10.1007/s100190000054>
- CA Composites Limited. (2019, November). Kevlar Fabric | CA Composites. <https://cacomposites.com/aramid-fiber-reinforcements/kevlar-fabric/>
- CEN/TS 19101. (2022, February). *Design of fibre-polymer composite structures* (Standard). European Committee for Standardization.
- Charlet, K., Eve, S., Jernot, J. P., Gomina, M., & Breard, J. (2009). Tensile deformation of a flax fiber. *Procedia Engineering*, 1, 233–236. <https://doi.org/10.1016/j.proeng.2009.06.055>
- Claassen, W., & Veltkamp, M. (2022). Lessons Learned van bruggen bouwen met biocomposiet. *Symposium Fiets+Voetbruggen*. <https://bruggenstichting.nl/images/Symposium2022/presentaties/Presentatie-MartijnVeltkamp-WouterClaassen.pdf>
- Claassen, W., & Zarifis, G. (2020). First Bio-Based Composite Movable bicycle bridge. *Structural Engineering International*, 31(2), 227–232. <https://doi.org/10.1080/10168664.2020.1840945>
- CUR 96. (2019, November). *Fibre-reinforced polymers in buildings and civil engineering structures* (CROW-CUR Recommendation 96:2019). CROW.

- Dittenber, D. B., & Gangarao, H. V. (2012). Critical review of recent publications on use of natural composites in infrastructure. *Composites Part A: Applied Science and Manufacturing*, *43*, 1419–1429. <https://doi.org/10.1016/J.COMPOSITESA.2011.11.019>
- Dlubal Software. (n.d.). *Cross-section properties & analysis | dlubal software*. <https://www.dlubal.com/en/cross-section-properties/shs-40x40x3-en-10219-2-voestalpine>
- Elfaleh, I., Abbassi, F., Habibi, M., Ahmad, F., Guedri, M., Nasri, M., & Garnier, C. (2023). A comprehensive review of natural fibers and their composites: An eco-friendly alternative to conventional materials. *Results in Engineering*, *19*, 101271. <https://doi.org/10.1016/J.RINENG.2023.101271>
- Eurocomp. (1996). *Structural design of polymer composites: Eurocomp design code and handbook* (J. Clarke, Ed.). E; FN Spon.
- Findley, W. N., Lai, J. S., & Onaran, K. (1989). *Creep and relaxation of nonlinear viscoelastic materials : With an introduction to linear viscoelasticity*. Dover.
- Giannopoulos, I. P., & Burgoyne, C. J. (2011). Prediction of the long-term behaviour of high modulus fibres using the stepped isostress method (ssm). *Journal of Materials Science*, *46*, 7660–7671. <https://doi.org/10.1007/s10853-011-5743-x>
- Giuliani, P. M., Giannini, O., & Panciroli, R. (2023). Creep and stress relaxation of unidirectional flax fiber reinforced laminates. *Composite Structures*, *310*, 116755. <https://doi.org/10.1016/J.COMPSTRUCT.2023.116755>
- Goertzen, W. K., & Kessler, M. R. (2006). Creep behavior of carbon fiber/epoxy matrix composites. *Materials Science and Engineering: A*, *421*, 217–225. <https://doi.org/10.1016/j.msea.2006.01.063>
- Guedes, R. M. (2018). A systematic methodology for creep master curve construction using the stepped isostress method (ssm): A numerical assessment. *Mechanics of Time-Dependent Materials*, *22*, 79–93. <https://doi.org/10.1007/s11043-017-9353-0>
- Hadid, M., Guerira, B., Bahri, M., & Zouani, A. (2014). Assessment of the stepped isostress method in the prediction of long term creep of thermoplastics. *Polymer Testing*, *34*, 113–119. <https://doi.org/10.1016/J.POLYMERTESTING.2014.01.003>
- Hao, J., Prapavesis, A., Lomov, S. V., Fuentes, C. A., & Vuure, A. W. V. (2024). Damage evolution in flax fibre composite under creep load. *Composite Structures*, *329*, 117786. <https://doi.org/10.1016/J.COMPSTRUCT.2023.117786>
- Hossain, A., Mach, R., Pellicote, J., & Stewart, C. M. (2020, June). Calibration of cdm-based constitutive model using accelerated creep test (sct) data.
- Hristozov, D., Wroblewski, L., & Sadeghian, P. (2016). Long-term tensile properties of natural fibre-reinforced polymer composites: Comparison of flax and glass fibres. *Composites Part B: Engineering*, *95*, 82–95. <https://doi.org/10.1016/J.COMPOSITESB.2016.03.079>
- Huang, C. W., Yang, T. C., Wu, T. L., Hung, K. C., & Wu, J. H. (2018). Effects of maleated polypropylene content on the extended creep behavior of wood-polypropylene composites using the stepped isothermal method and the stepped isostress method. *Wood Science and Technology*, *52*, 1313–1330. <https://doi.org/10.1007/S00226-018-1037-7/TABLES/2>
- Huda, Z. (2022, December). *Mechanical behavior of materials*. Springer Cham. <https://doi.org/10.1007/978-3-030-84927-6>
- ISO 527-5:2021. (2022, January). *Plastics-Determination of tensile properties-Part 5: Test conditions for unidirectional fibre-reinforced plastic composites* (Standard). International Organization for Standardization.
- ISO 899-1:2017. (2017, September). *Plastics-Determination of creep behaviour-Part 1: Tensile creep* (Standard). International Organization for Standardization.
- Jia, Y., & Fiedler, B. (2020). Tensile creep behaviour of unidirectional flax fibre reinforced bio-based epoxy composites. *Composites Communications*, *18*, 5–12. <https://doi.org/10.1016/J.COCO.2019.12.010>
- Kamarudin, S. H., Basri, M. S. M., Rayung, M., Abu, F., Ahmad, S., Norizan, M. N., Osman, S., Sari-fuddin, N., Desa, M. S. Z. M., Abdullah, U. H., Tawakkal, I. S. M. A., & Abdullah, L. C. (2022, September). A review on natural fiber reinforced polymer composites (nfrpc) for sustainable industrial applications. <https://doi.org/10.3390/polym14173698>
- Karimah, A., Ridho, M. R., Munawar, S. S., Adi, D. S., Ismadi, Damayanti, R., Subiyanto, B., Fatriasari, W., & Fudholi, A. (2021). A review on natural fibers for development of eco-friendly bio-

- composite: Characteristics, and utilizations. *Journal of Materials Research and Technology*, 13, 2442–2458. <https://doi.org/10.1016/J.JMRT.2021.06.014>
- Kolstein, M. H. (2008). *Fibre reinforced polymer (frp) structures, lecture ct5128*. Delft University of Technology.
- Kubát, J., & Seldén, R. (1978). The stress dependence of activation volumes in creep and stress relaxation. *Materials Science and Engineering*, 36, 65–69. [https://doi.org/10.1016/0025-5416\(78\)90195-7](https://doi.org/10.1016/0025-5416(78)90195-7)
- Lau, K.-t., Hung, P.-y., Zhu, M.-H., & Hui, D. (2018). Properties of natural fibre composites for structural engineering applications. *Composites Part B: Engineering*, 136, 222–233. <https://doi.org/10.1016/J.COMPOSITESB.2017.10.038>
- Lee, L. S. (2007). Creep and time-dependent response of composites. *Durability of Composites for Civil Structural Applications*, 150–169. <https://doi.org/10.1533/9781845693565.1.150>
- Lu, M. M., Fuentes, C. A., & van Vuure, A. W. (2022). Moisture sorption and swelling of flax fibre and flax fibre composites. *Composites Part B: Engineering*, 231, 109538. <https://doi.org/https://doi.org/10.1016/j.compositesb.2021.109538>
- Luo, W., Wang, C., Hu, X., & Yang, T. (2012). Long-term creep assessment of viscoelastic polymer by time-temperature-stress superposition. *Acta Mechanica Solida Sinica*, 25, 571–578. [https://doi.org/10.1016/S0894-9166\(12\)60052-4](https://doi.org/10.1016/S0894-9166(12)60052-4)
- Manconi, M., & Moonen, S. P. G. (2024). Monitoring high temperatures in the vartm production process of a novel flax fiber-reinforced composite footbridge with fbg sensors. *IASS Symposium 2024 Redefining the Art of Structural Design*.
- Merrild, H., Guldager Jensen, K., & Sommer, J. (2016). *Building a circular future* (1st ed., Vol. 248). GXN. <https://adk.elsevierpure.com/en/publications/building-a-circular-future>
- Ministerie van Infrastructuur en Waterstaat. (2024, February). Nederland circulair in 2050. <https://www.rijksoverheid.nl/onderwerpen/circulaire-economie/nederland-circulair-in-2050>
- More, A. P. (2021). Flax fiber-based polymer composites: A review. *Advanced Composites and Hybrid Materials 2021 5:1*, 5, 1–20. <https://doi.org/10.1007/S42114-021-00246-9>
- Nedjar, B. (2011). A time dependent model for unidirectional fibre-reinforced composites with viscoelastic matrices. *International Journal of Solids and Structures*, 48, 2333–2339. <https://doi.org/10.1016/J.IJSOLSTR.2011.04.007>
- Nijssen, R. (2015). *Composite materials, an introduction*. CompositesNL. <https://compositesnl.nl/en/compositesnl/knowledge-centre/>
- Noels, L. (n.d.). Fracture Mechanics online class. http://www.ltas-cm3.ulg.ac.be/FractureMechanics/?p=Lecture6_P4
- Papanicolaou, G. C., & Zaoutos, S. P. (2011). Viscoelastic constitutive modeling of creep and stress relaxation in polymers and polymer matrix composites. In R. M. Guedes (Ed.). Woodhead Publishing.
- Paris Agreement. (2015). Paris agreement. *United Nations Framework Convention on Climate Change*. https://unfccc.int/sites/default/files/english_paris_agreement.pdf
- Peng, H., Jiang, J., Zhan, T., Jiang, J., & Lyu, J. (2022). Flexural creep behavior of hierarchical bamboo structure using time-temperature-stress superposition principle. *Industrial Crops and Products*, 190, 115906. <https://doi.org/10.1016/J.INDCROP.2022.115906>
- Perruchoud, V., Alderliesten, R., & Mosleh, Y. (2024). The effects of in-situ temperature and relative humidity on the tensile response of flax vs. glass frp composites. In C. Binetury & F. Jaquemin (Eds.), *Proceedings of the 21st european conference on composite materials: Volume 3 - material and structural behavior – simulation & testing* (pp. 1477–1485, Vol. 3). The European Society for Composite Materials (ESCM); the Ecole Centrale de Nantes.
- Polynt-Group. (2022, June). Smart circular bridge made of bio-composite - polynt. Retrieved June 21, 2024, from <https://www.polynt.com/smart-circular-bridge-made-of-bio-composite/>
- SageZander. (2022, May). Carbon Fibre Composites: Discover this impressive material. <https://sagezander.com/carbon-fibre-composites-prepreg-towpreg/>
- Silva, M. P., Santos, P., Parente, J. M., Valvez, S., Reis, P. N., & Piedade, A. P. (2020). Effect of post-cure on the static and viscoelastic properties of a polyester resin. *Polymers 2020, Vol. 12, Page 1927*, 12, 1927. <https://doi.org/10.3390/POLYM12091927>
- Souren, W., & Velds, E. (2019, June). *Bio-based brug RitsumasyI DO Constructief Ontwerp* (No. 2016036-180125-1431). Lightweight Structures B.V.

- Staab, G. (2015). *Laminar composites* (2nd ed.). Butterworth-Heinemann.
- Tanks, J., Rader, K., Sharp, S., & Sakai, T. (2017). Accelerated creep and creep-rupture testing of transverse unidirectional carbon/epoxy lamina based on the stepped isostress method. *Composite Structures*, *159*, 455–462. <https://doi.org/10.1016/J.COMPSTRUCT.2016.09.096>
- Tedjini, M., Sedira, L., Guerira, B., & Meftah, K. (2022). On the use of the stepped isostress method in the prediction of creep behavior of polyamide 6. *Frattura ed Integrita Strutturale*, *16*, 336–348. <https://doi.org/10.3221/IGF-ESIS.62.24>
- Thornton, J. S., & Sandri, D. (1999). Introducing the stepped isothermal method. *Geotechnical Fabrics Report*, *17*.
- United Nations Environment Programme, Y. C. f. E. +. A. (2023, September). Building materials and the climate: Constructing a new future. <https://wedocs.unep.org/20.500.11822/43293>
- Waghmare, S., Shelare, S., Aglawe, K., & Khope, P. (2022). A mini review on fibre reinforced polymer composites. *Materials Today: Proceedings*, *54*, 682–689. <https://doi.org/10.1016/J.MATPR.2021.10.379>
- Wang, W. H., Huang, H. B., Du, H.-H., & Wang, H. (2015). Effects of fiber size on short-term creep behavior of wood fiber/hdpe composites. *Polymer Engineering & Science*, *55*, 693–700. <https://doi.org/10.1002/PEN.23935>
- Wang, X., & Petru, M. (2022). The effects of surface treatment on creep and dynamic mechanical behavior of flax fiber reinforced composites under hygrothermal aging conditions. *Surface Treatment Methods of Natural Fibres and their Effects on Biocomposites*, 203–242. <https://doi.org/10.1016/B978-0-12-821863-1.00010-7>
- Xu, B., Hurk, B. V. D., Lugger, S. J., Blok, R., & Teuffel, P. (2023). Creep analysis of the flax fiber-reinforced polymer composites based on the time-temperature superposition principle. *Science and Engineering of Composite Materials*, *30*. <https://doi.org/10.1515/secm-2022-0218>
- Xu, J.-W. ; Li, C.-C. ; Liu, J.-W. ; Chang, W.-C. ; Chang, W.-S. ; Wu, J.-H., Xu, J.-W., Li, C.-C., Liu, J.-W., Chang, W.-C., Chang, W.-S., & Wu, J.-H. (2023). Assessing the long-term creep behaviour of hydrothermally treated japanese cedar wood using the short-term accelerated stepped isostress method. *Polymers 2023, Vol. 15, Page 4149*, *15*, 4149. <https://doi.org/10.3390/POLYM15204149>
- Yan, L., Chouw, N., & Jayaraman, K. (2014). Flax fibre and its composites – a review. *Composites Part B: Engineering*, *56*, 296–317. <https://doi.org/10.1016/J.COMPOSITESB.2013.08.014>
- Yang, T. C., Wu, T. L., & Yeh, C. H. (2021). Water resistance and creep behavior of heat-treated moso bamboo determined by the stepped isostress method. *Polymers 2021, Vol. 13, Page 1264*, *13*, 1264. <https://doi.org/10.3390/POLYM13081264>
- Yeo, S. S., & Hsuan, Y. G. (2009). Predicting the creep behavior of high density polyethylene geogrid using stepped isothermal method. *Service Life Prediction of Polymeric Materials: Global Perspectives*, 205–218. https://doi.org/10.1007/978-0-387-84876-1_13/COVER

Appendices



Calculation of the Laminate Configurations

Table A.1: Specifications of fibres and resin, used to design the layup configurations

	Material	Weight	Unit
Type of fibres	Bcomp 5025 / Amplitex UD300	275	g/m ²
	Bcomp 5008 / Amplitex Biax 350	363	g/m ²
Density of flax fibres		1,400,000	g/m ³
Type of resin	Polynt 9759 IB (unsaturated polyester)		
Density of resin		1,200,000	g/m ³

Table A.2: Design of layup A (100% UD)

Design of layup A, 100% UD				
Desired total thickness [mm]	6.0			
Estimated fibre volume fraction	45%			
Fibre direction	UD 0°	UD 90°	±45°	
Desired layup configuration	100%	0%	0%	
Total needed thickness of flax sheets [mm]	2.70	0	0	
Amount of flax fibres needed [g/m ²]	3780	0	0	
Amount of layers needed	13.75	0	0	Total
Amount of layers used	14	0	0	14
Thickness fibres [mm]	2.75	0	0	2.75
Thickness of resin [mm]	3.36	0	0	3.36
Total estimated thickness of layup [mm]				6.11
After manufacturing of the layups				
Actual mean measured thickness [mm]				6.62
Actual mean fibre volume fraction				49%

Table A.3: Design of layup B (100% QI)

Design of layup B, 100% QI				
Desired total thickness [mm]	7.0			
Estimated fibre volume fraction	45%			
Fibre direction	UD 0°	UD 90°	±45°	
Desired layup configuration	25%	25%	50%	
Total needed thickness of flax sheets [mm]	0.79	0.79	1.58	
Amount of flax fibres needed [g/m ²]	1103	1103	1103	
Amount of layers needed	4.01	4.01	6.07	Total
Amount of layers used	4	4	6	14
Thickness fibres [mm]	0.79	0.79	1.56	3.14
Thickness of resin [mm]	0.96	0.96	1.90	3.82
Total estimated thickness of layup [mm]				6.96
After manufacturing of the layups				
Actual mean measured thickness [mm]				7.29
Actual mean fibre volume fraction				43%

Table A.4: Design of layup C (UD+QI)

Design of layup C, UD+QI				
Desired total thickness [mm]	6.0			
Estimated fibre volume fraction	45%			
Fibre direction	UD 0°	UD 90°	±45°	
Desired layup configuration	55%	15%	30%	
Total needed thickness of flax sheets [mm]	1.49	0.41	0.81	
Amount of flax fibres needed [g/m ²]	2079	567	1134	
Amount of layers needed	7.56	2.06	3.12	Total
Amount of layers used	8	2	3	13
Thickness fibres [mm]	1.57	0.39	0.78	2.74
Thickness of resin [mm]	1.92	0.48	0.95	3.35
Total estimated thickness of layup [mm]				6.09
After manufacturing of the layups				
Actual mean measured thickness [mm]				6.09
Actual mean fibre volume fraction				45%

B

Sample Locations on Original Plates

All plates are originally cut with a circular wood saw in four big pieces and two small strips. The parts are numbered 1 to 6 and plate parts 1 and 2 were used to cut samples from with a water jet cutter. Plate parts 6 were used to cut four small pieces, with a wood hand saw, to view under a microscope. The other plate parts are untouched and will be used in future research projects.

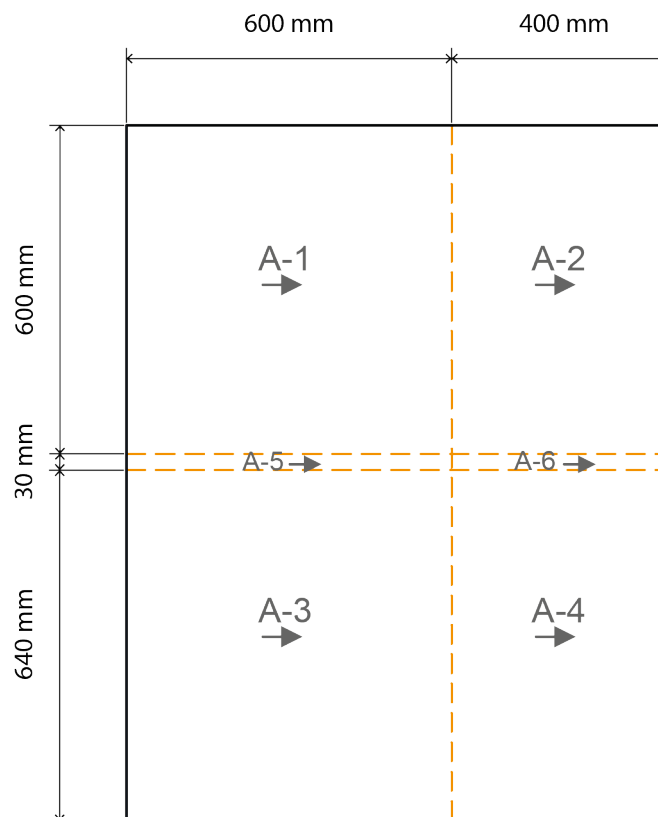


Figure B.1: The cutting lines (in orange) of the original plates into four main sections and two smaller strips, with corresponding numbers. This example is for plate A, but the cutting lines are the same for all three original plates

B.1. Samples Plate A

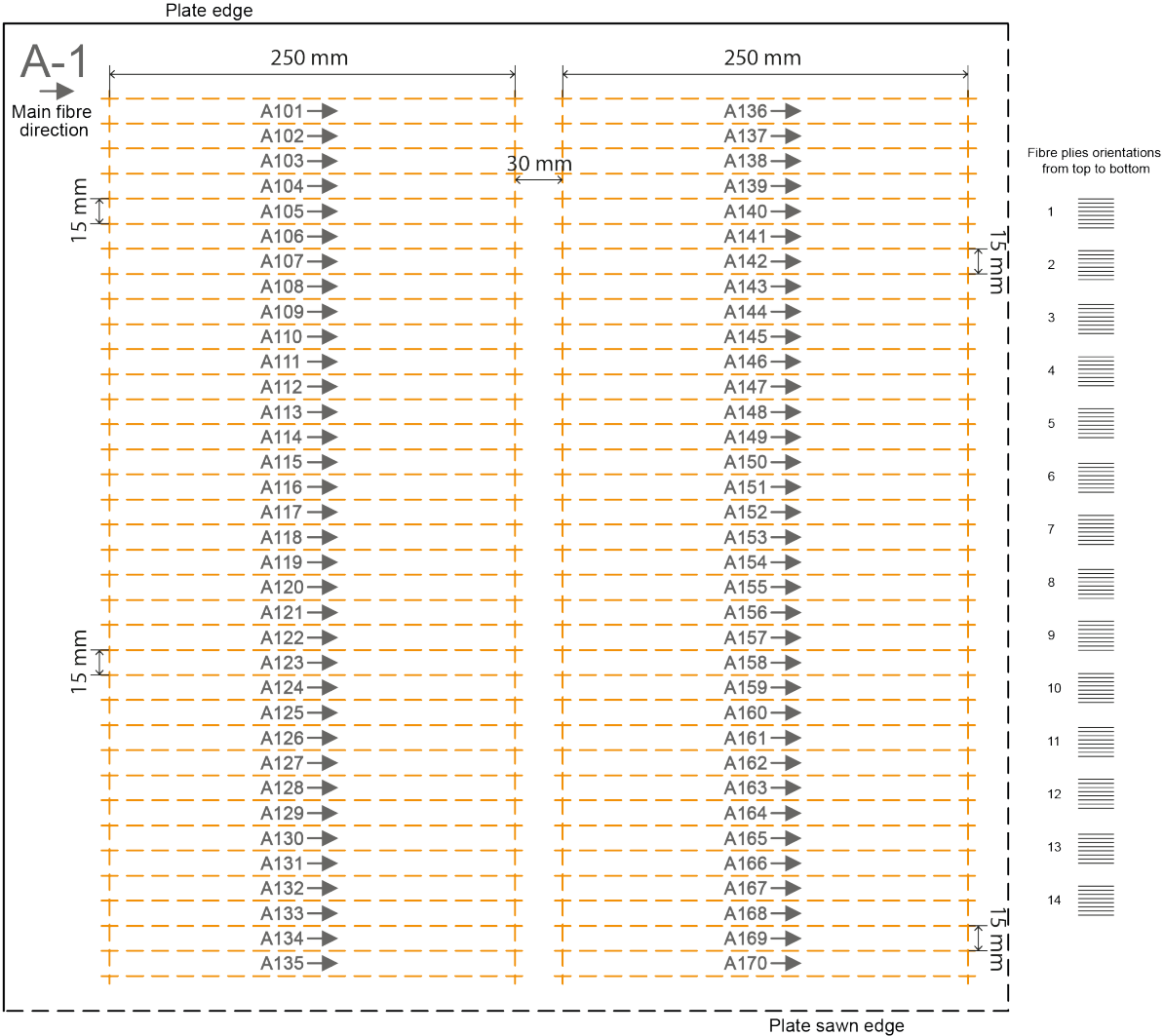


Figure B.2: The samples on plate A-1, the samples (in orange lines) are cut with a water jet cutter, the black dashed line of the edge plate was the saw line of the original plate

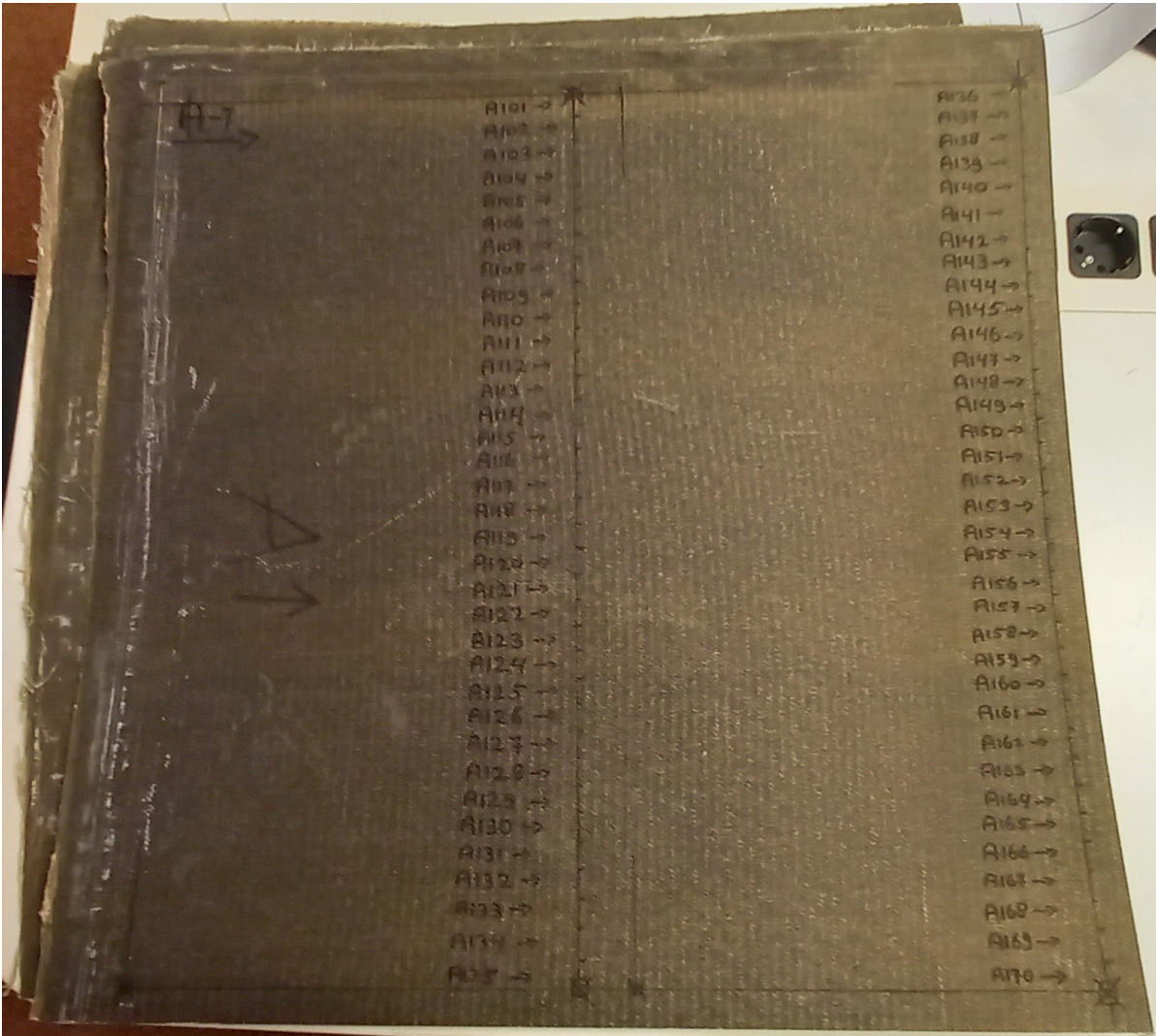


Figure B.3: Picture of plate A-1 before cutting the samples

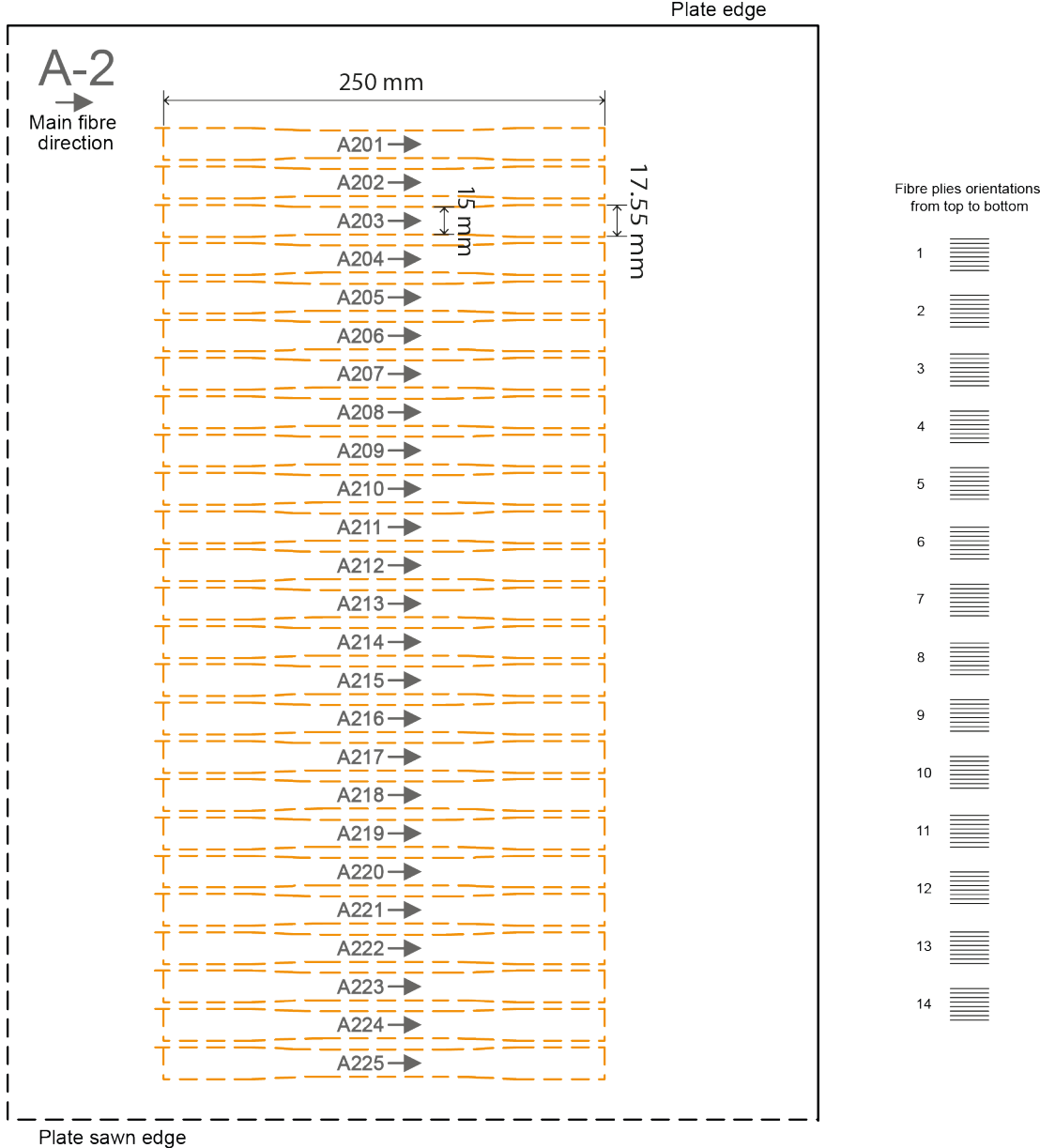


Figure B.4: The samples on plate A-2, the dog bone shaped samples (in orange lines) are cut with a water jet cutter, the black dashed line of the edge plate was the saw line of the original plate

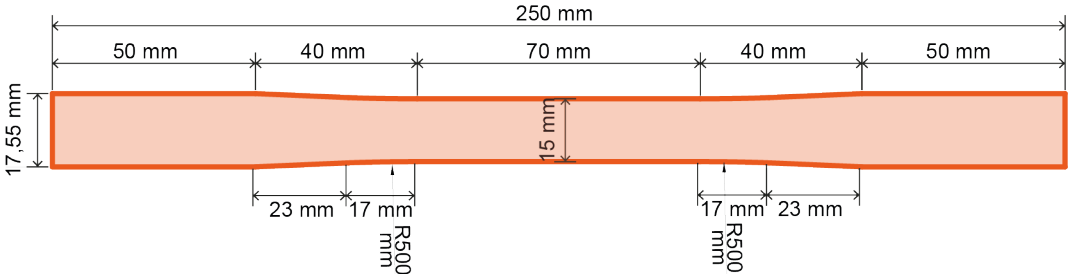


Figure B.5: Detailed dimensions of the dog bone shaped samples of layup A



Figure B.6: Picture of plate A-2 before cutting the samples

B.2. Samples Plate B

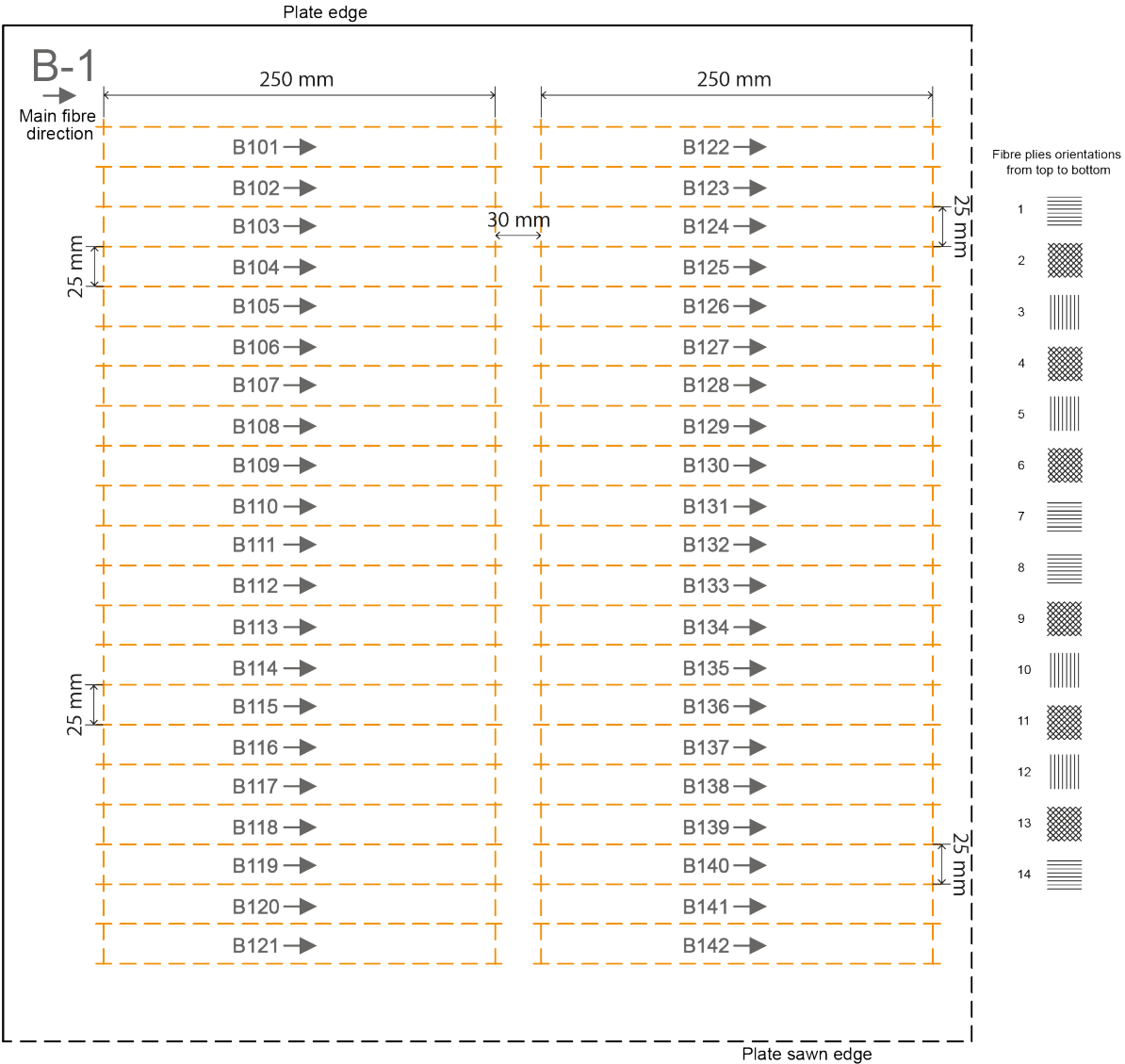


Figure B.7: The samples on plate B-1, the samples (in orange lines) are cut with a water jet cutter, the black dashed line of the edge plate was the saw line of the original plate

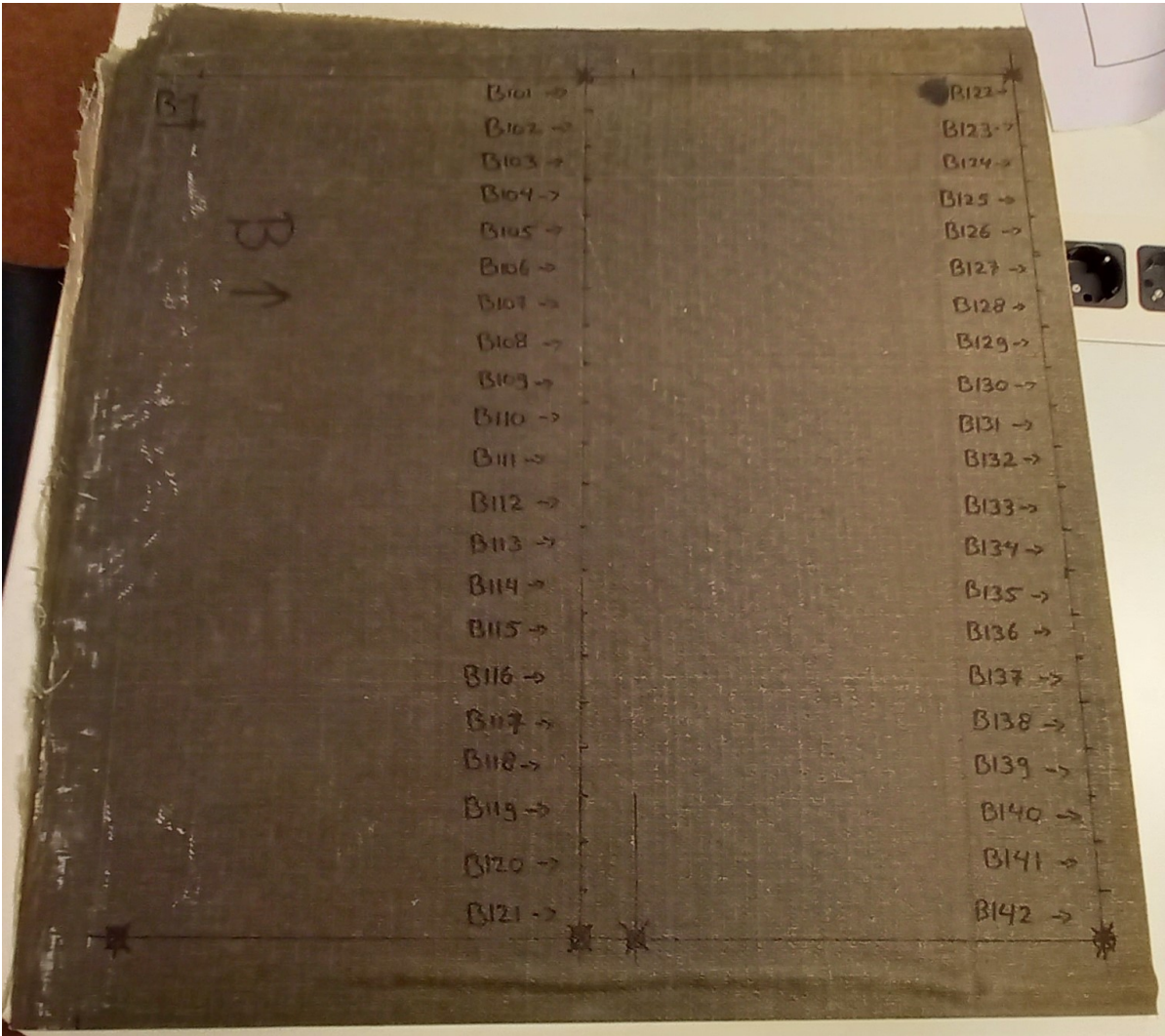


Figure B.8: Picture of plate B-1 before cutting the samples

Plate B-1 the fold at the bottom of the plate is avoided when cutting samples from the plate.

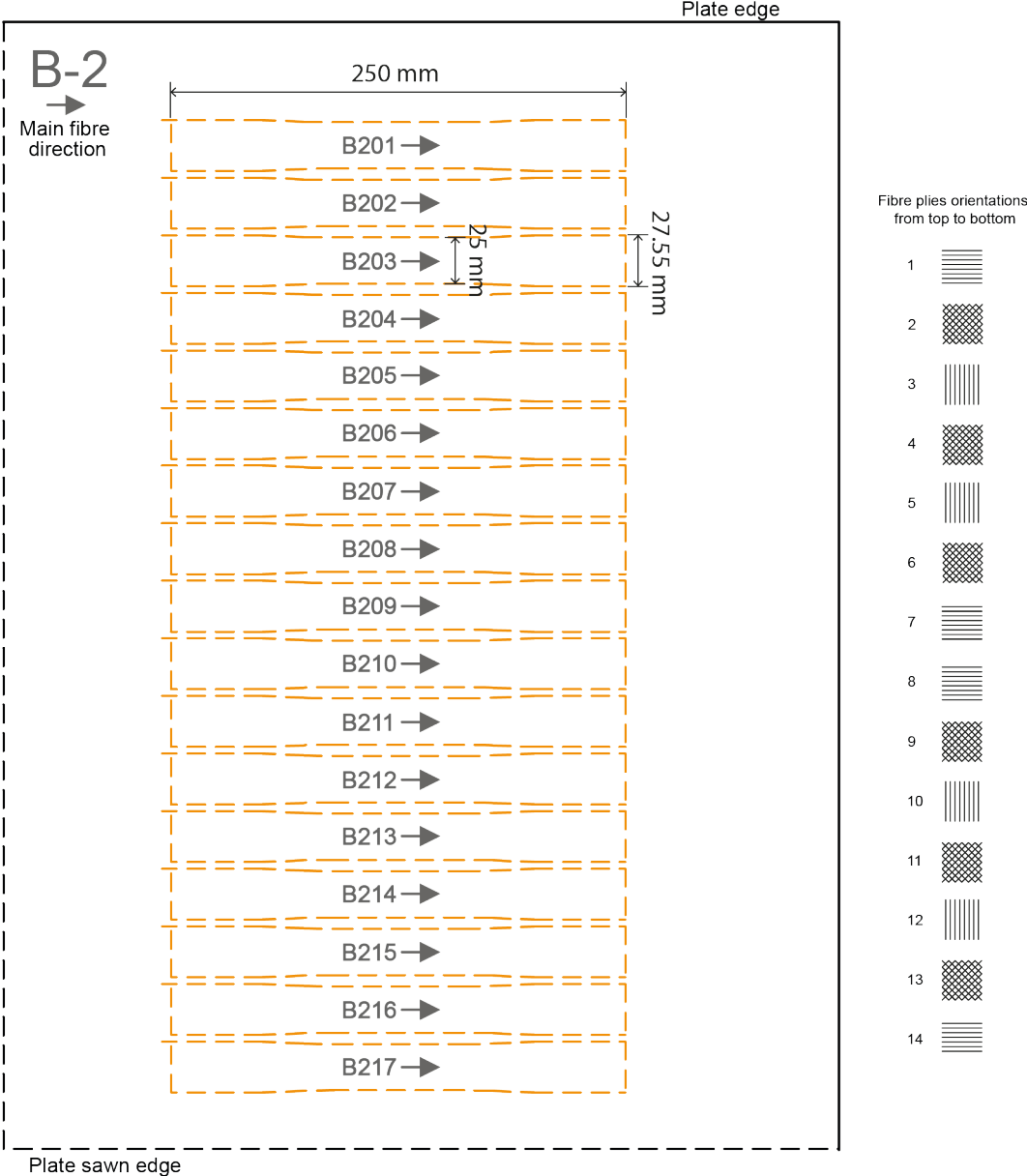


Figure B.9: The samples on plate B-2, the dog bone shaped samples (in orange lines) are cut with a water jet cutter, the black dashed line of the edge plate was the saw line of the original plate

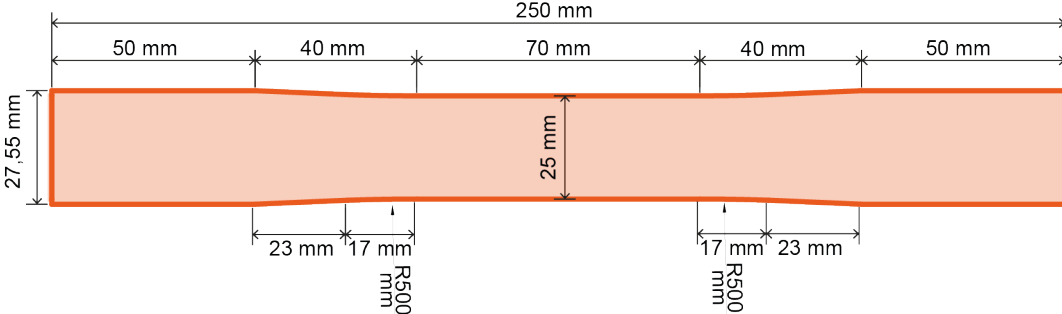


Figure B.10: Detailed dimensions of the dog bone shaped samples of layup B

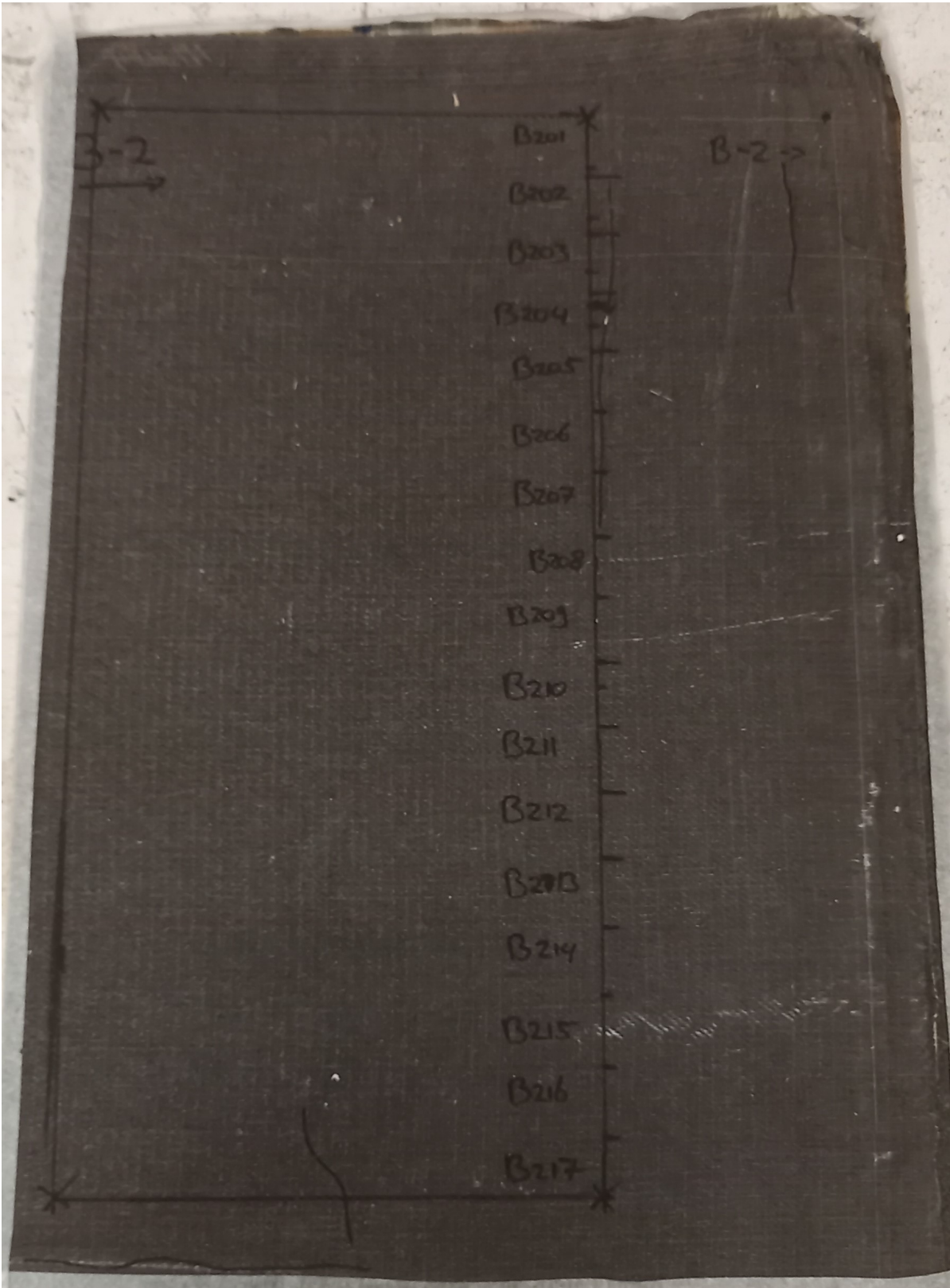


Figure B.11: Picture of plate B-2 before cutting the samples

B.3. Samples Plate C

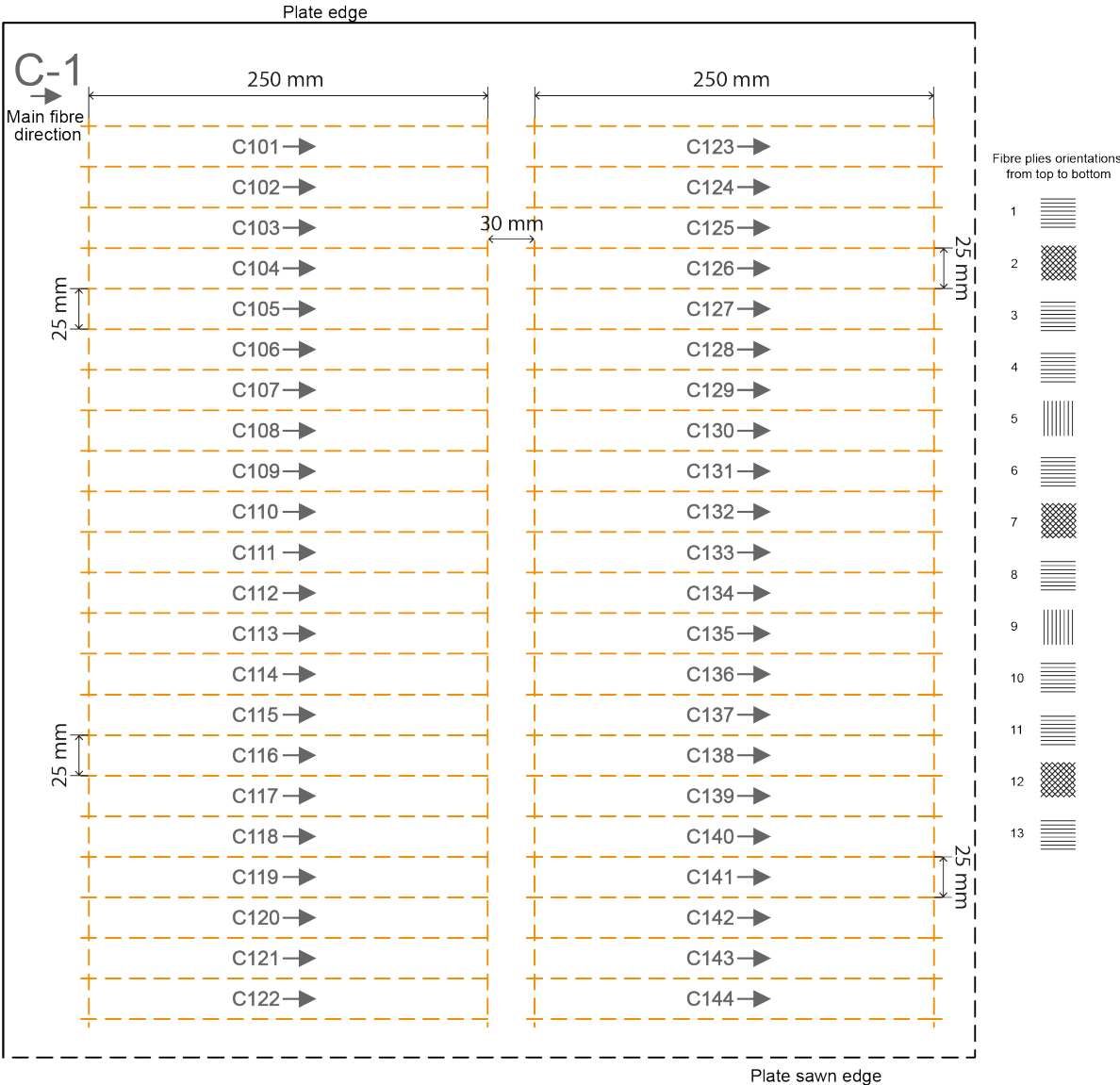


Figure B.12: The samples on plate C-1, the samples (in orange lines) are cut with a water jet cutter, the black dashed line of the edge plate was the saw line of the original plate

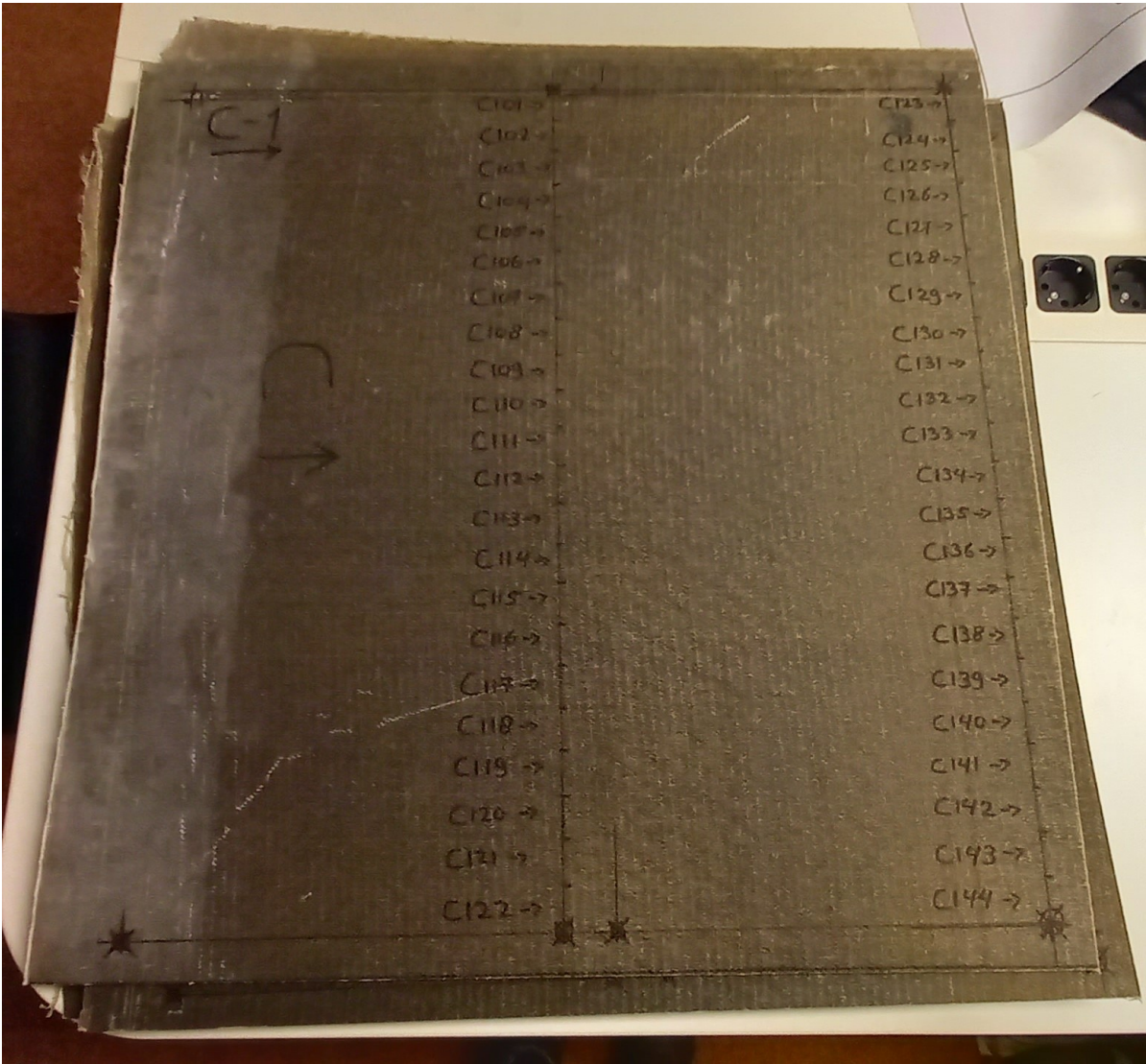


Figure B.13: Picture of plate C-1 before cutting the samples

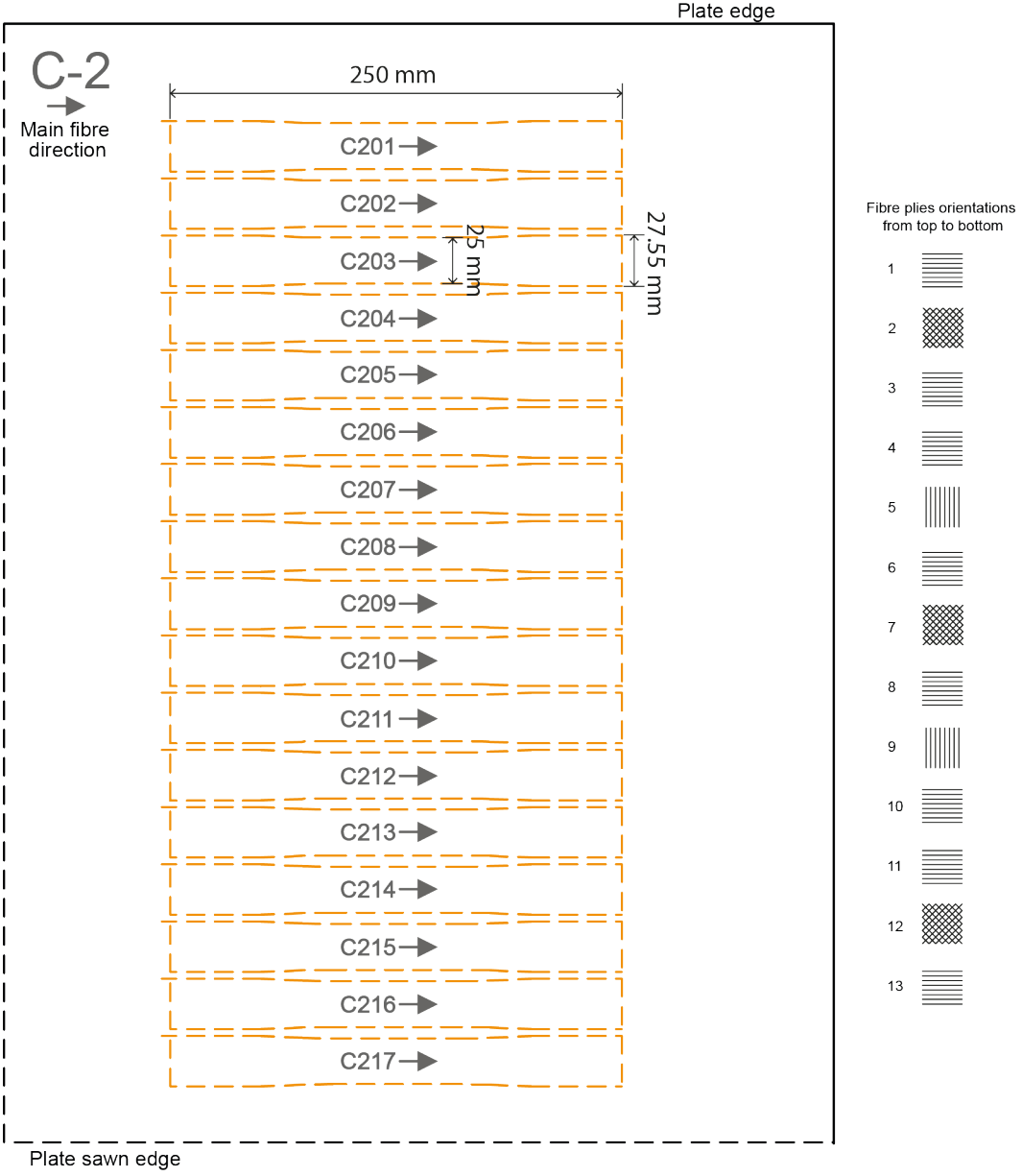


Figure B.14: The samples on plate C-2, the dog bone shaped samples (in orange lines) are cut with a water jet cutter, the black dashed line of the edge plate was the saw line of the original plate

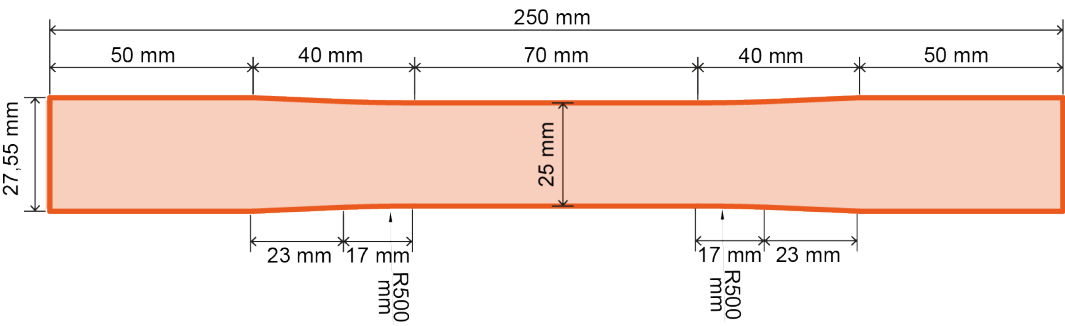


Figure B.15: Detailed dimensions of the dog bone shaped samples of layup C

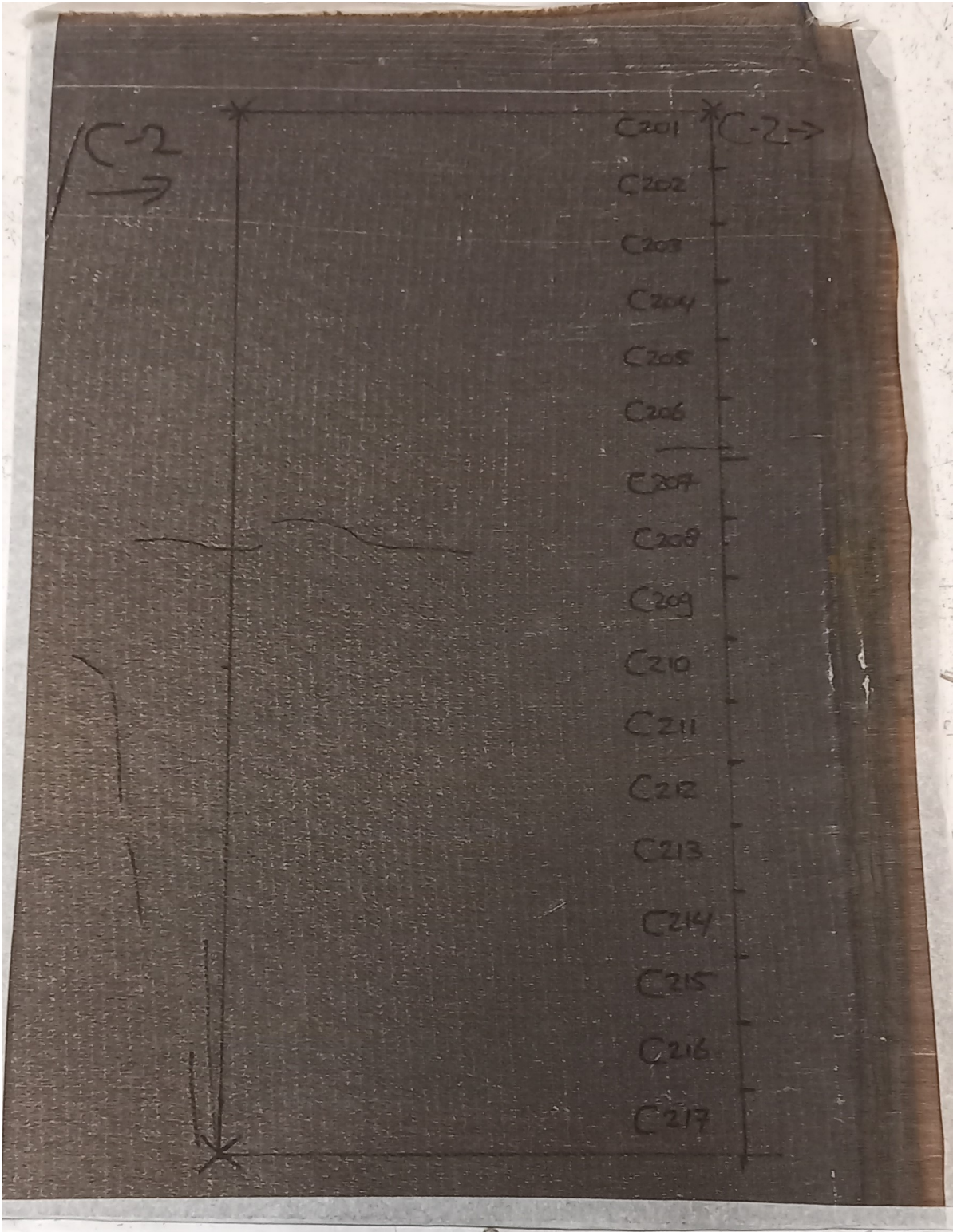


Figure B.16: Picture of plate C-2 before cutting the samples

Samples C208 and C206 or C207 seem to have a few folds on the surface of the samples. This is paid attention to when choosing samples for testing. The samples are excluded from the tests, or an additional sample is tested.

B.4. Plate Part 6

Plate part 6 is a small strip between plate parts 2 and 4. From this strip, four 15x15 mm blocks were cut with a hand saw (figure B.17). The blocks were poured into an epoxy block (figure B.19), and polished to be viewed under a microscope to check the material's quality.

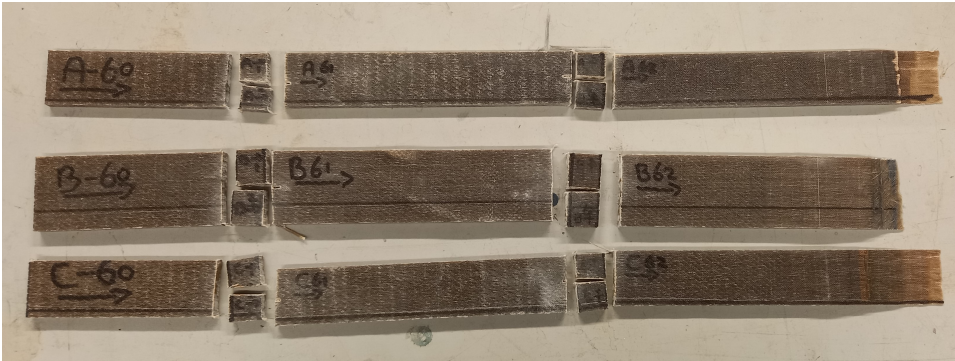


Figure B.17: Picture of plate parts 6 of each layup

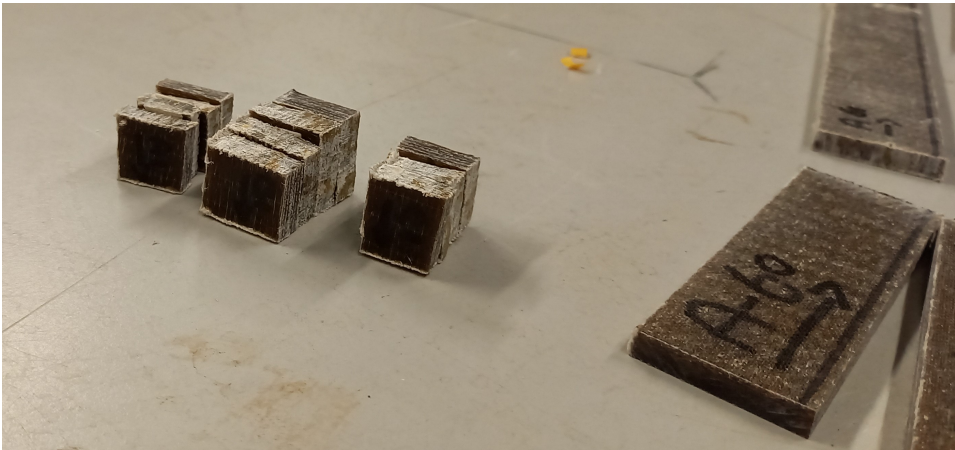


Figure B.18: The sawn blocks from plate parts 6

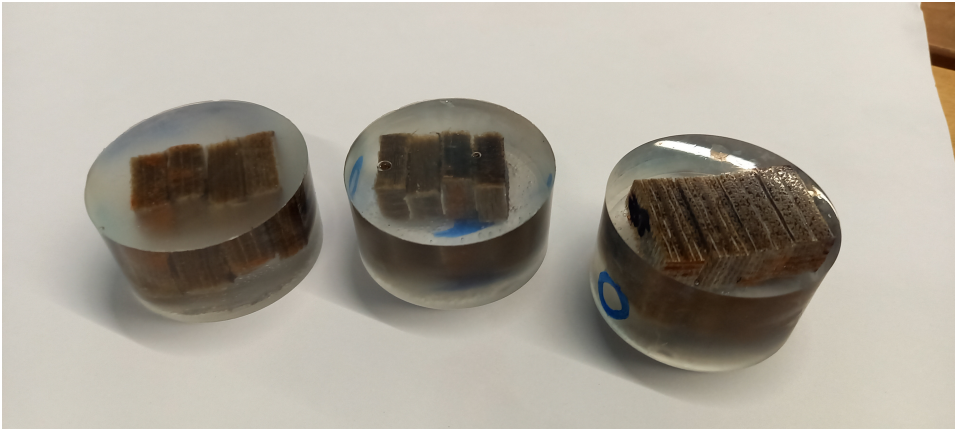


Figure B.19: The sawn blocks from plate parts 6 poured into epoxy, the right one already polished and ready to be viewed under a microscope



Measured Sample Thickness

MEASUREMENTS OF SAMPLE DIMENSIONS OF PLATE A

Sample	Width middle [mm]	Width top gauge [mm]	Width bottom gauge [mm]	Mean width [mm]	Thickness middle [mm]	Thickness top gauge [mm]	Thickness bottom gauge [mm]	Mean thickness [mm]	Mean cross section [mm ²]
A-101									
A-102	14,88	14,89	14,86	14,88	5,66	5,70	5,81	5,72	85,14
A-103	14,94	14,93	14,96	14,94	5,64	5,55	5,79	5,66	84,58
A-104	14,95	14,93	15,00	14,96	5,73	5,84	5,79	5,79	86,57
A-105	14,86	14,84	14,94	14,88	5,67	5,69	5,74	5,70	84,82
A-106									
A-107									
A-108									
A-109	14,93	14,91	14,94	14,93	5,11	5,66	5,47	5,41	80,80
A-110	14,92	14,98	15,02	14,97	5,63	5,73	5,43	5,60	83,80
A-111									
A-112	14,96	15,00	15,00	14,99	5,66	5,76	5,75	5,72	85,77
A-113									
A-114									
A-115									
A-116									
A-117	14,93	15,00	14,94	14,96	5,61	5,72	5,76	5,70	85,20
A-118	15,02	14,92	14,95	14,96	5,62	5,73	5,74	5,70	85,24
A-119									
A-120	14,96	14,95	15,07	14,99	5,72	5,77	5,74	5,74	86,11
A-121	14,91	14,95	14,90	14,92	5,62	5,63	5,52	5,59	83,40
A-122									
A-123									
A-124	15,02	15,03	15,00	15,02	5,65	5,79	5,71	5,72	85,85
A-125	14,98	15,00	15,04	15,01	5,54	5,44	5,44	5,47	82,14
A-126	14,92	14,89	14,98	14,93	5,71	5,76	5,79	5,75	85,90
A-127									
A-128									
A-129									
A-130	14,96	14,98	15,04	14,99	5,69	5,61	5,80	5,70	85,46
A-131									
A-132	14,89	14,88	15,01	14,93	5,82	5,58	5,54	5,65	84,29
A-133	14,95	15,00	14,98	14,98	5,77	5,60	5,67	5,68	85,07
A-134	14,94	14,98	14,96	14,96	5,63	5,59	5,69	5,64	84,32
A-135									
A-136									
A-137									
A-138									
A-139									

Sample	Width middle [mm]	Width top gauge [mm]	Width bottom gauge [mm]	Mean width [mm]	Thickness middle [mm]	Thickness top gauge [mm]	Thickness bottom gauge [mm]	Mean thickness [mm]	Mean cross section [mm ²]
A-140	14,97	15,03	15,00	15,00	5,66	5,73	5,56	5,65	84,75
A-141									
A-142	14,87	14,93	14,96	14,92	5,73	5,72	5,60	5,68	84,80
A-143									
A-144									
A-145									
A-146									
A-147	14,95	14,99	15,00	14,98	5,46	5,42	5,39	5,42	81,24
A-148	15,00	14,94	14,95	14,96	5,67	5,74	5,81	5,74	85,89
A-149									
A-150									
A-151									
A-152									
A-153									
A-154									
A-155									
A-156	15,01	14,94	15,03	14,99	5,33	5,31	5,40	5,34	80,16
A-157	15,03	15,04	15,05	15,04	5,71	5,63	5,57	5,64	84,78
A-158	15,07	15,03	15,00	15,03	5,65	5,47	5,46	5,53	83,08
A-159									
A-160	14,92	15,01	14,96	14,96	5,67	5,66	5,68	5,67	84,84
A-161									
A-162									
A-163	15,02	14,93	14,98	14,98	5,35	5,44	5,34	5,38	80,52
A-164									
A-165									
A-166									
A-167	15,02	14,94	14,95	14,97	5,36	5,47	5,48	5,44	81,39
A-168									
A-169									
A-170									
A-201									
A-202	15,20	15,26	15,23	15,23	5,69	5,72	5,68	5,70	86,76
A-203									
A-204	15,17	15,06	15,10	15,11	5,56	5,57	5,59	5,57	84,21
A-205									
A-206									
A-207	15,22	15,21	15,23	15,22	5,62	5,67	5,65	5,65	85,94
A-208	15,14	15,11	15,10	15,12	5,57	5,66	5,76	5,66	85,61
A-209									
A-210	15,24	15,25	15,22	15,24	5,51	5,57	5,58	5,55	84,61
A-211	15,18	15,14	15,17	15,16	5,62	5,59	5,60	5,60	84,97
A-212	15,24	15,27	15,19	15,23	5,49	5,56	5,69	5,58	85,00
A-213									
A-214									
A-215	15,13	15,21	15,15	15,16	5,52	5,62	5,53	5,56	84,26
A-216									
A-217	15,20	15,11	15,14	15,15	5,48	5,52	5,51	5,50	83,38
A-218	15,12	15,14	15,20	15,15	5,53	5,56	5,69	5,59	84,76
A-219									
A-220	15,25	15,20	15,19	15,21	5,50	5,65	5,60	5,58	84,94
A-221									
A-222	15,09	15,11	15,08	15,09	5,61	5,70	5,60	5,64	85,08
A-223	15,25	15,15	15,08	15,16	5,56	5,70	5,65	5,64	85,45
A-224									
A-225									
								Total mean thickness	5,62 mm
								StDev	0,11

MEASUREMENTS OF SAMPLE DIMENSIONS OF PLATE B

Sample	Width middle [mm]	Width top gauge [mm]	Width bottom gauge [mm]	Mean width [mm]	Thickness middle [mm]	Thickness top gauge [mm]	Thickness bottom gauge [mm]	Mean thickness [mm]	Mean cross section [mm ²]
B-101	25,08	25,03	25,05	25,05	7,32	7,38	7,35	7,35	184,14
B-102	24,95	25,04	25,03	25,01	7,37	7,39	7,26	7,34	183,55
B-103	25,20	25,12	25,14	25,15	7,12	7,45	7,36	7,31	183,87
B-104	25,08	24,99	24,98	25,02	7,35	7,18	7,37	7,30	182,62
B-105	25,09	25,05	25,02	25,05	7,39	7,52	7,45	7,45	186,73
B-106									
B-107									
B-108	25,01	25,03	24,98	25,01	7,44	7,27	7,32	7,34	183,63
B-109	25,06	25,07	25,06	25,06	7,28	7,26	7,25	7,26	182,04
B-110	25,05	25,07	24,99	25,04	7,41	7,26	7,29	7,32	183,27
B-111									
B-112									
B-113									
B-114	25,07	25,05	25,01	25,04	7,27	7,32	7,23	7,27	182,15
B-115									
B-116									
B-117	25,14	25,11	25,07	25,11	7,31	7,22	7,35	7,29	183,11
B-118	24,99	25,06	25,00	25,02	7,34	7,41	7,24	7,33	183,37
B-119									
B-120	25,03	24,98	25,08	25,03	7,18	7,24	7,23	7,22	180,63
B-121	25,03	25,02	25,00	25,02	7,34	7,39	7,31	7,35	183,79
B-122	25,11	25,13	25,05	25,10	7,39	7,37	7,19	7,32	183,62
B-123									
B-124	25,01	25,06	24,97	25,01	7,24	7,42	7,39	7,35	183,85
B-125	25,07	25,05	25,02	25,05	7,21	7,23	7,26	7,23	181,17
B-126									
B-127									
B-128									
B-129									
B-130	25,00	25,04	24,98	25,01	7,36	7,31	7,33	7,33	183,38
B-131	25,07	25,09	25,02	25,06	7,36	7,24	7,18	7,26	181,94
B-132									
B-133	25,09	25,07	25,10	25,09	7,22	7,32	7,35	7,30	183,05
B-134	25,05	24,98	25,08	25,04	7,37	7,21	7,23	7,27	182,02
B-135	25,02	25,06	24,99	25,02	7,41	7,23	7,24	7,29	182,50
B-136	25,00	25,02	25,05	25,02	7,24	7,30	7,15	7,23	180,92
B-137	25,00	25,03	25,06	25,03	7,29	7,25	7,32	7,29	182,39
B-138	25,01	25,08	25,03	25,04	7,43	7,19	7,31	7,31	183,04
B-139									
B-140	25,04	24,99	25,05	25,03	7,41	7,21	7,23	7,28	182,28
B-141									
B-142									
B-201	25,09	25,15	25,18	25,14	7,20	7,31	7,14	7,22	181,43
B-202	25,08	25,11	25,14	25,11	7,23	7,31	7,24	7,26	182,30
B-203									
B-204									
B-205	25,17	25,14	25,13	25,15	7,21	7,25	7,22	7,23	181,73
B-206	25,14	25,09	25,12	25,12	7,16	7,15	7,32	7,21	181,09
B-207	25,06	25,08	25,03	25,06	7,29	7,15	7,21	7,22	180,83
B-208									
B-209	25,11	25,07	25,08	25,09	7,30	7,31	7,28	7,30	183,05
B-210	25,02	25,09	25,10	25,07	7,36	7,39	7,19	7,31	183,35
B-211	26,06	25,11	25,08	25,42	7,22	7,23	7,14	7,20	182,92
B-212	25,08	25,13	25,12	25,11	7,22	7,28	7,31	7,27	182,55
B-213	25,13	25,11	25,12	25,12	7,15	7,33	7,28	7,25	182,20
B-214	25,02	25,07	25,07	25,05	7,20	7,29	7,31	7,27	182,05
B-215	25,04	25,02	25,09	25,05	7,29	7,27	7,12	7,23	181,03
B-216									
B-217									
								Total mean thickness	7,29 mm
								StDev	0,05

D

Design of Clamps for Long-Term Test Setup

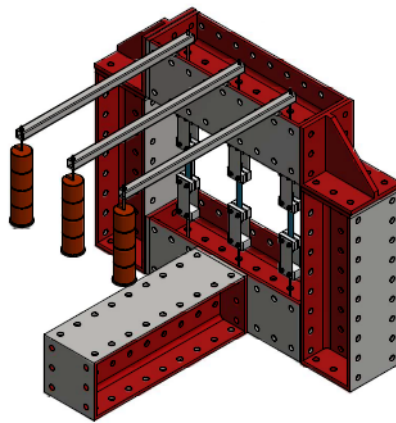


Figure D.1: Sketch of the lever arm long-term creep test setup design (made by Derek van Bochove)

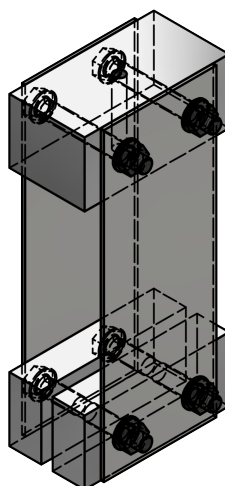
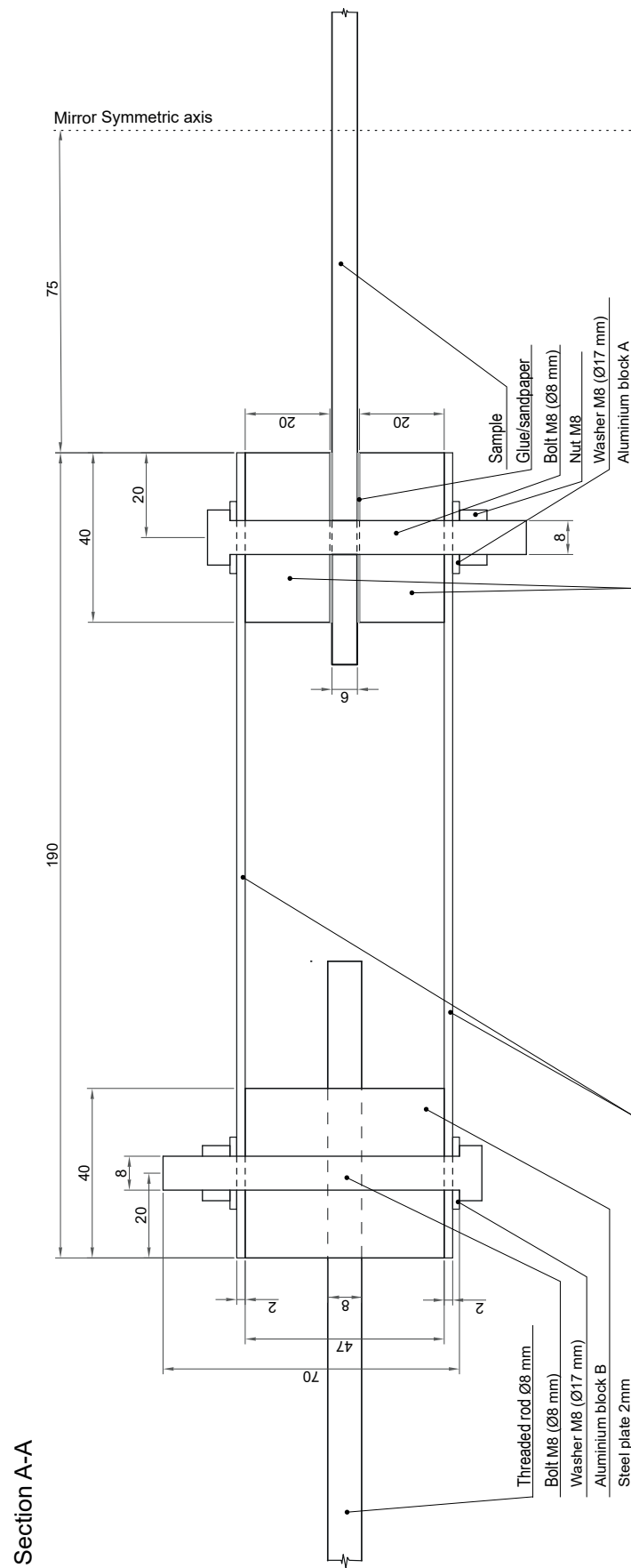
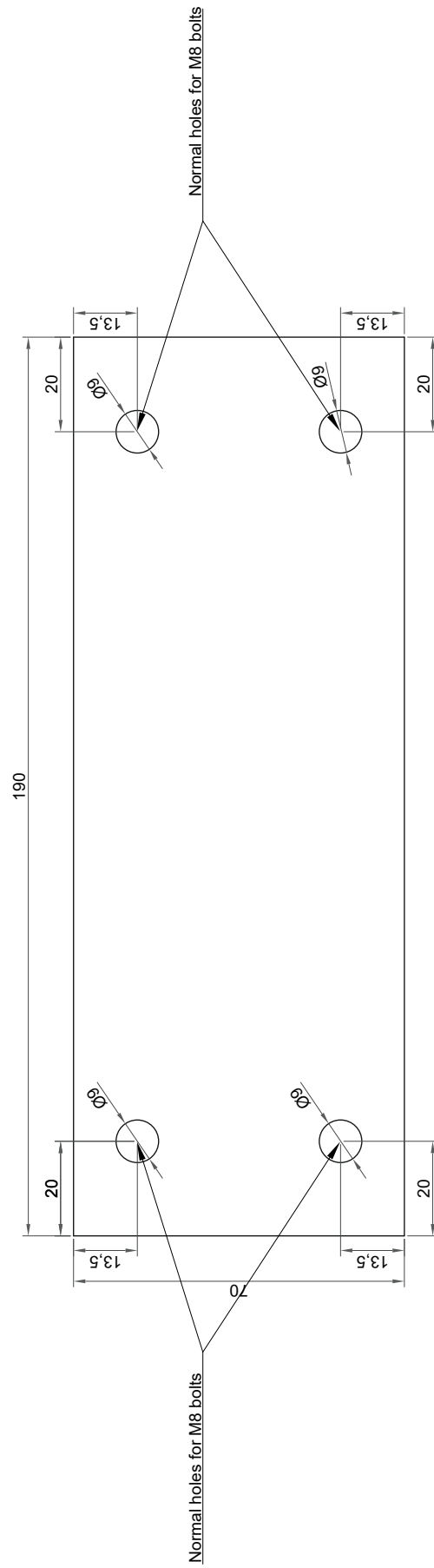


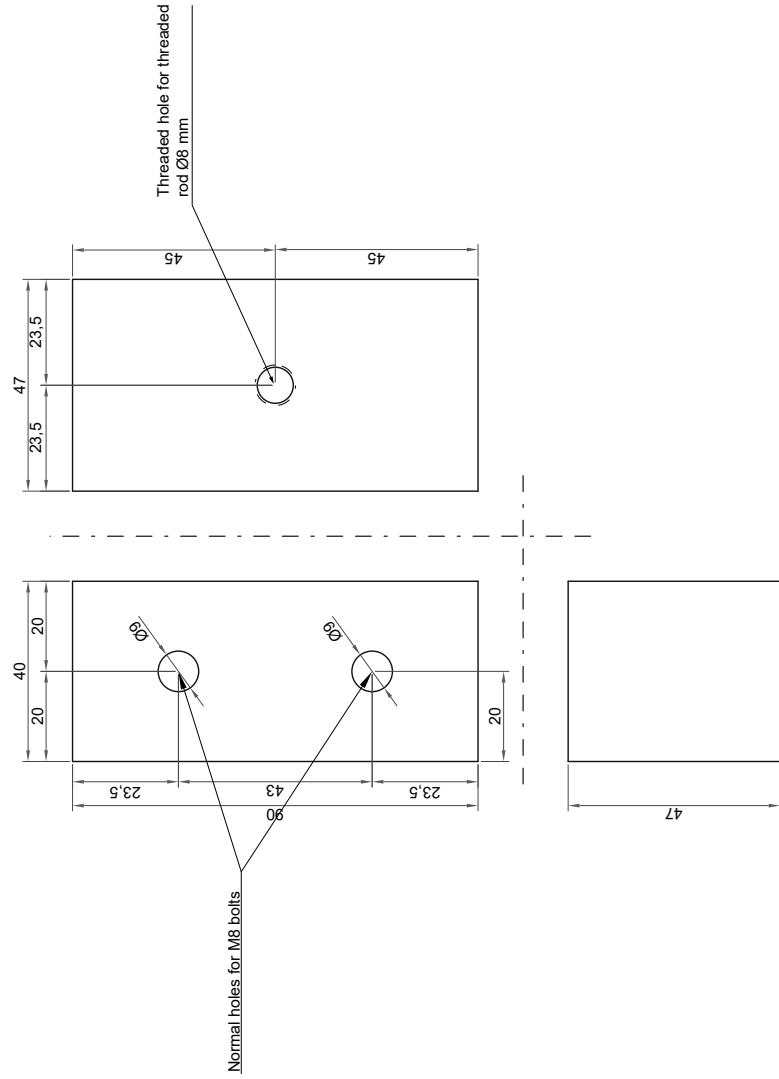
Figure D.2: 3D view of the clamps (made by Derek van Bochove)



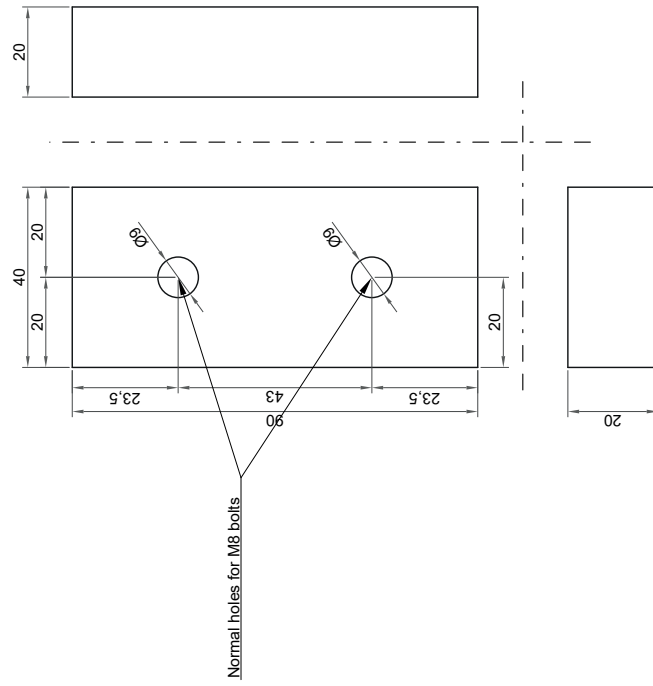
Steel plate, thickness of 2 mm



Aluminium block B



Aluminium block A



E

Preliminary Quasi-Static Tensile Test

A preliminary quasi-static tensile testing series was performed. The results were deemed inconsistent, but are still presented in this appendix. The test method and sample preparation are explained before the results are presented. A brief discussion is added to this chapter, including the improvements in testing methods to gain more consistent results. The results of the second series of tests are presented in chapter 6. An overview of all quasi-static test results is given in appendix F

E.1. Detailed Method

The preliminary quasi-static tensile tests were performed using a Schenk-600 kN machine. There was no climate control during the tests, though the temperature and relative humidity (RH) in the laboratory were monitored. The temperature during the tests ranged from 20.9°C to 21.7°C, with a RH of 38% \pm 1.5%. Hydraulic wedge clamps, with a sawtooth surface and a clamping length of 50 mm, were used to hold the samples in the machine. The strain was measured using an Instron static axial clip-on extensometer with a gauge length of 50 mm, and a Digital Image Correlation (DIC) camera. Data collection, including force, temperature, RH, strain by extensometer, displacement of machine heads, and the number of DIC camera pictures, was conducted at a sampling rate of 2 Hz. The tests were displacement controlled with a rate of 2 mm/min, as recommended in the ASTM D3039 (2002) and ISO 527-5:2021 (2022). The strain in each test was zeroed after clamping the specimen. For each layup configuration, at least five repetitions of the test were performed. A picture of the test setup is shown in figure E.1.



Figure E.1: Quasi-static tensile test setup, with a sample in the hydraulic clamps, a DIC camera, and an extensometer on the sample

E.1.1. Sample Preparation

The samples for the preliminary quasi-static tensile tests were extracted from plate part 1 of each of the three original plates (see the sample locations in appendix B). The samples were rectangular, with dimensions of 250x15 mm for layup A (UD) and 250x25 mm for layups B (QI) and C (UD+QI), in accordance with table 2 in the ASTM D3039 (2002) standard. The samples were conditioned and stored in a climate-controlled room at 20°C and 52% RH. Both ends of the sample coupons were lightly sanded, and paper end tabs were attached using Sencys universal contact adhesive to improve clamping grip and to prevent slippage from the clamps (see figures E.2a and E.2d). A speckle pattern for the DIC camera was applied to the smooth side of the samples using a base layer of white spray paint, followed by small drops of black spray paint (see figure E.2c). DIC tracks deformation by comparing a series of photos taken during the test, with the speckle pattern providing high-contrast reference points for accurate measurements. The extenso meter was attached to the rough side of the sample, using spring clips.

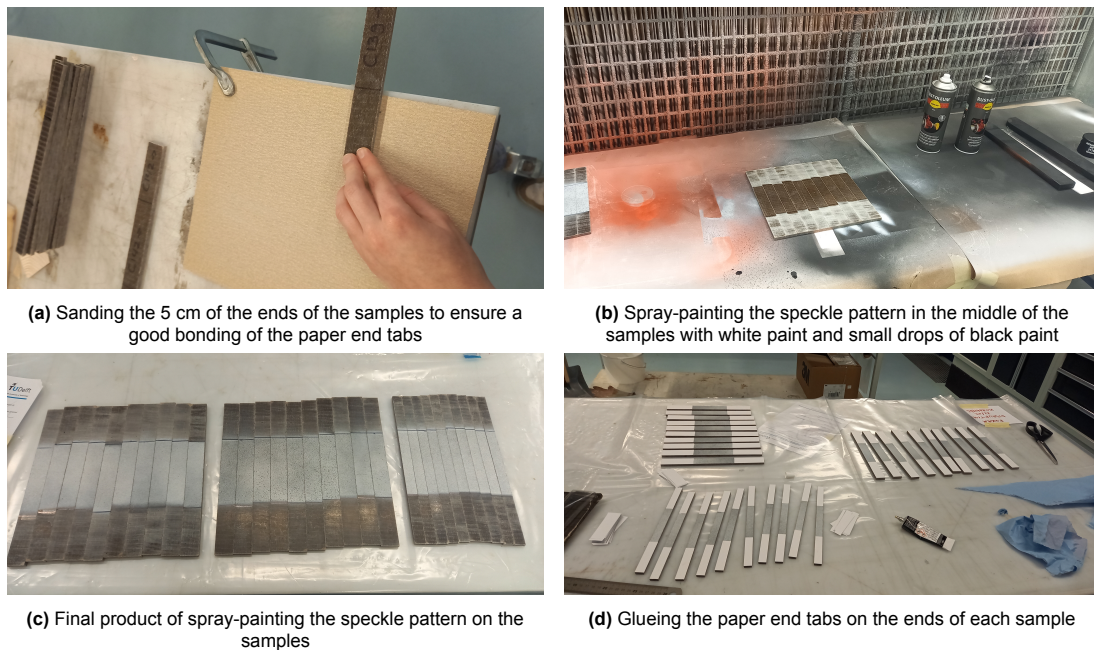


Figure E.2: Sample preparation for the quasi-static tensile tests

Table E.1: Summary of results of the quasi-static tensile tests for each layup

	Layup A (UD)	Layup B (QI)	Layup C (UD+QI)
Average max stress [MPa]	290.862	96.940	170.852
Standard deviation	34.641	6.806	27.664
Coefficient of variation [%]	11.910	7.021	16.192
Average stiffness [GPa]	24.974	9.017	14.558
Standard deviation	1.181	2.445	1.987
Coefficient of variation [%]	4.728	27.116	13.649
Average thickness [mm]	5.62	7.31	6.08
Fibre volume fraction [%]	48.96	42.78	45.07
Expected max stress [MPa]	300-360	80-100	120-140
Expected thickness [mm]	6.1	6.9	6.1
Expected FVF [%]	0.45	0.45	0.45

E.2. Results

The numerical results of the preliminary quasi-static tensile tests are summarized in table E.1, with the corresponding stress-strain curves provided in figures E.3, E.4, and E.5. The curves were cleaned by eliminating slippage (this was not needed for all samples) and were then realigned by shifting the curves over the strain axis, so that 0% strain corresponded with 0 stress. The mean values and standard deviations were calculated according to the ASTM D3039 (2002). Individual sample results are also included in appendix F. The stiffness was calculated over specific strain ranges: 0.05-0.15% for layup A, 0.05-0.25% for layup B, and 0.05-0.20% for layup C. These ranges are based on the stress, corresponding to the low stress of 10 MPa that is used as creep stress in the following tests. Due to a system failure, the DIC camera data was unusable, leaving only longitudinal strain measurements from the extensometer. Consequently, the information on transversal strain was lost.

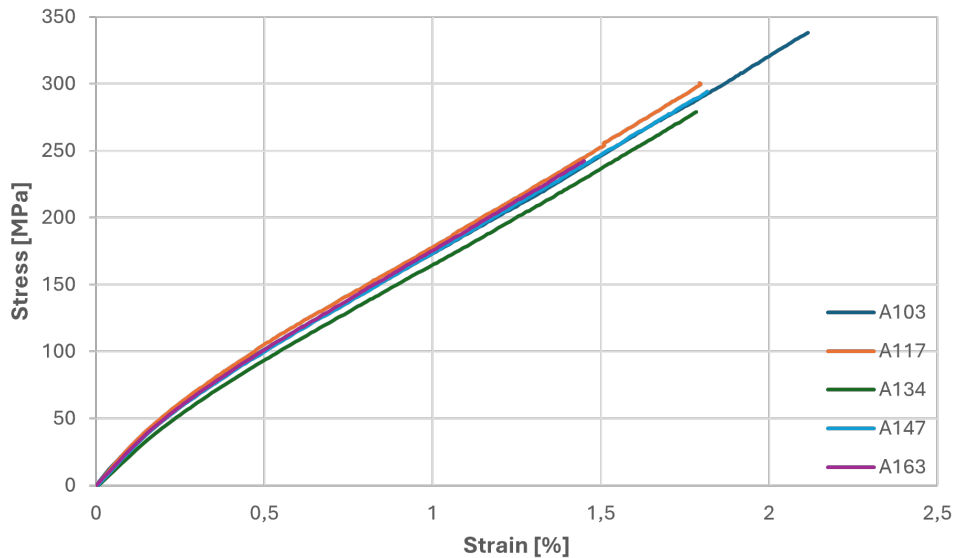


Figure E.3: Cleaned stress-strain diagram layup A, the stiffness calculated between 0.05-0.15% strain

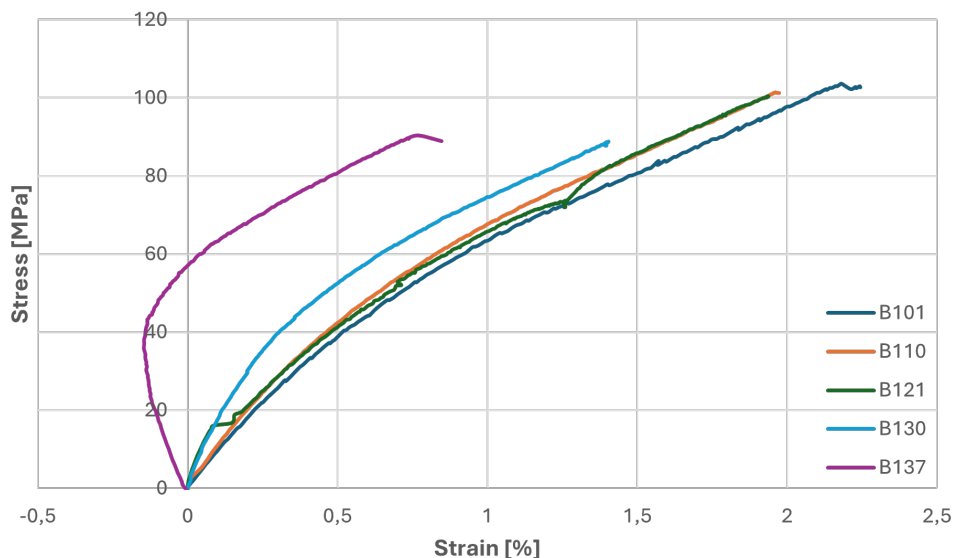


Figure E.4: Cleaned stress-strain diagram layup B, the stiffness calculated between 0.05-0.25% strain

For sample B137 (see figure E.4), the strain measurement is not correct due to slippage or incorrect

installation of the extensometer. Therefore, no stiffness was calculated for this test and the maximum strain is not taken into account for the average. This number is marked grey in table F.2.

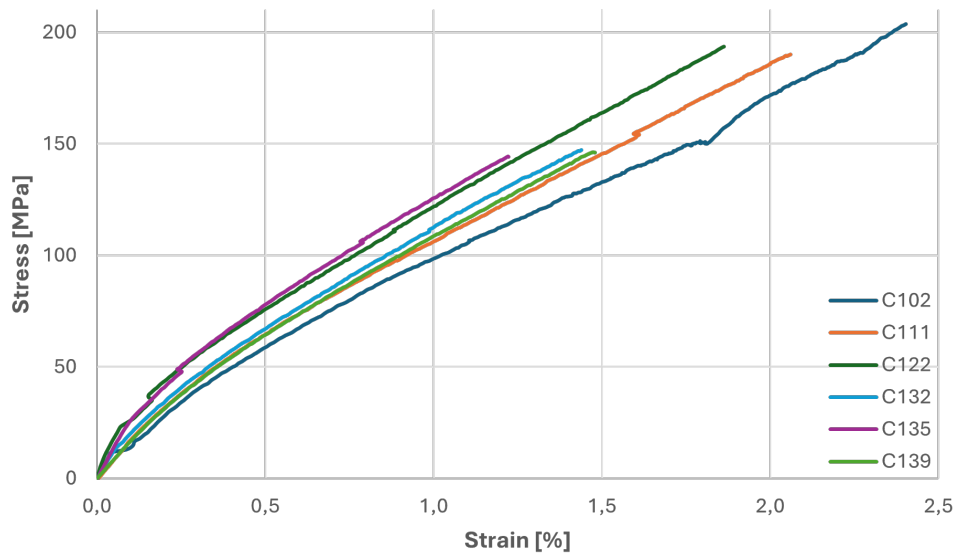


Figure E.5: Cleaned stress-strain diagram layout C, the stiffness calculated between 0.05-0.20% strain

In three samples of layout C (C132, C135, and C139), it is visible that the ultimate tensile strength is significantly lower than the strength of the first three samples (see figure E.5). This was probably due to a defect in the plate, discussed in paragraph E.3. Their numerical values are marked red in table F.3. The tests done by Wouter Claassen show the same division in the strength of samples from the left side of the plate, which show a higher UTS, and the right side of the plate, which show a lower UTS (see table F.3).

E.2.1. Failure Modes

Figure E.6 shows the failed samples of each layout for the preliminary quasi-static tensile tests, revealing that most failures occurred near the clamps. According to the ASTM D3039 (2002) standard, these failure modes can be categorized using a three-letter code, as visualized in figure 6.4. The majority of failures in figure E.6 can be classified as GAT or GAB. For layout A (figure E.6a), additional cracks parallel to the fibre direction were observed, which can be classified as SAM. This splitting over the length of the sample is typical for unidirectional layups. Since UD layups have no reinforcement in the transverse direction, the matrix is responsible for resisting the forces in that direction. The matrix is weaker and more brittle compared to the fibres, especially in shear and tension. Once the matrix is cracking, the load that was being carried by the matrix must be redistributed to the fibres, leading to stress concentrations along the length of the fibres, accelerating the propagation of longitudinal cracks. The failures near the clamps suggest that the failure is influenced by grip-related issues, such as uneven clamping pressure, slippage, or sharp edges, causing local stress concentrations. These factors may have led to premature failures that do not reflect the material's true tensile strength accurately.

Three samples of layout C failed in the middle of the specimen (classified as LGM), though these samples had a significantly lower maximum tensile stress than the other specimens (see appendix F, table F.3). A closer examination of the sample locations on plate C-1 (see appendix B, figure B.12), shows that the higher-strength samples were all taken from the left side of the plate, while the weaker samples were all from the right side of the plate. To verify this, a sixth sample from the right side of plate C-1 was tested and exhibited similar results.

Figure E.6c, shows that the failures in the middle of the samples occurred at nearly the same location in each specimen. This could indicate that the right side of plate C-1 has a defect, causing it to fail at a lower stress. Sample C142 was inspected with a portable microscope to identify any possible defects. The Microscopic images, shown in figure E.7, revealed voids in the composite layers, including at the failure location. These voids likely created weak spots, leading to premature failure. As a result,

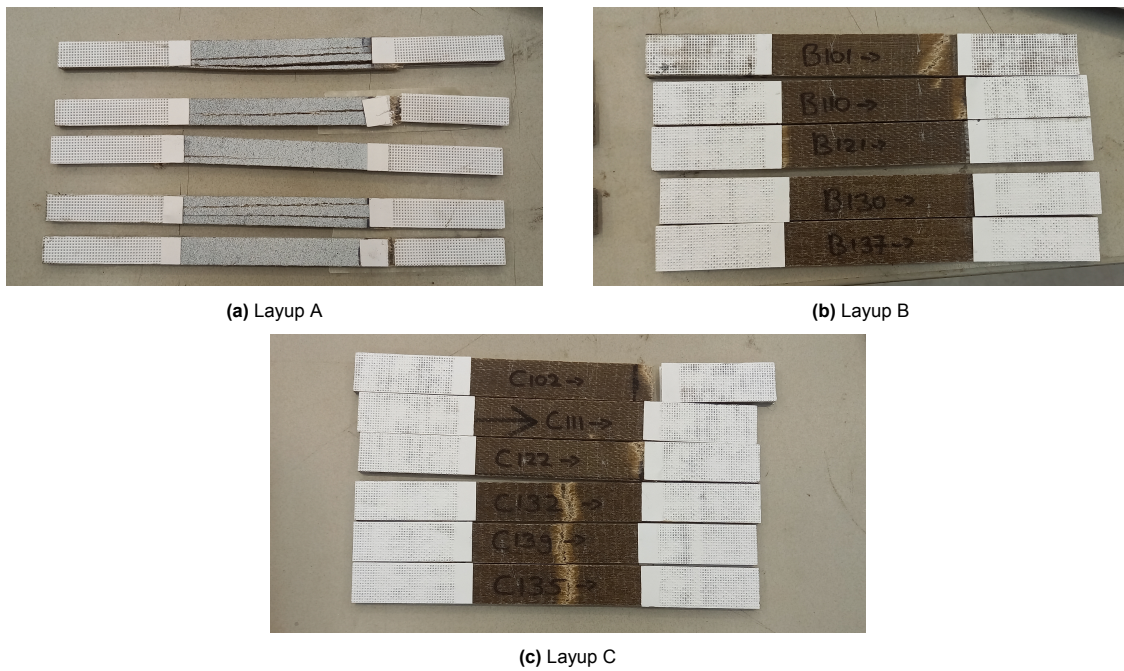


Figure E.6: Rectangular samples failed after quasi-static tensile tests

samples from the right side of plate C-1 were excluded from further testing, this includes all samples between C-123 to C-144.

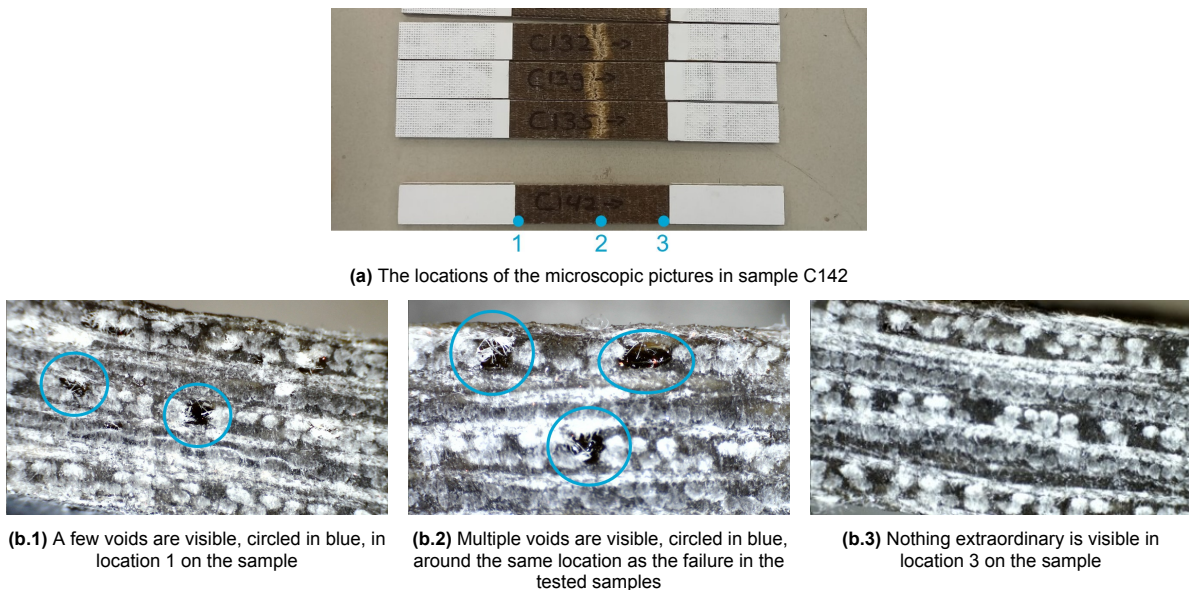


Figure E.7: Microscopic lens images on the side of sample C142 to check if any defects are present

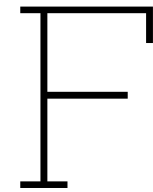
E.3. Discussion

The results in table E.1, show that the ultimate tensile strength (UTS) aligns with the expectations from paragraph 5.1.1. While layup A had a slightly lower strength than anticipated, this can be attributed to the clamp-related stress concentrations, which could have caused premature failure. On the contrary, layup C slightly exceeded its strength expectations. Layup A (UD) showed the highest tensile strength but also the highest variability, while layup B had the lowest UTS, about one-third of the strength of layup A, with the least variability. The values for layup C fell between the results of layup A and B in terms of both strength and standard deviation. The high variability in layup C's tensile strength appears to be

influenced by the differing properties of samples from the left and right side of plate C-1, as discussed in section paragraph E.2.1). This issue seems to distort the overall results for layup C in the quasi-static tensile tests.

A critical review of table E.1 and the stress-strain diagrams in figures E.3, E.4, and E.5, indicates overall inconsistencies in the results, particularly in the calculated stiffnesses. The lower parts of the stress-strain curves, especially for layups B and C, were noisy, making stiffness determination very difficult. At higher stress levels, the stiffness values became more consistent. Several factors may have contributed to these inconsistent results. First, the test environment was not climate-controlled, contrary to the original plan. Second, the 600 kN load cell used in the tests may have been too large for the tested material. The maximum forces recorded during the tests were around 25-30 kN, only 5% of the load cell's capacity, which can lead to inaccurate test results. A smaller load cell would have been more appropriate for these samples.

Due to the inconsistent results, it was decided to perform a second round of quasi-static tensile tests, using a different testing machine with a lower load cell capacity and a climate chamber to control the temperature and RH. To prevent clamp-related failures, the sample design was adjusted with slightly wider end tabs. These second quasi-static tests and their results are described in chapter 6.



Numerical Overview of Quasi-Static Tensile Test Results

An overview of the numerical results of all individual quasi-static tensile tests is presented in the following tables. Each table contains the numerical results of three quasi-static tensile tests. The first results are from the preliminary quasi-static tensile tests explained in appendix E (with rectangular shaped samples), the second series of results are from tests performed by Wouter Claassen at the Technical University of Eindhoven (with rectangular shaped samples), and the third series of results are from the quasi-static tensile tests presented in chapter 6 (with dog bone shaped samples). The numerical results are ordered tables per layup, starting on the next page.

F.1. Numerical Results Layup A (UD)

Table F.1: Numerical quasi-static tensile test results of layup A combined

Samples first round of quasi-static tensile tests			
Samples	Max Stress [MPa]	Stiffness [GPa]	Max strain [%]
A-103	338.12	24.757	2.115
A-117	300.30	26.338	1.797
A-134	279.03	23.141	1.784
A-147	294.23	25.510	1.817
A-163	242.63	25.126	1.470
Average and statistical data			
Average maximum stress	290.86 MPa		
Standard deviation	34.64		
Coefficient of variation	11.91%		
Average stiffness (0.05%-0.15%)	24.974 GPa		
Standard deviation	1.181		
Coefficient of variation	4.728%		
Average maximum strain	1.796%		
Standard deviation	0.228		
Coefficient of variation	12.707%		
Samples tested in Eindhoven by Wouter Claassen			
Samples	Max Stress [MPa]	Stiffness [GPa]	Max strain [%]
A-110	301.78	-	-
A-130	304.32	-	-
A-148	275.74	-	-
A-160	261.45	-	-
Average and statistical data			
Average maximum stress	285.82 MPa		
Standard deviation	20.76		
Coefficient of variation	7.26%		
Samples second round of quasi-static tensile tests			
Samples	Max Stress [MPa]	Stiffness [GPa]	Max strain [%]
A-207	314.43	21.534	2.13
A-210	290.63	23.021	2.01
A-215	282.29	21.116	1.89
A-217	314.03	22.579	2.13
A-220	287.04	21.923	1.99
A-222	308.55	21.426	2.16
Average and statistical data			
Average maximum stress	299.50 MPa		
Standard deviation	14.46		
Coefficient of variation	4.83%		
Average stiffness (0.05%-0.15%)	21.933 GPa		
Standard deviation	0.733		
Coefficient of variation	3.342%		
Average maximum strain	2.052%		
Standard deviation	0.106		
Coefficient of variation	5.183%		

Average thickness	5.62 mm	Expected max stress	300-360 MPa
Average fibre volume fraction	48.96%	Expected thickness	6.1 mm
		Expected fibre volume fraction	45%

F.2. Numerical Results Layup B (QI)

Table F.2: Numerical quasi-static tensile test results of layup B combined

Samples first round of quasi-static tensile tests			
Samples	Max Stress [MPa]	Stiffness [GPa]	Max strain [%]
B-101	103.66	8.216	2.241
B-110	101.36	9.295	1.973
B-121	100.44	6.356	1.938
B-130	88.85	12.200	1.403
B-137	90.39	-	0.847
Average and statistical data			
Average maximum stress	96.94 MPa		
Standard deviation	6.81		
Coefficient of variation	7.02%		
Average stiffness (0.05%-0.25%)	9.017 GPa		
Standard deviation	2.445		
Coefficient of variation	27.116%		
Average maximum strain	1.889%		
Standard deviation	0.351		
Coefficient of variation	18.580%		
Samples tested in Eindhoven by Wouter Claassen			
Samples	Max Stress [MPa]	Stiffness [GPa]	Max strain [%]
B-105	89.65	-	-
B-118	99.65	-	-
B-131	91.31	-	-
B-138	89.22	-	-
Average and statistical data			
Average maximum stress	92.46 MPa		
Standard deviation	4.88		
Coefficient of variation	5.28%		
Samples second round of quasi-static tensile tests			
Samples	Max Stress [MPa]	Stiffness [GPa]	Max strain [%]
B-201	110.58	8.020	2.319
B-205	107.55	8.258	2.254
B-209	105.74	8.257	2.207
B-212	106.70	8.322	2.250
B-213	106.65	8.180	2.258
Average and statistical data			
Average maximum stress	107.44 MPa		
Standard deviation	1.87		
Coefficient of variation	1.74%		
Average stiffness (0.05%-0.25%)	8.21 GPa		
Standard deviation	0.12		
Coefficient of variation	1.416%		
Average maximum strain	2.257%		
Standard deviation	0.040		
Coefficient of variation	1.772%		

Average thickness	7.31 mm	Expected max stress	80-100 MPa
Average fibre volume fraction	42.78%	Expected thickness	6.9 mm
		Expected fibre volume fraction	45%

F.3. Numerical Results Layup C (UD+QI)

Table F.3: Numerical quasi-static tensile test results of layup C combined

Samples first round of quasi-static tensile tests			
Samples	Max Stress [MPa]	Stiffness [GPa]	Max strain [%]
C-102	203.65	13.161	2.403
C-111	190.11	15.326	2.060
C-122	193.52	11.770	1.863
C-132	147.24	14.413	1.439
C-135	144.27	17.576	1.220
C-139	146.32	15.101	1.473
Average and statistical data			
Average maximum stress	170.85 MPa		
Standard deviation	27.66		
Coefficient of variation	16.19%		
Average stiffness (0.05%-0.20%)	14.558 GPa		
Standard deviation	1.987		
Coefficient of variation	13.649%		
Average maximum strain	1.743%		
Standard deviation	0.445		
Coefficient of variation	25.515%		
Samples tested in Eindhoven by Wouter Claassen			
Samples	Max Stress [MPa]	Stiffness [GPa]	Max strain [%]
C-110	174.77	-	-
C-119	185.01	-	-
C-123	153.67	-	-
C-133	143.74	-	-
C-138	138.23	-	-
Average and statistical data			
Average maximum stress	159.08 MPa		
Standard deviation	20.11		
Coefficient of variation	12.64%		
Samples second round of quasi-static tensile tests			
Samples	Max Stress [MPa]	Stiffness [GPa]	Max strain [%]
C-201	191.01	14.200	2.072
C-204	182.73	14.200	2.089
C-208	173.37	14.715	1.890
C-210	191.96	14.895	2.038
C-212	194.64	14.003	2.213
C-216	192.20	13.852	2.164
Average and statistical data			
Average maximum stress	190.51 MPa		
Standard deviation	4.55		
Coefficient of variation	2.39%		
Average stiffness (0.05%-0.20%)	14.311 GPa		
Standard deviation	0.409		
Coefficient of variation	2.855%		
Average maximum strain	2.12%		
Standard deviation	0.07		
Coefficient of variation	3.379%		

Average thickness	6.08 mm	Expected max stress	120-140 MPa
Average fibre volume fraction	45.07%	Expected thickness	6.1 mm
		Expected fibre volume fraction	45%



Long-Term Tensile Creep Test Results

G.1. Uncorrected Longitudinal Long-Term Creep Curves

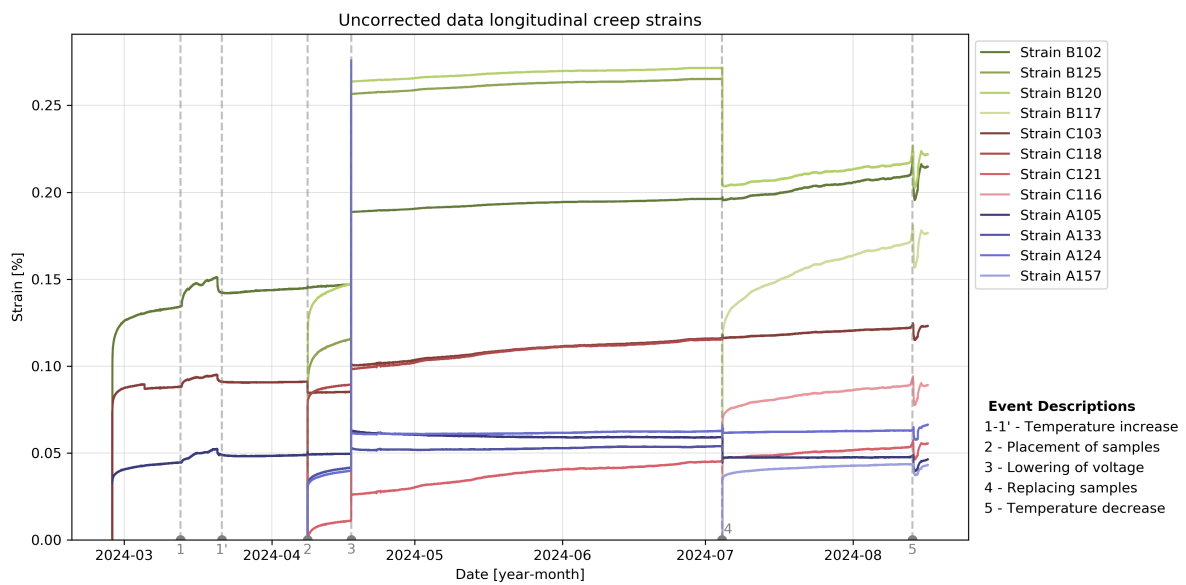


Figure G.1: Uncorrected longitudinal strain of the samples in the long-term creep test setup, with the absolute time on the horizontal axis, and the interruptions of the test marked by vertical grey dashed lines numbered 1 to 5. The curves are coloured by layup

G.1.1. Longitudinal Strain Measured in Dummy Samples

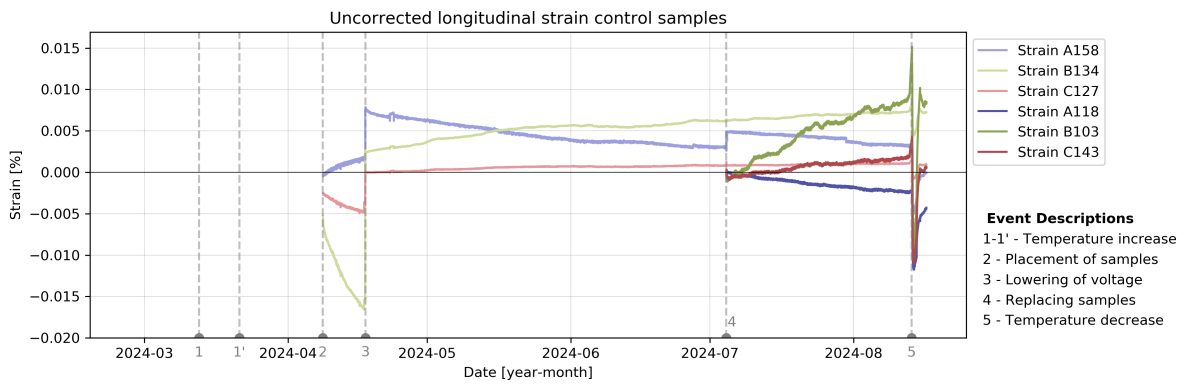


Figure G.2: Uncorrected longitudinal strain of the dummy samples , with the absolute time on the horizontal axis, and the interruptions of the test marked by vertical grey dashed lines numbered 1 to 5. The curves are coloured by layout

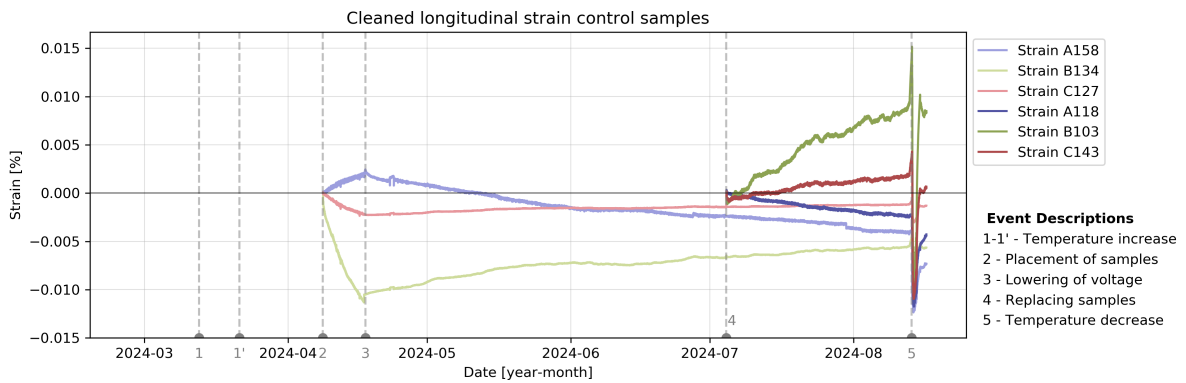


Figure G.3: Cleaned longitudinal strain of the dummy samples , with the absolute time on the horizontal axis, and the interruptions of the test marked by vertical grey dashed lines numbered 1 to 5. The curves are coloured by layout

G.2. Transversal Long-Term Creep Curves

Although the transversal strains were not used for the comparisons in the report, it was measured during the creep test and thus presented here as uncorrected and cleaned creep curves. The transversal creep curves are not compensated here, but this could be done in future research.

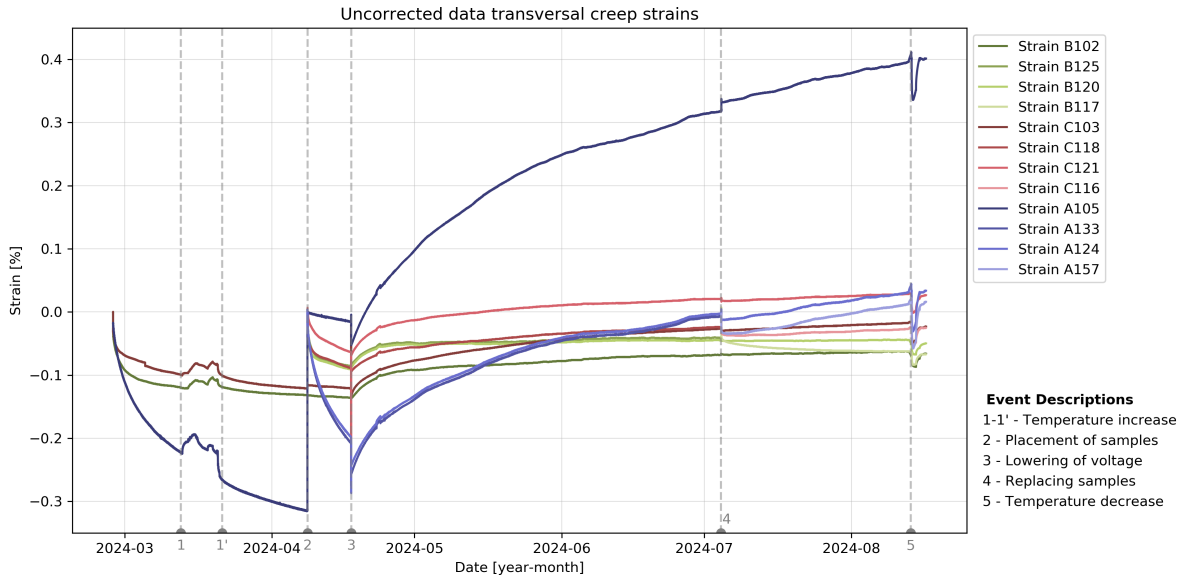


Figure G.4: Uncorrected longitudinal strain of the samples in the long-term creep test setup, with the absolute time on the horizontal axis, and the interruptions of the test marked by vertical grey dashed lines numbered 1 to 5. The curves are coloured by layup

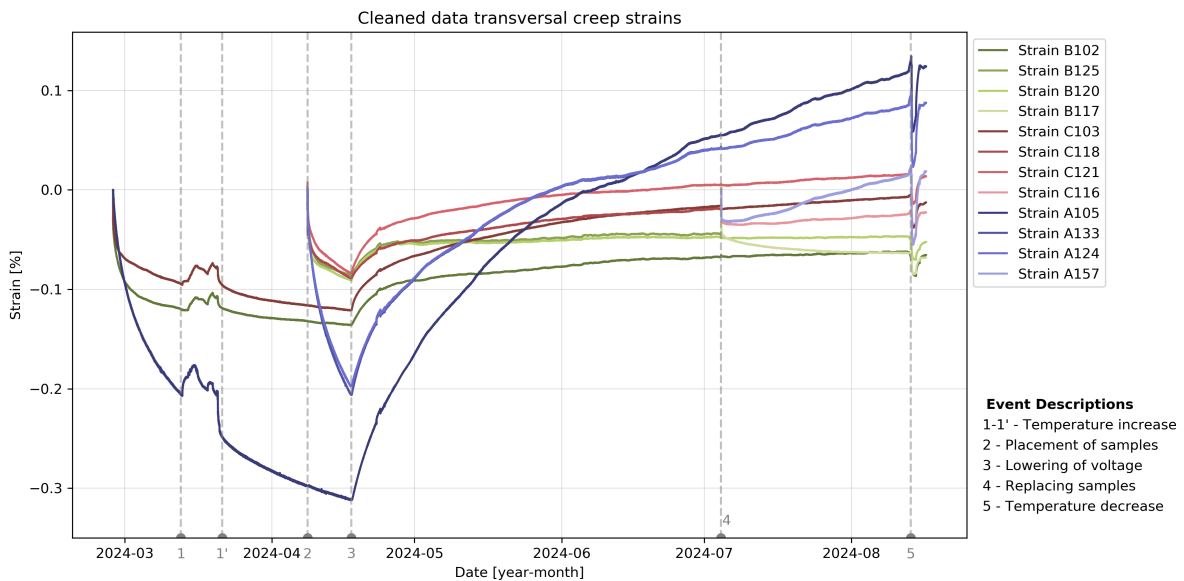


Figure G.5: Uncorrected longitudinal strain of the samples in the long-term creep test setup, with the absolute time on the horizontal axis, and the interruptions of the test marked by vertical grey dashed lines numbered 1 to 5. The curves are coloured by layup

G.2.1. Transversal Strain Measured in Dummy Samples

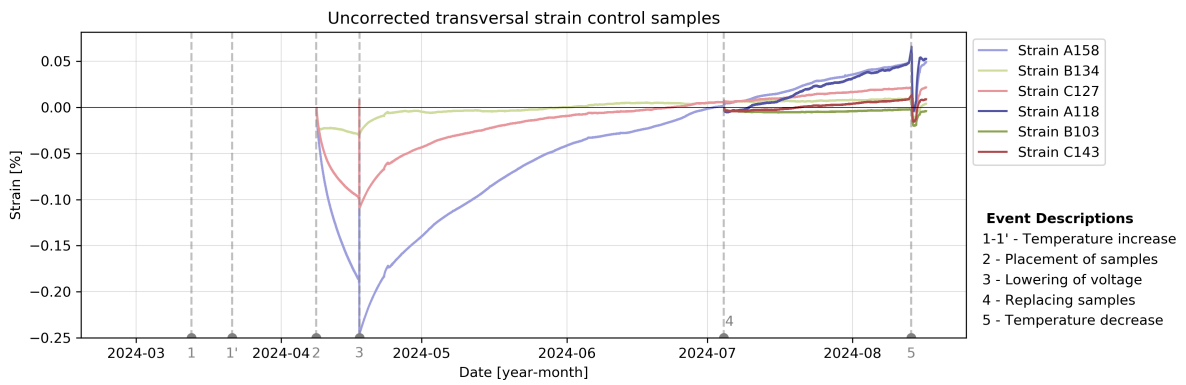


Figure G.6: Uncorrected longitudinal strain of the dummy samples , with the absolute time on the horizontal axis, and the interruptions of the test marked by vertical grey dashed lines numbered 1 to 5. The curves are coloured by layout

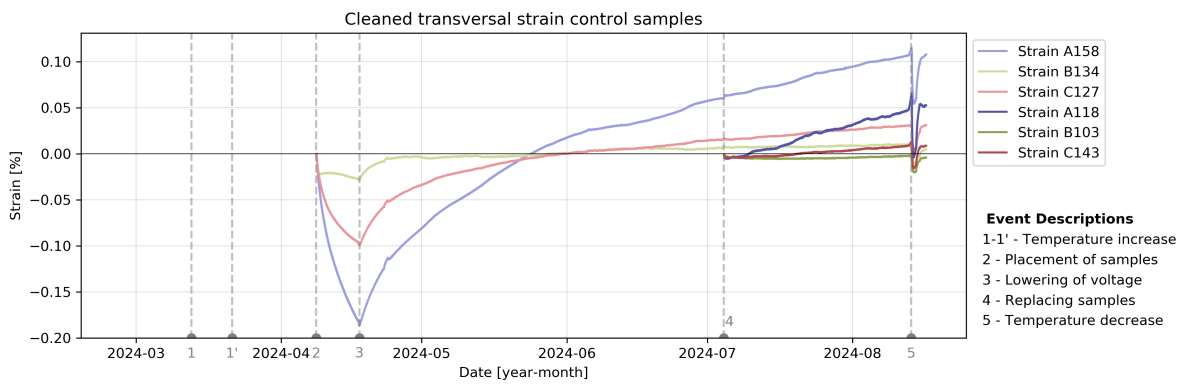
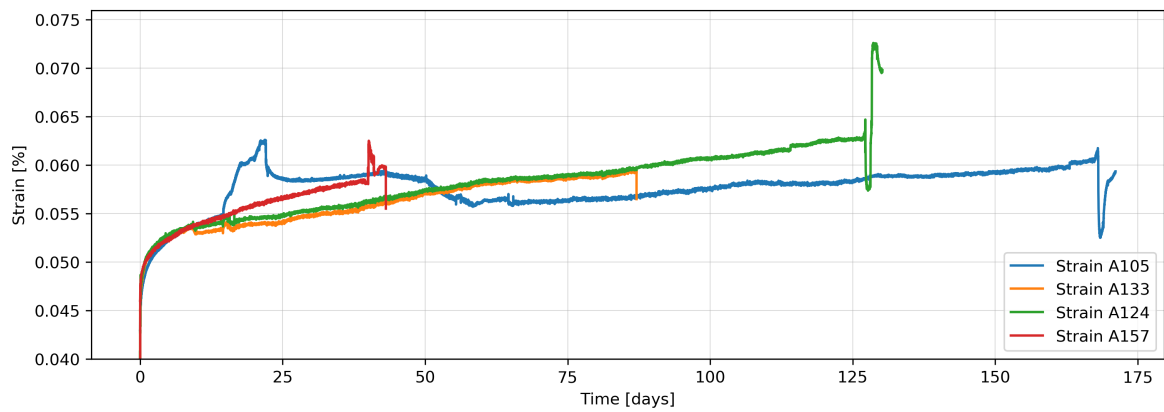
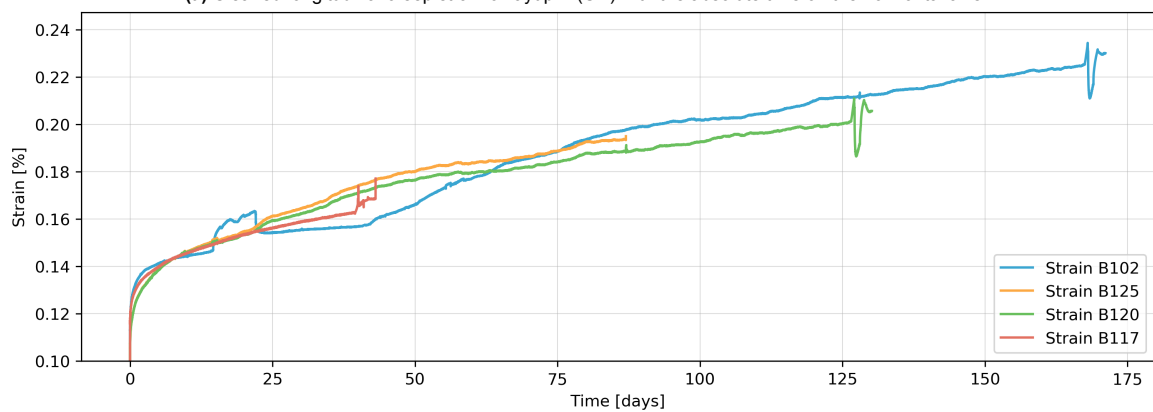


Figure G.7: Cleaned longitudinal strain of the dummy samples, with the absolute time on the horizontal axis, and the interruptions of the test marked by vertical grey dashed lines numbered 1 to 5. The curves are coloured by layout

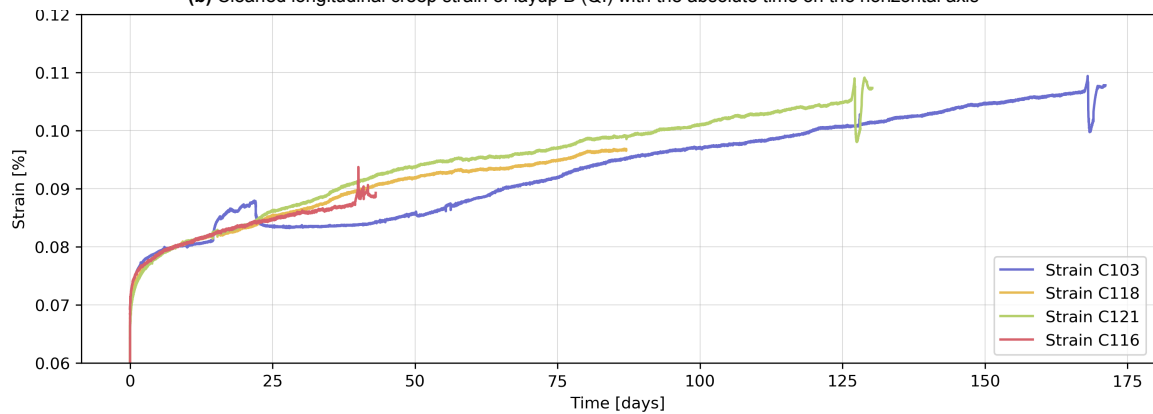
G.3. Re-Alignment of Cleaned Creep Curves to Compare the Slopes



(a) Cleaned longitudinal creep strain of layup A (UD) with the absolute time on the horizontal axis



(b) Cleaned longitudinal creep strain of layup B (QI) with the absolute time on the horizontal axis



(c) Cleaned longitudinal creep strain of layup C (UD+QI) with the absolute time on the horizontal axis

Figure G.8: Shifted, cleaned, and compensated long-term creep curves, with the relative time on the horizontal axis, and shifted to align the slopes of the curves around the relative time of 0.065×10^7 seconds, to compare the development of the slopes of the curves. Keep in mind that the curves did not endure the same conditions/disruptions

H

Accelerated Creep Test Results

H.1. Specifications of Each SSM Test

Starting date: May 30		Sample: A126	Picture after test
Before test	Lab conditions	-	
	Weight dummy samples	-	
	Cup of water in climate room?	no	
	Clamping strength	20 Nm, No tabs	
After tests	Failure mode	Failed in clamps (GAB)	
	Duration of test	± 12 hours	
	Conditions in climate room	T: 20°C	
	Weight dummy samples	-	
	Notes	<p>The strain gauge output is very noisy, the extensometer signal is much cleaner so for next samples the strain is only measured with an extensometer (gauge length 25 mm). Test was started a little too early before the temperature was stable. There is a small bump visible in the first step of the graph. The temperature measurement computer failed at some point during the test</p>	

Starting date: May 31, 15:30		Sample: A151	Picture after test
Before test	Lab conditions	T: 21°C RH: 50%	
	Weight dummy samples	-	
	Cup of water in climate room?	no	
	Clamping strength	15 Nm, No tabs	
After tests	Failure mode	Failed in clamps (GAT)	
	Duration of test	± 10.5 hours	
	Conditions in climate room	T: 20°C RH: 37%	
	Weight dummy samples	-	
Notes		The relative humidity drops when the nitrogen cooling system is turned on. It is not exactly clear what the mean RH is but it fluctuates between 25% and 60%. Add dummy samples to see what the relative humidity does with the moisture in the samples. The temperature measurement computer failed at some point during the test	

Starting date: June 3, 18:00		Sample: A168	Picture after test
Before test	Lab conditions	T: 19,9°C RH: 58%	
	Weight dummy samples	A128: 27.4383 gr A154: 26.7225 gr	
	Cup of water in climate room?	no	
	Clamping strength	14 Nm, no tabs	
After tests	Failure mode	Failed in clamps (GAB)	
	Duration of test	± 10.5 hours	
	Conditions in climate room	T: 20°C RH: %	
	Weight dummy samples	A128: 27.4122 gr (-0.095%) A154: 26.6973 gr (-0.094%)	
Notes		Sample failed in 5 th step already	

Starting date: June 5: 16:30		Sample: C209	Picture after test
Before test	Lab conditions	T: 23.8°C RH: 35%	
	Weight dummy samples	A128: 27.3978 gr A154: 26.6844 gr	
	Cup of water in climate room?	yes	
	Clamping strength	16 Nm	
After tests	Failure mode	Slipped (OAB)	
	Duration of test	±14 hours	
	Conditions in climate room	T: 20 °C RH: 43-25%	
	Weight dummy samples	A128: 27.3874 gr (-0.038%) A154: 26.6716 gr (-0.048%)	
	Notes	Paper end tab slipped from sample (dog bone-shaped). Used adhesive for paper tabs was: Sencys universal contact adhesive	
Starting date: June 6, 10:30		Sample: A208	Picture after test
Before test	Lab conditions	T: 23°C RH: 40%	
	Weight dummy samples	A128: 27.3874 gr A154: 26.6716 gr	
	Cup of water	yes	
	Clamping strength	16 Nm	
After tests	Failure mode	Slippage (OAB)	
	Duration of test	±10 hours	
	Conditions in climate room	T: 20 °C RH: 55-25%	
	Weight dummy samples	A128: 27.3797 gr A154: 26.6651 gr	
	Notes	Paper end tab slipped from sample (dog bone-shaped), used adhesive was Sencys universal contact adhesive	
Starting date: June 7, 11:30		Sample: B210	Picture after test
Before test	Lab conditions	T: 24°C RH: 45%	
	Weight dummy samples	B202: 56.3647 gr B215: 61.9714 gr	
	Cup of water	yes	
	Clamping strength	20 Nm	
After tests	Failure mode	Clamp failure (GAT)	
	Duration of test	±11 hours	
	Conditions in climate room	T: 23°C RH: 46 %	
	Weight dummy samples	-	
	Notes	Dummy sample B215 was not yet cut shorter to 23 cm and therefore heavier than the other sample. Paper end tabs with dog bone-shaped sample were used, with Sencys universal contact adhesive. The cooling system failed during the test, but probably after failure of the sample	

Starting date: June 10		Sample: C202	Picture after test
Before test	Lab conditions	T: 23°C RH: 45%	
	Weight dummy samples	-	
	Cup of water	yes	
	Clamping strength	18 Nm	
After tests	Failure mode	No failure	
	Duration of test	± 19 hours	
	Conditions in climate room	Lab conditions	
	Weight dummy samples	-	
	Notes	No cooling system available for this test, temperature slightly decreased over the test. The sample did not slip or fail. Paper end tabs were used with Sencys universal contact adhesive. Test was stopped before failure.	
Starting date: June 11		Sample: A218	
Before test	Lab conditions	T: 23°C RH: 37%	
	Weight dummy samples	A128: 27.3975 gr A154: 26.6828 gr	
	Cup of water	yes	
	Clamping strength	18 Nm	
After tests	Failure mode	Slippage (OAB)	
	Duration of test	±10.5 hours	
	Conditions in climate room	Lab conditions	
	Weight dummy samples	A128: 27.3842 gr A154: 26.6694 gr	
	Notes	No cooling system available, temperature slightly increased over the test temperatures stayed between 23 and 24°C. Paper end tabs were used with Sencys universal contact adhesive.	
Starting date: June 12		Sample: B214	
Before test	Lab conditions	T: 23°C RH: 37%	
	Weight dummy samples	A128: 27.3776 gr A154: 26.6669 gr	
	Cup of water	yes	
	Clamping strength	18 Nm	
After tests	Failure mode	Clamp failure (GAT)	
	Duration of test	±11 hours	
	Conditions in climate room	Lab conditions	
	Weight dummy samples	A128: 27.3766 gr A154: 26.6614 gr	
	Notes	No cooling system available, the test temperatures stayed between 20 and 23°C. Paper end tabs were used with Sencys universal contact adhesive. Temperature probe on sample failed.	

Starting date: June 13, 14:00		Sample: B202	Picture after test
Before test	Lab conditions	T: 24°C RH: 37%	
	Weight dummy samples	A128: 27.3766 gr A154: 26.6614 gr	
	Cup of water	yes	
	Clamping strength	18 and 16.5 Nm	
After tests	Failure mode	Sample failure (LGM)	
	Duration of test	±12 hours	
	Conditions in climate room	T: 20°C RH: 36-42%	
	Weight dummy samples	A128: 27.3713 gr A154: 26.6543 gr	
	Notes	Paper end tabs glued with two-component epoxy adhesive, Loctite EA 3425. Outer screws were more tightened than inner screws to gradually introduce the force. This is repeated for all next samples. T1 (temperature probe air inside climate chamber) failed.	
Starting date: June 14, 15:15		Sample: C217	
Before test	Lab conditions	T: 23°C RH: 49%	
	Weight dummy samples	C144: 48.5421 gr C141: 48.1923 gr	
	Cup of water	yes	
	Clamping strength	18 and 16.5 Nm	
After tests	Failure mode	No failure	
	Duration of test	±34 hours	
	Conditions in climate room	T: 20°C RH: 35-52%	
	Weight dummy samples	C144: 48.4764 gr C141: 48.1257 gr	
	Notes	Paper end tabs glued with two-component epoxy adhesive, Loctite EA 3425. Temp probes T1 and T5 (inside air and on sample) failed. The probes were replaced for the next tests	
Starting date: June 17, 14:45		Sample: C205	
Before test	Lab conditions	T: 24°C RH: 48%	
	Weight dummy samples	C144: 48.4764 gr C141: 48.1257 gr	
	Cup of water	yes	
	Clamping strength	18 and 16.5 Nm	
After tests	Failure mode	No failure	
	Duration of test	±19 hours	
	Conditions in climate room	-	
	Weight dummy samples	C144: 48.4533 gr C141: 48.1065 gr	
	Notes	Paper end tabs glued with two-component epoxy adhesive, Loctite EA 3425. Temperature probe T2 slipped from sample during testing	

Starting date: June 18, 15:00		Sample: A223	Picture after test
Before test	Lab conditions	T: 23°C RH:49 %	
	Weight dummy samples	A128: 27.3614 A154: 26.6482	
	Cup of water	yes	
	Clamping strength	18 and 16.5 Nm	
After tests	Failure mode	In tab and over length	
	Duration of test	±15 hours	
	Conditions in climate room	T: 20°C RH: 37-42%	
	Weight dummy samples	A128: 27.3584 gr A154: 26.6443 gr	
	Notes	Tapered composite end tabs glued with two-component epoxy adhesive, Loctite EA 3425. Temperature T2 slipped off sample, but could have been after failure	

Starting date: June 19, 15:00		Sample: B206	Picture after test
Before test	Lab conditions	T: 24°C RH: 48%	
	Weight dummy samples	B107: 58.9349 gr B128: 58.1282 gr	
	Cup of water	yes	
	Clamping strength	18 and 16.5 Nm	
After tests	Failure mode	Sample failure (LGT)	
	Duration of test	±12.5 hours	
	Conditions in climate room	T: 21°C RH: 37-41%	
	Weight dummy samples	B107: 58.8933 gr B128: 58.0870 gr	
	Notes	Paper end tabs glued with two-component epoxy adhesive, Loctite EA 3425.	

Starting date: June 20, 15:30		Sample: B215	Picture after test
Before test	Lab conditions	T: 22°C RH: 50%	
	Weight dummy samples	B107: 58.8933 gr B128: 58.0870 gr	
	Cup of water	yes	
	Clamping strength	18 and 16.5 Nm	
After tests	Failure mode	Sample failure (LGT)	
	Duration of test	±12 hours	
	Conditions in climate room	T: 21°C RH: 38-50%	
	Weight dummy samples	B107: 58.8871 gr B128: 58.0818 gr	
	Notes	Paper end tabs glued with two-component epoxy adhesive, Loctite EA 3425. At the start of the test, very heavy vibrations were present in the machine force control	

Starting date: June 21, 13:45		Sample: C213	Picture after test
Before test	Lab conditions	T: 23°C RH: 55%	
	Weight dummy samples	C144: 48.4793 gr C141: 48.1316 gr	
	Cup of water	yes	
	Clamping strength	18 and 16.5 Nm	
After tests	Failure mode	No failure	
	Duration of test	±34 hours	
	Conditions in climate room	-	
	Weight dummy samples	C144: 48.4311 gr C141: 48.0820 gr	
	Notes	Paper end tabs glued with two-component epoxy adhesive, Loctite EA 3425.	

Starting date: June 24, 14:00		Sample: C211	Picture after test
Before test	Lab conditions	T: 25°C RH: 46%	
	Weight dummy samples	C144: 48.4311 gr C141: 48.0820 gr	
	Cup of water	yes	
	Clamping strength	18 and 16.5 Nm	
After tests	Failure mode	No failure	
	Duration of test	±19 hours	
	Conditions in climate room	T: 21°C RH: 37-47%	
	Weight dummy samples	C144: 48.4321 gr C141: 48.0846 gr	
	Notes	Paper end tabs glued with two-component epoxy adhesive, Loctite EA 3425.	

Starting date: June 26, 15:30		Sample: B211	Picture after test
Before test	Lab conditions	T: 28°C RH: 47%	
	Weight dummy samples	B107: 58.8832 gr B128: 58.0788 gr	
	Cup of water	yes	
	Clamping strength	18 and 16.5 Nm	
After tests	Failure mode	Sample failure (LGT)	
	Duration of test	±12.5 hours	
	Conditions in climate room	T: 20°C RH: 39-49%	
	Weight dummy samples	B107: 58.8743 gr B128: 58.0698 gr	
	Notes	Paper end tabs glued with two-component epoxy adhesive, Loctite EA 3425. Temperatures in the lab were very high	

Starting date: June 27, 14:00		Sample: B207	Picture after test
Before test	Lab conditions	T: 28°C RH: 50%	
	Weight dummy samples	B216: 62.1974 gr B216: 62.5293 gr	
	Cup of water	yes	
	Clamping strength	18 and 16.5 Nm	
After tests	Failure mode	Sample failure (LGB)	
	Duration of test	±11.5 hours	
	Conditions in climate room	T: 20°C RH: 38-45%	
	Weight dummy samples	B216: 62.1117 gr B216: 62.4497 gr	
	Notes	Paper end tabs glued with two-component epoxy adhesive, Loctite EA 3425. Temperatures in the lab were very warm	

Starting date: June 28, 14:30		Sample: C207	Picture after test
Before test	Lab conditions	T: 25°C RH: 40%	
	Weight dummy samples	C131: 48.2710 gr C140: 47.9955 gr	
	Cup of water	yes	
	Clamping strength	18 and 16.5 Nm	
After tests	Failure mode	Sample failure (LGT)	
	Duration of test	±36 hours	
	Conditions in climate room	-	
	Weight dummy samples	C131: 48.1908 gr C140: 47.9182 gr	
	Notes	Paper end tabs glued with two-component epoxy adhesive, Loctite EA 3425. The sample failed, but this happened after the test. The test ran during the weekend. The measurements stopped after 32 hours but the force stayed on the sample. The sample broke (triggering the machine interlock) at July 1 at 01:30 AM	

Starting date: July 1, 14:00		Sample: A204	Picture after test
Before test	Lab conditions	T: 23°C RH: 45%	
	Weight dummy samples	A128: 27.3556 gr A154: 26.6428 gr	
	Cup of water	yes	
	Clamping strength	18 and 16.5 Nm	
After tests	Failure mode	In tab and over length	
	Duration of test	±13 hours	
	Conditions in climate room	T: 20°C RH: 37-48%	
	Weight dummy samples	A128: 27.3524 gr A154: 26.6404 gr	
	Notes	Tapered composite end tabs glued with two-component epoxy adhesive, Loctite EA 3425. This sample has started a test before, which only ran for 2 hours. The test was restarted, starting again at a reference stress of 10 MPa. T2 temperature probe was detached from the sample after the test	

H.2. Raw Data of the SSM Tests with Large Stress Increments

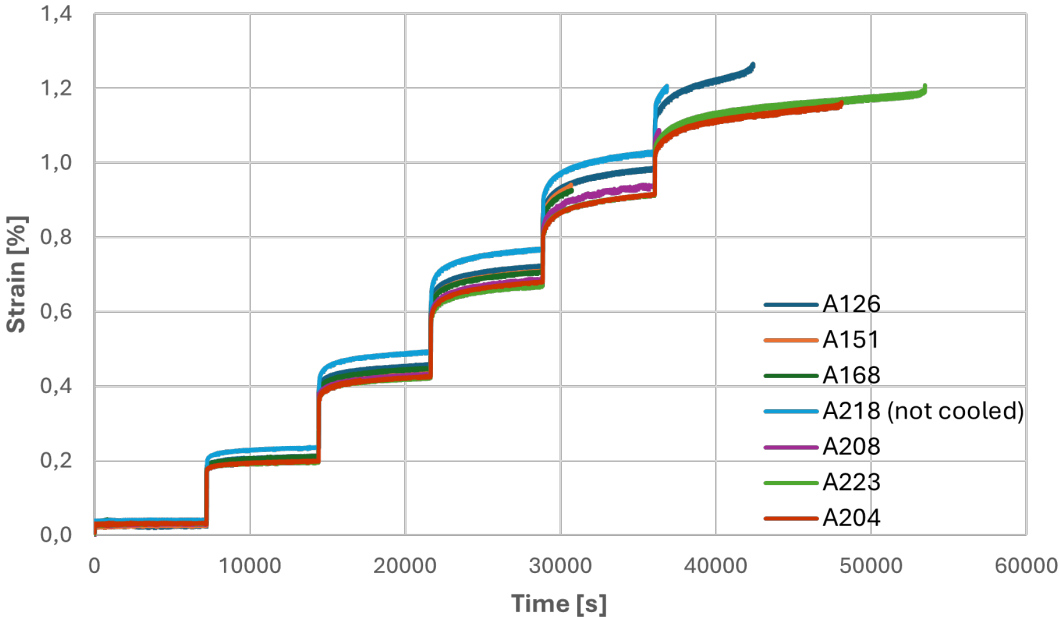


Figure H.1: Raw data of the accelerated tensile creep test using the SSM for layup A, showing only the tests with the large stress increments

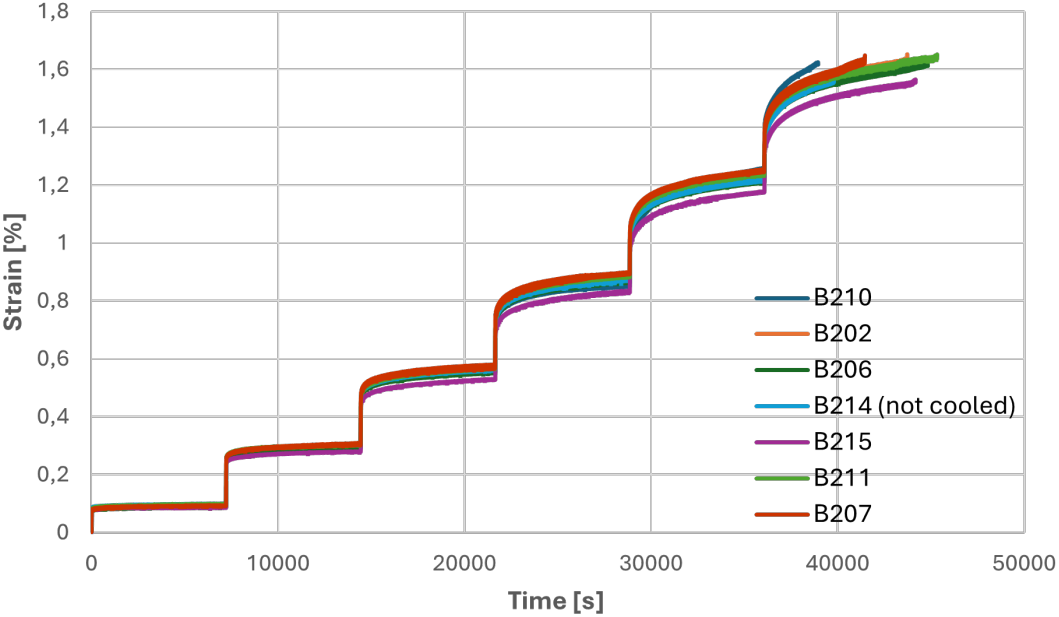


Figure H.2: Raw data of the accelerated tensile creep test using the SSM for layup B, showing only the tests with the large stress increments

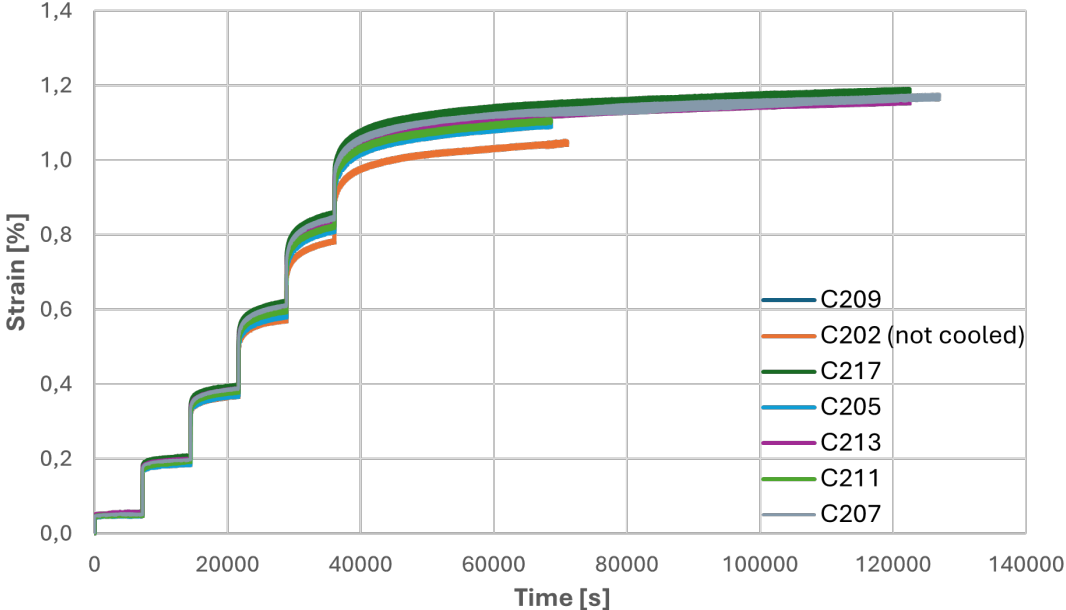


Figure H.3: Raw data of the accelerated tensile creep test using the SSM for layup C, showing only the tests with the large stress increments

H.3. SSM Processed Creep Master Curves on Full Timescale

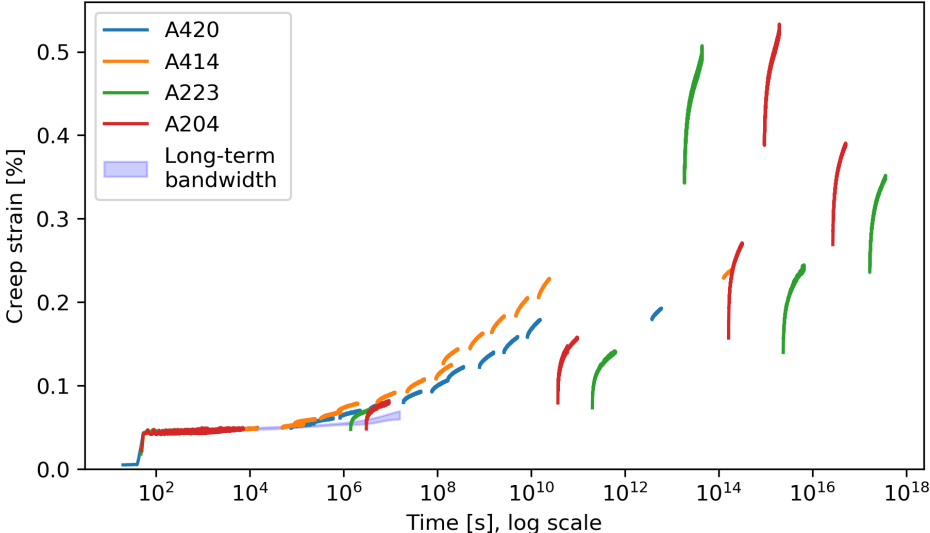


Figure H.4: SSM constructed creep master curves for layup A (UD), all steps are visible as the timescale is not cut at 300 years

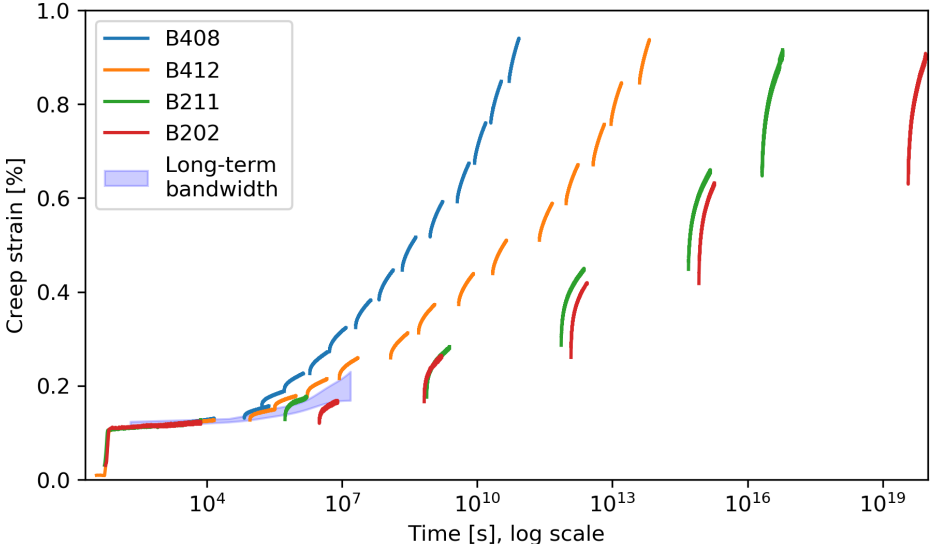


Figure H.5: SSM constructed creep master curves for layup B (QI), all steps are visible as the timescale is not cut at 300 years